Institut für Geowissenschaften

Mathematisch-Naturwissenschaftliche Fakultät

Universität Potsdam

Fluvial sediment routing and the carbon cycle

Insights from the Rio Bermejo, Argentina

Marisa Repasch

CUMULATIVE DISSERTATION

for obtaining the academic degree

"Doctor of Natural Sciences" (Dr. rer. nat.)

in the discipline of *Geochemistry*

Submitted to the

Faculty of Mathematics and Natural Sciences

Institute for Geosciences

of the University of Potsdam, Germany

Potsdam, 28 September 2020

Published online on the
Publication Server of the University of Potsdam:
https://doi.org/10.25932/publishup-49397
https://nbn-resolving.org/urn:nbn:de:kobv:517-opus4-493978

DECLARATION

I hereby declare that this dissertation was prepared independently by the author, Marisa Repasch. All ideas derived from other sources are identified as such. The manuscripts composing the main body of this work were collaborative efforts, and co-authors and their respective roles are defined in the author contributions. Finally, this work has not been submitted to any other institution of higher education.

Potsdam, 28 September 2020

Marisa Repasch
PhD Candidate

Supervisors:
Dr. Niels Hovius
Dr. Dirk Sachse

Reviewers:
Dr. Gesine Mollenhauer
Dr. A. Joshua West
Dr. Niels Hovius

GENERAL SUMMARY

The global carbon cycle describes the circulation of carbon through our planet's major reservoirs, primarily the biosphere (living plants and soil), the oceans, the lithosphere (rocks), and the atmosphere. The amount of carbon contained in our atmosphere regulates our planet's surface temperature, and ultimately the ability of our planet to sustain life. Understanding the future of Earth's habitability requires knowing how the amount of carbon in Earth's reservoirs has changed in the past and the mechanisms driving those changes, including the role of human activities. By establishing a baseline for how the natural carbon cycle works without human influence, we can build models to predict the possible influence of human activities on Earth's future climate. This dissertation focuses on the organic carbon cycle. Organic carbon is produced by plants, and when plants die or lose their leaves seasonally, their organic carbon is transferred to soil. Soil can be eroded into rivers, which transfer organic carbon from the biosphere into the oceans and the lithosphere. Because organic carbon molecules are not stable at Earth's surface, organic carbon can transform into carbon dioxide during downstream transit in rivers, resulting in a flux of carbon dioxide to the atmosphere. The aim of this dissertation is to understand what happens to organic carbon during its travel through rivers between mountain sources and ocean sinks. I use geochemical methods to study how long it takes sediment to move downstream through a river, how organic carbon changes during long-distance river transport, and how erosion and deposition processes affect the amounts of organic carbon that are preserved versus transformed to carbon dioxide in river systems.

ALLGEMEINE ZUSAMMENFASSUNG

Der globale Kohlenstoffkreislauf beschreibt die Zirkulation von Kohlenstoff durch die Hauptreservoire unseres Planeten, in erster Line die Biosphäre (lebende Pflanzen), Ozeane, die Lithosphäre (Gestein) und die Atmosphäre. Der Kohlenstoffanteil in unserer Atmosphäre reguliert die Oberflächentemperatur unseres Planeten und damit letztendlich die Fähigkeit unseres Planeten, Leben zu erhalten. Um zu verstehen, wie sich die zukünftige Bewohnbarkeit der Erde entwickelt, ist Wissen darüber erforderlich, wie sich die Kohlenstoffmenge in den Reservoiren der Erde in der Vergangenheit verändert hat und welche Mechanismen diese Veränderungen antreiben. Dies beinhaltet auch die vom Menschen verursachten Veränderungen. Indem wir die Funktionsweise des natürlichen Kohlenstoffkreislaufs ohne menschlichen Einfluss ergründen, sind wir in der Lage Modelle zu erstellen, die den menschlichen Einfluss auf das zukünftige Klima der Erde vorhersagen. Diese Dissertation befasst sich mit dem organischen Kohlenstoffkreislauf. Organischer Kohlenstoff wird von Pflanzen produziert. Sterben diese Pflanzen ab, oder verlieren saisonal bedingt ihre Blätter, verlagert sich der organische Kohlenstoff in den Boden. Der Boden kann erodiert und in Flüssen eingetragen werden, die den organischen Kohlenstoff von der Biosphäre in Ozeane und die Lithosphäre transportieren. Da organische Kohlenstoffmoleküle an der Erdoberfläche nicht stabil sind, kann organischer Kohlenstoff beim Übergang von der Biosphäre in die Ozeane in Kohlendioxid umgewandelt werden. Dies führt zu einem Kohlendioxidfluss in die Atmosphäre. Ziel dieser Dissertation ist es, zu verstehen was mit organischem Kohlenstoff aus einem Quellgebiet im Gebirge auf seinem Weg durch die Flüsse bis hin zu ozeanischen Senken passiert. Ich verwende in dieser Dissertation geochemische Methoden, um die Dauer von Sedimenttransport flussabwärts zu untersuchen, wie sich organischer Kohlenstoff bei diesem Langstreckentransport verändert und wie Erosions- und Ablagerungseffekte das Verhältnis zwischen konserviertem und oxidiertem Kohlenstoff in Flusssystemen beeinflussen.

ABSTRACT

By regulating the concentration of carbon in our atmosphere, the global carbon cycle drives changes in our planet's climate and habitability. Earth surface processes play a central, yet insufficiently constrained role in regulating fluxes of carbon between terrestrial reservoirs and the atmosphere. River systems drive global biogeochemical cycles by redistributing significant masses of carbon across the landscape. During fluvial transit, the balance between carbon oxidation and preservation determines whether this mass redistribution is a net atmospheric CO_2 source or sink. Existing models for fluvial carbon transport fail to integrate the effects of sediment routing processes, resulting in large uncertainties in fluvial carbon fluxes to the oceans.

In this Ph.D. dissertation, I address this knowledge gap through three studies that focus on the timescale and routing pathways of fluvial mass transfer and show their effect on the composition and fluxes of organic carbon exported by rivers. The hypotheses posed in these three studies were tested in an analog lowland alluvial river system – the Rio Bermejo in Argentina. The Rio Bermejo annually exports more than 100 Mt of sediment and organic matter from the central Andes, and transports this material nearly 1300 km downstream across the lowland basin without influence from tributaries, allowing me to isolate the effects of geomorphic processes on fluvial organic carbon cycling. These studies focus primarily on the geochemical composition of suspended sediment collected from river depth profiles along the length of the Rio Bermejo.

In Chapter 3, I aimed to determine the mean fluvial sediment transit time for the Rio Bermejo and evaluate the geomorphic processes that regulate the rate of downstream sediment transfer. I developed a framework to use meteoric cosmogenic ^{10}Be ($^{10}Be_m$) as a chronometer to track the duration of sediment transit from the mountain front downstream along the ~1300 km channel of the Rio Bermejo. I measured $^{10}Be_m$ concentrations in suspended sediment sampled from depth profiles, and found a 230% increase along the fluvial transit pathway. I applied a simple model for the time-dependent accumulation of $^{10}Be_m$ on the floodplain to estimate a mean sediment transit time of 8.5±2.2 kyr. Furthermore, I show that sediment transit velocity is influenced by lateral migration rate and channel morphodynamics. This approach to measuring sediment transit time is much more precise than other methods previously used and shows promise for future applications.

In Chapter 4, I aimed to quantify the effects of hydrodynamic sorting on the composition and quantity of particulate organic carbon (POC) export transported by lowland rivers. I first used scanning electron miscroscopy (SEM) coupled with nanoscale secondary ion mass spectrometry (NanoSIMS) analyses to show that the Bermejo transports two principal types of POC: 1) mineral-bound organic carbon associated with <4 μm, platy grains, and 2) coarse discrete organic particles. Using *n*-alkane stable isotope data and particle shape analysis, I showed that these two carbon pools are vertically sorted in the water column, due to differences in particle settling velocity. This vertical sorting may drive modern POC to be transported efficiently from source-to-sink, driving efficient CO_2 drawdown. Simultaneously, vertical sorting may drive degraded, mineral-bound POC to be deposited overbank and stored on the floodplain for centuries to millennia, resulting in enhanced POC remineralization. In the Rio Bermejo, selective deposition of coarse material causes the proportion of mineral-bound POC to increase with distance downstream, but the majority of exported POC is composed of discrete organic particles, suggesting that the river is a net carbon sink. In summary, this study shows that selective deposition and hydraulic sorting control the composition and fate of fluvial POC during fluvial transit.

In Chapter 5, I characterized and quantified POC transformation and oxidation during fluvial transit. I analyzed the radiocarbon content and stable carbon isotopic composition of Rio Bermejo suspended sediment and found that POC ages during fluvial transit, but is also degraded and oxidized during transient floodplain storage. Using these data, I developed a conceptual model for fluvial POC cycling that allows the estimation of POC oxidation relative to POC export, and ultimately reveals whether a river is a net source or sink of CO_2 to the atmosphere. Through this study, I found that the Rio Bermejo annually exports more POC than is oxidized during transit, largely due to high rates of lateral migration that cause erosion of floodplain vegetation and soil into the river. These results imply that human engineering of rivers could alter the fluvial carbon balance, by reducing lateral POC inputs and increasing the mean sediment transit time.

Together, these three studies quantitatively link geomorphic processes to rates of POC transport and degradation across sub-annual to millennial time scales and nanoscale to 10^3 km spatial scales, laying the groundwork for a global-scale fluvial organic carbon cycling model.

ZUSAMMENFASSUNG

Der globale Kohlenstoffkreislauf bestimmt das Klima und die Bewohnbarkeit unseres Planeten durch die Regulierung der Kohlenstoffkonzentration in unserer Atmosphäre. Erdoberflächenprozesse spielen eine zentrale, aber nicht ausreichend verstandene Rolle in der Regulierung der Kohlenstoffflüsse zwischen terrestrischen Reservoiren und der Atmosphäre. Flusssysteme steuern globale biogeochemische Kreisläufe, indem sie große Mengen Kohlenstoff in der Landschaft umverteilen. Dabei bestimmt das Gleichgewicht zwischen Kohlenstoffoxidation und -konservierung, ob der Flusstransport in einer atmosphärischen Netto CO2-Quelle oder -Senke resultiert. Die Auswirkungen von Sedimentverlagerungsprozessen werden in bestehenden Modellen für den Kohlenstofftransport in Flüssen jedoch nicht berücksichtigt, was zu großen Unsicherheiten in der Bestimmung von Kohlenstoffflüssen von Quellen zu Senken führt.

In dieser Dissertation adressiere ich diese Wissenslücke mithilfe von drei Studien, die verschiedene Komponenten des Stofftransfers von Quelle zu Senke und seine Auswirkungen auf die Zusammensetzung und den Transfer des organischen Kohlenstoffs im Fluss herausgreifen. Die in diesen drei Studien aufgestellten Hypothesen wurden in einem analogen alluvialen Tieflandflusssystem - dem Rio Bermejo in Argentinien - getestet. Der Rio Bermejo exportiert jährlich mehr als 100 Mt Sedimente und organisches Material aus den Zentralanden und transportiert dieses fast 1300 km flussabwärts ohne Einfluss von Nebenflüssen durch das Tieflandbecken. Dies erlaubt die Isolierung der Auswirkungen geomorphologischer Prozesse auf den organischen Kohlenstoffkreislauf im Fluss. Die Studien basieren auf geochemischen Daten eines Satzes Sedimentproben der Suspensionsfracht, die entlang des Rio Bermejo aus Flusstiefenprofilen entnommen wurden.

In Kapitel 3 habe ich mir das Ziel gesetzt die mittlere Flusssedimenttransitzeit des Rio Bermejo sowie die geomorphologischen Prozesse, die die Geschwindigkeit des Sedimenttransfers flussabwärts regulieren, zu bestimmen. Dazu habe ich ein Framework entwickelt, wie meteorisches kosmogenes ^{10}Be ($^{10}Be_m$) als Chronometer verwendet werden kann, das die Dauer des Sedimenttransits von der Bergfront stromabwärts entlang des ~ 1300 km langen Kanals des Rio Bermejo misst. Ich habe $^{10}Be_m$ -Konzentrationen an den Tiefenprofilen der Suspensionsfracht gemessen und dabei einen Anstieg von 230% entlang des Flusstransfers festgestellt. Für die zeitabhängige Akkumulation von $^{10}Be_m$ auf der Überflutungsebene habe ich ein einfaches Modell angewendet und dadurch eine mittlere Sedimenttransitzeit von ~ 8,5 ± 2,2 kyr abgeschätzt. Meine Daten haben zusätzlich gezeigt, dass Unterschiede in der lateralen Migrationsrate und der Kanalmorphodynamik Unterschiede in der Sedimenttransitgeschwindigkeit verursachen. Dieser Ansatz zur Messung der Sedimenttransitzeit ist viel präziser als andere bisher verwendete Methoden und hat ein großes Potential für zukünftige Anwendungen.

Kapitel 4 habe ich darauf ausgerichtet die Auswirkungen der vorübergehenden Speicherung in Überflutungsebenen, der Verfeinerung der Korngrößen flussabwärts und der organomineralischen Assoziationen auf die Zusammensetzung und Menge des Exports von fluvialem partikulärem organischem Kohlenstoff (POC) zu quantifizieren. Daten stabiler *n*-Alkan-Isotope zeigten eine vertikale Sortierung organischer Stoffe in der Flusswassersäule, durch die ^{13}C -angereichertes, mineralassoziiertes POC am oberen Ende der Wassersäule konzentriert wurde. Mithilfe von Rasterelektronenmikroskopie (SEM) und nanoskalige Sekundärionen-Massenspektrometrie (NanoSIMS) -Analysen habe ich gezeigt, dass Organomineralassoziationen größtenteils in feinen, plattigen Mineralkörnern mit niedrigen Absetzgeschwindigkeiten gefunden werden, welche zum Aufsteigen des mineralgebundenen POC in der Wassersäule führen. Organomineralassoziationen und ^{13}C -Anreicherung sind

typisch für den Abbau von organischem Kohlenstoff im Boden, was darauf hindeutet, dass mineralgebundener POC größtenteils aus der Erosion verwitterter Auenböden stammt. Ich habe gezeigt, dass> 70% des suspendierten POC-Exports in Zusammenhang mit feinem Sediment seht. Dieser POC ist wahrscheinlich aufgrund des Abbaus während der vorübergehenden Lagerung in den Überflutungsebenen stärker an ^{13}C angereichert. Da mineralgebundenes POC und diskrete organische Partikel in der Wassersäule in unterschiedlichen Tiefen transportiert werden, weisen sie wahrscheinlich unterschiedliche Flusslaufzeiten und damit unterschiedliche Oxidationswahrscheinlichkeiten während des Flusstransfers auf. Zusammenfassend zeigt diese Studie, dass hydrodynamische Sortiereffekte die Zusammensetzung und das Schicksal des fluvialen POC während des Transits von Quelle zu Senke steuern.

In Kapitel 5 habe ich die POC-Transformation und -Oxidation während des Flussdurchgangs charakterisiert und quantifiziert. Dazu habe ich den Radiokohlenstoffgehalt und die stabile Kohlenstoffisotopenzusammensetzung der Suspensionsfracht des Rio Bermejo analysiert. Die Daten zeigten sowohl eine Alterung des POC während des Flusstransits und als auch den Abbau von POC während der vorübergehenden Ablagerung in Überflutungsebenen. Unter Verwendung dieser Daten entwickelte ich ein konzeptionelles Modell für den Fluss-POC-Kreislauf, das die Abschätzung der POC-Oxidation im Verhältnis zum POC-Export ermöglicht und zeigt, ob ein Fluss eine Nettoquelle oder -senke für CO2 in der Atmosphäre darstellt. Durch diese Studie fand ich heraus, dass der Rio Bermejo jährlich mehr POC exportiert, als während des Transits oxidiert wird, was hauptsächlich auf die hohen seitlichen Migrationsraten zurückzuführen ist, die zur Erosion der Auenvegetation und der Auenböden in den Fluss führen. Diese Ergebnisse deuten darauf hin, dass die menschliche Gestaltung von Flüssen die Kohlenstoffbilanz im Fluss verändern könnte, indem die seitlichen POC-Einträge reduziert und die mittlere Sedimenttransitzeit erhöht werden.

Zusammengenommen verknüpfen diese drei Studien geomorphologische Prozesse quantitativ mit den Raten des POC-Transports und der POC-Degradation über sub-jährliche bis tausendjährige Zeitskalen und Nano bis 10^3 km räumlichen Skalen und bilden die Grundlage für ein Modell des globalen, fluvialen, organischen Kohlenstoffkreislaufs.

ACKNOWLEDGEMENTS

This dissertation is the culmination of four years of work, which began with a PhD fellowship from the StRATEGy international research training group, funded by DFG (Deutsche Forschungsgemeinschaft) grant STR 373/34-1 and the Brandenburg Ministry of Sciences, Research and Cultural Affairs. Special thanks are owed to Dr. Manfred Strecker for generating and maintaining this training group, organizing field schools, and for encouraging interdisciplinary research. Additional financial support came from the Helmholtz Association through GFZ Potsdam (Deutsches GeoForschungsZentrum).

During the course of this work, I crossed paths with many professors, scientists, and students, who all contributed to the evolution of this dissertation, my professional development, and my personal growth in immeasurable ways. First and foremost, I have the utmost gratitude for my supervisors, Dirk Sachse and Niels Hovius. I thank them both for investing in me as a young scientist, for encouraging me to explore different methods, for guiding me toward the "big picture" questions, and for reading so many manuscript drafts. I am also unbelievably grateful for their flexibility, understanding, and advice with respect to balancing my personal life with my research and professional goals. I would not have made it here without their support. Second, I am indebted to Joel Scheingross, who devoted time and energy to my first Bermejo field campaign and to each manuscript comprising this dissertation. I would have been lost without his guidance over the past four years.

I am grateful for the support from the geochemistry labs I had the pleasure to work in. I owe many thanks to Hella Wittmann, for her time and energy training me in the cosmo lab and for inspiring me to become a geochemist. I thank Oliver Rach and David Maas for training me in the biomarker lab, and Andrea Vieth-Hillebrand for her collaboration and for always having an open door. I thank Carsten Müller and the staff at TU Munich for showing me the potential of NanoSIMS. I thank Daniel Montluçon, Negar Haghipour, and the biogeochemistry group at ETH Zurich for support during long hours in the lab. I am also appreciative of all the wonderful people in the Geomorphology group at GFZ Potsdam. This was a truly exceptional place to carry out my PhD studies. Special thanks are owed to Camilla Brunello and Luc Illien for creating a brilliantly dynamic office environment, to Denise Postler and Nina Golombek for teaching me how to be a mentor, and to Johanna Menges for all the enlightening discussions about science, uncertainty, and life.

Finally, I thank my family for supporting me through every stage of my education, including my decision to move to a different continent, and my husband Bill for his patience and understanding as I pursue my educational and career goals, and for all the amazing adventures along the way.

TABLE OF CONTENTS

LIST OF FIGURES

LIST OF TABLES

PREFACE

Geoscience research has an essential role in solving societal challenges. Earth's natural resources are needed to sustain billions of lives. Changes to Earth's surface, induced by seismicity, volcanic activity, or extreme meteorological events, dictate where and how we live. The fertility of the soils on which we farm is determined by the underlying rocks, grain size, precipitation, and time. Development of new technologies that drive commerce and globalization depends on minerals sometimes only found where certain geologic phenomena have ensued. Powering homes, vehicles, and factories requires quantifying our natural resources and predicting their variability over time. And understanding the future of Earth's habitability requires knowing how the Earth's climate changed in the past and the mechanisms driving those changes. Perhaps the most essential life-sustaining resource is the atmosphere, whose chemical composition allows for efficient heterotrophic respiration, limits the ultraviolet radiation reaching Earth's surface, and insulates our planet to a temperature range at which water can circulate through the ocean, atmosphere, and living organisms, together allowing life to thrive. We rely on the predictability of Earth's atmosphere, such that we need to know that its composition will not deviate wildly from the composition known to support habitable conditions. Predictive power can only be achieved if we know how complex Earth systems interact, how gaseous fluxes are transferred between Earth's interior, the oceans, the atmosphere, and the biosphere, what factors control these gaseous fluxes, and how these factors might change over time.

Chemical reactions are responsible for these fluxes, by which matter is transformed from one phase to another, in some states flowing rapidly down a river, and in other states lying dormant for millions of years. Observations by Antoine Lavoisier ca. 1789 gave rise to the law of conservation of mass, which requires that the mass of any one element at the beginning of a reaction equates its mass at the conclusion of the reaction. This holds true for elements within the Earth system – elements may be exchanged among different chemical compounds and phases, but the same number of atoms will always exist within the effectively closed system. The law of conservation of mass allows us to develop models for geochemical cycling through the Earth system, such that we can estimate the flux out of a reservoir if we measure the flux into and the residence time of the element in that reservoir. Such models provide the predictive power needed to prepare for changes in the Earth's atmosphere, to manage our use of natural resources in a manner that prevents human activity from destabilizing the natural elemental cycles that have persisted for the last ~400 million years (since the rise of land plants) (Berner,

1997; Foster et al., 2017). By establishing a baseline for how the natural elemental cycles should behave without human influence, we can model and predict the possible influence exerted on these cycles by human activities.

Despite the urgency of predicting how changes in atmospheric composition will influence Earth's climate, large uncertainties remain in models of critical element cycles. Geochemical cycling within a complex system cannot be studied as a whole, but models of such systems must be a choreographed ensemble of studies investigating individual components of the system and their controlling factors. Models of natural phenomena also require data, importantly data from different natural environments spanning a range of climates where reactions transpire at different rates. Data provides validation of the physical mechanisms and chemical reactions theorized to control geochemical cycles.

Perhaps the most critical geochemical cycle for life on Earth is the carbon cycle. In this Ph.D. dissertation, I investigate one component of the carbon cycle: the transfer of organic carbon from terrestrial uplands to marine basins through fluvial routing systems. This land to sea transfer is key to balancing the amount of organic carbon among the terrestrial biosphere, where carbon is continuously cycled between plants and the atmosphere, the ocean, where carbon can be stored for hundreds of years, and sedimentary rocks, where carbon can be isolated from the atmosphere for millions of years. While divided into three separate projects, this work comprises a unified field-based analog study that generated new geochemical data to capture the timescale of fluvial sediment transit and the transformation of organic carbon during long-distance fluvial transfer. As an analog for lowland alluvial rivers, I took advantage of a natural river system, which has perhaps the longest reach in the world without tributaries – the Rio Bermejo in Argentina. Analog studies are often performed with controlled laboratory experiments, where variables can be controlled and effects can be isolated. However, the Rio Bermejo acts as a natural laboratory experiment, where mass fluxes entering the system have only one original source, and the effects of geomorphology on transformation of that mass flux during fluvial transit can be isolated.

1 INTRODUCTION

Source-to-sink systems drive global biogeochemical cycles by redistributing significant masses of sediment, solutes, and organic matter across the landscape (Allen, 2008). The global carbon cycle is intimately linked to Earth surface processes, but current carbon cycle models do not account for the potential transformations of organic carbon in source-to-sink systems, due to the complex interplay among physical, biological, and chemical processes that regulate this mass transfer. Rivers are the backbones of source-to-sink systems, as they are responsible for delivering large fluxes of sediment and carbon across the landscape. During fluvial transit, organic carbon is vulnerable to microbially-mediated or photochemical degradation, which cause remineralization to CO_2 and CO, structural alteration, or sorption-desorption with mineral substrate. While many biogeochemical reactions contribute to carbon transformations, Earth surface processes are thought to play an important modulating role through their influences on reaction timescales, the physical properties of soils/sediments, and mass fluxes, among other key parameters. In this dissertation, my goal is to deconvolve the relationship between fluvial geomorphic processes and organic carbon cycling at Earth's surface. I present three studies that constrain different aspects of fluvial processes and link them to the transformation of organic molecules to CO_2, as well as the preservation of organic molecules in the sedimentary record. In this first chapter, I outline my motivation for this work, and I summarize previous efforts which have paved the way for my Ph.D. research.

1.1 The global carbon cycle

1.1.1 Carbon and Earth's climate

Carbon dioxide, CO_2, is a trace gas in Earth's atmosphere, comprising ~0.04% of the atmosphere by volume. Despite its small relative abundance, a strong positive correlation

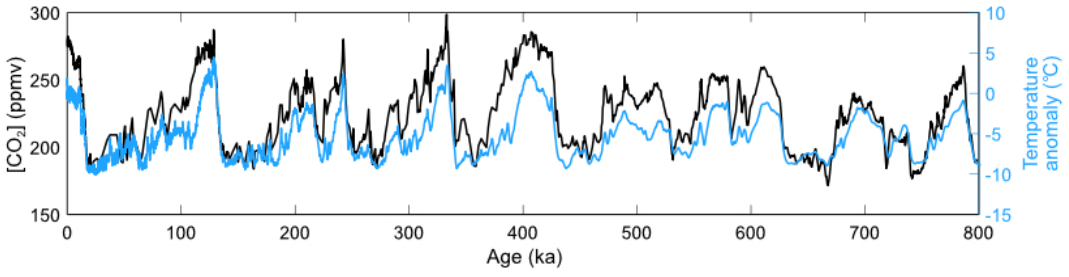

Figure 1.1. CO_2-temperature record. 800 kyr record of CO_2 concentrations measured in the Antarctic Dome C ice core (black line) (Lüthi et al., 2008). Temperature anomaly relative to the mean temperature of the last 1000 yr (blue line) reconstructed from δ^2H_{ice} measurements from the same ice core (Jouzel et al., 2007). Comparing these two datasets shows the positive feedback between atmospheric CO_2 concentrations and surface temperatures, with a lag time such that temperature changes follow changes in CO_2.

between the atmospheric CO_2 concentration and Earth's surface temperature over geologic timescales suggests that CO_2 exchange between terrestrial carbon reservoirs and the atmosphere regulates global climate (**Fig. 1.1**) (Jouzel et al., 2007; Lüthi et al., 2008). Fluctuations in atmospheric CO_2 concentrations have been attributed to changes in the storage capacity of Earth's major carbon reservoirs (Brook, 2008). These reservoirs include the lithosphere (>75x10^6 GtC stored in sedimentary rocks and hydrocarbons), the oceans (~40x10^3 GtC), the terrestrial biosphere (soils ~2.4x10^3 GtC and vegetation ~650 GtC), and the atmosphere (~830 GtC) (**Fig. 1.2**) (IPCC, 2013). Relative to terrestrial and oceanic reservoirs, the atmosphere holds a small amount of carbon and is sensitive to changes in the carbon storage capacity and residence time of other reservoirs. The residence time of carbon in the lithosphere is long – ~100-200x10^6 yr – and annual fluxes of ~0.1 GtC/yr from solid-earth degassing are slow. Conversely, due to seasonal litter fall, plant mortality, and carbon decomposition in soils, the residence time of carbon in the terrestrial biosphere is short – on the order of ~10^1 yr. Carbon is rapidly exchanged between the biosphere and atmosphere (~107 GtC/yr released to the

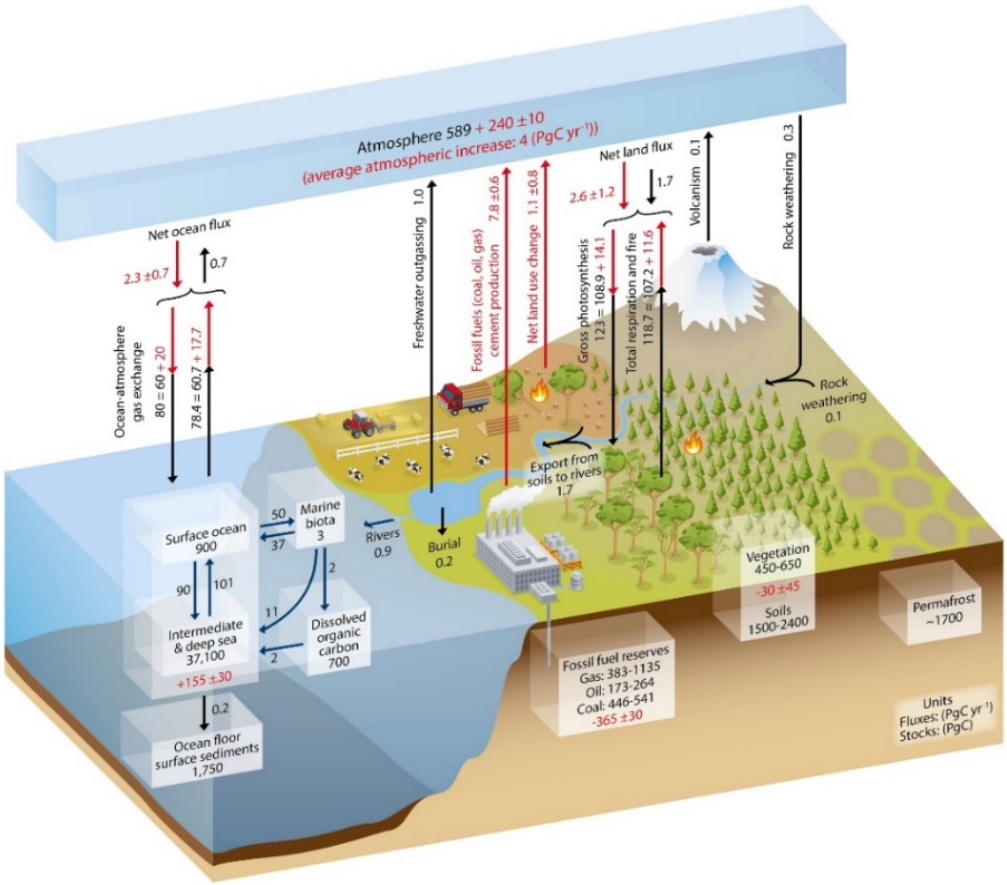

Figure 1.2. The global carbon budget, as depicted in the 2013 Intergovernmental Panel on Climate Change report (IPCC, 2013). Black arrows and text indicate "natural" (pre-industrial) carbon fluxes between two carbon reservoirs. Red arrows and text indicate anthropogenic carbon fluxes (industrial) between reservoirs. The key fluxes focused on in this dissertation are export from soils to rivers, inland burial, and fluvial export to the oceans.

atmosphere and ~109 GtC/yr sequestered by the biosphere). This rapid exchange is primarily driven by the instability of biological molecules at Earth's surface, where they are prone to chemical oxidation (Galvez et al., 2020). Sedimentary rocks are the largest reservoir of organic carbon at Earth's surface (Falkowski & Godfrey, 2008), but for organic carbon to be transferred to the lithosphere, it must escape oxidation during transit from the biosphere to sedimentary basins. Annually, a significant flux of biospheric organic carbon is eroded from hillslopes and floodplains and delivered to rivers (estimated to be ~1.7 GtC/yr (Tranvik et al., 2009)). Only ~0.9 GtC/yr is delivered to the oceans by rivers, suggesting that a significant amount of carbon may be sequestered in river floodplains, trapped behind dams, or oxidized to CO_2 during fluvial transit. River systems are a nexus between the short term and long-term carbon cycles, and the sediment routing pathway through these systems is key for determining whether organic molecules have the opportunity to be buried, graphitized, and isolated from the atmosphere for millions of years.

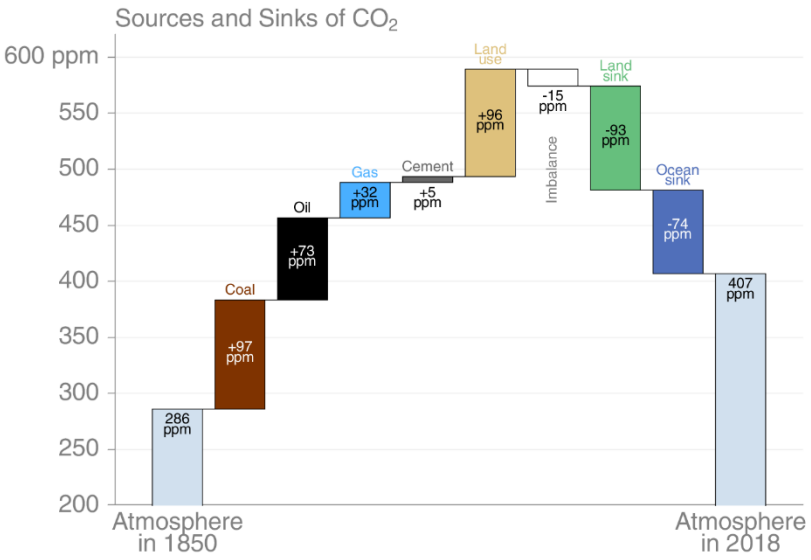

Figure 1.3. Balance of global CO_2 sources and sinks. Carbon budget shows that sources currently contribute 15 ppm more CO_2 than is estimated to be stored in the ocean, land, and atmosphere sinks. From Friedlingstein (2019) and the Global Carbon Project.

Uncertainties on global carbon flux estimates are >20%, suggesting that the processes regulating these fluxes are not well constrained. Current estimates of the global carbon budget reveal a 15 ppm/yr imbalance between CO_2 sources and sinks, equivalent to a net gain of +0.4 GtC/yr atmospheric CO_2 (**Fig. 1.3**). This imbalance suggests either overestimation of carbon sources or underestimation of carbon sinks (Friedlingstein et al., 2019), and represents a gap in our understanding of the mechanisms transferring carbon among Earth's reservoirs. We can reduce this knowledge gap by studying the physical and biogeochemical mechanisms driving organic carbon transfer between reservoirs. Source-to-sink sedimentary systems play an important, yet insufficiently constrained, role in balancing carbon sources and sinks, and thus may be key to this filling this knowledge gap.

1.1.2 Earth surface processes and the carbon cycle

Earth surface processes regulate the global carbon cycle in numerous ways, but we have yet to mechanistically explain the relationships between the physical processes driving biogeochemical mass transfer across Earth's surface and their associated carbon fluxes. Actively uplifting mountain ranges are hotspots for physical erosion, and are thus significant sources of clastic sediment, reactive elements, and organic molecules (Hilton & West, 2020). Rivers draining these orogens become loaded with these erosion products, and the geomorphology of river systems determine whether they are ultimately delivered to the oceans, or chemically transformed during transit from source to sink. As such, the fate of these erosion products has a significant impact on the carbon cycle over a range of timescales.

Weathering of silicate minerals has been associated with significant drawdown of atmospheric CO_2 over 10^3 to 10^6 yr timescales, with an estimated annual flux of ~0.3 GtC/yr (IPCC, 2013). Erosion is often accompanied by chemical weathering, as rocks are exposed to water and carbon dioxide for the first time since genesis. Hydrolysis reactions between mildly acidic waters and silicate minerals, such as plagioclase feldspar, olivine, pyroxene, and amphibole, break down primary minerals and yield new clay minerals, along with calcium ions and carbonic acid, as described by the Urey equation (Urey, 1952):

$$XSiO_{3\,(s)} + 2CO_{2\,(aq)} + H_2O_{\,(l)} \leftrightarrow X_{\,(aq)} + 2HCO_3^-{}_{(aq)} + SiO_{2\,(aq)} \quad (1.1)$$

where X represents a cation, such as Ca^{2+}, Na^{+}, Al^{3+}, Mg^{2+}, and Fe^{3+}. When these weathering products are delivered to the ocean, additional reactions between calcium and carbonic acid lead to calcium carbonate precipitation, which locks carbon in the lithosphere for millions of years.

Weathering can also act as a CO_2 source if sulfide minerals, like pyrite, react with dioxygen or oxidized metal species in the presence of water, producing sulfuric acid:

$$4FeS_2 + 15O_2 + 14H_2O \rightarrow 4Fe(OH)_3 + 18H_2SO_4 \quad (1.2)$$

Release of sulfuric acid in the environment can result in the breakdown of carbonate minerals and CO_2 release into the ocean-atmosphere system (Torres et al., 2014):

$$CaCO_3 + H_2SO_4 \rightarrow CO_{2(g)} + H_2O + Ca^{2+} + SO_4^{2-} \quad (1.3)$$

The sulfate byproduct from pyrite oxidative weathering may be delivered to the oceans, where it has a long residence time – up to 10 million years until it is reduced and forms sulfide minerals in marine sediments. Pyrite oxidation has been observed to correlate positively with

erosion rate, suggesting that pyrite oxidation is a supply-limited process (Calmels et al., 2007). This feedback suggests that mountain building and exhumation of fresh rock, in tandem with its composition, drive both drawdown and release of CO_2. The relative rates of geomorphic processes then determine the balance between these two fluxes, and their net effect on the global carbon cycle.

In addition to these erosion-weathering-CO_2 feedbacks, erosion also drives the transport of terrestrial organic carbon to ocean basins where it may be deposited and preserved in marine sediments (Berner, 1982; Burdige, 2007; Hilton, 2017; Hilton et al., 2012; Schlünz & Schneider, 2000). Organic carbon burial in marine sediments is a long-term geologic carbon sink, because organic molecules that were unstable in aerobic environments become rapidly buried in near anoxic conditions and are ultimately lithified, locking those molecules in the lithosphere for millions of years (barring any subsequent exhumation and erosion). Terrestrial organic carbon burial is assumed to be insignificant in deep-sea sediments, with most burial focused in deltas and continental shelves. This burial flux is estimated to be ~0.04-0.08 GtC/yr (Burdige, 2005).

In the organic carbon cycle, CO_2 is initially sequestered from the atmosphere via photosynthesis. In plants, carbon is incorporated into organic molecules and oxygen is released as O_2, shown here in its general form:

$$n\mathrm{CO_2} + n\mathrm{H_2O} \xrightarrow{\text{light,nutrients}} \mathrm{C}_n\mathrm{H}_{2n}\mathrm{O}_n + n\mathrm{O_2} \qquad (1.4)$$

Where n represents the number of CO_2 and H_2O molecules incorporated into the reaction products. Ecosystems with high net primary productivity (NPP) can sequester vast amounts of carbon, and store it in the form of living biomass, leaf litter, and soil. These regions are typically located in upland landscapes, where bedrock denudation releases nutrients and precipitation rates are high, catalyzing photosynthesis. These regions are also prone to erosion, which can denude hillslopes of their soil and biomass. Downstream fluvial transport of this eroded carbon can result in net CO_2 drawdown if the carbon is buried in sediments, or it may result in net CO_2 release if the carbon is oxidized during transit. Organic carbon oxidation can be carried out photochemically, or via microbial-mediation, but both reactions assume the general form:

$$n\mathrm{CH_2O} + n\mathrm{O_2} \xrightarrow{\text{enzymes}} n\mathrm{CO_2} + n\mathrm{H_2O} \qquad (1.5)$$

where microbial extracellular enzymes aid the breakdown of high-molecular-weight compounds, enabling microbial metabolism and hydrolysis to dissolved phases that can readily undergo photochemical oxidation (Battin et al., 2008).

One grand challenge for estimating global carbon fluxes is determining the timescales over which organic carbon reactions play out at Earth's surface. The mean residence time, or "turnover time", of an organic molecule in the terrestrial biosphere is set by its decomposition rate. This rate is regulated by the interplay of temperature, soil moisture, nitrogen availability, carbon supply, and microbial activity (Sierra et al., 2015), as well as where the molecule physically sits at Earth's surface. Thus, organic carbon degradation is largely climatically-controlled and will vary across spatial and temporal scales. The turnover time of organic carbon (τ) is the time required for all carbon in a carbon pool to be decomposed. This timescale is calculated as the total amount of carbon in a pool divided by the CO_2 flux into and out of that pool. The global average ecosystem turnover time is ~23 yr, with short turnover times near the equator (~15 yr) and long turnover times at high latitudes (~255 yr) (Carvalhais et al., 2014). Mineral associations can also modulate organic carbon turnover time, by which reactive cations in secondary minerals bind with organic compounds and stabilize them over millennial timescales (Hemingway et al., 2019; Kleber et al., 2007; Torn et al., 1997). Most studies of organic carbon turnover have focused on soils, which serve as the largest stock of organic carbon in the terrestrial biosphere. However, a significant amount of soil organic carbon is eroded into fluvial systems every year, and its fate is not well understood.

1.1.3 Rivers and the organic carbon cycle

By connecting modern carbon sources and long-term sinks, rivers are key links in the global carbon cycle. Rivers transport two general types of organic carbon: dissolved organic carbon (DOC) and particulate organic carbon (POC). DOC is sourced from labile soil organic matter that readily dissolves in throughflow and runoff, and is transferred to rivers relatively rapidly. DOC travels downstream at the rate of water velocity and can be photochemically oxidized over timescales of days to weeks, suggesting that it cycles through the environment quickly and has no significant long-term effects on the global carbon cycle (Battin et al., 2008). Conversely, POC has a much slower degradation rate than DOC, allowing it to be preserved for decades to millennia. POC can be buried in sedimentary basins and isolated from the atmosphere over geologic timescales, a process that has modulated atmospheric CO_2 concentrations throughout Earth's history (Berner & Caldeira, 1997).

A primary mechanism driving the long-term burial of terrestrial OC is the transport of fluvial POC to the oceans, where it can be rapidly buried in depocenters, like deltas and continental shelves (Bianchi et al., 2018; Burdige, 2005; Schlünz & Schneider, 2000). Rivers deliver ~19 Gt/yr of terrigenous sediment to the world's oceans (Milliman and Farnsworth, 2011), which includes 0.13-0.34 GtC/yr of POC (Galy et al., 2015). If this POC escapes oxidation, it may be buried in marine sediments, ultimately sequestering atmospheric CO_2. However, because fluvial sediment routing is complex, during source-to-sink transit POC can be stored in lowland basins, subaqueous floodplains, and wetlands, where it is susceptible to oxidation (Blair & Aller, 2012; Richey, 2004) (**Fig. 1.4**). Oxidation drives imbalances between the POC fluxes delivered to river systems and the POC fluxes leaving those systems. However, lowland floodplains also generate fluvial POC, as many rivers laterally erode and mobilize floodplain soil and vegetation. While many studies have focused on the composition and fluxes of fluvial POC exported to the oceans (e.g., Bouchez et al., 2014; Clark et al., 2017; Galy et al., 2011; McClelland et al., 2016; Waterson, 2005), few have investigated the balances among fluvial POC fluxes resulting from source-to-sink transit (Bianchi et al., 2013; Bouchez et al., 2010; Hilton et al., 2015; Richey et al., 1980). These missing fluxes are not accounted for in our modern estimates of the global carbon budget, but may be key for modeling the global fluvial carbon cycle.

Recent work has elucidated some of the mechanisms driving organic carbon cycling in river systems (Galy et al., 2015; Hage et al., 2020; Hemingway et al., 2019; Hilton et al., 2011; Hilton & West, 2020; Scheingross et al., 2019a; Torres et al., 2017; Tranvik et al., 2009). While fluvial POC fluxes can be spatially and temporally variable at small scales (e.g., Clark et al.,

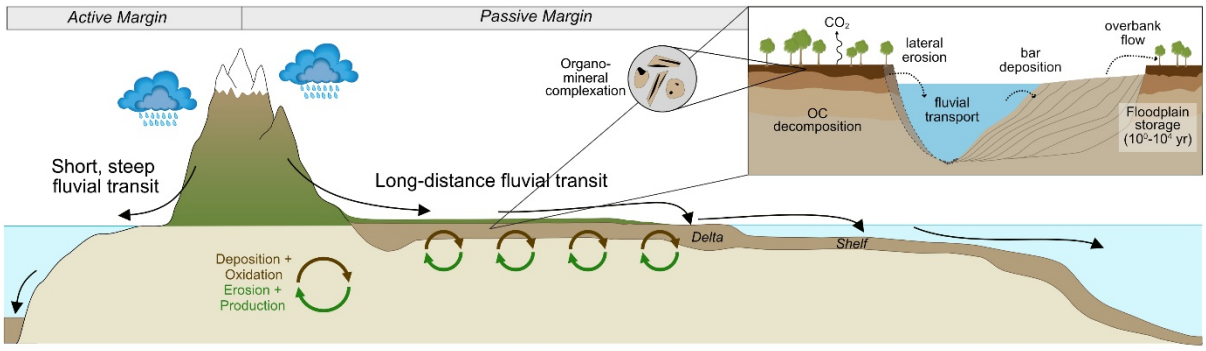

Figure 1.4. Source-to-sink routing systems. Schematic representation of source-to-sink transit systems in active and passive margins settings (adapted from Blair and Aller, 2012). Active margins are generally characterized by short ($<10^2$ km), steep transit pathways, resulting in efficient carbon burial in near-shore marine basins. Passive margins are generally characterized by long ($>10^3$ km), low-sloping transit pathways, where sediment and organic matter are subject to episodes of deposition, soil formation, and erosion on its journey to marine depositional settings. Fluvial processes can be complex, resulting in millennial floodplain storage timescales during which carbon can be oxidized, or stabilized by mineral interactions. Active margins comprise just 35% of all continental margins (Harris and Macmillan-Lawler, 2016), suggesting that long-distance sediment transit processes dominate global fluvial export.

2017; Menges et al., 2020), fluvial export of biospheric POC to the oceans is largely controlled by upland erosion rates and river sediment transport capacity, suggesting that POC export from large rivers is tightly coupled to suspended sediment fluxes (Galy et al., 2015). Sediment aggradation and inland deposition can modify global fluvial POC export fluxes, but these sedimentation processes are rarely considered in carbon cycle models (Stallard, 1998; Richey, 2004). POC traveling with the fluvial sediment load is subject to hydrodynamic forces, like gravitational settling, lift, and drag (Dietrich, 1982), and consequently experiences episodes of deposition during decreasing flow and remobilization during increasing flow conditions. POC can also be deposited onto floodplains during overbank flow events, where fine particles with a low settling velocity are carried out of the channel and fall out of the water column as flood waters slowly recede (Dunne & Aalto, 2013). Whether POC survives these episodes of deposition and re-mobilization during fluvial transit will be determined by its decomposition rate and the duration of these storage episodes (Torres et al., 2020). Currently, these two factors are key unknown variables for fluvial carbon cycle models.

If the decomposition rate of fluvial POC is slower than the average rate of downstream transit, POC may be largely preserved during source-to-sink transfer. While the rate of downstream transit is regulated by geomorphology, decomposition rates depend on other factors. Organo-mineral associations have been shown to stabilize OC, protecting it from heterotrophic degradation for millennial timescales (Blattmann et al., 2019; Hemingway et al., 2019; Keil et al., 1994; Wagai et al., 2011). This mineral protection mechanism allows organic carbon to be stored in hillslope and riparian soils, and in lowland floodplain sediment before being exported by a river. In many river systems, exported POC can be significantly aged. This "pre-aging" effect was initially thought to be due to fossil POC, however, mixing models have been used to tease apart the contributions of fossil, aged biospheric, and modern biospheric POC in sediments (e.g., Drenzek et al., 2009). In the Yellow River, compound-specific ^{14}C ages of long-chain fatty acids, lignin phenols, and long-chain *n*-alkanes in surface water suspended sediment revealed that 50-60% of fluvial POC may have aged 1500-1800 yr before being exported to the ocean (Tao et al., 2015). In the Bengal Fan, POC delivered by the Ganges-Brahmaputra system was dominated by labile compounds with average ^{14}C-ages ~1000-1200 yr, while refractory compounds had average ^{14}C-ages >15000 yr (French et al., 2018). Coastal marine sediments at the mouth of the Congo River contained organic matter with apparent ^{14}C-ages of up to 3,000 yr, and ages became older from the mid- to the late Holocene (Schefuß et al., 2016). In the Congo basin, increased aridification and subsequent erosion of previously

anoxic floodplain sediments led to the remobilization of stored refractory POC. Labile POC that had no mineral protection mechanism was likely rapidly oxidized upon remobilization (Schefuß et al., 2016).

Enhanced release of pre-aged organic matter from catchments has been correlated with high precipitation and water discharge events in several rivers, including the Mississippi River (Rosenheim et al., 2013) and the Ganges-Brahmaputra (Hein et al., 2020). In high latitude settings where decomposition is slow, POC can be stored in permafrost soils for up to 14000 yr before being exported to the coast (Vonk et al., 2016; Wild et al., 2019). However, POC ^{14}C-ages have been found to vary among rivers across the Arctic, with Mackenzie River POC averaging ~5500 ^{14}C-yr and the Ob River averaging ~2000 ^{14}C-yr (McClelland et al., 2016), suggesting that differential erosion and sediment transit pathways play an important role in the fate of fluvial POC. These studies suggest that the potential for POC to be preserved during fluvial transit will be determined by the length, duration, and complexity of the fluvial sediment routing pathway.

POC can also be degraded and oxidized to CO_2 during fluvial transit. Few studies have investigated the remineralization of fluvial POC in transport systems, but it is important to quantify the sources of riverine CO_2 outgassing and its magnitude relative to fluvial carbon export. Many rivers have been characterized as net heterotrophic (Cole & Caraco, 2001), meaning that they export more carbon in the form of CO_2 than they sequester. Globally, rivers and streams are estimated to release 1.8 GtC/yr CO_2 to the atmosphere via outgassing (Raymond et al., 2013), which is twice the amount of POC exported annually to the oceans. Because of its global significance, the Amazon River system has been a focus of more detailed CO_2 outgassing studies. These studies find that the CO_2 outgassing flux from the Amazon River system is more than ten times greater than its total organic carbon export to the ocean, and the dominant source of this CO_2 is young, fast-cycling organic matter in riparian wetlands (Abril et al., 2014; Mayorga et al., 2005; Richey et al., 1980).

Collectively, these studies show that rivers vary in their capacity to store organic carbon over long timescales, which influences the amount and composition of organic carbon released to the oceans. Key processes driving this variability in fluvial POC cycling include OC composition, mineral protection, sediment transit time (floodplain storage time), erosional fluxes, lateral channel mobility, and climate. To accurately model the fluvial carbon budget, the interactions among these biogeochemical and geomorphic processes need to be further explored and their net effect must be quantified.

1.2 Source-to-sink routing

In fluvial routing systems, the rate and the pathway of downstream sediment and carbon transport influence the propagation of environmental signals to depositional archives, and can alter the magnitude of fluxes leaving river systems (Allen, 2008; Romans et al., 2016). The downstream routing of sediment through river networks can be complex, involving channel-floodplain sediment exchange (Dunne et al., 1998), downstream comminution (Frings, 2008; Paola & Seal, 1995), selective deposition and mass loss (Paola & Martin, 2012; Wright & Parker, 2005), as well as mixing with tributary influxes (Lane et al., 2008). The time material spends in transit from source to sink scales with the complexity of sediment routing systems, due to transient storage in bar deposits, floodplains, and terraces. Transient storage filters, dampens, and shreds climatic and tectonic signals produced by discrete episodic events in sediment source areas, such that short timescale temporal variability is not detectable in the sedimentary record (Armitage et al., 2011; Douglas et al., 2014; Jerolmack & Paola, 2010). To determine how signals are propagated downstream in source-to-sink systems, it is imperative to know where and for how long sediment is stored en route.

1.2.1 Fluvial sediment transit time

According to Martin and Church (2004), "sediment particles, in fact, remain at rest during most of their journey through the landscape, only rarely undergoing actual transport." Thus, the fluvial sediment "transit time" (*sensu* Bolin & Rodhe, 1973) is the mean time it takes sediment particles to move through a river system, including both the time spent in active transport and in storage within alluvial compartments. The transit velocity is then the average rate at which sediment moves downstream through a system. Transit time can be influenced by channel shape (e.g., slope, sinuosity), the balance of sediment supply to accommodation space, vertical incision and lateral migration rates, and the mode and frequency of channel breaching and avulsion (Jerolmack & Mohrig, 2007; Romans et al., 2016). The sediment transit time is a first order control on the alteration of sediment and organic matter transported downstream, including weathering and organic carbon decomposition, which play major roles in global biogeochemical cycling.

Measuring sediment transit time in natural fluvial systems is challenging because of the complexity of sediment routing. Numerous approaches have been taken to resolve sediment transit times. Short-lived fallout radionuclides (Walling & He, 1993), dendrochronology (Everitt, 1968; Gottesfeld & Gottesfeld, 1990; Nakamura & Kikuchi, 1996), optically-stimulated luminescence (OSL) (Rowland et al., 2005), and radiocarbon dating (Lancaster et

al., 2010) have been used to constrain sediment residence time in channel margins over relatively small spatial (<100 km) and temporal scales (10^{-1}-10^{3} yr). Over larger spatial (>100 km) and temporal scales (10^{3}-10^{5} yr) expected in many large river systems, other methods have been able to broadly constrain sediment transit time, but with limitations. The Uranium series isotope system provides a long timescale chronometer for the time passed since particles were reduced to <63 μm (i.e., comminution age), and has been used to estimate river sediment transit time (Depaolo et al., 2006; Anthony Dosseto et al., 2008; Granet et al., 2007). However, this method is limited to fine grain sizes, thus excluding sand-sized particles that are common in many rivers. More recent studies reported that small changes to input parameters of U-series comminution age models, such as the uranium leaching rate, result in large uncertainties on transit time estimates (e.g., Handley et al., 2013; Martin et al., 2019). In addition to dating sediment depositional ages, OSL has been used as a tracer for fluvial sediment transport (Gray et al., 2017, 2018), based on the conceptual model where sediment is bleached ("age" is re-set) during transport and its luminescence signal is regenerated during storage. Tests of OSL as a sediment transit time proxy for a large perennial river (~10^{3} km long) yielded long-term storage times that were inconsistent with values derived from sediment-budget studies, suggesting that this method is not yet fully developed for transit time estimation. These previous efforts highlight the need for a transit time proxy that is sensitive on timescales of 10^{3}-10^{6} yr and can yield results commensurate with geomorphic data.

Efforts to model sediment transit time have taken several different approaches. Sediment transit time distributions show the probability that a particle will reside in a river system for a given amount of time. This distribution cannot be measured directly, but recent work suggests that a power-law probability distribution function (PDF) fits for existing transit time data (Bradley & Tucker, 2013; Pizzuto et al., 2017). Exponential distributions may arise if all sediment within a river system has an equal probability of being eroded, but this is rarely the case in natural settings. Rather, sediment closer to the active channel has a higher probability of being eroded than sediment sitting in the floodplain far from the active channel. The power-law PDF implies that short transit times (<10^{3} yr) are much more probable than long transit times (>10^{3} yr). These modeled distributions show that the sediment transit time is ultimately a function of the river sediment flux, the floodplain mass or volume, and lateral channel migration rate. However, because direct measurements of sediment transit time over long timescales are rare and many natural rivers are not in geomorphic steady state, it is unclear whether these distributions accurately constrain natural sediment transit times.

Sediment budget approaches have also been used to estimate the duration of sediment storage within channel belts, based on the idea that transit time scales with accommodation space and volumetric sediment flux. Transfer of sediment between the active channel and sediment storage compartments is caused by lateral migration, channel widening/narrowing, downward incision, or avulsion. Fluvial sediment transit times can reach 10^4 yr because the magnitude of lateral channel-floodplain exchange can be substantial. For example, in the Amazon river system, the lateral sediment flux from bank erosion, overbank flow, and bar deposition is greater than the sediment flux exported at the river mouth (Dunne et al., 1998). This lateral exchange leads to repeated episodes of transient storage that reduce the rate of source-to-sink transit. Based on this conceptual model, sediment budget frameworks (e.g., Dietrich et al., 1982; Reid & Dunne, 2016) generally estimate the mean sediment storage time, *t*, as:

$$t = \frac{V}{Q_s} \quad (1.6)$$

where V is the volume of all storage compartments in a fluvial system (e.g., channel belt volume) and Q_s is the volumetric sediment flux delivered from the upstream basin area. Increased available storage volume leads to increased transit time, while increased sediment flux leads to decreased transit time. Sediment budgeting methods assume that the river is in steady state (i.e., constant sediment flux over time, no aggradation, constant lateral migration rates), which is typically not the case in natural systems, especially those affected by anthropogenic activity.

As work to constrain sediment transit time progresses, it is becoming clear that sediment can reside in river floodplains for 10^1 to $>10^5$ years before being transported downstream out of the river system (Bradley & Tucker, 2013; Granet et al., 2010; Pizzuto et al., 2017). This timescale is significant for biogeochemical mass fluxes, and may govern the carbon budget of rivers.

1.2.2 Hydrodynamic sorting

In tandem with long-term downstream sediment transit, in-river hydraulic processes can further convolute the geochemical signature of sediment and organic matter traveling from source to sink. Sediment and organic matter originating in mountainous uplands will be transported down relatively steep slopes. Depending on the routing pathway, this material may be transferred efficiently to ocean basins, or it may be delivered to low gradient lowland rivers with vast floodplains. In lowland settings with long routing pathways, sediment is subject to

numerous hydrodynamic processes that can alter the particle size and composition. In this dissertation, I focus on selective sediment deposition and vertical sorting in the water column as two key processes modulating sediment and organic carbon fluxes in lowland rivers.

Downstream grain size fining is a natural dynamic adjustment to reduced energy along a gradient of decreasing slope (Gasparini et al., 1999). In lowland alluvial rivers, the dominant mode of sediment transport is suspension, and thus particles are viscously damped and the probability of particle-particle collisions is low (Joseph et al., 2001). As a result of viscous damping, any downstream reduction of grain size, or comminution, in lowland river basins may be attributed to weathering during floodplain storage. However, the mass loss due to weathering in the floodplain likely plays a secondary role in downstream fining relative to selective deposition.

Selective deposition of coarse sediment is connected to changes in sediment transport capacity, which is a function of grain size and bed shear stress (τ_b) (Engelund & Hansen, 1967). τ_b is calculated as:

$$\tau_b = \rho g H S \quad (1.7)$$

where ρ is the sediment density, g is the gravitational constant, H is the flow depth, and S is the bed slope. In relative terms, steeper slopes are needed to transport more sediment and greater transport capacity is needed to carry coarser sediment. For rivers flowing from mountainous headwaters into lowland basins, channel slope decreases significantly, and bed shear stress and sediment transport capacity decrease accordingly. This results in selective deposition of coarse sediment, and aggradation and channel-filling near the mountain front that has been linked to channel avulsions (Ganti et al., 2014). This mechanism results in burial of coarse sediment and particulate organic matter in upstream reaches of lowland river floodplains, leading to a net mass loss between source and sink.

Vertical sorting in the water column also leads to selective transport of material with different sizes, shapes, and possibly chemical compositions (Blom & Parker, 2004; Bouchez, Gaillardet, et al., 2011). Suspended sediment transported in rivers travels at a depth determined by its settling velocity, i.e. the rate at which a particle drops through a fluid (Dietrich, 1982). The settling velocity of a particle is a function of its size, shape, and density, such that large round particles generally have a high settling velocity and will travel near the bottom of the water column, and small platy particles have a low settling velocity and will travel at the top of the water column. This effect ultimately leads to a suspended sediment concentration gradient in river profiles, where concentrations of coarse sediment are highest near the river bed and

lowest near the surface (Rouse, 1937). Concentration profiles will behave differently for different particle size fractions, resulting in variability in the suspended sediment flux of different types of sedimentary particles. Both downstream grain size fining and vertical sorting will change the fluxes and composition of sediment and organic carbon between source and sink, but the effects of these hydrodynamic processes on organic carbon cycling have not been quantified for natural systems.

1.3 Research questions and hypotheses

As links between the terrestrial biosphere and the oceans, rivers are an important component of the carbon cycle, yet the linkage between fluvial geomorphology and organic carbon cycling is insufficiently constrained. This lack of constraint may be one root cause for the imbalance in global carbon sources and sinks, as quantified by Friedlingstein et al. (2019). Previous work described above laid the foundation for developing a physically-based model of organic carbon cycling in rivers. From this work, I identified three key knowledge gaps in our understanding of how rivers regulate source-to-sink organic carbon transfer: 1) the duration of source-to-sink transit, 2) the role of hydrodynamic sorting in modifying sediment and organic carbon fluxes during long-distance fluvial transit, and 3) the oxidation and chemical transformation of organic carbon during fluvial transit. This dissertation aims to fill these three knowledge gaps in fluvial carbon cycle research by tackling three key sets of questions:

Q1) How long does it take for sediment and organic matter to transit large river systems? Can meteoric 10-beryllium ($^{10}Be_m$) serve as a reliable sediment transit time proxy?

In Chapter 3, I test the hypothesis that sediment transit time is set by the rates of channel morphodynamics, including lateral migration, channel depth and width, and avulsion frequency. To estimate sediment transit time, I test the application of cosmogenic meteoric $^{10}Be_m$ as a chronometer to track the residence time of sediment from its source to a river outlet.

Q2) How does hydrodynamic sorting affect the quantity and composition of particulate organic carbon fluxes exported by rivers? How does particle size, shape, and density relate to fluvial organic matter composition?

In Chapter 4, I test the hypothesis that longitudinal hydrodynamic sorting results in increased export of fine sediment and mineral-associated organic matter relative to coarse sediment and labile organic matter. I also test the hypothesis that mineral-associated organic

carbon has a different isotopic signature from labile organic carbon, resulting in biased export of ^{13}C-enriched organic carbon to downstream sedimentary basins.

Q3) Does organic carbon undergo transformation during source-to-sink transit? Do organic molecules survive multiple cycles of deposition and erosion while traversing continental-scale drainage basins? What are the mechanisms that inhibit organic carbon degradation?

In Chapter 5, I test the hypothesis that organo-mineral complexation protects organic carbon during fluvial transit, allowing it to survive deposition on the floodplain and age during transit. I also test the hypothesis that labile organic carbon is oxidized during transit, acting as a CO_2 source to the atmosphere.

1.4 Dissertation structure

This dissertation is divided into six chapters. Chapter 1 details the previous state of knowledge in the field and the motivation for pursuing the following research. Chapter 2 introduces the study area, sampling approach, and primary methods that provide the basis for the three studies central to this dissertation. The main body of this dissertation consists of three chapters (3, 4, and 5) representing manuscripts that are either published, under review, or in preparation for publication in international peer-reviewed journals. These three chapters address the three main research questions introduced at the end of Chapter 1. Finally, Chapter 6 is a synthesis of the key findings presented in Chapters 3, 4, and 5, which concludes with a discussion of the implications and outlook for fluvial carbon cycling at a global scale. Appendices A, B, and C contain supplementary material for the manuscripts in Chapters 3, 4, and 5, respectively.

1.5 Publications and author contributions

Chapter 3 is published in the *Journal of Geophysical Research: Earth Surface* and Chapter 5 is in review at *Nature Geoscience*. Chapter 4 is in preparation for publication in *Geophysical Research Letters*, with an anticipated submission date within the next two weeks. While I performed the majority of the work composing this cumulative dissertation, Chapters 3, 4, and 5 were collaborative efforts and author contributions are described below.

Chapter 3

Repasch, M., Wittmann, H., Scheingross, J. S., Sachse, D., Szupiany, R., Orfeo, O., Fuchs, M., and Hovius, N. (2020). Sediment Transit Time and Floodplain Storage

Dynamics in Alluvial Rivers Revealed by Meteoric ^{10}Be. *Journal of Geophysical Research: Earth Surface*, *125*(7), 1–19. https://doi.org/10.1029/2019jf005419

Author contributions: MR and HW performed the ^{10}Be and ^{9}Be sample processing and measurements, as well as data processing and analysis. MR performed specific surface area analysis. JSS contributed significantly to sample collection, sediment budget analysis and manuscript writing. DS, RS, OO, and NH supported field work. MF performed OSL analyses. MR wrote the manuscript with contributions from JSS, NH, HW, and DS.

Chapter 4

Repasch, M., Hovius, N.., Scheingross, J. S., Vieth-Hillebrand, A., Müller, C., Höschen, C., Szupiany, R., and Sachse, D., (in prep.). Hydrodynamic sorting drives the fate of river particulate organic carbon. To submit to *Geophysical Research Letters*.

Author contributions: MR authored the manuscript, with input from all co-authors. JSS, NH, and DS contributed to study design. MR collected the sample material with assistance from JSS, NH, DS, and RS. MR processed sample material, performed the biomarker analyses, grain size analyses, and sediment and POC flux analyses. AVH facilitated the n-alkane ^{13}C measurements. CM facilitated the NanoSIMS measurements.

Chapter 5

Repasch, M., Scheingross, J.S., Hovius, N., Lupker, M., Wittmann, H., Haghipour, N., Grocke, D.R., Orfeo, O., Eglinton, T.I., and Sachse, D., (*in review*). Fluvial organic carbon cycling regulated by sediment transit time. *In review at Nature Geoscience.*

Author contributions: MR, JSS, NH, and DS designed the study and contributed to data interpretation and model development. MR and JSS collected and processed samples, with help from DS, NH, OO, and HW. HW provided analytical assistance reactive metal extraction and measurement. DG performed bulk ^{13}C measurements. ML, NH, and TIE provided the radiocarbon measurements. MR analyzed the data, produced the figures, and authored the manuscript (with significant input from JSS, NH, DS, and ML). All co-authors reviewed, commented on, and approved the manuscript.

In addition to these three publications, I contributed to two additional manuscripts during the course of my PhD, one which is published and one which is accepted for publication:

Scheingross, J.S., **Repasch, M.**, Hovius, N., Sachse, D., Lupker, M., Fuchs, M., Halevy, I., Grocke, D.R., Golombek, N., Haghipour, N., Eglinton, T.I., Orfeo, O., Schleicher, A., The fate of fluvially-deposited organic carbon during transient floodplain storage. Accepted for publication in *Earth and Planetary Science Letters.*

Author contributions: JSS designed the study with NH and DS. ***MR*** *contributed to sample collection, preparation for geochemical analysis and data interpretation. NG prepared samples for measurements. DRG made bulk TOC and* ^{13}C *measurements.* ^{14}C *measurements were made by ML, NH, and TIE. OO facilitated field work. AS performed XRF measurements. All authors contributed to manuscript writing with significant input from* ***MR****, NH, DS, ML, and TIE.*

Scheingross, J. S., Hovius, N., Dellinger, M., Hilton, R. G., **Repasch, M.**, Sachse, D., et al. (2019). Preservation of organic carbon during active fluvial transport and particle abrasion. *Geology*, *47*(10), 958–962. https://doi.org/10.1130/G46442.1

Author contributions: JSS designed the study with NH, DS, and JMT. MD and RGH conducted rhenium measurements and data interpretation. ***MR*** *assisted with collection of shale samples, made specific surface area measurements, and contributed to geochemical data interpretation. DRG made carbon isotope measurements. AVH made DOC measurements. JSS wrote the manuscript with contributions from all co-authors.*

2 STUDY AREA AND APPROACH

We address the above research questions by studying sediment and organic carbon transported by the Rio Bermejo fluvial system in the Gran Chaco region of northern Argentina. Because of its unique geomorphic and topological characteristics and high suspended sediment load, this river serves as a model system in which lowland river processes can be isolated. In this chapter, I discuss the unique characteristics of the Rio Bermejo and justify its suitability as a model fluvial system. I also describe the geochemical methods I used to study the residence time and organic carbon composition of Rio Bermejo sediment, which are the basis for Chapters 3-5.

2.1 The Rio Bermejo

Emanating from an elevation of more than 5800 meters above sea level, the Rio Bermejo drains the eastern flank of the Andes between latitudes -22° and -25° in NW Argentina (**Fig. 2.1**). The central Andes are an efficient erosional engine. Subduction of the Nazca plate beneath the South American plate drives topographic uplift and crustal thickening, resulting in a present-day elevation gradient ranging from 300 m in the foreland basin to >5000 m in the Eastern Cordillera over a distance <100 km (**Fig. 2.1**). Active shortening in the eastern flank of the mountain belt expresses itself as a fold-and-thrust belt, which sets a relatively shallow exhumation depth. Evolution of this high relief setting ~5 million years ago created an orographic barrier to northerly and easterly air masses and moisture, resulting in formation of the South American Low Level Jet stream (Mulch et al., 2010; Rohrmann et al., 2016) and a steep rainfall gradient (<0.25 m/yr on the high plateau to >2 m/yr in the lower elevation foreland). The collective effect of this tectonic-climatic interaction is focused erosion along the eastern flank of the central Andes, where

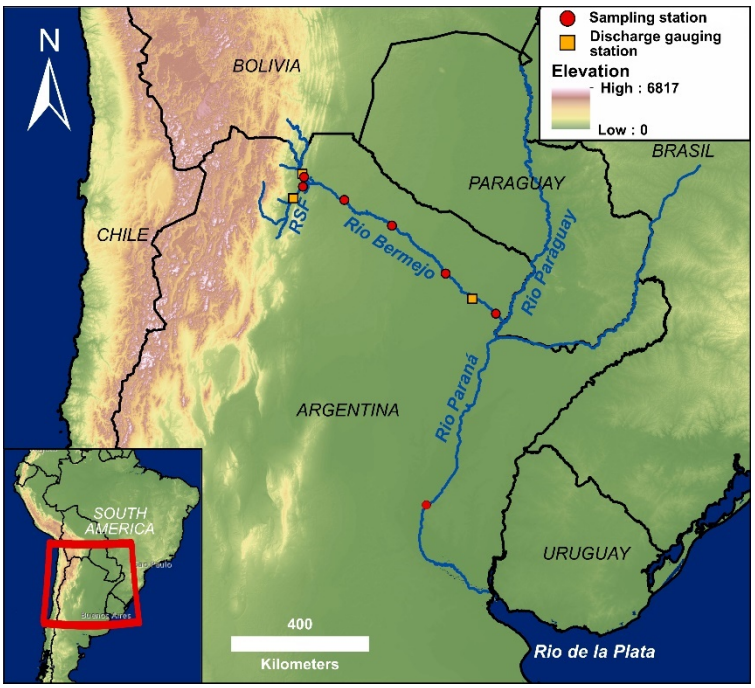

Figure 2.1. Study area map. Topographic map of the study area showing the Rio Bermejo system and major rivers downstream, Rio Paraguay and Rio Paraná. RSF = Rio San Francisco. Red points show the catchment-integrated sampling locations discussed in this dissertation.

erosion rates range from <0.1 mm/yr on the high, dry plateau to >1 mm/yr in the steep, wet foreland (Bookhagen & Strecker, 2012).

Along this erosional gradient, numerous headwater tributaries converge to form the mainstem Rio Bermejo, which flows uninhibited and without additional tributaries for nearly 1300 km from the mountain front to the Rio Paraguay-Rio Paraná system, where the elevation is just 45 meters above sea level. The Rio Paraná ultimately delivers erosional products from the Rio Bermejo to the Rio de la Plata estuary. The entirety of the Bermejo drainage basin comprises 1.2×10^5 km^2, with a headwater drainage area of 5.2×10^4 km^2 and a lowland fluvial fan of 7.0×10^4 km^2. The last major tributary to the Rio Bermejo is the Rio San Francisco (RSF), located at the mountain front. The RSF drainage basin comprises roughly half of the Rio Bermejo headwater area, but contributes only ~18% of the total discharge and ~15% of the annual suspended sediment flux.

With an annual mean water discharge of ~432 m^3/s, the Bermejo is not a volumetrically important tributary to the Rio Paraná, however, its annual mean suspended sediment export of ~80 Mt/yr is the largest supply of suspended sediment to the major river system. This is equivalent to a sediment yield of ~650 t km^{-2} yr^{-1}, but nearly all of the sediment is produced in the headwaters, where the sediment yield is ~1600 t km^{-2} yr^{-1}. Out of the entire Rio de la Plata drainage basin, the Rio Bermejo contributes only ~2% of the water discharge, but ~70% of the sediment discharge (Amsler & Drago, 2009; Dogliotti et al., 2016). The Paraná exports on the order of 1.27 MtC/yr (0.49 tC/km^2 yr^{-1}) in the form of particulate organic carbon (Depetris & Cascante, 1985), and given its contribution to the total sediment flux, the Bermejo likely discharges a significant portion of this organic carbon.

The explorer John Page (1889) was perhaps the first to publish on the dynamic behavior of the Rio Bermejo, noticing the power of the sediment load and the rate of morphodynamic change:

> "The amount of sediment it brings down is enormous, and it is deposited with such extraordinary rapidity that it cannot but be considered a peculiarly strong feature of the mechanical work of this river, by which its geological formations are rapidly made, and, indeed, unmade as well."

The large sediment supply from the central Andes leads to high rates of aggradation. While aggradation rates in this system have not been previously quantified, they are rapid enough to cause frequent avulsions, where the channel may overtop or breach its levees and relocate to a new position in a topographic depression. The last known major avulsion of the

Rio Bermejo occurred ~150 years ago, between the years 1869 and 1870, when the river flooded and moved northward ~40 km from its old channel, which is now referred to as the Rio Bermejito (Page, 1889).

Despite attempts to exploit the Rio Bermejo's connectivity as a trans-continental shipping route in the late 1800s, the Rio Bermejo lowland floodplain remains largely unaffected by anthropogenic land-use change (Piquer-Rodríguez et al., 2015) and its channel remains undammed. Because the floodplain is relatively remote and undeveloped, there are few places where the river can be accessed by motor vehicle. Just upstream from the Rio Bermejo-Rio San Francisco confluence, bridges span each tributary, but from the mountain front to downstream km 865, the river can only be accessed by a few primitive dirt roads that have been carved into the dense subtropical forest. Unlike many rivers that have been heavily developed and engineered, this unique setting makes the Rio Bermejo the ideal study area to discern the natural effects of fluvial morphodynamics on fluvial sediment and organic carbon transfer.

2.2 Geochemical tools used to trace fluvial organic carbon cycling

For this dissertation, I applied a unique combination of geochemical methods to determine the fluvial sediment transit time, and to analyze the composition and quantify the amount of organic carbon transported by the Rio Bermejo.

To constrain the fluvial sediment transit time for material transported downstream in the Rio Bermejo system, I applied cosmogenic meteoric 10-beryllium ($^{10}Be_m$) as a chronometer. $^{10}Be_m$ is a rare isotope produced in the atmosphere via spallation of nitrogen and oxygen atoms by cosmic rays. Through rain and aerosol deposition, $^{10}Be_m$ is delivered to Earth's surface where it is readily adsorbed to mineral particles, particularly those with high surface area and reactive secondary coatings (Willenbring & von Blanckenburg, 2010). $^{10}Be_m$ accumulates in soil and sediment at Earth's surface at a relatively constant rate, averaged over 10^2-10^3 yr (Beer et al., 1984; Vonmoos et al., 2006). $^{10}Be_m$ concentrations can be measured by first leaching the amorphous and crystalline oxyhydroxide phases (containing the $^{10}Be_m$) from a sediment sample, then purifying, concentrating, and oxidizing the $^{10}Be_m$ to prepare for measurement by accelerator mass spectrometry (AMS). By assuming a known depositional flux over time, $^{10}Be_m$ inventories (i.e., total measured $^{10}Be_m$ in a soil profile or a mass of sediment) have been used as a chronometer for soil residence time (e.g., Monaghan et al., 1983; Pavich et al., 1984) and to measure catchment-averaged denudation rates (e.g., von Blanckenburg et al., 2012). Building on these applications, I show that sediment transit time can be derived from the downstream increase in $^{10}Be_m$ concentrations in river suspended sediment collected along a source-to-sink

transect. For the Rio Bermejo, this derived timescale provides a basis for interpreting changes in fluvial organic carbon composition and concentration with distance downstream.

Key measurements for quantifying the fluvial carbon budget are total organic carbon (TOC) concentrations of river sediment. When measured for different sediment samples from different locations within a river system, TOC concentrations inform us about the amount and spatial distribution of carbon in soil, sediment, and vegetation in a catchment. Total carbon and total organic carbon concentration can be measured for solid material by means of elemental analysis. Organic carbon is typically isolated from inorganic species by treating samples with an acid that readily dissolves inorganic carbon (e.g., hydrochloric).

Carbon isotopes are commonly used to characterize both organic and inorganic carbon, and trace its pathway from the atmosphere, into plants, soils, sediments, and water, and then back into the atmosphere. Carbon has three naturally-occurring isotopes: ~98.89% of all carbon is ^{12}C, while ~1.1% is ^{13}C (Craig, 1953), and ^{14}C occurs in trace amounts ($<10^{-10}$ %) (Chanton et al., 2015). Measurement of the abundance of ^{13}C and ^{14}C relative to ^{12}C in organic compounds can provide insight to biogeochemical cycling in the environment. Mass-dependent fractionation causes differences in the ratios of ^{13}C and ^{14}C to ^{12}C for different carbon-based compounds, due to variability in chemical bond strength or kinetic rates (Hayes, 2004). These differences make carbon isotopes useful for tracing biogeochemical cycling of carbon between the atmosphere, biosphere, ocean, and lithosphere.

Because differences between isotope species are very small, typically just a few percent, stable isotope measurements are quantified by a ratio of one isotope species relative to the most abundant species (e.g., $^{13}C/^{12}C$, $^{14}C/^{12}C$) (Hayes, 1983). High precision measurements are required to detect these ratios. While instruments are capable of the required precision, absolute measurements can still vary over time due to changes in internal and external measurement conditions. Instead of absolute measurements, isotope ratios are normalized to reference samples with a constant isotopic composition.

$^{13}C/^{12}C$ measurements are reported using δ notation (McKinney et al., 1950):

$$\delta = \left(\frac{R_{sample}}{R_{standard}} - 1\right) * 1000 \qquad (2.1)$$

where R_{sample} and $R_{standard}$ are the isotope ratios of the sample and the reference material, respectively. $^{13}C/^{12}C$ ratios are normalized to the Vienna PeeDee Bellemnite (VPDB) standard, and measurements are reported in parts per thousand (*per mille*, ‰) (Coplen, 1996).

The atmospheric $\delta^{13}C$ value is about -8‰, but isotopic fractionation during carbon transformation results in divergence from this value (Bowling et al., 2008). For carbonate rocks, $\delta^{13}C$ values are typically around 2-4‰, if in equilibrium with modern surface waters. For organic carbon, photosynthesis results in significant depletion of ^{13}C in plants relative to the atmosphere (Degens, 1969). Due to divergent photosynthetic pathways, C3 and C4 plants have distinct isotopic signatures. C3 plants (most tree and shrub species) have $\delta^{13}C$ values ranging from -20 to -35‰ and C4 plants (most grass and sedge species) have $\delta^{13}C$ values ranging from -10 to -16‰ (Deines, 1980; Tipple & Pagani, 2007). This distinction allows us to use $\delta^{13}C$ values to trace the source of vegetation in river systems and to reconstruct vegetation changes from organic compounds preserved in sedimentary archives. Heterotrophic microbial metabolism also results in CO_2 that is more depleted of ^{13}C because ^{12}C-^{12}C bonds require lower energy to break than ^{13}C-^{12}C bonds (Degens, 1969). Following microbial processing, the remaining reduced organic carbon is generally more enriched in ^{13}C. Accordingly, $\delta^{13}C$ measurements can be used to trace organic matter decomposition, because heterotrophic respiration causes selective preservation of ^{13}C-enriched compounds (Hirave et al., 2020).

Radiocarbon (^{14}C) provides a clock for the carbon cycle. ^{14}C is a cosmogenic nuclide produced in the atmosphere through the bombardment of thermal neutrons with ^{14}N, and subsequently decays with a half-life of 5730 years (Godwin, 1962). Like $^{10}Be_m$, ^{14}C is also measured via AMS due to its low isotopic abundance. Before aboveground nuclear weapons testing (1945-1998) the atmosphere was roughly in equilibrium with respect to ^{14}C, but atmospheric ^{14}C concentrations spiked during this period ("bomb spike") and have been declining through the 21st century (Keeling, 1979). Due to this bomb spike, ^{14}C measurements are normalized to 95% of the ^{14}C activity measured in the NBS oxalic acid standard in the year 1950 (Stuiver & Polach, 1977). This normalized value is termed "Fraction Modern" ($F^{14}C$), and is calculated as follows:

$$F^{14}C = \frac{\left(\frac{^{14}C}{^{12}C}\right)_{sample,-25}}{0.95\left(\frac{^{14}C}{^{12}C}\right)_{OX1,-19}} \qquad (2.2)$$

where $^{14}C/^{12}C$ of the sample is corrected to a common $\delta^{13}C$ of -25‰ with respect to VPDB, and $^{14}C/^{12}C$ of the OX1 standard is corrected to -19‰ with respect to VPDB. $F^{14}C$ values can be converted into ^{14}C-ages to estimate the mean residence time of carbon in an open system (e.g. soil, sediment), or the age of carbon in a closed system (e.g., wood, leaf) (Torn et al., 2009).

Organic carbon in soils and sediments comprises a complex matrix of compounds, which can vary in origin, degradation state, and isotopic composition. This complexity often makes it difficult to explain bulk $\delta^{13}C$ and $F^{14}C$ values, but by combining the two isotopes, it is usually possible to separate different components of bulk organic carbon. Further methodological advances within the last four decades have enabled the separation of unique compounds from these complex organic matrices for compound-specific isotope measurement. Compound-specific analyses can be used to investigate different components of sedimentary organic matter, such as *n*-alkane compounds derived from vascular plants. Gas chromatography mass spectrometry (GC-MS) is a method employed to identify the mass spectra of complex organic matrices, and resulting mass/charge ratios can be used to identify the chemical structures of individual organic compounds.

Compound-specific carbon isotope analyses were first applied in biogeochemistry to reconstruct ancient biogeochemical processes (Hayes et al., 1989), revealing that $\delta^{13}C$ values of *n*-alkanes covaried with $\delta^{13}C$ values of bulk organic carbon in shale rock samples. Later, compound-specific hydrogen isotopes measured in algal lipids from marine and freshwater environments revealed that lipid $\delta^{2}H$ values correlated with $\delta^{2}H$ values of aquatic waters (Sauer et al., 2001). Eglinton et al. (1996) developed a method to isolate and recover target organic compounds for natural abundance radiocarbon measurement using automated preparative capillary gas chromatography (PCGC). The ^{14}C content of recovered compounds could then be measured by AMS. This methodological advancement allows us to distinguish the sources of various components within a sample (e.g., modern vascular plants, fossil organic carbon, aged soil organic carbon), as well as their age or residence time at Earth's surface and in sedimentary deposits (e.g., Bao et al., 2018; Eglinton et al., 1997; Kusch et al., 2010; Mollenhauer & Eglinton, 2007).

While compound-specific isotopes provide detailed information on the chemical composition of complex organic matrices, it is not entirely clear how organic carbon is distributed in sediment samples, and whether it is more often present as coatings on mineral grains or as discrete organic particles. Nano-scale secondary ion mass spectrometry (NanoSIMS) is a relatively new approach used to study elemental cycling in soil and sediment with nanometer resolution. The Cameca NanoSIMS50 is an ion microprobe designed to simultaneously detect up to five ion species, including ^{12}C and ^{13}C, within the top five nm of a sample with a lateral resolution of 50 nm (Herrmann et al., 2007). For natural isotope abundance studies, ^{12}C and ^{13}C cannot be resolved sufficiently to determine a $\delta^{13}C$ value, but NanoSIMS

have been used to measure $^{13}C/^{12}C$ ratios in ^{13}C labeling studies tracing microbial carbon sequestration in soils (Mueller et al., 2012; Vogel et al., 2014). The ability to measure multiple ions simultaneously shows promise for studying the associations between organic carbon and reactive metals, like aluminum and iron, on sedimentary particles.

2.3 Field campaigns and sampling strategy

To make these geochemical measurements for the Rio Bermejo, I carried out several field campaigns to collect samples representative of the sediment and organic carbon conveyed by and produced within the river system. Here, I describe the approaches used to collect this valuable material.

2.3.1 Catchment-integrated sampling

River catchment areas are large relative to the spatial scale of biogeochemical heterogeneity, such that river sediment captures the average signal of erosional and biogeochemical processes playing out in a catchment. River sediment samples effectively represent an integration of erosional products delivered from the upstream contributing drainage area (**Fig. 2.2**). Sampling at multiple points along a large river system allows for comparison of erosion and sediment storage dynamics in different parts of a catchment. Several studies have shown that river sediment chemistry varies with flow depth due to heterogeneity in particles that are vertically sorted in the water column due to size, shape, and density differences (Bouchez et al., 2011; Lupker et al., 2011; Wittmann et al., 2012; Yu et al., 2019). By collecting sediment samples from different depths along this vertical profile, we ensure that we capture the range of particle sizes and associated chemical compositions.

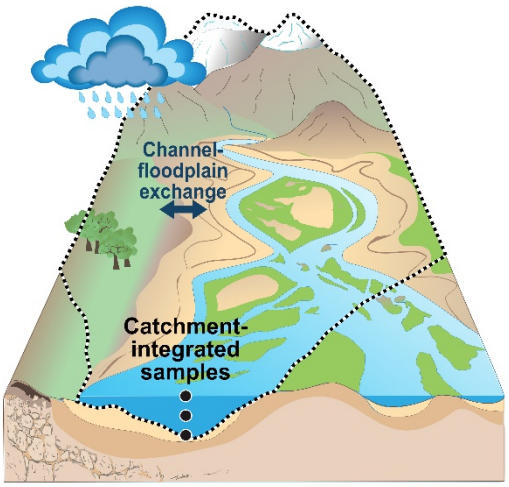

Figure 2.2. Catchment-integrated sampling. Illustrative representation of a catchment-integrated sample, with the black dashed line showing the contributing drainage area represented by the sample. Adapted from Wittmann et al. (2018).

The primary sample set used in Chapters 3, 4, and 5 of this dissertation was collected in March 2017, during the South American Monsoon Season. At five stations along the mainstem Rio Bermejo, I collected actively-transported river suspended sediment from multiple depths in the water column, plus bedload sediment where possible (river km -10, 135, 420, 865, 1220, where river km 0 is the RSF confluence at the mountain front). Additionally, we collected surface water and bedload sediment samples from the RSF ~15 km upstream of its confluence with the Rio Bermejo. Sampling was conducted by boat equipped with an Acoustic Doppler

Current Profiler (ADCP), which was used to survey the channel cross section, measure surface water velocity, and locate the channel thalweg.

2.3.2 Floodplain chronosequence

A history of floodplain sediment deposition and periodic avulsions is recorded in the Rio Bermejo fluvial fan. Abandoned channels, or 'paleochannels,' represent past positions of the Rio Bermejo and can be observed in satellite imagery (**Fig. 2.3**). These geomorphic units contain river sediment that was deposited shortly before an avulsion. They are visible on the landscape because, once abandoned, these units were filled with standing water and became wetlands, as the surrounding landscape continued to flourish as a subtropical forest. These wetlands slowly desiccated over time and evolved into grasslands, making it easy to distinguish these features from the adjacent forests.

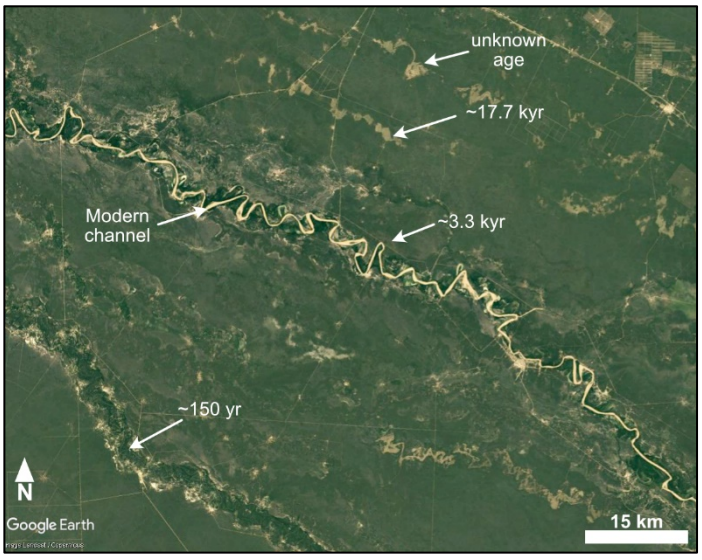

Figure 2.3. Rio Bermejo paleochannels. Google Earth-derived satellite image of the Rio Bermejo fluvial fan/floodplain surface. Arrows point to the modern channel, and to paleochannels that were abandoned between 150 and 20,000 years ago.

In the Rio Bermejo fan, ancient floodplain sediment was sampled from a chronosequence of paleochannel deposits by boring down to <5 m with an Edelman-type hand auger. In each sediment core, material was collected from 20-40 cm intervals to obtain a sample set that captures the changes in grain size and geochemical composition with depth. In Chapter 3, I present meteoric ^{10}Be concentration data from four floodplain sediment profiles, which I use to calculate a local long-term delivery rate of cosmogenic meteoric ^{10}Be to the Rio Bermejo floodplain. In Chapters 4 and 5, I use the organic carbon composition of floodplain sediment samples to estimate the contribution of floodplain material to the modern Rio Bermejo suspended sediment load.

2.3.3 High temporal-resolution sampling

It is well known that the source and composition of river suspended sediment and organic carbon changes throughout the year, as river discharge fluctuates and patterns of precipitation, ecosystem production, and geomorphic activity change (Clark et al., 2017; Hemingway et al., 2017; Hilton, 2017; McClelland et al., 2016; Wang et al., 2012). To capture these temporal changes, surface water suspended sediment was collected weekly from the Rio Bermejo at downstream km 865 for a period of one year. This sampling was achieved by employing a local resident equipped with sampling apparatus. In Chapter 4, I present biomarker isotopic composition data for a subset of these samples to evaluate the changes in organic matter source during different hydrological conditions. This subset covers a river discharge range of <60 m^3/s to >1200 m^3/s, which is representative of the hydrological variability observed over a typical water year in this river system.

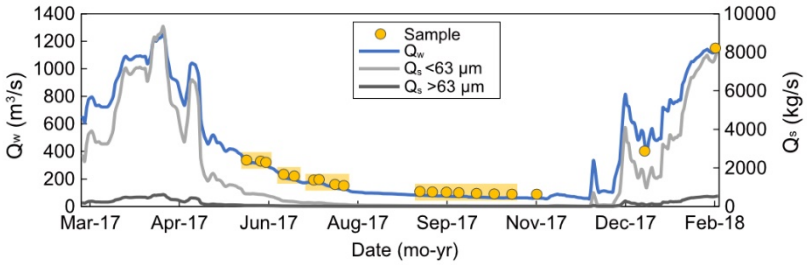

Figure 2.4. Temporal discharge variability. Time-series of water discharge (blue curve), silt and clay sediment discharge (light gray curve), and coarse sediment discharge (dark gray curve). Yellow circles indicate samples collected and analyzed in Chapter 4. Data from the Argentina National Hydrological Database.

3 METEORIC ^{10}BE AS A FLUVIAL SEDIMENT TRANSIT TIME PROXY

Published as:

Repasch, M., Wittmann, H., Scheingross, J. S., Sachse, D., Szupiany, R., Orfeo, O., Fuchs, M., and Hovius, N. (2020). Sediment Transit Time and Floodplain Storage Dynamics in Alluvial Rivers Revealed by Meteoric ^{10}Be. Journal of Geophysical Research: Earth Surface, 125(7), 1–19. https://doi.org/10.1029/2019jf005419.

Key Points

- Meteoric ^{10}Be measured in depth-integrated river suspended sediment geochemically records mean fluvial sediment transit time.
- In the Rio Bermejo (Argentina), ^{10}Be concentrations increase 230% over ~1300 km transit distance, yielding a mean total transit time of 8.4 ± 2.2 x10^3 yr.
- Reach-scale analysis of ^{10}Be-derived transit times shows that tectonics, channel migration rates, and incision depth are primary drivers.

Abstract

Quantifying the timescales of sediment transport and storage through river systems is fundamental for understanding weathering processes, biogeochemical cycling, and improving watershed management, but measuring sediment transit time is challenging. Here we provide the first systematic test of measuring cosmogenic meteoric Beryllium-10 (^{10}Be$_m$) in the sediment load of a large alluvial river to quantify sediment transit times. We take advantage of a natural experiment in the Rio Bermejo, a lowland alluvial river traversing the east Andean foreland basin in northern Argentina. This river has no tributaries along its trunk channel for nearly 1300 km downstream from the mountain front. We sampled suspended sediment depth profiles along the channel and measured the concentrations of ^{10}Be$_m$ in the chemically extracted grain coatings. We calculated depth-integrated ^{10}Be$_m$ concentrations using sediment flux data, and found that ^{10}Be$_m$ concentrations increase 230% from upstream to downstream, indicating a mean total sediment transit time of 8.4 ± 2.2 kyr. Bulk sediment budget-based estimates of channel belt and fan storage times suggest that the ^{10}Be$_m$ tracer records mixing of old and young sediment reservoirs. On a reach scale, ^{10}Be$_m$ transit times are shorter where the channel is braided and superelevated above the floodplain, and longer where the channel is incised and

meandering, suggesting that transit time is controlled by channel morphodynamics. This is the first systematic application of $^{10}Be_m$ as a sediment transit time tracer and highlights the method's potential for inferring sediment routing and storage dynamics in large river systems.

Plain Language Summary

Understanding how long sediment takes to travel downstream in rivers, a.k.a. sediment "transit time," is crucial for responsible watershed management and constraining global biogeochemical cycles. We aim to measure transit times for large rivers and determine the processes regulating this timescale. We present a new transit time proxy based on beryllium-10 (^{10}Be), a rare isotope produced in the atmosphere and delivered to Earth by rain. If river sediment collected downstream has more ^{10}Be than sediment upstream, this indicates that sediment was trapped in the floodplain for many years before continuing to travel downstream. We collected river sediment at multiple locations from upstream to downstream along a large, undammed river, the Rio Bermejo in Argentina. We found that ^{10}Be increased 230% from upstream to downstream, translating to a transit time of ~8500 years. This long timescale implies that sediment and carbon delivered to rivers have enough time to be weathered or oxidized to CO_2 before they are buried in the ocean. We also show that transit time is controlled by the river's shape and lateral mobility, suggesting that human alteration of channel shape or sediment supply will reduce a river's ability to use its floodplain for natural flood and erosion control.

3.1 Introduction

The residence time of sediment at Earth's surface influences multiple time-dependent processes, including soil formation, weathering, nutrient production, and biogeochemical cycling. Furthermore, sediment deposition and remobilization during source-to-sink transit can dampen or transform sedimentary signals produced by discrete episodic events (Armitage et al., 2011; Jerolmack & Paola, 2010; Pizzuto et al., 2017), conflating the record of climatic and tectonic forcing preserved in sedimentary archives. Knowing the amount of time river sediment takes to travel from source to sink is essential to understand the effects that can accumulate during transit and to elucidate the processes that regulate routing pathways.

In this study, we explore fluvial sediment "transit time," which we define as the mean time required for all sedimentary particles delivered to a river channel to be conveyed downstream to the river's outlet, including time spent in transient storage in the channel margins. Our main objectives are to 1) quantify transit times using a geochemical proxy, and 2) determine the geomorphic and/or tectonic mechanisms regulating sediment transit time.

Various proxy methods have been tested to resolve sediment transit time in river systems, which have progressively improved our ability to quantify the rate of sediment transit. Uranium series isotopes provide a chronometer for the time since sediment reached 63 μm or smaller and have been used to estimate river sediment transit times and comminution ages (e.g., Depaolo et al., 2006; Dosseto et al., 2008; Granet et al., 2010). However, this method cannot estimate transit time for larger grain size fractions that are common in many rivers, and newer studies identify that small changes to input parameters of U-series comminution age models, such as the uranium leaching rate, result in large uncertainties in transit time estimates (e.g., Handley et al., 2013; Martin et al., 2019). Luminescence has also been explored as a tracer of fluvial sediment transport (Gray et al., 2017, 2018), based on the idea that sediment is bleached (re-set) during transport and regenerated during storage. However, tests of this model yielded long-term storage times and transport length scales inconsistent with values derived from sediment budget-based methods (Gray et al., 2017). These previous efforts highlight the need for additional transit time proxies that are sensitive on timescales of 10^3-10^5 yr and can yield results commensurate with geomorphic data.

Fluvial sediment transit times have also been approximated using theoretical models (e.g., Bradley & Tucker, 2013; Lauer & Parker, 2008a; Pizzuto et al., 2014), but thus far these theories are developed for steady-state, mass-balanced rivers. Transit time can be influenced by a number of processes, including channel length and steepness, its morphology and dynamics (e.g., vertical incision, lateral migration), the balance of sediment supply to transport capacity, accommodation space, and the frequency of channel breaching and avulsion (Dade & Friend, 1998; Lauer & Parker, 2008a; Phillips et al., 2007; Sheets et al., 2002; Strong et al., 2005). As a result, simple, steady-state modeling approaches to estimate sediment transit time are often not representative of a system's dynamic response to periodic climatic or tectonic change. For example, in actively developing foreland basins, dynamic processes including foredeep subsidence, forebulge uplift, and backbulge subsidence drive rivers to aggrade, incise, and distribute sediment differentially across the lowland (Lane & Richards, 1997). How such tectonic and geomorphic processes influence sediment transit time is largely unknown, due to the lack of suitable techniques to track sediment over ~10^3-10^5 yr timescales during which these processes play out. Once transit times can be estimated with higher precision, we can study how morphodynamic processes influence the duration of sediment transport and storage.

In this study we systematically test the use of meteoric ^{10}Be ($^{10}Be_m$) in river sediment as a proxy for fluvial sediment transit time. We measure $[^{10}Be]_m$ in river sediment sampled from

river depth profiles along the Rio Bermejo, a large alluvial river traversing the East Andean foreland in northern Argentina. We use these data to calculate the change in $[^{10}Be]_m$ with distance downstream from the mountain front and thereby estimate the transit time for sediment moving across the lowland basin. To support that the $^{10}Be_m$ proxy provides reasonable transit time estimates, we compare our $^{10}Be_m$-derived transit time to theoretical short and long timescale transit times estimated with sediment budgeting methods. We evaluate the controls on sediment transit time by comparing four reaches of the mainstem Rio Bermejo, which have distinct differences in channel planform, incision depth, and lateral migration rate, and sit in different morphotectonic domains of the Andean foreland basin.

3.2 Meteoric ^{10}Be as a transit time proxy

$^{10}Be_m$ has potential to trace sediment transit over large spatial and temporal scales. $^{10}Be_m$ is a cosmogenic radionuclide produced in Earth's atmosphere through the bombardment of nitrogen and oxygen atoms by cosmic rays (Lal and Peters, 1967), with a half-life of 1.387×10^6 yr (Chmeleff et al., 2010; Korschinek et al., 2010), which is sufficiently long such that radioactive decay is negligible over 10^4 yr or less. After production in the atmosphere, $^{10}Be_m$ is captured by water vapor and aerosol particles, and then delivered to Earth's surface primarily through precipitation and aerosol deposition (Willenbring & von Blanckenburg, 2010). As a cation, $^{10}Be_m$ is adsorbed onto mineral surfaces and is incorporated into the secondary mineral coatings on all sedimentary particles, particularly oxyhydroxides. To measure $^{10}Be_m$ concentrations $[^{10}Be_m]$, these coatings, or "reactive phases," can be easily detected in as little as 0.5 g of sediment with heterogeneous mineralogy.

$^{10}Be_m$ concentrations have been measured to determine soil residence time, and rates of erosion, weathering, and denudation (e.g., von Blanckenburg et al., 2012; Egli et al., 2010; Jelinski et al., 2019; Wittmann et al., 2015). Monaghan et al. (1983) first explored $^{10}Be_m$ as a soil residence time chronometer, demonstrating that the inventory of $^{10}Be_m$ derived from its accumulation in soil profiles correlates with soil age, and is retained within soil profiles over 10^4-10^6 yr timescales. When soil profile age is known, the inventory of $^{10}Be_m$ in the soil profile can be used to derive a local $^{10}Be_m$ depositional flux ($F^{10}Be_m$) (e.g., Graly et al., 2011).

We employ a similar concept here, but use the inventory of $^{10}Be_m$ in river sediment load to estimate the average time sediment particles are stored within the river system before being exported, which we term "transit time." Sediment stored in the river banks and floodplain receives a local $F^{10}Be_m$ (at m^{-2}) at the surface, and over time, this $^{10}Be_m$ is re-distributed down the sediment profile. In a laterally-migrating river system, sediment is frequently deposited on

the floodplain, and remains there for many years before being re-entrained. Particles re-mobilized from storage have $^{10}Be_m$ concentrations ($[^{10}Be]_m$) representing the cumulative storage time. The depth to which the channel remobilizes stored sediment is defined as the 'remobilization depth,' *h*, which ultimately determines how much active channel sediment is exchanged with floodplain sediment. Increasing *h*, along with channel migration rate, increases the probability that sediment is stored during transit. Accordingly, the net sediment transit time increases with progressively more lateral sediment exchange along the channel. This net transit time is recorded by $[^{10}Be]_m$ in active channel sediment, which should increase downstream at a corresponding rate. We assume the addition of $^{10}Be_m$ during active in-channel transport is negligible because time spent in motion is a small fraction of the total transit time (Pizzuto et al., 2014).

The validity of this concept has been shown by Wittmann et al. (2015), who showed that measured $^{10}Be_m$ concentrations in depth-integrated river sediment profiles in the Amazon River basin increase substantially through ~1000 km of downstream transit. This increase validates the concept of using $^{10}Be_m$ to measure transit time, but interpreting the data in terms of a sediment transit time yields a large range of uncertainty (1.6 kyr to 29 kyr), largely due to insufficient quantification of the remobilization depth. To reduce uncertainty and to realize the potential of this approach, the transit time estimate requires additional geomorphic data, such as the depth of incision, channel migration rates, and increased spatial resolution of $^{10}Be_m$ measurements.

River sediment $^{10}Be_m$ concentration data may be a powerful tool for catchment scale sediment dynamics studies (e.g. Belmont et al., 2014; Rahaman et al., 2017; Reusser & Bierman, 2010; Stout et al., 2014; Wittmann et al., 2015). However, $[^{10}Be]_m$ in sediment is dependent on specific surface area (SSA) and the composition and abundance of grain coatings (Shen et al., 2004; Singleton et al., 2017). SSA relates inversely to grain size, and thus is subject to hydrodynamic particle sorting in rivers (Rouse, 1937). This can be accounted for by calculating depth-integrated concentrations based on samples collected from full river water depth profiles (Bouchez et al., 2011; Wittmann et al., 2015, 2018). Many lowland rivers also experience downstream particle size fining (e.g., Frings, 2008; Sternberg, 1875) and weathering, which may increase downstream $^{10}Be_m$ sorption capacity and abundance of grain coatings, respectively, causing apparently longer transit times. To correct for downstream changes in SSA and secondary mineral abundance, $[^{10}Be]_m$ can be normalized to concentrations of reactive phase Beryllium-9 ($^{9}Be_{reac}$). $^{9}Be_{reac}$ exhibits similar geochemical behavior as $^{10}Be_m$,

but its supply is limited by weathering and reactive transport, whereas $^{10}Be_m$ is continuously supplied via atmospheric delivery (von Blanckenburg et al., 2012). If both SSA and $[^{10}Be]_m$ increase downstream, but $[^{9}Be]_{reac}$ does not, then these effects have no control on Be concentrations, and increases in $[^{10}Be]_m$ are exclusively due to increasing transit time.

3.3 Study area and sampling

3.3.1 Rio Bermejo, Andean foreland basin

An ideal setting to study source-to-sink transit time is a river system with a single, well-constrained sediment source, and one long, channel without tributaries or distributaries that interacts with its floodplain by overbank flow and lateral migration. The Rio Bermejo in northern Argentina (Figure 3.1) is a unique setting where a high sediment flux delivered from the Andes is conveyed through a lowland basin along a ~1300 km channel with no tributaries. At the mountain front, headwater streams draining the eastern Andes fold-and-thrust belt converge into one trunk channel – the mainstem Rio Bermejo. The Rio San Francisco (RSF) is the last major tributary to deliver water and sediment to the Bermejo near the mountain front (river km 0), after which the river runs 1267 river km downstream (nearly 700 km linear

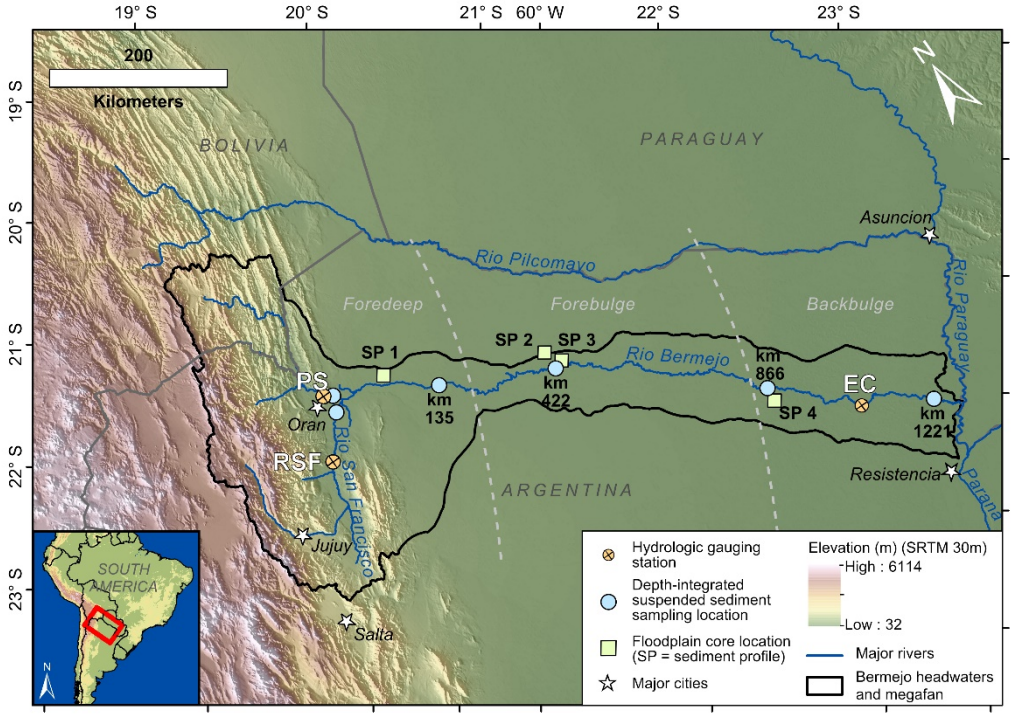

Figure 3.1. Study area map. Overview shaded relief map of the Rio Bermejo fluvial system in the Andean foreland basin of NW Argentina. Inset map shows the location in the South American continent. The thick black line delineates the extent of the Rio Bermejo headwaters and the extent of the megafan in the lowland basin, which is not equivalent to the flow-routed drainage area. Dark blue lines show only the rivers relevant to this study. Pale blue circles show the locations of the six suspended sediment depth profiles, labeled with their distance downstream along the channel in kilometers. Pale green squares mark the locations of sediment profile (SP) samples. Pale orange quartered circles represent three hydrologic gauging stations: PS – Pozo Sarmiento, RSF – Rio San Francisco, EC – El Colorado. Grey dashed lines show the approximated boundaries between the foredeep, forebulge, and backbulge depozones.

distance from the mountain front) before reaching the Rio Paraguay. Sediment sourced upstream of the RSF confluence can only be transported downstream or deposited in the channel margins and is not mixed with tributary inputs, making the Rio Bermejo an ideal natural laboratory to study long distance sediment transit.

Repeated avulsions of the Rio Bermejo since the late Pleistocene have given rise to a narrow fluvial megafan extending from the Andean mountain front to the valley of the Rio Paraguay (Iriondo, 2007). Despite subtle, low-relief topography, the modern channel belt is perched atop this megafan, preventing tributaries from joining the river. The headwaters and megafan comprise an area of 120,280 km^2, of which 70,000 km^2 belongs to the megafan (Figure 3.1).

Previous studies identify three distinct depozones across the megafan (Figure 3.1), related to lithospheric flexure in the periphery of the Andean orogen (Cohen et al., 2015; Horton & DeCelles, 1997; Horton & Decelles, 2001; McGlue et al., 2016), which appear to influence the morphodynamics, and potentially the sediment transit time, of the Rio Bermejo. After exiting the mountain front, the river traverses the foredeep basin for ~175 km, where the channel is braided and ~1.5 m deep. In this reach, persistent aggradation has lifted the active channel belt above the surrounding lowland. Downstream from the foredeep, the river encounters a zone of forebulge uplift, where the channel abruptly transitions to a single-thread meandering planform with a channel depth of ~5 m, a cut bank height of up to 8 m, and high channel migration rates of 10-50 m yr^{-1}, as estimated from time-series satellite image analysis (Text A1). This pattern persists from ~175 to ~450 km east of the mountain front, where the river enters the backbulge depozone. There the channel is variably super-elevated and incised as it traverses previous channel belts, the average channel migration rate is <10 m yr^{-1}, and lateral erosion is restricted to separate short reaches along the river (Text A1). We use $^{10}Be_m$ to evaluate the differences in transient storage time within and across these three depozones.

A first order control on the amount of $^{10}Be_m$ in the river sediment load is the modern erosional flux from upstream. Water and suspended sediment discharge records are available at three gauging stations in the lower Rio Bermejo system (PS, RSF, and EC on Figure 3.1), which allow us to evaluate water and sediment fluxes from upstream to downstream (see Text A1). Analysis of gauging station data suggest that 86% of the suspended sediment delivered to the mainstem Rio Bermejo is eroded from the northern half of the headwaters, and only 14% of the sediment flux is derived from the RSF catchment, despite roughly equal drainage areas. Total annual sediment flux calculated for the Rio Bermejo just downstream of the RSF confluence is

103 Mt yr^{-1}, while 80 Mt yr^{-1} is recorded at EC (Text A1). This upstream-downstream disparity reflects the loss of 23% of sediment load to storage in the foredeep basin, while 80 Mt yr^{-1} of sediment transits the megafan.

3.3.2 River sediment and floodplain profile sampling

To estimate the mean transit time of sediment conveyed by the Rio Bermejo, we measured [$^{10}Be_m$] in suspended sediment collected at multiple locations along the mainstem and evaluated the change in concentration from upstream to downstream. We then determined the time required to accumulate the additional $^{10}Be_m$, given the local $F^{10}Be_m$. We constrained this local depositional flux by using independently dated (OSL) floodplain soil profiles (see below).

We collected fluvial suspended sediment in vertical depth profiles at five sampling locations along the length of the Rio Bermejo (Figure 3.1) during near-bankfull conditions, when discharge varied between 675 and 1080 m^3 s^{-1} and banks were actively eroding. Additionally, we collected one depth profile from RSF and one from the Rio Bermejo 10 km upstream of the RSF confluence. We calculate an integrated headwater depth profile by combining these profiles upstream of the mainstem and weighting them by their respective proportions of the total sediment load input to the mainstem. We located the channel thalweg at each sampling location using a 600 kHz ADCP (Acoustic Doppler Current Profiler, Teledyne Workhorse). In the thalweg, we collected water and suspended sediment from a boat using a weighted 8-liter horizontal sampling bottle (Wildco Beta Plus bottle) with an attached pressure transducer to measure sampling depth. To capture the range and distribution of grain sizes and sediment concentrations in the river, suspended sediment samples were collected from two to four discrete depths within a vertical profile and complemented with a bed sediment sample collected using a weighted sampling net, when possible.

Sediment-laden water was transferred from the sampling bottle to 15 liter vessels for interim storage prior to filtration. We separated sediment from the water using a custom-built 5-liter pressurized filtration unit with a 293 mm diameter, 0.2 μm polyethersulfone filter. Sediment remained on the filters and was stored in combusted amber glass bottles for shipping. Bed sediment samples were stored in sterile plastic bags. In the laboratory, we rinsed sediment off the filters directly into an evaporating dish with ultrapure 18.2 MΩ water (pH~7; when needed, we added NH_3 solution to the water to maintain pH~7). Samples were dried in an oven at 40ºC, and subsequently homogenized.

To determine the local $F^{10}Be_m$, we measured [$^{10}Be_m$] in sediment samples collected from four OSL-dated floodplain sediment depth profiles along the megafan (Figure 3.1). To simplify

the OSL age determination, we attempted to sample paleochannel point bars, under the assumption that these areas have experienced rapid sediment deposition such that the timescale of deposit formation may be less than the error associated with OSL measurements. We used a stainless-steel hand auger to collect sediment down to a maximum depth of ~5 m. For $^{10}Be_m$ and $^{9}Be_{reac}$ analysis, we extracted samples that integrated material from 0-20 cm below the surface, 20-50 cm, and regularly spaced 40 cm intervals for lower depths. We homogenized the material prior to packing into clean plastic bags. For OSL analysis, we collected light-sealed samples by driving an opaque tube into our floodplain cores at select depths (see Text A3 for complete OSL methods).

3.4 Methods

3.4.1 Grain size and specific surface area analysis

Sediment particle size distributions were measured on ~10 mg aliquots using a laser diffraction particle size analyzer (Horiba LA-950). Ten replicate measurements were made for each sample. Using the mean of the ten measured grain size distributions, we calculated the 50th percentile value (D_{50}) and the fraction of silt and clay as the fraction of sample with grain size diameter <63μm.

Specific surface area (SSA) of bulk sediment samples was measured on ~4 g aliquots using a Quantachrome NOVAtouch LX gas sorption analyzer. For each sample, a linear adsorption isotherm was calculated using measurements at five pressure conditions, and SSA was determined using the Brunauer, Emmett, and Teller (BET) theory (Brunauer et al., 1938). R^2 values for all BET isotherms used to calculate SSA were greater than 0.9997.

3.4.2 Extraction and measurement of $^{10}Be_m$ and $^{9}Be_{reac}$

0.5-1 g sediment aliquots were oven-dried overnight at 110°C, and immediately weighed. The total reactive phase, including amorphous oxyhydroxides and crystalline oxide grain coatings, was extracted from the sediment samples using a procedure adapted from Wittmann et al. (2012). ^{10}Be was purified from the extracted material, spiked with a ^{9}Be carrier solution containing 150 μg of ^{9}Be, and packed into targets for AMS measurement at the University of Cologne Centre for Accelerator Mass Spectrometry (Cologne, Germany). $^{10}Be/^{9}Be$ measurements were normalized to the KN01-6-2 and KN01-5-3 standards (Dewald et al., 2013) that are consistent with a ^{10}Be half-life of $1.36 \pm 0.07 \times 10^6$ yr^{-1} (Nishiizumi et al., 2007). $[^{10}Be]_m$ was calculated from the normalized and blank-corrected $^{10}Be/^{9}Be$ ratios. The reported 1σ uncertainties include counting statistics and the uncertainties of both standard normalization and blank correction. Stable ^{9}Be concentrations were measured on a separate aliquot of the

sample solution using inductively coupled plasma optical emission spectroscopy (ICP-OES). Uncertainty of ICP-OES measurements was 5%.

3.4.3 River profile depth-integration

To account for variability in $[^{10}Be]_m$ with sampling depth due to hydrodynamic sorting, we calculated depth-integrated $[^{10}Be]_m$ ($[^{10}Be]_{m\text{-}DI}$) for each river depth profile following the approach of Wittmann et al. (2018). We modified the method by using the relationship between $[^{10}Be]_m$ and specific surface area, rather than grain size. For each river depth profile, we estimated the depth-integrated suspended sediment concentration (SSC_{DI}) used a Rouse-type model (Rouse, 1937), following the approach presented in Bouchez et al. (2011). After determining SSC_{DI} for each profile, we calculated depth-integrated SSA (SSA_{DI}) using linear regressions between individual SSC and SSA measurements in each depth profile, following:

$$SSA_{DI} = m * SSC_{DI} + b \qquad (3.1),$$

where *m* and *b* are the slope and y-intercept, respectively, of the linear regression for SSC and SSA modeled for each depth profile. Depth-integrated nuclide concentrations were calculated for each depth profile by solving for $[^{10}Be]_m$ and $[^{9}Be]_{reac}$ as a function of the SSA, following:

$$[N]_{DI} = n * SSA_{DI} + c \qquad (3.2),$$

where $[N]_{DI}$ represents the depth-integrated concentration of a given nuclide, and *n* and *c* are the slope and y-intercept, respectively, of the linear regression for SSA and [N] calculated for each depth profile. Uncertainty is quantified using the root mean square error of the linear regression for [N] and SSA. Because we could not collect samples directly downstream of the RSF confluence, we calculated headwater-integrated $[^{10}Be]_m$ and $[^{9}Be]_{reac}$ values for the mainstem Rio Bermejo at river km 0. We weighted both $[^{10}Be]_{m\text{-}DI}$ and $[^{9}Be]_{reac\text{-}DI}$ by the modern sediment discharges of the two tributary channels.

We then use the $(^{10}Be/^{9}Be)_{reac}$ ratio to correct for SSA and secondary metal effects on $[^{10}Be]_m$ in river sediment (von Blanckenburg et al., 2012; Wittmann et al., 2012). Following this approach, we effectively isolate the depth-integrated $^{10}Be_m$ signal along the river transect by normalizing $[^{10}Be]_m$ values to the river-averaged $[^{9}Be]_{reac}$, which is relatively uniform along the river transect (Figure 3.2) using:

$$[^{10}Be]_{norm_{x=n}} = \left(\frac{[^{10}Be]}{[^{9}Be]}\right)_{reac,x=n} * \overline{[^{9}Be]}_{reac-riv} \qquad (3.3).$$

Here, $[^{10}Be]_{norm}$ is the normalized $^{10}Be_m$ concentration (now independent of SSA), $(^{10}Be/^{9}Be)_{reac}$ is the ratio for a given sampling location *x*, and $\overline{[^{9}Be]}_{reac\text{-}riv}$ is the average of all $[^{9}Be]_{reac}$ values measured in river sediment. The resulting $[^{10}Be]_{norm}$ value is then used to estimate average transit times for the bulk sediment load.

3.4.4 Estimation of local $F^{10}Be_m$ from floodplain sediment profiles

The globally-averaged $F^{10}Be_m$ is ~1.09 x10^6 atoms cm^{-2} yr^{-1} derived from time-averaged general circulation model (GCM) runs (Heikkilä & von Blanckenburg, 2015). These authors combined modern ("industrial" conditions) and early Holocene ("pre-industrial" conditions) models for ^{10}Be deposition to produce time-averaged estimates of $F^{10}Be_m$. These two models have large differences that may result from strong precipitation gradients at the eastern flank of the Andes, or time-variable moisture circulation patterns. Therefore we estimated a representative $F^{10}Be_m$ for the Rio Bermejo floodplain, using measured $^{10}Be_m$ inventories in dated soil profiles (Reusser et al., 2010). $F^{10}Be_m$ (at cm^{-2} yr^{-1}) was calculated following a method adapted from Willenbring & von Blanckenburg (2010):

$$F^{10}Be_m = \frac{\left[\int_{z=0}^{z}\left([^{10}Be]_{m,z}-[^{10}Be]_{m,i}\right)\rho_s\, dz\right]\lambda}{(1-e^{-\lambda t})} \qquad (3.4).$$

The numerator gives the sediment or soil inventory of reactive ^{10}Be (at cm^{-2}), *z* is the depth below the surface (cm), ρ_s is the sediment bulk density (g cm^{-3}), $[^{10}Be]_{m,z}$ is the measured concentration (at g^{-1}) for a sampled depth interval, and $[^{10}Be]_{m,i}$ is the ^{10}Be concentration (at g^{-1}) inherited from previous floodplain storage events experienced by the sediment prior to deposition at the sample location. We estimate the value of this inherited $^{10}Be_m$ as the ^{10}Be concentration measured in modern active channel sediment sampled just upstream of the sediment profile location, $[^{10}Be]_{m,i}$ (at g^{-1}), assuming this inherited concentration has been constant through time. To derive $F^{10}Be_m$, we divide the inventory by *t*, the sediment depositional age (yr), while accounting for radioactive decay with the ^{10}Be decay constant, λ.

3.4.5 Estimation of fluvial sediment transit time from $[^{10}Be]_m$

Using $^{10}Be_m$ as a proxy for fluvial sediment transit time was suggested by Wittmann et al. (2015), who tested this approach on the Amazon River system. Their model is based on the soil $^{10}Be_m$ inventory equation of Willenbring & von Blanckenburg (2010). In principle, River suspended sediment at the mountain front begins its journey downstream with an inherited $[^{10}Be_m]$, and any additional $^{10}Be_m$ adsorbed to the sediment records time particles spend in storage as they travel downstream. $^{10}Be_m$ accumulates in river sediment at a rate proportional to its transit time, under the assumption that 1) the local $F^{10}Be_m$ is spatially constant along the

river and is constant through time, 2) particles stored in the floodplain incorporate $^{10}Be_m$ into their secondary mineral coatings at a rate consistent with $F^{10}Be_m$, and 3) the channel exchanges sediment with stored floodplain sediment at a uniform rate through time via lateral channel migration and avulsions. Under these conditions, a net downstream increase in [$^{10}Be_m$] represents added floodplain storage time, which can be solved for.

Here we estimate the sediment transit time through the Rio Bermejo from the mountain front to river km 1221 using depth-integrated $^{10}Be_m$ measurements for the total suspended load. Following Wittmann et al. (2015), we model the evolution of $^{10}Be_m$ in river sediment through time, using:

$$I_{^{10}Be_m}(t) = \frac{F^{10}Be_m}{\lambda}\left(1 - e^{-\lambda t}\right) + \left[^{10}Be_m\right]_{x=0} * \rho_s * h * e^{-\lambda t} \qquad (3.5),$$

where $I_{^{10}Be_m}$ is the measured $^{10}Be_m$ inventory (at m^{-2}) at a downstream sampling site, given by equation (3.6):

$$I_{^{10}Be_m\,x=n} = \left[^{10}Be_m\right]_{x=n} * \rho_s * h \qquad (3.6).$$

In equations (3.5) and (3.6), t is the mean time (yr) passed since the sampled sediment entered the river at distance $x = 0$, h is the remobilization depth (m) to which the river laterally erodes into floodplain sediment, and ρ_s is the bulk sediment density (kg m^{-3}). $F^{10}Be_m$ is the flux of $^{10}Be_m$ from the atmosphere to the floodplain, derived from equation (3.4) and sediment profile concentration data. The two terms on the right side of equation (3.5) represent first, the supply and decay of $^{10}Be_m$ to stored floodplain sediment via atmospheric deposition, and second, the radioactive decay of $^{10}Be_m$ in sediment supplied from upstream and collected at the sampling point. This equation assumes that all variables are invariant through time. $I_{^{10}Be_m}$ will be smaller if particles comprising the sample passed downstream without storage, and thus the mean particle transit time derived from equation (3.5) will be shorter. The opposite is true for particles stored during transit.

3.5 Results

3.5.1 Grain size distributions and specific surface area

The depth-integrated D_{50} of suspended sediment ranged from 142 µm in the depth profile sampled upstream of the RSF confluence to 9 µm at river km 1221 (Table A1). The D_{50} of river bed sediment ranged from 325 µm at river km 0 to 160 µm at river km 866. The fraction of silt and clay in the river load (f_{s+c}) showed patterns similar to the grain size. Depth-integrated f_{s+c} was 0.33 at the confluence and increased to 0.92 at km 1221, respectively (Table S1).

SSA values follow an inverse power law relationship with grain size (Figure A1, Text A2). SSA ranged from 1.16 m^2 g^{-1} for the coarsest sample (D_{50} 325 µm) to 22.49 m^2 g^{-1} for the finest sample (D_{50} 7.8 µm). Depth-integrated SSA increased by nearly a factor of 3 from upstream to downstream (7 to 21 m^2 g^{-1}, Table A1). SSA of river bed sediment did not change strongly from upstream to downstream (Table A1). SSA normalized by D_{50} (SSA/D_{50}) for individual samples exhibited strong gradients within river depth profiles, indicating a range of particle shapes. Surface suspended sediment samples had the highest SSA/D_{50} ratio, and bed sediment exhibited the lowest ratios (Figure A3).

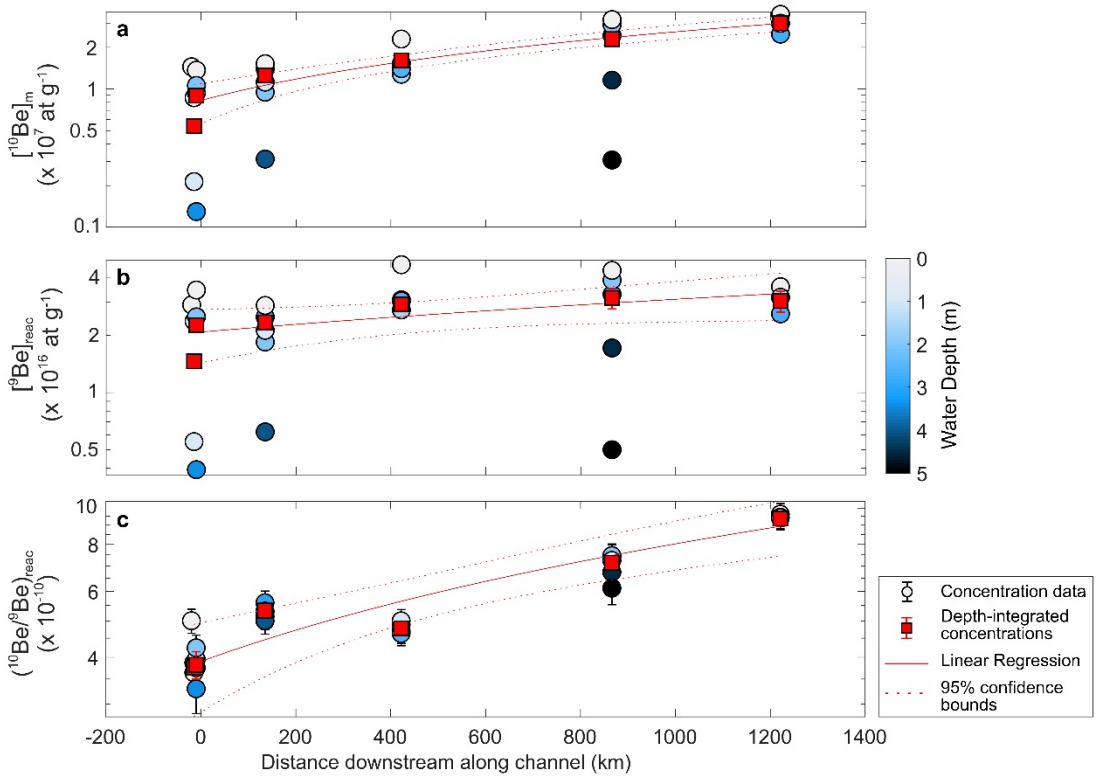

Figure 3.2. Downstream trends in (a) $[^{10}Be]_m$, (b) stable $[^9Be]_{reac}$, and (c) $(^{10}Be/^9Be)_{reac}$. Circles represent individual samples, colored by depth below the water surface at the sampling location (total water depth differs among locations). Red squares show the depth-integrated values. The red trend lines show the linear regressions with 95% confidence intervals calculated for the depth-integrated samples. Error bars for individual samples represent the analytical uncertainty, and error bars on the depth-integrated values represent the root-mean-square errors for the depth-integration models.

3.5.2 Beryllium isotopes in river sediment depth profiles

$[^{10}Be]_m$ was lowest at the upstream sampling locations, where the RSF values ranged from 0.21 x10^7 to 0.86 x10^7 at g^{-1} and the Bermejo upstream of the confluence ranged from 0.13 x10^7 to 1.37 x10^7 at g^{-1} (Table A2). $[^{10}Be]_m$ increased with distance downstream of the confluence, and the highest concentrations were observed at river km 1221, where values ranged from 2.49 x10^7 to 3.47 x10^7 at g^{-1} (Figure 3.2a, Table A2). $[^9Be]_{reac}$ ranged from 0.39 x10^{16} at g^{-1} to 4.7 x10^{16}, but did not exhibit clear trends from upstream to downstream (Figure 32b, Table A2). $(^{10}Be/^9Be)_{reac}$, exhibited significantly reduced variability among samples at a

single site compared to individual $[^{10}Be]_m$ values and shows a clear increase with distance downstream (Figure 3.2c, Table A2).

Hydrodynamic sorting of river suspended sediment created strong gradients in both $[^{10}Be]_m$ and $[^{9}Be]_{reac}$ with depth in the water column (Figure 3.2a, 3.2b), due to particle surface area dependence. $[^{10}Be]_m$ exhibited a strong linear relationship with SSA (mean $R^2 = 0.9390$) (Figure 3.3), with the lowest concentrations in river bed sediment and the highest concentrations in surface water suspended sediment. Depth-integrated values were calculated by weighting $[^{10}Be]_m$ by sediment concentrations in the river water (SSC), according to equation (3.2), so that they represent the total sediment load.

We calculated sediment load-weighted $[^{10}Be]_{m\text{-}DI}$ and $[^{9}Be]_{reac}$ values of 0.86 x10^7 at g^{-1} and 2.19 x10^{16}, respectively, for river km 0 (Table A2, Figure 3.2a, 3.2b). $[^{10}Be]_{m\text{-}DI}$ progressively increased downstream to a concentration of 2.99 x10^7 at g^{-1} at km 1221, representing a 231% overall increase (p-value 3.0 x10^{-4}, F-test). Over the same distance, $[^{9}Be_{reac}]_{DI}$ increased more modestly, by 38%, from 2.19 x10^{16} at g^{-1} to 3.03 x10^{16} at g^{-1} at river km 1221 (p-value 0.051, F-test) (Figure 3.2b). $(^{10}Be/^{9}Be)_{reac\text{-}DI}$ started at 3.81 x10^{-10} at river km 0, and increased 145% over the 1221 km transit distance (p-value 2.2 x10^{-3}, F-test) (Figure 3.2c). $(^{10}Be/^{9}Be)_{reac\text{-}DI}$ decreased at river km 422, due to an increase in $[^{9}Be]_{reac}$ (Figure 3.2b). Downstream of this station, $(^{10}Be/^{9}Be)_{reac}$ values gradually increased to a final ratio of 9.37 x10^{-10} at km 1221. $[^{10}Be]_{norm\text{-}DI}$ increased from 0.90 x10^7 at g^{-1} to 2.99 x10^7 at g^{-1}, which represents a 232% increase over the entire transit distance (p-value 2.0 x10^{-4}, F-test) (Figure 3.4a). While normalizing $[^{10}Be]_m$ to $[^{9}Be]$ increased the uncertainty on $[^{10}Be]_{norm}$ of individual samples, this treatment reduced the variability among samples within a given depth profile, thereby

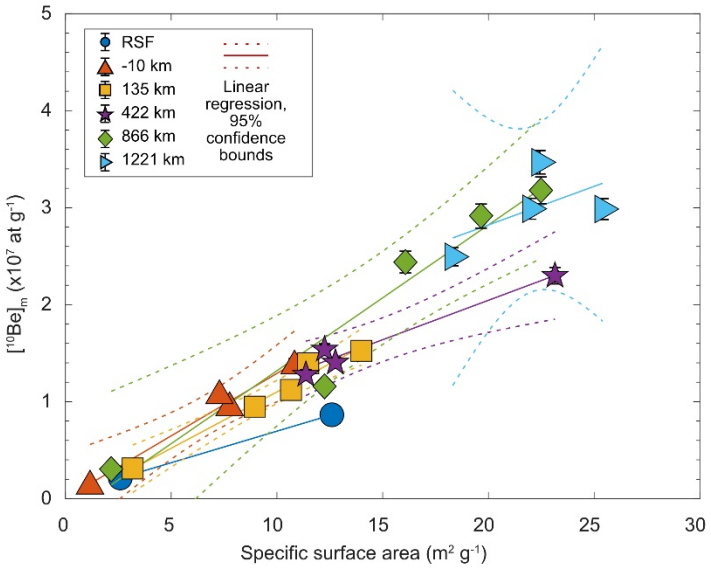

Figure 3.3. Specific surface area vs. $^{10}Be_m$. Relationship between $[^{10}Be]_m$ (atoms g^{-1} dry sediment) and specific surface area (m^2 g^{-1} dry sediment) for each suspended sediment sample. Colors and symbols differentiate the depth profiles at multiple locations along the Rio Bermejo. Trend lines represent linear regressions and 95% confidence intervals for each depth profile. The coefficients of these regressions were used to calculate the depth-integrated $[^{10}Be]_{m\text{-}DI}$ values.

reducing the uncertainty of $[^{10}Be]_{norm\text{-}DI}$.

3.5.3 *Estimated local $F^{10}Be_m$*

OSL ages constrain the minimum and maximum depositional ages for the floodplain sediment cores, with SP1 at 0.8-1.9 ka, SP2 at 13.3- 20.2 ka, SP3 2.10- 3.70 ka, and SP4 at 0.4-0.9 ka (Text A3, Table A3). SP1 and SP4 demonstrate exponential decline of $[^{10}Be]_m$ with increasing sediment depth (Figure 3.5, Table A4), which is typically observed in poorly-developed soils (Graly et al., 2010) and allows for derivation of the local $F^{10}Be_m$. SP2 and SP3 show more complicated concentration-depth distributions resulting from post-depositional erosion/burial, incomplete Be retention, or incomplete sampling of depth profiles (Text A3). SP1 has a $^{10}Be_m$ soil inventory of 5.68 x10^9 at cm^{-2}, resulting in $F^{10}Be_m$ of 3.0 x10^6 at cm^{-2} yr^{-1} averaged over the last 1.9 kyr (OSL age) (equation (3.4)). In agreement, SP4 has a $^{10}Be_m$ soil inventory of 2.56 x10^9, which yields a $F^{10}Be_m$ of 2.85 x10^6 at cm^{-2} yr^{-1} averaged over the last 0.9 kyr. In comparison, $F^{10}Be_m$ values from GCM-based datasets for the Rio Bermejo catchment range from 3.8 x10^6 atoms cm^{-2} yr^{-1} in the headwaters to 2.4-2.7 x10^6 atoms cm^{-2} yr^{-1}in the floodplain (Heikkilä & von Blanckenburg, 2015), bracketing our sediment profile-derived $F^{10}Be_m$ values.

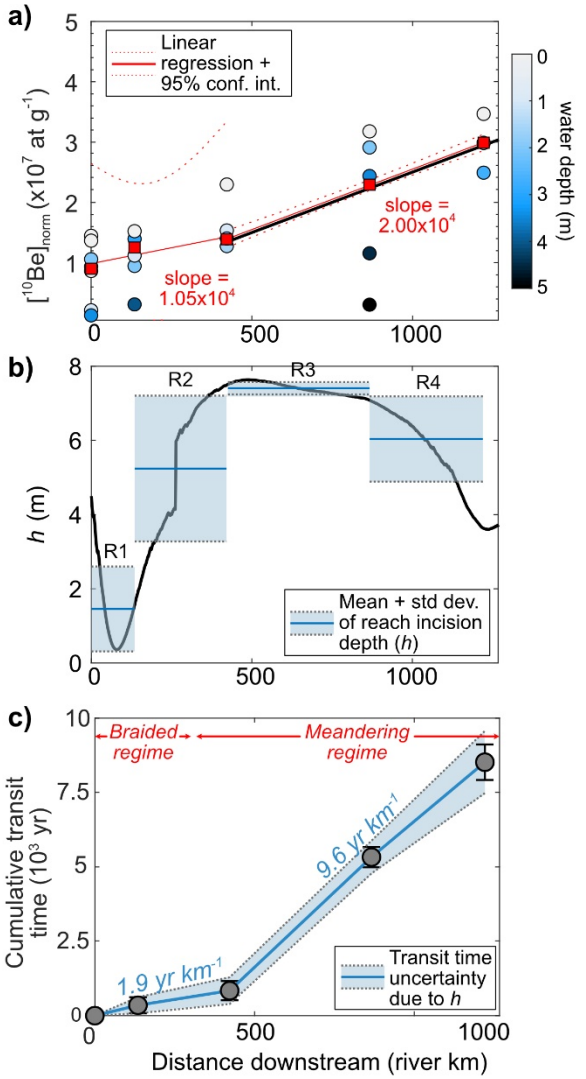

Figure 3.4. Transit time derivation. a) $[^{10}Be]_{norm}$ and $[^{10}Be]_{norm\text{-}DI}$ (atoms g^{-1}), calculated using equation (3), plotted against distance downstream. Circles represent individual samples, colored by depth below the water surface. Error bars on individual sample points represent the propagation of analytical uncertainty and weighted error. Red squares show the depth-integrated, normalized concentrations with error bars representing the root-mean-square errors of equation (1), normalized by $[^9Be]_{reac}$. The red trend lines are linear regressions with 95% confidence interval fitted to the $[^{10}Be]_{norm\text{-}DI}$ data for the braided and meandering reaches, respectively. b) Remobilization depth, h, measured along the channel (heavy black line) and mean remobilization depths for reaches 1-4 (R1-R4). c) Cumulative transit time for each reach (heavy blue line) plotted against distance downstream, with minimum and maximum bounds associated with the standard deviation of h in each reach.

Because it averages over a longer time period than SP4, we use the $F^{10}Be_m$ value of 3.0 x10^6 at cm^{-2} yr^{-1} from SP1 as input to the transit time model.

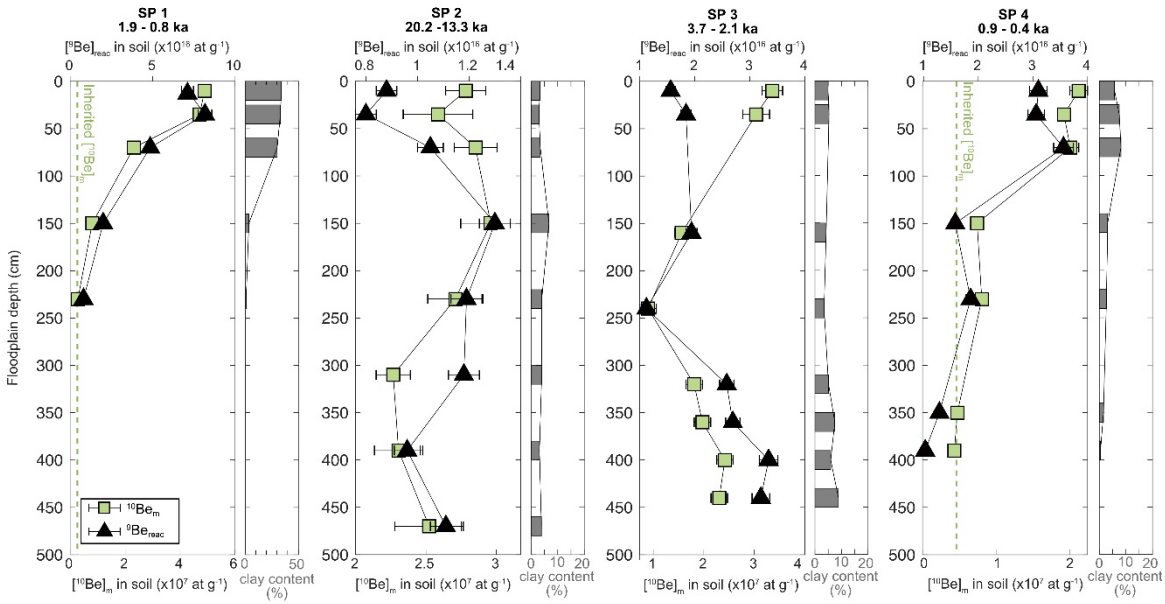

Figure 3.5. Floodplain sediment profiles. $[^{10}Be]_m$ (pale green squares), $[^{9}Be]_{reac}$ (black triangles), and clay content (<2μm; gray bars) in floodplain sediment profiles SP1, 2, 3, and 4. Note differences in x-axis scales. SP1 and SP4 demonstrate a typical exponential decrease in concentrations with depth, as shown in poorly-developed soils by Graly et al. (2010).

3.5.4 Estimating sediment transit time with $^{10}Be_m$ concentrations

To estimate the mean total sediment transit time, we employed equation (3.5), translating the difference in $[^{10}Be]_{m\text{-}DI}$ between upstream and downstream stations into a measure of time. This requires constraining several parameters. For the initial and final $[^{10}Be]_m$, we use $[^{10}Be]_{norm\text{-}DI}$ values at the 0 km and 1221 km locations, respectively (Figure 3.4a, Table A2). $F^{10}Be_m$ for the Rio Bermejo floodplain is 3.0 x10^6 at cm^{-2} yr^{-1}, as calculated from floodplain profile SP1. Rio Bermejo sediment is organic-poor, quartz-rich, and composed of ~15% clay, ~60% silt, and ~25% fine-medium sand, on average, suggesting a bulk density, ρ_s, of 1.5-2.0 g cm^{-3} (e.g., Snyder et al., 2004). We determined values for the remobilization depth, *h*, by DEM analysis of the incision depth of the channel into the floodplain, as described in the supporting information (Text A1). *h* ranged from 0.36 m in the foredeep to 8.2 m in the forebulge reaches of the river (Figure 3.4b), and we used the mean and standard deviation of this dataset (n = 694), 6.1 ± 2.1 m, in our principal calculation.

The resulting mean transit time for the entire 1221 km length of the Rio Bermejo is 8.4 ± 2.2 kyr (Figure 3.6, Table 3.1). According to this estimate, sediment is transported downstream at a virtual velocity (transit distance normalized by total transit time) of ~145 m yr^{-1}, which can also be interpreted as an average particle aging rate of 6.9 years km^{-1} (Table 3.1). Cumulative

transit time increases with distance along the channel, but the downstream trend is different in the braided (foredeep) and meandering reaches (forebulge and backbulge), respectively (Figure 3.4c). Particles transiting the river system age at a rate of 1.9 yr km^{-1} through the superelevated, braided reach, and 9.6 yr km^{-1} through the meandering section (Figure 3.4c). The longer transit time through the meandering reach relative to the braided reach is consistent with superelevation of the foredeep channel keeping aged sediment out of the reach, while the high lateral migration rates in the incised meandering reach entrain stored floodplain sediment (Figure 3.7).

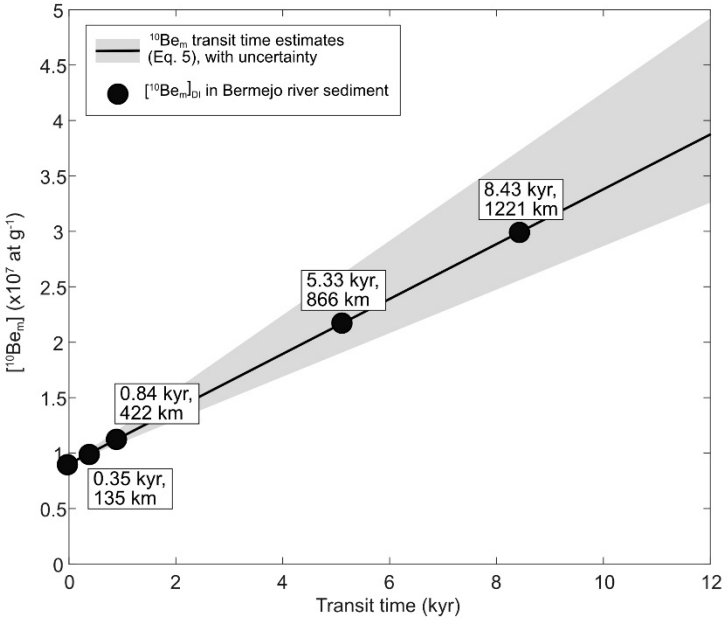

Figure 3.6. a) A linear model of $[^{10}Be]_m$ in fluvial sediment through time, based on equation (5). The solid black line shows the modeled evolution of $[^{10}Be]_{norm\text{-}DI}$ through time for the river mean remobilization depth of 6.03 ± 2.12 m (uncertainty shown by the gray shaded region). Black circles show the measured $[^{10}Be]_{norm\text{-}DI}$ values at the mountain front and in the four depth profiles downstream. b) Cumulative transit time, calculated as the sum of transit times for upstream reaches, plotted against distance downstream. Two linear fits describe the behavior of sediment transit in the predominantly braided regime (0-263 km) and meandering regime (264-1267 km), respectively.

3.6 Discussion

3.6.1 Sensitivity of $^{10}Be_m$ as a transit time tracer

The increase in $^{10}Be_m$ with distance downstream supports using $^{10}Be_m$ as a tracer to estimate mean sediment transit times. This technique provides a method to resolve lag times for signals propagating from upstream sediment sources to downstream sediment sinks (e.g., Romans et al., 2016), resolve timescales associated with biogeochemical cycling, and investigate the geomorphic and tectonic mechanisms that regulate transit time. However, before this method can be applied, several assumptions and underlying mechanisms of the $^{10}Be_m$ proxy need to be considered, as follows:

i) Our $^{10}Be_m$ transit time estimate of 8.4 ± 2.2 kyr represents the mean time particles spent in transit from river km 0 to river km 1221. While this method cannot estimate the distribution of individual transit times for all particles traversing a system, multiple transit time distributions have been proposed, including exponential (Everitt, 1968; Nakamura & Kikuchi, 1996), power

law (Lancaster et al., 2010; Pizzuto et al., 2017), and pareto (Ganti et al., 2011) distributions, while Bradley and Tucker (2013) suggest different distributions for different timescales. These distributions are often heavy-tailed, implying the $^{10}Be_m$-derived mean transit time of 8.4 kyr is likely biased toward a minor population of particles with long transit times, while most particles in the river have shorter transit times.

ii) The concentration of $^{10}Be_m$ in river sediment may depend on the abundance of secondary mineral coatings and particle surface area. In Rio Bermejo sediment, we observe a significant positive linear relationship between $[^{10}Be]_m$ and SSA (Figure 3.3), but not between $^{9}Be_{reac}$ and SSA. $^{9}Be_{reac}$ and SSA show greater variability within a depth profile than with distance downstream (Figure 2B), suggesting that changes in these $^{10}Be_m$-regulating parameters do not control the downstream increase in $[^{10}Be]_m$. Depth-integration characterizes the full suspended load, capturing the full range of concentration variability. ^{9}Be-normalization reduces $[^{10}Be]_m$ variability among samples within depth profiles, ultimately reducing the uncertainty of the depth-integrated $[^{10}Be]_{norm}$ values, and thus the estimated transit time (Figure 3.4a).

iii) On timescales up to 10^4 yr, all $^{10}Be_m$ delivered to the floodplain is retained in the sediment that is then eroded into the river. $^{10}Be_m$ retention on sedimentary particles can be influenced by pH, leaching intensity, and adsorption capacity in soil. Under acidic pH conditions or a positive water budget, $^{10}Be_m$ can desorb from particles or reactive phases can be mobilized to the dissolved phase (von Blanckenburg et al., 2012; Dixon et al., 2018). While floodplain soil pH was not measured for the Rio Bermejo, water measurements indicate consistent pH between 7.4 and 7.8 for Rio Bermejo river water, and higher pH values between 8 and 9 in local spring-fed streams (Table A1). Mean annual discharge is low at ~500 m^3 s^{-1}, and sediment export is high at ~100 Mt yr^{-1}, suggesting conditions for high Be retention (von Blanckenburg et al., 2012). Floodplain soils are poorly-developed due to the frequency of channel avulsions (Hartley et al., 2013), so $^{10}Be_m$ adsorption capacity should not be affected by strong soil development. In summary, while profiles SP1 and SP4 show consistent behavior, the difference exhibited in profiles SP2 and SP3 $[^{10}Be]_m$ (Figure 3.7) are likely due to the floodplain deposits having complex histories, including changes in inherited $[^{10}Be]_m$ due to translocation of 10Be to depths greater than those sampled or multiple depositional events. However, by sampling river suspended sediment depth profiles we capture the full range of variability among sediment transiting the Rio Bermejo.

iv) Constraining geomorphic variables used in equation (3.5). The remobilization depth, *h*, has a significant impact on the resulting transit time because the total $^{10}Be_m$ inventory of the river suspended load is assumed to be distributed over one channel depth. We find that *h* ranges from ~2-7 m along the length of the river, and we use the standard deviation of the measured remobilization depths to constrain uncertainty on the total mean sediment transit time (Figure 3.4). *h* may be precisely constrained for any river system, using remote sensing methods or detailed field surveys (Text A1).

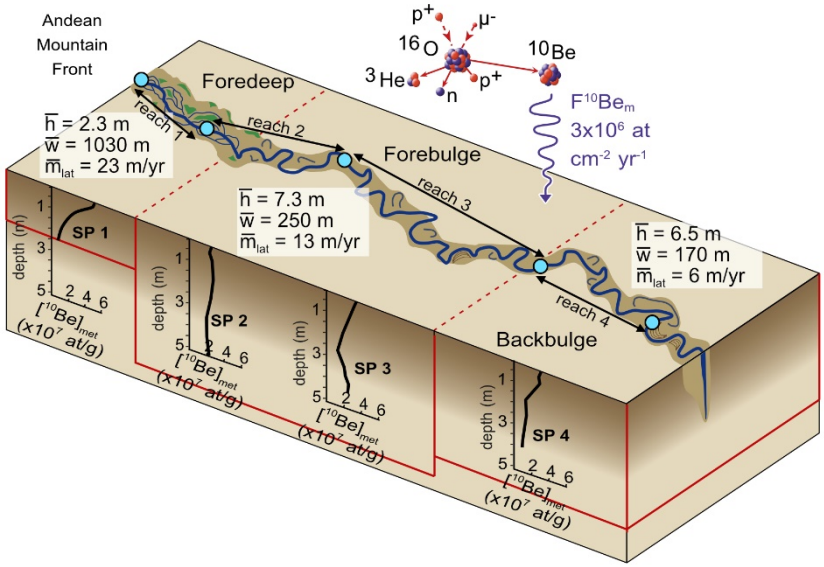

Figure 3.7. Schematic model of the Rio Bermejo system showing geomorphic constraints on the river system through the three morphotectonic domains of the Andean foreland basin. Shown in the white boxes are mean remobilization depth (h), channel width (w), and channel migration rate (m_{lat}) for the three domains (Text A1). Blue circles indicate locations of river depth profiles, between which are reaches 1, 2, 3, and 4 where we evaluate differences in transit times and sediment storage dynamics. Red boxes delineate the remobilization depths for lateral channel-floodplain exchange in each depozone. $F^{10}Be_m$ is the flux of $^{10}Be_m$ from the atmosphere to the floodplain. ^{10}Be concentrations ($[^{10}Be]_m$) in floodplain soil profiles SP1 to SP4 are shown by the plots in the subsurface.

3.6.2 Comparison of $^{10}Be_m$ transit times to sediment budget-based predictions

To support that our $^{10}Be_m$-derived transit time estimate is reasonable, here we compare our results to channel belt and fluvial fan storage times estimated with simple sediment budgeting methods (e.g., Jerolmack & Mohrig, 2007; Pizzuto et al., 2014; Torres et al., 2017), the full details of which are described in the Supporting Information (Text A4, Tables A5 and A6). We assume a conceptual model where a lowland alluvial river migrates laterally across a narrow active channel belt within a wider fluvial fan. Between periodic river avulsions, sediment is reworked exclusively within the active channel belt as it is deposited and re-entrained several times during downstream transit. Periodic avulsions allow the channel belt to occupy new areas of the fan, and this process is repeated until the entire fan surface is reworked. This conceptual model allows for two separate transit time estimates, providing minimum and

maximum bounds on the total mean sediment transit time. To constrain the minimum transit time, we estimate a characteristic length scale for particle transport between periods of deposition, x_{trans}, of ~280 km (equation (A3)) (cf. Torres et al., 2017). Over the 1221 km Rio Bermejo transit distance, sediment thus averages $n_{trans} \approx 4.4$ cycles of erosion and deposition (equation (A2)). Stored sediment is remobilized at a timescale, $t_c \approx 0.14$ kyr, set by the average migration rate and channel width (equation (A4)). Accordingly, we estimate a minimum transit time for sediment stored exclusively within the channel belt, $t_{belt} = n_{trans}\, t_c \approx 0.61$ kyr (equation (A5)). Over longer timescales, we assume avulsions occur when the active channel belt aggrades one channel depth, yielding a characteristic avulsion recurrence interval, $t_a \approx 0.41$ kyr (equation (A7)). For the Rio Bermejo, $t_a < t_{belt}$, suggesting the channel must reoccupy previous positions before all sediment can be transported out of the system. Complete fan-resurfacing requires $N_a \approx 51$ avulsions, resulting in a maximum transit time estimate of $t_{fan} = N_a\, t_a \approx 21$ kyr. These estimates are consistent with the range of depositional ages for floodplain deposits SP1-SP4 (0.4-0.9 kyr to 13.3-20.2 kyr (OSL)).

These estimates of $t_{belt} \approx 0.61$ kyr and $t_{fan} \approx 21$ kyr bracket our $^{10}Be_m$-derived transit time of 8.4 ± 2.2 kyr, suggesting that sediment within the Rio Bermejo is a mixture of sediment stored for relatively short timescales within the modern channel belt and sediment stored over longer timescales outside of the channel belt. Indeed, in its present form, the Rio Bermejo frequently breaches the edge of its belt and erodes older deposits (Figure A5), thereby incorporating stored floodplain sediment, enriched in $^{10}Be_m$, into the active channel load and increasing the sediment transit time beyond our t_{belt} estimate. Comparing our sediment-budget and $^{10}Be_m$-derived transit time estimates suggests that the $^{10}Be_m$ method accurately captures this incorporation of aged sediment. Interpreting the mean $^{10}Be_m$ transit time of 8.4 ± 2.2 kyr as a result of binary mixing of young (mean t_{belt} ~0.61 kyr) and old (mean t_{fan} ~21 kyr) sediment reservoirs, we estimate that ~60 ± 10% of sediment in the active channel is derived from within the modern channel belt, and ~40 ± 10% from beyond the channel belt. These values seem reasonable given the frequency that the Rio Bermejo breaches the modern channel belt boundaries, as observed in satellite imagery (Figure A5), and are consistent with the tendency for migrating rivers to preferentially erode younger deposits (Bradley and Tucker, 2013). The agreement between $^{10}Be_m$-derived and sediment budget-based transit time estimates highlights the utility of the latter for simple constraint of bulk sediment transit times.

3.6.3 Tectonic and morphodynamic controls on sediment transit times

During the wet season, water flowing through the Rio Bermejo mainstem channel at a velocity of 1 m s^{-1} takes about 14 days to travel from the Andean mountain front to the confluence with the Rio Paraguay. The sediment transit times estimated above therefore indicate that along the entire length of the mainstem Rio Bermejo, clastic particles spend 4-5 orders-of-magnitude more time in storage than in motion. Accordingly, $^{10}Be_m$-derived transit times intrinsically contain information about sediment storage dynamics, which can be extracted by estimating transit times at the reach scale. Below we assess these reach-specific transit time estimates with respect to the morphodynamics of each reach to describe extrinsic controls on fluvial sediment transit time.

The morphodynamics of the Rio Bermejo change as the river crosses three foreland depozones: 1) 0-175 km away from the mountain front (river km 0-263) is a braided, super-elevated channel traversing the foredeep basin, 2) 176-475 km from the mountain front (river km 264-867) is an incised, tightly meandering reach crossing the uplifting forebulge, with high channel migration rates (up to 50 m/yr), and 3) 476-695 km from the mountain front (river km 868-1267) is an incised, sinuous reach with cohesive banks and low channel migration rates (0-10 m/yr) (Figure 3.7). Because the foredeep basin is overfilled, and the channel is braided with rapid lateral reworking and shallow re-mobilization depths, we hypothesize that sediment has a low probability of being stored on the floodplain for long timescales and subsequently remobilized. In the forebulge, high channel migration rates and deep incision depths suggest that river sediment experiences multiple deposition-erosion cycles, and thus sediment has a high probability of being deposited on the floodplain and stored for 10^2-10^4 yr. In the backbulge, channel migration rates are low due to more cohesive river banks, which should result in little channel-floodplain exchange and short transit times. In the following sub-sections, we evaluate the differences in $^{10}Be_m$-derived transit times calculated for four reaches in between our five sampling locations to constrain how sediment storage dynamics differ across these three domains (Figure 3.7). To calculate reach-specific transit times, we employed equation (3.5), using the $[^{10}Be]_{norm\text{-}DI}$ values at the upstream and downstream ends of the reach for $[^{10}Be_m]_{x=0}$ and $[^{10}Be_m]_{x>0}$, respectively.

Sediment transit through Reach 1 (foredeep, braided channel)

Reach 1 (river km 0-135 km) is braided and spans the foredeep basin. We expect only a limited increase in $[^{10}Be]_{norm\text{-}DI}$, primarily driven by remobilization of sediment from levees fringing the active channel. These levees are likely not long-lived features, so sediment has a

low probability of being stored there long-term. One exception sits between river km 35 and 70, where the right bank is elevated by a buried thrust fault and river sediments of a presumably older age are exposed. Indeed, we observe a 0.35×10^7 at g^{-1} increase in $[^{10}Be]_{norm\text{-}DI}$ and a mean remobilization depth of 1.46 ± 1.15 m (Figure 3.4a-b), which equates to a transit time of 350 ± 270 yr (Table 3.1). These results agree with our hypothesis, as sediment travels relatively rapidly through reach 1, at a virtual velocity of 386 ± 168 m yr^{-1} and aging rate of 2.6 ± 2.0 yr km^{-1} (Table 3.1). However, this does not account for the sediment spilled into the surrounding, low-lying floodplain, from where the river cannot presently re-entrain it. Fundamentally, the foredeep is a location of sediment storage on geological time scales, so the short sediment transit times measured by $^{10}Be_m$ reflect the dynamics of the active river channel belt, rather than overall fluvial fan transit and storage between avulsions.

Sediment transit through Reach 2 (braided-meandering transition)

Through reach 2 (river km 136-422), $[^{10}Be]_{norm\text{-}DI}$ increases by 0.14×10^7 at g^{-1} and the mean remobilization depth is 5.26 ± 1.94 m (Figure 3.4a-b), resulting in a transit time of 490 ± 180 yr (Table 3.1). Here, the channel transitions from braided to meandering as it crosses from the foredeep into the forebulge depozone (McGlue et al., 2016) (Figure 3.7). Sediment transport capacity increases through this reach due to narrowing and deepening of the channel, at an approximately constant channel slope, and reduced channel belt width drives the reduction of accommodation space within the active channel belt. These factors all contribute to a relatively high virtual sediment velocity of 590 ± 160 m yr^{-1} and aging rate of only 1.7 ± 0.6 yr km^{-1}. Mobilization of stored sediment exposed in cut banks with known OSL ages of up to 13.3-20.2 kyr (Table A3) drives the increase of $[^{10}Be]_{norm}$. Although such banks exist along ~65% of reach 2, the relatively high virtual sediment velocity suggests that re-entrainment of aged river sediment by lateral channel migration and/or downcutting is limited, consistent with the tendency of migrating rivers to erode most rapidly through the youngest deposits (Bradley & Tucker, 2013).

Sediment transit through Reach 3 (forebulge, meandering channel)

The greatest increase in $[^{10}Be]_{norm}$ is 0.90×10^7 at g^{-1} in reach 3 (river km 422-866, forebulge), resulting in a transit time of 4.49 ± 0.1 kyr, using a remobilization depth of 7.40 ± 0.17 m (Figure 3.4a-b, Table 3.1). This is the most deeply incised segment of the river, with a narrower active channel belt than in reach 2. Channel migration rates are high, 10-50 m yr^{-1} (Text A1), indicating sediment is frequently exchanged between the channel and floodplain. These factors would act to reduce the sediment transit time. However, the significant increase

of $[^{10}Be]_{norm\text{-}DI}$ compared to reach 2, and the associated high aging rate of 10.1 ± 0.2 yr km^{-1} suggest that a large component of the river sediment load is mobilized from stored deposits outside the margins of the active channel belt. Consequently, erosion-deposition cycles cause "younger" particles to be deposited on point bars and "older" particles to be re-entrained. According to our data, the forebulge is an erosional zone where particles are removed from long-term storage in the fluvial fan via lateral migration.

Sediment transit through Reach 4 (backbulge, meandering channel)

Reach 4 (river km 867-1221) has a $[^{10}Be]_{norm\text{-}DI}$ increase of 0.70 x10^{7} at g^{-1} and a mean remobilization depth of 6.83 m (Figure 3.4a-b), resulting in an estimated transit time of 3.19 ± 0.49 kyr (Table 3.1). This suggests a relatively high aging rate of 9.0 ± 1.4 yr km^{-1}, despite low channel migration rates. The long transit time through this reach suggests that, like in reach 3, the active channel remobilizes old fan deposits that have aged significantly in now abandoned channel belts, as demonstrated by the floodplain sediment OSL ages (Table A3). The rate of channel migration in reach 4 is low compared to upstream reaches, ~6.5 m yr^{-1} (Table 3.1), suggesting limited re-entrainment of stored particles, so apparent transit through this reach should be short in comparison to reach 3. However, the strong downstream increase in $[^{10}Be]_m$ indicates that the channel must be mobilizing stored sediment with a significantly older mean age in the few places with active lateral migration.

3.6.4 The utility of $^{10}Be_m$ to study fluvial processes

Our analysis of the geomorphic control on $^{10}Be_m$-derived transit times across the Andean foreland basin reveals the ability of $^{10}Be_m$ concentrations to resolve the mean fluvial sediment transit time over 10^3-10^5 yr timescales. While there are limitations to the $^{10}Be_m$ transit time method, it overcomes many challenges faced by other approaches. Estimating fluvial sediment transit times with a sediment budget-based approach provides only coarse bounds on transit time, as input parameters (e.g., Q_s, m_{lat}, w_{chan}) are naturally variable and cannot be confidently constrained over 10^2-10^5 yr. While the $^{10}Be_m$ method cannot resolve the full transit time distribution, the catchment-integrated sampling approach is a more efficient way to ascertain the mean transit time than comprehensive dating of floodplain deposits. Accurate assessment of biogeochemical cycling and sedimentary signal propagation require chronometers, like $^{10}Be_m$, which can estimate sediment transit duration over the same timescales that chemical reactions take place and signals are dampened. While we demonstrated the efficacy of this method in a simple river system, the next challenge is to apply the method to dendritic channel networks. In more complex settings, upstream and downstream $[^{10}Be]_m$ data may be used to

simply estimate basin-averaged bulk sediment transit times, or to determine transit times within individual reaches between tributary junctions. To try to resolve the full transit time distribution, it may be possible to apply the method to grain size fractions and calculate a $^{10}Be_m$ transit time for each individual size class. For smaller river systems, our approach may also be applied using cosmogenic radionuclides having shorter half-lives, such as ^{7}Be and ^{137}Cs, which are also incorporated into the reactive phase. Additionally, we see the potential for using $^{10}Be_m$ transit time data to test existing transit time models and identify zones of storage that should be modeled (e.g., Czuba et al., 2015; Murphy et al., 2019).

3.7 Conclusions

We demonstrated the potential of meteoric cosmogenic ^{10}Be ($^{10}Be_m$) as a proxy to estimate fluvial sediment transit time in a large river system, and combined that data with measurements of channel geometry and lateral migration rates to evaluate the controls on transit time. We measured $[^{10}Be]_m$ in suspended sediment river depth profiles collected from the Rio Bermejo, a large lowland alluvial river that traverses ~1200 km from the Eastern Andean mountain front to its confluence with the Rio Paraguay with no tributaries. We observed a strong increase in depth-integrated $[^{10}Be]_m$ with increasing transit distance, and used this increase to estimate a mean sediment transit time of 8.4 ± 2.2 kyr. This estimated mean transit time is within bounds of sediment budget-based estimates that use geomorphic input parameters such as sediment flux, channel migration rate, and channel avulsion timescale. We compared $^{10}Be_m$-derived transit times for superelevated and braided vs. incised and meandering reaches, and for reaches with high vs. low lateral migration rates, revealing that braided channels exhibit less floodplain storage than laterally migrating channels.

Using $^{10}Be_m$ as a transit time tracer has advantages over other geochemical transit time methods. The method is neither grain size-, nor mineralogy-specific (Willenbring & von Blanckenburg, 2010). The half-life of ^{10}Be is sufficiently long relative to fluvial sediment transit, such that decay of $^{10}Be_m$ in river sediment is negligible. Measuring concentrations in depth-integrated suspended sediment samples allows us to characterize the full sediment load, from fine wash load to coarse sandy bed sediment, as previously shown by Wittmann et al. (2015). Challenges of using $^{10}Be_m$ as a transit time tracer include constraining the depositional flux of $^{10}Be_m$ ($F^{10}Be_m$) in the local floodplain and the potential for pedogenic ^{10}Be loss in high precipitation-low pH settings, which can be resolved by collecting additional geochemical data for floodplain deposits.

In conclusion, this study provides the first systematic application of $^{10}Be_m$ as a sediment transit time tracer in a field setting. We built a framework for new applications of $^{10}Be_m$ to study fluvial sediment routing and to constrain time-dependent geochemical processes transpiring in lowland river floodplains, such as weathering and organic carbon oxidation. Furthermore, we show that combining geochemical data and geomorphic measurements can provide new insight on river responses to climatic and tectonic processes.

3.8 Acknowledgements

This study was funded by the Deutsche Forschungsgemeinschaft (DFG) grant STR 373/34–1 and the Brandenburg Ministry of Sciences, Research and Cultural Affairs (Germany) through the international research training group IGK2018 (StRATEGy), led by Prof. Dr. Manfred Strecker. We thank Steve Binnie and Stefanie Heinze at the University of Cologne Centre for Accelerator Mass Spectrometry for conducting ^{10}Be measurements, Daniel Montluçon at the ETH Zürich Biogeoscience laboratory for assistance with BET surface area analysis, and Christoff Andermann and Stefan Liening at GFZ Potsdam for assistance with hydrologic data analyses and grain size data measurement at the GFZ Sed Lab. Sample collection and channel depth measurements would not have been possible without field assistance from Roberto Lopez, Francisco Latosinski, and Hima Hassenruck-Gudipati. We thank Friedhelm von Blanckenburg and Jens Turowski for supportive discussions, and Jim Pizzuto, Joseph Graly, and one anonymous reviewer for comments that greatly improved the manuscript. Additional methods, figures, and data referred to in the main text are available in the Supporting Information file. Data can be accessed at: https://doi.pangaea.de/10.1594/PANGAEA.913993.

Table 3.1. Transit time estimates and geomorphic parameters for reaches 1-4 and the full river.

	Distance along channel	Reach length	Channel migration rate	h[a]	$[^{10}Be]_{no\ rm\text{-}Dl}$ initial	$[^{10}Be]_{no\ rm\text{-}Dl}$ final	$[^{10}Be]_{no\ rm\text{-}Dl}$ increase	Transit time through reach[b]	Cumulative Transit Time[c]	Sediment aging rate	Virtual sediment velocity
	km	km	m yr^{-1}	m	x10^7 at g^{-1}	x10^7 at g^{-1}	x10^7 at g^{-1}	yr	yr	yr km^{-1}	m yr^{-1}
Reach 1	0 - 135	135	0	1.46 ± 1.15	0.90	1.25	0.35	350 ± 270	350 ± 270	2.6 ± 2.0	386 ± 168
Reach 2	135 - 422	287	28.1	5.26 ± 1.94	1.25	1.39	0.14	490 ± 180	840 ± 324	1.7 ± 0.6	586 ± 157
Reach 3	422 - 866	444	21.9	7.4 ± 0.17	1.39	2.29	0.90	4490 ± 100	5330 ± 340	10.1 ± 0.2	99.0 ± 2.25
Reach 4	866-1221	355	6.26	6.83 ± 1.05	2.29	2.99	0.70	3190 ± 490	8520 ± 596	9.0 ± 1.4	111 ± 15.0
Full river length	0 - 1221	1221	23.23	6.03 ± 2.12	9.02	2.99	2.09	8430 ± 2200	8520 ± 596	6.9 ± 1.8	145 ± 65.0

[a]Mean and standard deviation of incision depths along the channel

[b]Calculated using equation (3.5) using parameters for each reach

[c]Calculated as the sum of upstream reach transit times, with uncertainty

4 HYDRODYNAMIC SORTING EFFECTS ON FLUVIAL ORGANIC CARBON EXPORT

Manuscript in preparation:

Repasch, M., Hovius, N.., Scheingross, J. S., Vieth-Hillebrand, A., Müller, C., Höschen, C., Szupiany, R., and Sachse, D., (in prep.). Hydrodynamic sorting drives the fate of river particulate organic carbon. To submit to Geophysical Research Letters.

Key Points

- In the Rio Bermejo (Argentina), downstream particle size fining and vertical sorting influence particulate organic carbon (POC) fluxes.
- NanoSIMS data reveal two primary POC pools in suspended sediment: 1) mineral-associated POC and 2) discrete organic particles.
- Our findings suggest that selective deposition of coarse, labile POC enhances oxidation, while entrainment of mineral-associated POC drives long-term burial.

Abstract

Fluvial sediment routing influences the flux of particulate organic carbon (POC) transferred from terrestrial landscapes to marine sedimentary basins. During fluvial transit, hydrodynamic sorting processes, such as vertical sorting and downstream fining, modify composition and fluxes of sediment and POC. However, we lack a mechanistic understanding of how these physical processes drive changes in biogeochemical fluxes, generating large uncertainties in fluvial carbon budgets. We address this knowledge gap by studying POC transported by a natural flume-like river – the Rio Bermejo in Argentina. Nanoscale secondary ion mass spectrometry (NanoSIMS) analyses reveal two dominant types of POC: 1) mineral-bound organic carbon associated with <4 μm platy grains, and 2) coarse discrete organic particles. *n*-alkane stable isotope data reveal distinct transport mechanisms, i.e., fine, mineral-associated POC is concentrated at the water surface, while discrete organic particles are primarily transported at depth, due to differences in settling velocity. Consequently, modern, relatively labile POC dominates the exported POC flux, perhaps driving long-term CO_2 drawdown if rapidly buried in marine sediments. Because coarse particles are prone to selective deposition, downstream transit may cause enhanced oxidation of labile POC, while entrainment of fine floodplain sediment enhances export of mineral-bound POC.

Consequently, the balance between selective deposition of labile POC and entrainment of mineral-bound POC determines whether rivers contribute more to long-term CO_2 drawdown or release.

Plain Language Summary

The carbon cycle regulates Earth's climate by determining the amount of carbon in our atmosphere. Rivers are important for the carbon cycle because they deliver large amounts of carbon from mountains to the oceans. However, some carbon can be oxidized to CO_2 in river systems, and it is difficult to measure the amount of carbon that is delivered to the ocean versus released to the atmosphere. In a 1300-km-long river in Argentina, we measured the amount of sediment and organic carbon in the river water, and identified two types of organic carbon: 1) plant particles, which are easily oxidized to CO_2, and 2) carbon attached to minerals, which is resistant to oxidation. We calculated the fluxes of these two organic carbon pools, and found that the flux of plant particles is much larger than the flux of mineral-bound organic carbon. This suggests that most riverine organic carbon will be oxidized to CO_2 during transport to the ocean. Our data show that we need to differentiate between plant particles and mineral-bound organic carbon to accurately measure the fluxes of organic carbon moving from rivers to the ocean and atmosphere.

4.1 Introduction

Cycling of organic carbon (OC) between the lithosphere, biosphere and atmosphere regulates Earth's climate over multiple timescales. Rivers influence this cycle by redistributing significant amounts of carbon from forested uplands to sedimentary basins. If fluvially-transported OC is preserved during source-to-sink transit, its long-term sequesters atmospheric CO_2 over geologic timescales. Current estimates of this burial flux are uncertain (Berner, 1982; Blair & Aller, 2012; Burdige, 2005), as we have yet to mechanistically explain what drives the composition and quantity of OC exported by rivers (Galy et al., 2015). This is challenging because fluvially-transported OC is a complex mixture of organic molecules ranging in chemical stability, and rivers can deposit OC on their floodplains where it can be stored for many years before being re-mobilized and transported to the oceans.

Fluvial particulate organic carbon (POC) comprises a mixture of petrogenic POC (POC_{petro}) and biospheric POC (POC_{bio}), which differ in physical form and chemical decomposition rate at Earth's surface (Galy et al., 2015; Hage et al., 2020; Hemingway et al., 2019; Rosenheim & Galy, 2012). Petrogenic POC has a low decomposition rate, allowing preservation during long-distance fluvial transit and recycling through the lithosphere over

million-year cycles (Galy et al., 2008; Sparkes et al., 2020). POC_{bio} comprises both relatively modern plant-derived POC and aged POC derived from soils. Aged POC_{bio} typically associates with microaggregates, which are metastable in aerobic environments, allowing POC_{bio} to age up to 10^4 yr (Blair & Aller, 2012; Kleber et al., 2007). Modern POC_{bio} consists of wood and leaf particles, which readily decompose (e.g., Gordon & Goñi, 2004; Leithold et al., 2016). Once transported to coastal marine settings, these two POC_{bio} pools differ in their probabilities of long-term burial versus decomposition. While distinctions among refractory and labile POC_{bio} pools have been recognized in soils (e.g., Cotrufo et al., 2019; Mueller et al., 2017; Prater et al., 2020), they have not yet been differentiated in actively-transported river sediments. Due to their physical and chemical differences, these two POC_{bio} pools must behave differently during source-to-sink transit. Here we aim to deconvolve the effects of hydrodynamic processes on the fluxes of modern and aged POC_{bio} exported by rivers to accurately estimate POC transfer from the terrestrial biosphere into geological storage.

Hydrodynamic sorting is driven by channel morphodynamics and river hydraulics. Channel depth and slope determine the shear stress of the river water column, which limits the amount of material a river can carry in suspension. The rate of downstream POC transport is set by the vertical water velocity profile (Vanoni & Brooks, 1957), which generates different transport rates at different depths. While models exist for vertical sediment concentration profiles (Rouse, 1937), the vertical distribution of POC is not universally understood. The size, shape, and density of POC determine its depth in the water column (Dietrich, 1982; Lamb et al., 2020). Consequently, coarse, water-logged plant debris may settle rapidly and travel at depth with quartz sand (e.g., Bouchez et al., 2014; Turowski et al., 2016). Over long transport distances, selective deposition of coarse particles can lead to downstream particle size fining (Wright & Parker, 2005), potentially changing the relative proportions of modern and aged POC exported by rivers.

Effects of hydrodynamic sorting on fluvially-transported POC have been observed in many rivers and delta-shelf transport systems (Bao et al., 2018; Bouchez et al., 2014; Goni et al., 1997; Wakeham et al., 2009; Yu et al., 2019a), but are rarely linked to physical processes. Aged POC is often associated with fine sediment (<63 μm, silt and clay) (Bouchez et al., 2014; Galy et al., 2008; Peterse & Eglinton, 2017; Tao et al., 2015; Yu et al., 2019), suggesting that hydrodynamic sorting affects the POC age distribution in the water column. Biomarker analyses have revealed compositional differences with river flow depth. In the Madre de Dios River, *n*-alkanes and lignin compounds in suspended sediment revealed that POC transported at the water surface had a more ^{13}C-enriched and weathered chemical signature than POC deeper in

the water column (Feakins et al., 2018; Feng et al., 2016). Compositional differences among POC in different particle size fractions have also been observed in coastal depositional settings. (Bianchi et al., 2007; Gordon & Goñi, 2004; Yu et al., 2019). Despite these observations, it remains unclear how fluvial hydrodynamic sorting alters the overall composition and relative fluxes of modern and aged POC along fluvial source-to-sink pathways.

Here we aim to identify the primary mechanisms driving fluvial POC sorting and quantify their effects on modern and aged POC fluxes during long-distance fluvial transit. This study focuses on a lowland alluvial river, the Rio Bermejo in Argentina. We test two hypotheses: 1) Aged, degraded POC is associated with fine, clay minerals and has a lower particle settling velocity than fresh, water-logged POC, and 2) Downstream fining and lateral erosion of modern floodplain vegetation drive the total POC flux to increase with distance downstream. We test these hypotheses using nano-scale secondary ion mass spectrometry (NanoSIMS) and leaf-wax biomarker stable isotope data for river suspended sediment collected from depth profiles at multiple locations along the fluvial transit pathway. We couple these geochemical data with particle size and suspended sediment concentrations to quantify the changes in amount and composition of fluvial POC between upstream sources and downstream sinks.

4.2 Study area and methods

4.2.1 Rio Bermejo, Argentina: A natural flume experiment

The Rio Bermejo drains the eastern flank of the central Andes, delivering sediment and organic matter from the mountains to the lowland Paraguay-Paraná river system. From the mountain front, the Bermejo flows for ~1270 km without any significant tributaries, working like a natural flume (**Fig. 4.1a**). At the mountain front, the last major tributary is the Rio San Francisco (RSF). The total headwater drainage area is ~5.2x10^4 km^2, while the lowland fluvial fan containing the active channel belt comprises ~7.0x10^4 km^2 of the Gran Chaco Plain. This area is covered predominantly by subtropical forests and shrublands, where C3 plants (most

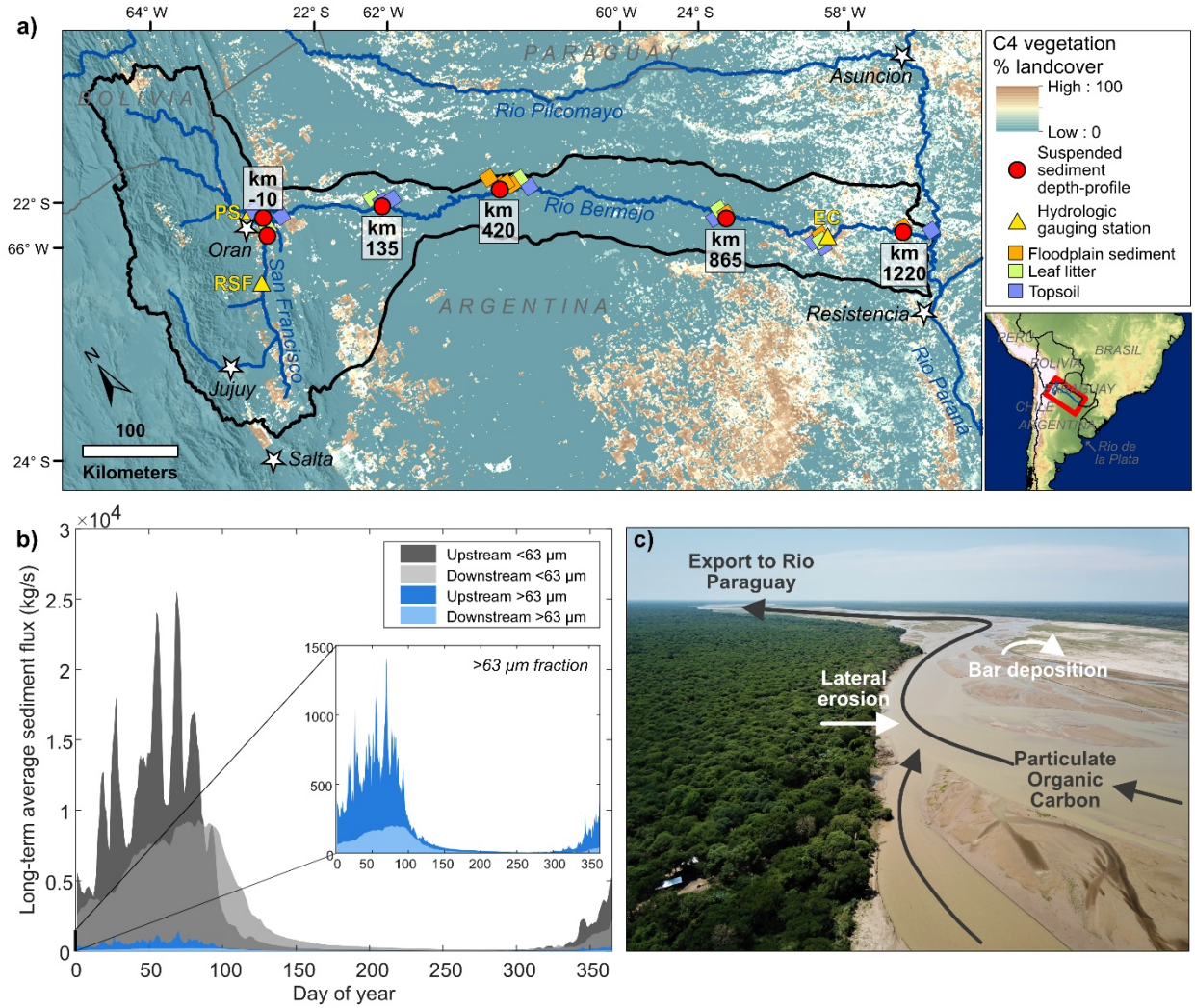

Figure 4.1. a) Map of the Rio Bermejo study area showing C3 and C4 vegetation-type coverage. Blue-green colors indicate predominantly C3 plants, and brown-yellow colors indicate predominantly C4 plants, which have different carbon isotopic signatures (Powell and Still, 2012). Gauging stations: EC – El Colorado, PS – Pozo Sarmiento, and RSF – Rio San Francisco. **b)** Long-term mean daily suspended sediment fluxes (grey = <63 µm, blue = >63 µm; darker colors = upstream (river km 0), lighter colors = downstream (river km 1085)). Inset shows the >63 µm sediment flux curves at a larger scale to highlight differences between upstream and downstream fluxes. Data from Argentina National System of Hydrologic Information, SNIH. **c)** Aerial image of the Rio Bermejo at river km 135 during low flow conditions, with arrows showing downstream and lateral movement of fluvial sediment and POC.

trees, shrubs, and forbs) prevail (**Fig. 4.1a**). Any changes in the stable carbon isotope composition of river POC with distance downstream should therefore reflect chemical transformation of POC, rather than changes in source vegetation.

The Rio Bermejo annual mean water discharge is ~432 m^3/s, but often reaches ~2000 m^3/s at the peak of South American Monsoon season (February-March) (*Argentina National System of Hydrologic Information, SNIH*). The Rio Bermejo receives ~103 Mt/yr sediment from its Andean headwaters (Repasch et al., 2020), 92% of which is transported during monsoon season (1 December – 1 May) (**Fig. 4.1b, 4.1c**). Grain size and sediment flux data suggest progressive downstream particle size fining (**Figs. 4.1b**) (McGlue et al., 2016; *Argentina National System of Hydrologic Information, SNIH*), allowing us to test the effects of downstream fining on POC fluxes. High suspended sediment concentrations up to 60 g/L and typical grain size distributions ranging from clay to medium sand allow us to test the effect of vertical hydrodynamic sorting on fluvial POC.

4.2.2 Sample collection

To capture differences in particle size and POC composition within the water column, we collected suspended sediment from vertical water depth profiles in the channel thalweg during March 2017. To capture downstream variability in particle size and composition, we sampled at four locations along the mainstem Rio Bermejo (river km 135, 420, 865, 1220), one location on the Rio San Francisco (RSF) (river km -15), and one location on the Rio Bermejo upstream from the RSF confluence (river km -10) (**Fig. 4.1a**). We identified the thalweg with an Acoustic Doppler Current Profiler (ADCP) (Teledyne Workhorse). Flow depths at sampling points varied between 3.5 m and 5.7 m. Suspended sediment was collected from 2-5 depths between the river bed and the water surface using an 8-liter van Dorn-type sampling bottle equipped with an electronic pressure transducer and deployed from a boat. Samples were filtered under pressure through 0.22 μm polyethersulfone membranes and stored in combusted glass vials. Bedload material was collected at RSF, river km -10, 135, and 865 using a weighted mesh net. Additionally, to characterize potential POC sources to the river, we sampled floodplain sediment, topsoil, and leaf litter from land adjacent to the channel at each sampling station. We collected floodplain sediment by coring down to <5 m with an Edelman-type hand auger into sediment deposits ranging in age from ~600 yr to ~17 kyr (Scheingross et al., in review). Sample material was oven dried at 40°C for ~48 hours, and suspended sediment was weighed to calculate suspended sediment concentrations.

4.2.3 n-alkane stable carbon and hydrogen isotope analyses

To investigate compositional differences in fluvial POC with varying water depth and distance along the channel, we measured concentrations and stable isotope values of *n*-alkane biomarkers extracted from our samples. Sediment samples were prepared and analyzed at the GFZ Potsdam Organic Surface Geochemistry Lab. We homogenized and disaggregated dry sediment using mortar and pestle, and removed visible plant material >1 mm. We weighed and loaded sediment aliquots into aluminum cells for lipid extraction. Total lipid extracts (TLE) were recovered using an accelerated solvent extraction system (Dionex ASE) with 9:1 v/v dichloromethane: methanol. We added exactly 10 µg of internal standard (5-α-Androstane) to the TLE for compound quantification. The *n*-alkane fraction was isolated following the manual solid phase extraction method described by Rach et al. (2020).

n-alkanes were identified and quantified using an Agilent gas chromatograph (GC 7890-A) with flame ionization detection (FID) coupled to a single quadrupole mass spectrometer (MS 5975-C). We quantified *n*-alkane concentrations relative to the internal standard, and normalized the abundance to the sediment aliquot mass. We measured *n*-alkane $\delta^{13}C$ via GC-C-IRMS (gas chromatography-combustion-isotope ratio mass spectrometry) with helium carrier gas (Agilent 7890N, ThermoFisher Delta V Plus). All compounds were measured in triplicate with a standard deviation of ≤0.5‰. Measurement quality was checked regularly by measuring *n*-alkane standards (nC_{15}, nC_{20}, nC_{25}) with known isotopic composition (Campro Scientific, Germany). $\delta^{13}C$ values were normalized to the Vienna Pee Dee Belemnite (VPDB) standard. We measured *n*-alkane $\delta^{2}H$ via GC-IRMS using a ThermoFisher Scientific Trace GC 1310 coupled to a Delta-V isotope ratio mass spectrometer. All $\delta^{2}H$ measurements were made in duplicate, and measurement quality was checked using an *n*-alkane standard mix with known $\delta^{2}H$ values (A6 mix, nC_{16} – nC_{30}, A. Schimmelmann/Indiana University). $\delta^{2}H$ values were normalized to the Vienna Standard Mean Ocean Water (VSMOW) standard.

4.2.4 NanoSIMS and SEM analysis

To characterize the nature of fluvial POC at a finer scale, we employed nano-scale secondary ion mass spectrometry (NanoSIMS). This technique simultaneously detects seven ion species with high lateral resolution, enabling study of associations between organic and inorganic species on sediment particle surfaces (Herrmann et al., 2007; Mueller et al., 2013). We analyzed nine river sediment samples (four surface water and five depth samples) plus four floodplain soil and sediment samples, choosing samples with the highest POC concentrations and median grain size diameter <30 µm (maximum size of NanoSIMS measurement window). For each sample, we weighed ~0.7 mg of dry sediment in a combusted glass vial, and added 10

ml of ultrapure 18.2 MΩ water. We shook the vial to suspend all particles, waited one minute for coarse particles to settle, then used a pipette to place a 100 µl drop of the sample onto a Si-wafer. The sample aliquot was placed in a desiccator at room temperature until dry, then gold coated (~5 nm thick). To show the size and shape of the particles analyzed by NanoSIMS, we captured SEM images of the samples using a Zeiss Ultra Plus scanning electron microscope (SEM). For each sample, we captured SEM images of five to ten areas of interest (AOIs) representing the heterogeneity of each aliquot.

NanoSIMS measurements were performed on the Cameca NanoSIMS 50L at the Lehrstuhl für Bodenkunde, TU München, Germany, using the Cs^+ primary ion beam with 16 keV primary ion impact energy. To compensate for charging effects on non-conductive sample material, the samples were sputter coated with Au/Pd (~30 nm coat) and electron flood gun was used when needed. Contaminants and excess gold coating were sputtered away with high primary beam current, implanting Cs^+ ions into the sample and enhancing the secondary ion response. In imaging mode, 30x30 µm AOIs (256x256 px, dwell time 1 ms/px) were scanned by the primary ion beam with lateral resolution of 100-200 nm. We detected five secondary ions in parallel via electron multipliers: $^{12}C^-$, $^{12}C^{14}N^-$, $^{16}O^-$, $^{27}Al^{16}O^-$, and $^{56}Fe^{16}O^-$. The electronic dead time was fixed at 44 ns. Using the OpenMIMS plugin for Fiji/ImageJ, we processed 505 NanoSIMS images for 101 unique AOIs. Stacks of 40 measurement planes were deadtime-corrected, autotracked, and compressed to single images. We focused on ^{12}C, $^{12}C^{14}N$, and $^{27}Al^{16}O$ signals, which indicate the presence of organic carbon, nitrogen-containing organic matter (e.g., microbially-processed organic matter (Kopittke et al., 2018, 2020)), and Al-rich secondary minerals, respectively.

4.3 Results

4.3.1 Biomarker evidence for vertical POC sorting

n-alkane data provide insight to the composition and sources of fluvial POC. nC_{31} was the most abundant homologue in all suspended sediment samples (**Fig. B3**). Average chain length (ACL) and carbon preference index (CPI) values were similar across all water depths, indicating vascular plant sources for all samples, with the exception of two mineral-rich bedload samples with low CPI and ACL values (**Table B1**). Organic carbon-normalized *n*-alkane concentrations in surface water samples averaged 420±142 µg/gOC, while samples from depth averaged 355±128 µg/gOC. Bedload samples had *n*-alkane concentrations of 0.0-0.7 µg/gOC, excluding organic-rich bedload sampled at river km 865 (**Table B1**). We observed no statistically significant changes in *n*-alkane composition or concentration with distance

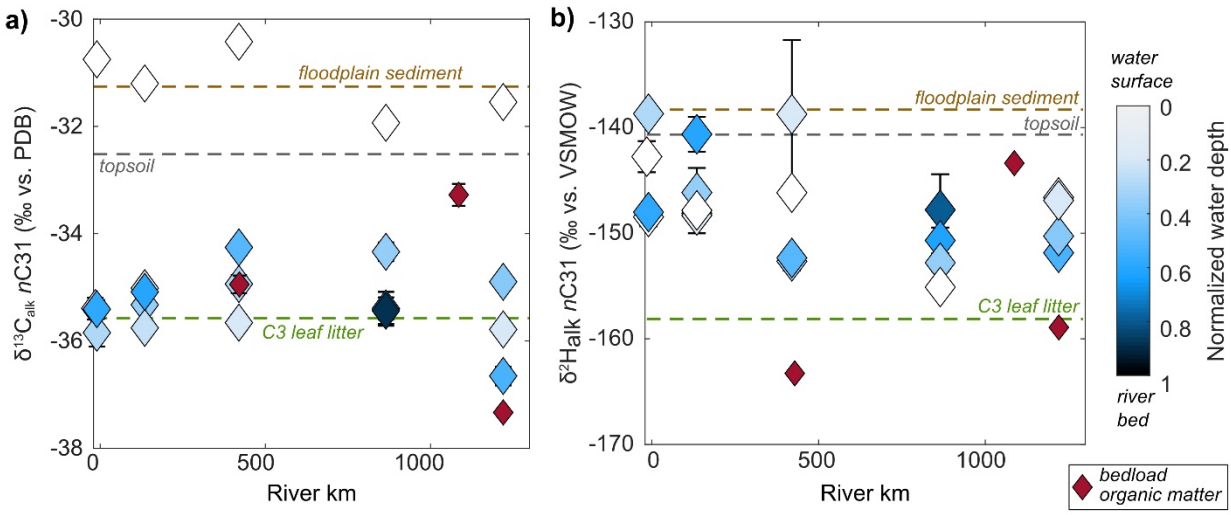

Figure 4.2. $\delta^{13}C_{alk}$ and $\delta^{2}H_{alk}$ values for the nC_{31} alkane plotted against distance downstream along the channel. River km 0 represents the Bermejo-San Francisco confluence at the mountain front. Samples are colored by their relative depth within the water column. Red points represent samples of organic matter traveling near the river bed. Error bars represent analytical uncertainty determined by triplicate or duplicate measurements. Horizontal dashed lines represent the mean values of POC sources in the Bermejo lowland basin (leaf litter (n=6) = green, topsoil (n=18) = gray, floodplain sediment (n=16) = brown).

downstream, but we did observe strong compositional differences between surface water samples and samples collected deeper than 10% of the flow depth.

$\delta^{13}C_{alk}$ values for suspended sediment ranged from -36.7‰ to -30.3‰, suggesting C3 vascular plant origins (**Table B1**). Within river depth profiles, there was a statistically significant difference between $\delta^{13}C_{alk}$ in surface water samples and samples deeper than 10% of flow depth ($p < .01$ for all homologues) (**Text B2, Fig. B4**). Averaged across all *n*-alkane homologues, $\delta^{13}C_{alk}$ values were 3.2‰ more positive in surface water samples than samples at depth difference ($p < .005$, k-s test) (**Fig. 4.2, Table B2**).

$\delta^{2}H_{alk}$ of river suspended sediment samples ranged from -165.6‰ to -127.0‰ for the nC_{27}-nC_{33} odd-numbered homologues, with nC_{27} having the most enriched values and nC_{29} the most depleted values (**Fig. B4**). We did not observe any significant trend between $\delta^{2}H_{alk}$ and water depth. However, we did observe a statistically significant trend in nC_{31} $\delta^{2}H_{alk}$ with distance downstream, where samples became more depleted of ^{2}H with increasing transit distance (Pearson's rho = -0.44, $p<.05$) (**Fig. 4.2**).

We analyzed the *n*-alkane composition of three samples of bedload organic matter (BOM) in the mainstem Rio Bermejo, and one sample from the Rio San Francisco (**Table B1**). For Rio San Francisco BOM, $\delta^{13}C_{alk}$ of the most abundant homologue, nC_{31}, was -20.2‰ and $\delta^{2}H_{alk}$ was -154.1‰. For the three mainstem BOM samples nC_{31} was more depleted of ^{13}C and ^{2}H, with $\delta^{13}C_{alk}$ ranging from -37.3‰ to -33.3‰ and $\delta^{2}H_{alk}$ ranging from -163.3‰ to -143.4‰ (**Fig. 4.2**).

To constrain the composition of possible sources of fluvial POC, we measured the *n*-alkane isotope composition of nC_{27}-nC_{33} odd-numbered homologues from leaf litter, topsoil, and floodplain sediment (**Fig. 4.1, Table B3**). For leaf litter samples (n=6), mean $\delta^{13}C_{alk}$ varied between -33.6±7.7‰ and -31.4±6.7‰, and $\delta^{2}H_{alk}$ between -172.8±14.1‰ and -159.9±16.5‰. For topsoil samples (n=15), mean $\delta^{13}C_{alk}$ ranged from -31.4±4.0‰ to -28.9±3.3‰, and mean $\delta^{2}H_{alk}$ ranged from -139.2±14.2‰ to -127.4±14.1‰. For floodplain sediment sampled >20 cm depth (n=15), mean $\delta^{13}C_{alk}$ ranged from -32.4±2.3‰ to -28.8±2.6‰, and $\delta^{2}H_{alk}$ ranged from -140.9±21.8‰ to -134.6±9.6‰.

4.3.2 NanoSIMS images of Rio Bermejo POC

The NanoSIMS images, supplemented by SEM images, reveal the detailed nature of organic carbon in Rio Bermejo suspended sediment (**Fig. 4.3**). In SEM images, most particles <4 µm in diameter have a platy shape, while particles >4 µm in diameter are generally blocky or cylindrical. In samples collected from depth, we observed microaggregates composed of many <4 µm particles with strong $^{27}Al^{16}O$ and ^{12}C NanoSIMS signals (**Fig. 4.3b**), indicating the presence of mineral-associated OC. This mineral-associated OC was amorphous (no visible plant cell structure) and was often co-located with $^{12}C^{14}N$. In our analyses, we found very little evidence for mineral-associated OC in individual particles >4 µm.

SEM and NanoSIMS images of both river sediment at the water surface, at depth, and floodplain sediment reveal discrete organic particles varying in size, shape, and cell structure (**Fig. 4.3a–c**).

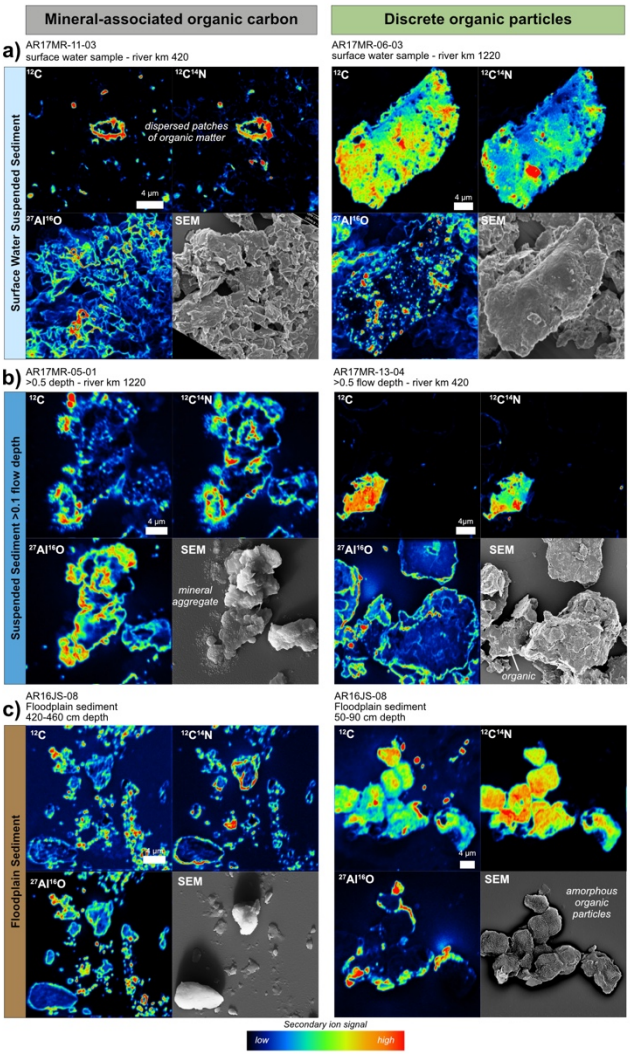

Figure 4.3. NanoSIMS and SEM images for six areas of interest (AOIs) for small aliquots of river suspended sediment. These AOIs highlight mineral-associated organic carbon (left column) and discrete organic particles (right column) in a) surface water, b) depth samples, and c) floodplain samples. For each AOI, we show secondary ion intensity signals for ^{12}C, $^{12}C\ ^{14}N$, and $^{27}Al^{16}O$, and SEM images. Color bar represents relative secondary ion intensity.

Discrete organic particles have relatively uniform ^{12}C signals, low $^{12}C^{14}N$, $^{27}Al^{16}O$, and ^{16}O signals (**Text B1, Fig. B1**), and visible cell structures, suggesting vascular plant origins. We also observed several particles resembling fungal hypha, indicating a soil source (**Fig. B1**).

In NanoSIMS images of floodplain sediment, mineral-associated organic matter with high ^{12}C, $^{12}C^{14}N$, and $^{27}Al^{16}O$ signals were common, and discrete organic particles with low $^{27}Al^{16}O$ and ^{16}O signals were also present (**Figs. 4.3a, B2**). Mineral-associated organic matter was primarily found in microaggregates, similar to those in river sediment.

4.4 Discussion

4.4.1 Two pools of fluvial particulate organic carbon

Biomarker stable isotope data revealed compositional differences between POC transported at the river water surface and POC transported deeper in the water column. On average, $\delta^{13}C_{alk}$ of surface water samples was 3.2‰ more positive than $\delta^{13}C_{alk}$ of depth samples, consistent with a more degraded chemical composition than samples from depth (**Table B2**). Our NanoSIMS data revealed two primary POC pools in Rio Bermejo suspended sediment: 1) mineral-associated organic carbon and 2) discrete organic particles (**Fig. 4.3**). NanoSIMS and SEM images reveal that mineral-bound POC is primarily associated with fine (<4 μm), platy clay minerals and/or Al-oxyhydroxides (e.g., Kleber et al., 2007). This mineral-bound POC was amorphous and generally nitrogen-rich, suggesting a microbially-processed or degraded chemical signature (Nadelhoffer & Fry, 1988). OC-bearing microaggregates were observed in suspended sediment from >10% flow depth (**Fig. 4.3**), which likely originated as soil microaggregates in the floodplain that were eroded into the river and transported at depth due to their large composite diameter (Lamb et al., 2020). In contrast, discrete organic particles were typically >4 μm in diameter, with visible cell structures and low ^{16}O NanoSIMS signals (**Fig. B1**), indicating reduced plant organic matter. This is the first direct evidence that these two POC pools are concentrated in different particle size fractions, and this finding greatly improves our ability to quantify their fluxes.

4.4.2 Floodplain sediment as a primary source of mineral-bound POC

The compositional differences between <4 μm and >4 μm POC in the Rio Bermejo are driven by differences among POC sources. Samples from <10% of total flow depth had $\delta^{13}C_{alk}$ values approximating leaf litter and BOM. *n*-alkanes in topsoil and floodplain sediment were overall more ^{13}C-enriched than leaf litter and BOM, with similar $\delta^{13}C_{alk}$ as surface water suspended sediment samples (**Fig. 4.2, Table B1**). These data suggest that floodplain sediment and soil are primary sources of <4 μm POC, while fresh plants are the primary source of >4 μm POC.

We estimated the relative contributions of three endmember POC sources to suspended sediment using a Bayesian stable isotope mixing model, MixSIAR (e.g., Blake et al., 2018; Menges et al., 2020). We used floodplain sediment (>20 cm depth), topsoil (<20 cm depth), and leaf litter as endmembers, and the measured $\delta^{13}C$ and $\delta^{2}H$ values of n-C_{27}, n-C_{29}, n-C_{31}, and n-C_{33} alkane compounds as tracers (eight unique descriptors) (**Text B3**). Mixing model results support that floodplain sediment was the dominant source of POC in surface water suspended sediment (**Table B4**). Surface water samples had the highest proportions of floodplain-derived POC (0.56-0.67), and the lowest proportions of leaf litter-derived POC (0.11-0.19) (**Fig. B8**). Samples collected from depth had higher proportions of leaf-litter (0.30-0.45), supporting that POC transported at depth was primarily from modern plants.

n-alkane ^{13}C-enrichment in mineral-associated POC is likely driven by pedogenesis in the floodplain. POC with elevated $\delta^{13}C$ values is well-documented in clay-rich soils (Kleber et al., 2007; Mikutta et al., 2009; Rasmussen et al., 2018; Wagai et al., 2015), attributed to heterotrophic organic matter degradation (Hirave et al., 2020; Wagai et al., 2015). The 10^{1}-10^{3} yr timescale of transient floodplain storage is sufficient for these isotopic transformations to occur (Scheingross et al., in review). These data highlight lateral erosion as a key process for delivering mineral-stabilized POC into rivers, perhaps driving long-term POC burial in sedimentary basins.

4.4.3 Effects of vertical sorting and downstream fining on fluvial POC fluxes

Our data show that vertical hydraulic sorting drives mineral-bound POC to the top of the water column where water velocity is highest, while discrete organic particles dominate POC transported at depth where water velocity is lower (**Fig. 4.4**). Additionally, downstream particle size fining changes the grain size distributions of the river sediment load, and therefore must change the overall composition of fluvial POC between source and sink (**Text B4**). To test the effects of these physical processes on fluvial POC fluxes, we evaluated the changes in instantaneous fluxes of <4 μm mineral-associated POC and >4 μm discrete organic particles with distance downstream along the Rio Bermejo.

For each river depth profile, we used a Rouse-based method (Rouse, 1937) to calculate the sediment (Q_s) and POC (Q_{POC}) fluxes of the <4 µm and >4 µm size fractions (**Text B6**). At each river cross section, >4 µm particles dominated both Q_s and Q_{POC}. However, due to downstream fining, the proportion of <4 µm sediment increased with distance downstream, from 10% of the total Q_s at river km -10 to 28% at river km 1220 (**Table B7**). This strong increase in the relative abundance of fine particles may not only result from selective deposition, but also addition of weathered floodplain sediment. Lateral channel erosion is enhanced in downstream reaches of the Rio Bermejo, increasing the amount of fine clay minerals in the active channel. From the mountain front to river km 1220, discharge-normalized <4 µm Q_{POC} increased from 60 to 910 gC/m^3, while the discharge normalized >4 µm Q_{POC} increased more modestly, from 500 to 2190 gC/m^3. These estimates suggest that discrete organic particles dominate Rio Bermejo Q_{POC}, but downstream fining drives the flux of mineral-associated POC to increase with distance downstream.

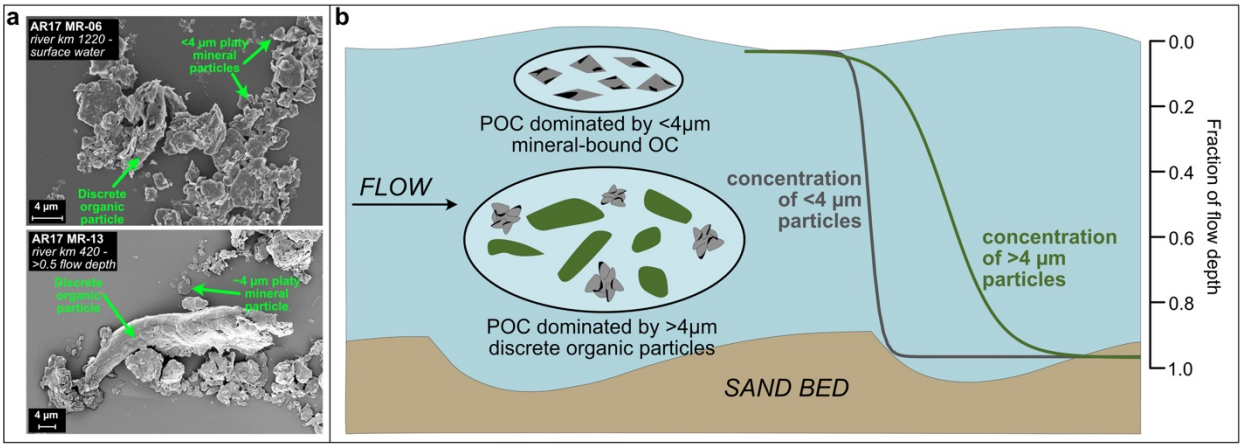

Figure 4.4. a) SEM images of Rio Bermejo suspended sediment samples showing an example of surface water sediment abundant in <4 µm mineral particles (top), and an example of suspended sediment from depth with a large discrete organic particle (bottom). b) Conceptual figure illustrating vertical sorting of POC in the water column, showing characteristic concentration-depth profiles for <4 µm (gray) and > 4 µm particles (green).

4.4.4 Implications for the global carbon cycle

The amount of POC oxidized during fluvial transit is a function of the amount of time spent in transit. Vertical sorting of diverse POC particles can regulate their routing pathways, and thus their source-to-sink transit times. Particles traveling high in the water column are prone to overbank deposition during flooding, resulting in a higher probability of long-term floodplain storage and subsequent oxidation. However, most POC transported at the surface is mineral-stabilized and has a slow decomposition rate (Hemingway et al., 2019; Mikutta et al., 2006; Torn et al., 1997), therefore CO_2 released by its oxidation is likely negligible. Additionally, our data suggest that residence time in the floodplain enables mineral stabilization, so long transit times may enhance long-term POC preservation. Conversely, discrete organic particles are

unstable at Earth's surface over long timescales (Galvez et al., 2020) and are not likely to survive deposition episodes. Coarse discrete organic particles are susceptible to selective deposition on braid bars and point bars where they may be remineralized before being re-entrained. By quantifying the transit time of different particle size fractions, we could predict the fate of fluvially-transported POC with greater confidence.

In the Rio Bermejo, most fluvial POC takes the form of >4 μm discrete organic particles transported at depth. A significant amount of water-logged plant debris also travels in an undercurrent near the river bed, similar to observations by Feng et al. (2016). While we were unable to quantify the flux of this organic undercurrent, it is likely a substantial component of the total fluvial POC flux. Because this POC is labile, it may be susceptible to degradation during offshore transport. However, in settings with large sediment fluxes and high near-shore sedimentation rates, significant amounts of plant debris can be preserved in coastal sediments (Bianchi et al., 2007; Hage et al., 2020; Lee et al., 2019; Sparkes et al., 2015), acting as a long-term carbon sink.

Our analysis showed that the flux of <4 μm mineral-associated POC increased downstream, potentially resulting from enhanced erosion of floodplain soil and sediment. This highlights the importance of floodplain sediment storage and pedogenesis/weathering for mineral stabilization of POC. Erosion is a key mechanism for delivering this mineral-bound POC to downstream sedimentary sinks (Galy et al., 2015; Hilton & West, 2020), where it has high preservation potential in sedimentary basins (Barber et al., 2017; Keil et al., 1994; Mead & Goñi, 2008), contributing to long-term CO_2 drawdown.

4.5 Conclusions

We combined geochemical, hydrologic, and geomorphic data for river sediment and particulate organic carbon (POC) in a flume-like lowland river (Rio Bermejo, Argentina) to show that hydrodynamic sorting plays a key role in regulating fluvial POC fluxes from source to sink. *n*-alkane stable isotope data showed that ^{13}C-enriched POC is concentrated at the top of the water column, while ^{13}C-depleted POC dominated at depth. NanoSIMS analyses revealed two general POC pools: 1) <4 μm mineral-associated POC, and 2) >4 μm discrete organic particles. Differences in particle settling velocity drive vertical sorting of these two POC pools in the water column. Consequently, mineral-associated POC may be efficiently transported downstream, while coarse discrete organic particles are susceptible to selective deposition and oxidation during storage episodes. Combining our geochemical data with grain size distributions and sediment flux estimates, we showed that the Rio Bermejo POC flux is

dominated by coarse discrete organic particles. However, downstream fining drives increased fluxes of fine, mineral-associated POC with distance downstream.

While the fate of fluvial POC will differ among river systems, our findings from the Rio Bermejo are likely characteristic of most lowland alluvial rivers. Our data suggest that estimated fluxes of fluvial biospheric POC export should be subdivided into two separate fluxes: mineral-associated POC and discrete organic particles. Because they have different decomposition rates, estimating the relative proportions these two pools in river sediment loads can reduce uncertainty in long-term POC burial estimates.

4.6 Acknowledgements

We acknowledge Manfred Strecker for support through the StRATEGy international research training group (Deutsche Forschungsgemeinschaft (DFG) grant STR 373/34-1 and the Brandenburg Ministry of Sciences, Research and Cultural Affairs (Germany)). We thank Doreen Novak and Oliver Rach for assistance with compound-specific carbon and hydrogen isotope analyses, Gertraud Harrington and Johann Lugmeier for NanoSIMS measurements, Sathish Mayanna for SEM imaging, and Jens Turowski for helpful discussion. Sample collection was supported by Oscar Orfeo and Roberto Lopez. Additional text, figures, and tables can be found in the supplementary material. All data generated for this study are available at: https://doi.pangaea.de/10.1594/PANGAEA.925626.

5 THE ROLE OF SEDIMENT TRANSIT TIME AND MINERAL PROTECTION IN FLUVIAL ORGANIC CARBON CYCLING

Manuscript in review:

Repasch, M., Scheingross, J.S., Hovius, N., Eglinton, T.I., Lupker, M., Haghipour, N., Gröcke, D., Sachse, D., (in review). Fluvial organic carbon turnover regulated by sediment transit time. Nature Geoscience.

Abstract

Rivers transfer terrestrial organic carbon (OC) fluxes from mountain ranges to ocean basins, playing a key role in the global carbon cycle. During fluvial transit, OC may be oxidized and emitted to the atmosphere as CO_2, or escape oxidation via burial in sedimentary deposits. The balance between oxidation and burial determines whether fluvial OC transfer results in a net atmospheric OC source or sink, but the factors regulating this balance are poorly known. Here we quantify the effects of fluvial transit on particulate OC (POC) fluxes along a ~1300 km lowland channel with no tributaries. We show that sediment transit time and mineral protection regulate the magnitude and rate of fluvial POC turnover, respectively. Using a simple turnover model, we estimate that the river's annual POC export flux is two orders of magnitude greater than its oxidation flux, resulting in a net OC sink. Modeling shows that lateral erosion into OC-rich floodplains can offset POC oxidation, driving rivers with high channel mobility to be net OC sinks, while management practices that stabilize river courses likely result in net CO_2 release.

5.1 Introduction

The carbon cycle controls atmospheric CO_2 concentrations over geological timescales, thereby regulating Earth's habitability. Silicate weathering and terrestrial organic carbon burial drive long-term CO_2 drawdown from the atmosphere, while natural CO_2 emissions are generated primarily by solid earth degassing and organic carbon oxidation. Rivers deliver 125-335 MtC/yr particulate organic carbon (POC) to the oceans (Galy et al., 2015), playing a central role in regulating CO_2 fluxes. This fluvial export is composed of both recent photosynthetically-fixed biospheric POC (POC_{bio}), which sequesters CO_2 upon burial, and petrogenic POC from organic-rich rocks (POC_{petro}), which releases CO_2 to the atmosphere when oxidized. Sediment routing may lead to oxidation and replacement (turnover) of POC in the fluvial transport system. If total oxidation from POC turnover exceeds the amount of POC preserved plus new

additions from vegetation, then fluvial transit is a net CO_2 source. However, the feedbacks between the geomorphic and geochemical processes regulating these fluxes are insufficiently constrained, making fluvial carbon budgets highly uncertain (Bouchez et al., 2010; Clark et al., 2017; Hilton & West, 2020; Leithold et al., 2016).

We hypothesize that fluvial POC budgets are primarily controlled by two factors: 1) source-to-sink transit time, and 2) mineral protection of POC_{bio}. First, source-to-sink transit time determines the residence time of POC in river systems (Bouchez et al., 2014; Hilton et al., 2011; Leithold et al., 2016; Lyons et al., 2002). In coastal mountains with short (10^1-10^2 km), steep rivers linking to the ocean, the initial POC load may be efficiently transferred to depocenters (Bianchi et al., 2018; Hilton et al., 2011). In continental settings, fluvial transit lengths extend beyond 10^3 km, and many large rivers have been characterized as net carbon sources due to CO_2 degassing from channels and floodplains (Aufdenkampe et al., 2011; Battin et al., 2008; Cole & Caraco, 2001; Mayorga et al., 2005; Raymond et al., 2013).

Where measured, ^{14}C-ages of exported fluvial POC are an order of magnitude younger than mean clastic sediment transit times, which can exceed 20 kyr in the Amazon basin, and may reach 100 kyr in the Ganges basin (Anthony Dosseto et al., 2008; Granet et al., 2007; Torres et al., 2020). This age discrepancy indicates that significant POC turnover occurs during lowland transit (Hedges et al., 1986; Quay et al., 1992). As POC likely avoids oxidation during in-river transport (Scheingross et al., 2019b), turnover likely occurs primarily during transient storage in floodplains. Fluvial morphodynamics govern the timescale of this storage (Torres et al., 2017, 2020), however, transit time data are scarce, making it difficult to quantify the net effect of sediment routing on the fluvial carbon budget.

A second possible control on POC turnover is the degree of coupling between clastic sediment and POC_{bio}. Fluvial POC_{bio} may travel as discrete particles, or bound to mineral phases (Bouchez et al., 2014; Hemingway et al., 2019; Rosenheim & Galy, 2012). Reactive mineral phases, such as aluminum, iron, and manganese oxyhydroxides may protect organic carbon from microbial degradation (Johnson et al., 2015; Lalonde et al., 2012; Roy et al., 2013; Wagai & Mayer, 2007) via cation-bridging reactions with phyllosilicates (Blattmann et al., 2019) or ligand-exchange on hydroxylated mineral surfaces (Kleber et al., 2007). This may dramatically reduce the turnover rate of POC_{bio} and allow a significant portion to escape oxidation. The fact that exported fluvial POC often contains POC_{bio} that has aged up to 10^4 yr (Drenzek et al., 2007; Feng, Benitez-Nelson, et al., 2013; French et al., 2018) suggests that the mechanisms inhibiting its decomposition can be volumetrically important. However, the relative importance of organo-mineral complexes in preserving fluvial POC remains unclear (Galy et al., 2008).

Here we quantify the effects of sediment transit time and organo-mineral interactions on the fate of fluvial POC, by tracing organic matter through a river system that has no tributaries for nearly 1300 km. Building on existing fluvial sediment transit time estimates from cosmogenic radionuclide chronometry (Repasch et al., 2020), we add new POC radiocarbon and stable carbon isotope measurements, and secondary mineral data for actively transported sediment sampled at multiple stations along the river. With these data, we develop a simple model to estimate POC turnover during source-to-sink transit and explore the geomorphic and geochemical drivers of the fluvial carbon budget.

5.2 Rio Bermejo: A natural flume experiment

We exploit the natural simplicity of the Rio Bermejo in northern Argentina (Fig. 5.1). Its headwaters drain eastward from the Andes, delivering ~103 Mt/yr sediment and POC to the lowland basin (Repasch et al., 2020), with little aquatic productivity due to high turbidity (Pedrozo & Bonetto, 1987). The river flows ~1270 km from the last tributary confluence at the mountain front (Rio San Francisco, river km 0) to the Rio Paraguay. Over this distance, the Rio Bermejo has no notable tributaries and is largely unaffected by anthropogenic activity.

From river km 0 to km 265, the river is braided and perched above the flood basin. The remaining ~1000 km are a single-thread, meandering channel with migration rates up to 30 m/yr (Repasch et al., 2020) (**Fig. 5.1**). POC may transit this lowland system in ~14 days if traveling at water velocity, or it may be deposited onto the floodplain where sediment can reside for >20 kyr (Repasch et al., 2020) before it is re-entrained by lateral channel migration. Thus,

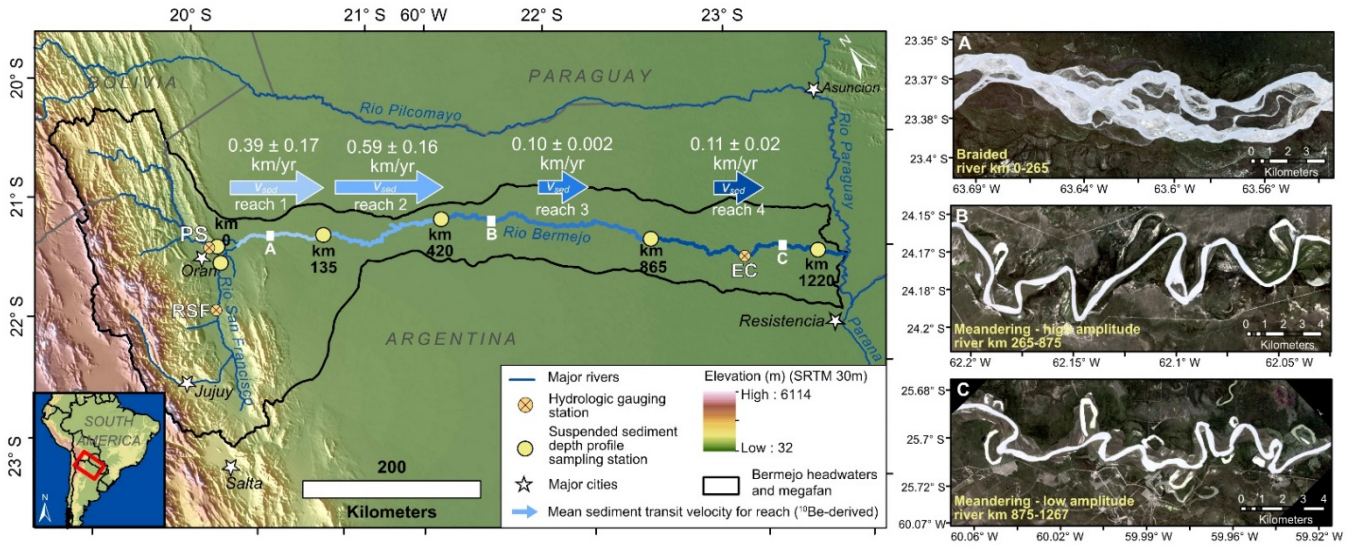

Figure 5.1. Study area. Left: Topographic map of the Rio Bermejo system. Blue arrows show the sediment transit velocity (v_{sed}) for the four corresponding reaches between sampling points. Right: A, B, and C are Planet satellite images showing the differences in morphology along the channel.

Rio Bermejo sediment comprises a mixture of POC ranging from modern biomass to aged, mineral-bound POC.

The mean fluvial sediment transit time between the mountain front and the Rio Paraguay is ~8500 yr (~0.15 km/yr) (Repasch et al., 2020). However, sediment transit velocity (v_{sed}) varies along the channel, from ~0.59 km/yr in the braided reach to ~0.1 km/yr in the lower meandering reach, reflecting local channel morphodynamics (**Fig. 5.1**). As a result of lateral migration, sediment experiences on average ~4.5 deposition-erosion episodes over the lowland channel length, each taking ~1.9 kyr (Repasch et al., 2020). Below we show that v_{sed} is a first-order control on POC oxidation during fluvial transit.

5.3 Downstream changes in POC composition

To assess POC fate during transit, we measured POC concentrations, stable ($\delta^{13}C$) and radioactive (^{14}C) carbon isotopes, and mineral specific surface area (SSA) of suspended sediment from river depth profiles at six stations during monsoon season, when ~89% of the annual sediment load is discharged (**Methods**). To account for hydrodynamic sorting and characterize the composition of the entire suspended load, we depth-integrated each profile, weighting individual samples by suspended sediment and POC concentrations (**Table C1**). At river km 0, the depth-integrated POC concentration (POC_{DI}) was 0.18±0.06%. Assuming POC_{DI} is constant through time (within uncertainty), this gives a mean annual headwater POC flux (Q_{hw}) of 1.85±0.62x10^5 tC/yr (**Methods**). POC_{DI} increased to 0.28±0.02% at river km 1220, yielding a mean annual POC export of 2.24±0.16x10^5 tC/yr to the Rio Paraguay (Q_{out}). The difference between the mean headwater and export fluxes is +0.39x10^5 tC/yr, suggesting that, under modern conditions, lateral POC inputs may exceed POC lost during transit.

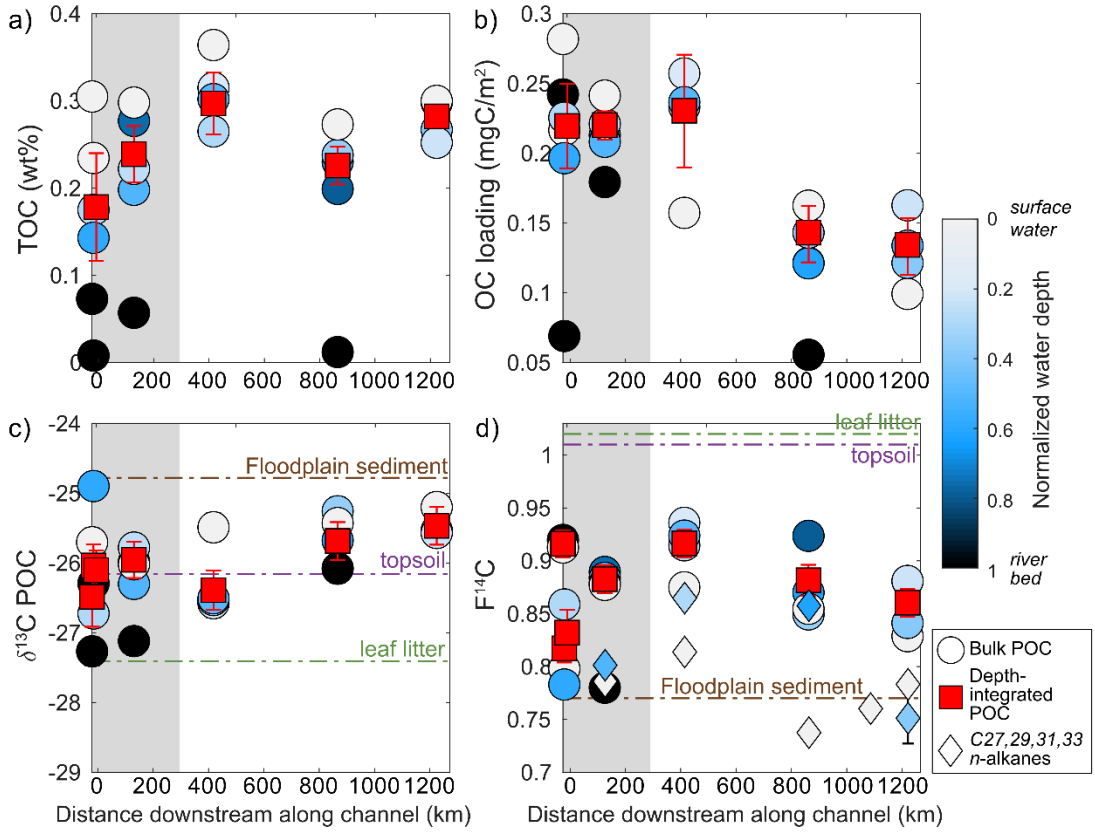

Figure 5.2. a) POC concentration (TOC), **b)** OC loading, **c)** $\delta^{13}C_{POC}$, and **d)** $F^{14}C_{POC}$ and $F^{14}C_{alk}$ measurements for samples collected from depth profiles along the Rio Bermejo. Distance 0 represents the last tributary confluence at the mountain front. Gray shading indicates the braided reach. Circles/diamonds are individual samples colored by depth in water column relative to total flow depth, with error bars representing analytical precision. Red squares are depth-integrated (DI) values for each depth profile, with error bars representing standard error of the weighted mean. Dashed horizontal lines indicate mean isotopic values for floodplain sediment, leaf litter, and topsoil in the catchment.

POC concentrations increased along the river's braided reach, while OC loading (mass of POC per unit SSA) remained constant (0.21-0.23 mgC/m^2) (**Fig. 5.2, Table C1**). These diverging trends likely arise from selective deposition of coarse sediment with low POC (**Fig. C1**). OC loading decreased significantly in the meandering reach (to ~0.13 mgC/m^2), due to SSA increase downstream, as weathered floodplain minerals were increasingly incorporated into the river load. We further explored downstream POC transformations using stable and radiocarbon isotope measurements.

$\delta^{13}C$ values ($\delta^{13}C_{POC}$) of individual suspended sediment samples ranged from -27.3‰ to -24.9‰, and radiocarbon content (expressed as fraction modern, $F^{14}C_{POC}$) ranged from 0.78 to 0.94 (**Fig. 5.2**). All $\delta^{13}C_{POC}$ and $F^{14}C_{POC}$ values were within the compositional range of OC sources within the catchment (**Fig. 5.2, Table C2**), indicating that fluvial POC comprises a mixture of compounds ranging in age and turnover time. Without bedrock outcrops downstream of the mountain front, we can exclude any influence of POC_{petro} inputs along the study reach. $F^{14}C$ values of refractory terrestrial leaf wax *n*-alkanes ($F^{14}C_{alk}$) ranged from 0.74 to 0.86,

significantly lower than $F^{14}C_{POC}$ values for the same samples, suggesting they represent an older POC pool of preferentially preserved vascular plant residues (van der Voort et al., 2017).

Within depth profiles, water surface samples generally had higher POC concentrations, more positive $\delta^{13}C_{POC,}$ and lower $F^{14}C_{POC}$ values than samples collected >0.5 m below the surface (**Fig. 5.2**). In agreement, $F^{14}C_{alk}$ values were generally lower for surface samples. These compositional differences reflect hydrodynamic sorting of POC (Galy et al., 2008; Yu et al., 2019). Sediment at depth appeared to be enriched in water-logged plant debris, while surface water sediment was enriched in low density pedogenic clay and secondary mineral phases, which can host ^{13}C-enriched OC (Johnson et al., 2015; Lalonde et al., 2012; Wedin et al., 1995). With increasing transit distance along the meandering segment, surface water sediment became consistently more ^{13}C-enriched and ^{14}C-depleted, reflecting progressive addition of aged, fine mineral-associated POC.

Between river km 135 to 420, where v_{sed} was highest, $\delta^{13}C_{DI}$ remained constant, but $F^{14}C_{DI}$ increased significantly from 0.83 to 0.92 (^{14}C-age decrease of ~780 yr) (**Fig. 5.2**). This may reflect mass loss of ^{14}C-depleted sediment through selective deposition of coarse sand (including lithic fragments and POC_{petro}), and/or gain of fresh organic matter. Along the meandering reach with low v_{sed} (river km 420-1220), $\delta^{13}C_{DI}$ values increased from -26.4±0.3‰ to -25.5±0.3‰, and $F^{14}C_{DI}$ values decreased from 0.92 to 0.86 (~510 yr ^{14}C-age increase). These changes reflect entrainment of aged, ^{13}C-enriched POC from floodplain deposits. These data suggest that v_{sed} exerts a strong control over POC composition, by determining the time allowed for POC aging and transformation.

Complete POC turnover during floodplain storage would cause a downstream increase of $F^{14}C$ values. Consequently, the ^{13}C-enrichment and apparent POC aging trends along the meandering reach suggest that some POC is preserved during floodplain storage, surviving multiple episodes of deposition and erosion. However, even this refractory POC is susceptible to turnover because the degree of apparent POC aging is less than the clastic sediment transit time. Below, we test the hypothesis that mineral protection drives these observations, by inhibiting POC decomposition (Blattmann et al., 2019; Hemingway et al., 2019).

5.4 Organo-metal complexation slows POC decomposition

Without mineral protection mechanisms, or anoxic floodplain burial, most POC traveling through river systems is likely to be oxidized on decadal to centennial timescales. ^{14}C-ages of POC and *n*-alkanes in the Rio Bermejo reach ~1500 yr and ~2500 yr, respectively, indicating that decomposition of vascular plant-derived POC is inhibited during long-distance

fluvial transit. To test if organo-metal complexation slows the turnover of POC in fluvial transit, we measured extractable metal concentrations in the oxyhydroxide phases of suspended sediment (**Methods**), as proxies for the abundance of reactive oxyhydroxides (Rasmussen et al., 2018).

Extractable [Al], [Fe], [Mg], [Mn], and SSA, were significantly correlated with $F^{14}C_{POC}$ (negative), $F^{14}C_{alk}$ (negative), and $\delta^{13}C_{POC}$ (positive) (**Fig. 5.3, Figs. C2, C3**); samples with higher metal concentrations contained older, ^{13}C-enriched POC. All correlations between $F^{14}C_{POC}$ and metal concentrations are stronger than the correlation between $F^{14}C_{POC}$ and SSA, suggesting that organic compounds are not only adsorbed onto mineral surfaces, but also bound to secondary minerals via complexation reactions (Kleber et al., 2007). ^{13}C-enrichment of mineral-stabilized POC may result from decomposition in the floodplain (Lawrence et al., 2015), and/or preferential reaction of minerals with ^{13}C-enriched organic compounds (Lalonde et al., 2012; Mikutta et al., 2006). These data highlight metal complexation in fluvial systems as an important stabilization mechanism facilitating long-term POC_{bio} burial.

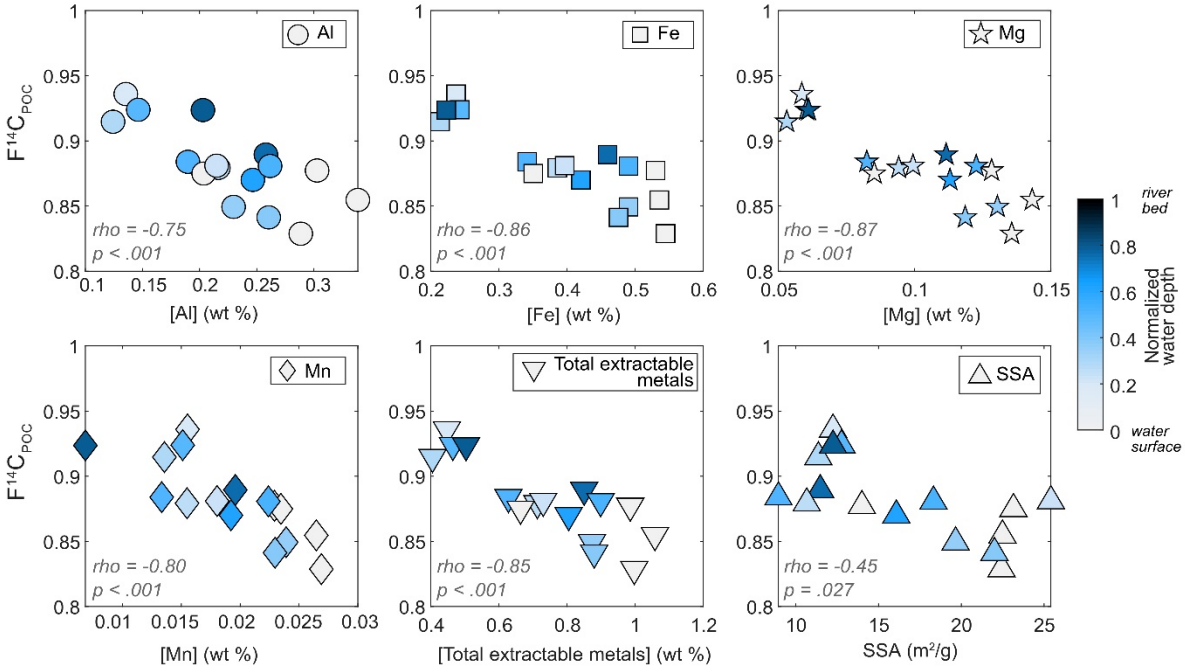

Figure 5.3. Concentrations of acid extractable metal ions Al, Fe, Mg, Mn, total extractable metals, and mineral specific surface area (SSA) vs. $F^{14}C_{POC}$ of river suspended sediment (excluding bed sediment). Color scale indicates the normalized sample depth in the water column. Rho is the Pearson linear correlation coefficient, and the p-value indicates the statistical significance of those correlations.

5.5 Net carbon flux of the Bermejo river system

Our data provide evidence for POC oxidation, input of young biomass via lateral channel migration, and POC preservation by organo-mineral complexation during fluvial transit. Below

we use these findings to estimate the POC budget of the Bermejo fluvial system, as regulated by sediment transit time and mineral protection.

We calculated the annual Rio Bermejo POC oxidation flux by defining a relationship between sediment transit time and POC decomposition rate. We assume that POC travels with clastic sediment at v_{sed}, and the reactivity of POC can be described by a decomposition rate constant (k, 1/yr) (**Methods**). Linking v_{sed} and k, the characteristic channel length (x_c) over which the fluvial POC load is turned over (depleted) is:

$$x_c = \frac{v_{sed}}{k} \qquad (5.1)$$

Then, the number of POC turnover cycles (n_c) during transit along a river system of length, L, is:

$$n_c = \frac{L}{x_c} \qquad (5.2).$$

Finally, the annual POC oxidation flux (Q_{ox}) resulting from fluvial transit of the mean-annual headwater POC load (POC_{in}, tC) over transit time t is:

$$Q_{ox} = \frac{n_c * POC_{in}}{t} \qquad (5.3).$$

We assume the river is in geomorphic steady state, where mean POC_{in} and v_{sed} are constant over ~10^4 yr transit timescales. Fluvial POC is composed of multiple carbon pools ranging in source, age, and decomposition rate (Feng, Vonk, et al., 2013; Galy & Eglinton, 2011; Marwick et al., 2015; Rosenheim & Galy, 2012). For simplicity, we divided fluvial POC into two pools: 1) fast-cycling discrete organic particles, POC_{fast}, and 2) slow-cycling mineral-associated POC, POC_{slow} (French et al., 2018; Torres et al., 2017). We assume that each POC pool is homogenous and decomposes at steady state, although this is rarely the case in nature (Sierra et al., 2017).

We estimate k using radiocarbon data following Torn et al. (2009) (**Methods**). For POC_{fast} we set the turnover time to ~17 yr, estimated from a global model of vegetation and soil carbon turnover (Carvalhais et al., 2014), which yields k_{fast} ~$6x10^{-2}$ yr^{-1} (**Methods, Table C4**). For k_{slow}, we utilized *n*-alkane $F^{14}C_{alk}$ data, because of their recalcitrance and association with secondary minerals (van der Voort et al., 2017). As a conservative estimate of POC_{slow} oxidation, we used most depleted $F^{14}C_{alk}$ value (0.74), yielding k_{slow} ~$3.4x10^{-4}$ yr^{-1} (turnover time of ~2900 yr) (**Methods**).

Using equations (1-3), we estimated separate turnover fluxes for POC_{slow} and POC_{fast} during the 8500 yr fluvial transit along the Rio Bermejo (**Methods**). x_c for POC_{fast} is 2±1 km,

resulting in n_c of 520±160 along the ~1270 km channel (**Fig. 5.4**). In contrast, x_c for POC_{slow} is 426±191 km, resulting in n_c of 3.0±0.9. Since the Rio Bermejo sediment load experiences ~4.5 sediment deposition-erosion cycles along the same pathway (Repasch et al., 2020), POC_{slow} must be tied to the clastic sediment trajectory, while POC_{fast} is completely decoupled from it.

Annually the Rio Bermejo receives ~1.85×10^5 tC POC from the headwaters (POC_{in}). According to a Bayesian end-member isotope mixing model, 47±10% of this load behaves as POC_{slow} and 53±17% as POC_{fast} (**Methods, Table 5.3**). Over the ~8500 yr transit between the mountain front and Rio Paraguay, turnover results in oxidation fluxes (Q_{ox}) of 30.4 (+23.8/-17.0) tC/yr for POC_{slow} and 6050 (+4410/-3210) tC/yr for POC_{fast}. The river exports ~2.24×10^5 tC/yr POC to the Rio Paraguay, which is two orders of magnitude greater than the combined POC_{slow} and POC_{fast} release of ~6080 tC/yr, and is therefore an efficient carbon sink.

POC turnover varies significantly along the Rio Bermejo (**Table C5**). Lower transit velocity and increased storage time make the meandering reach the locus of turnover, and there the POC turnover length scale is nearly an order of magnitude smaller than where the channel

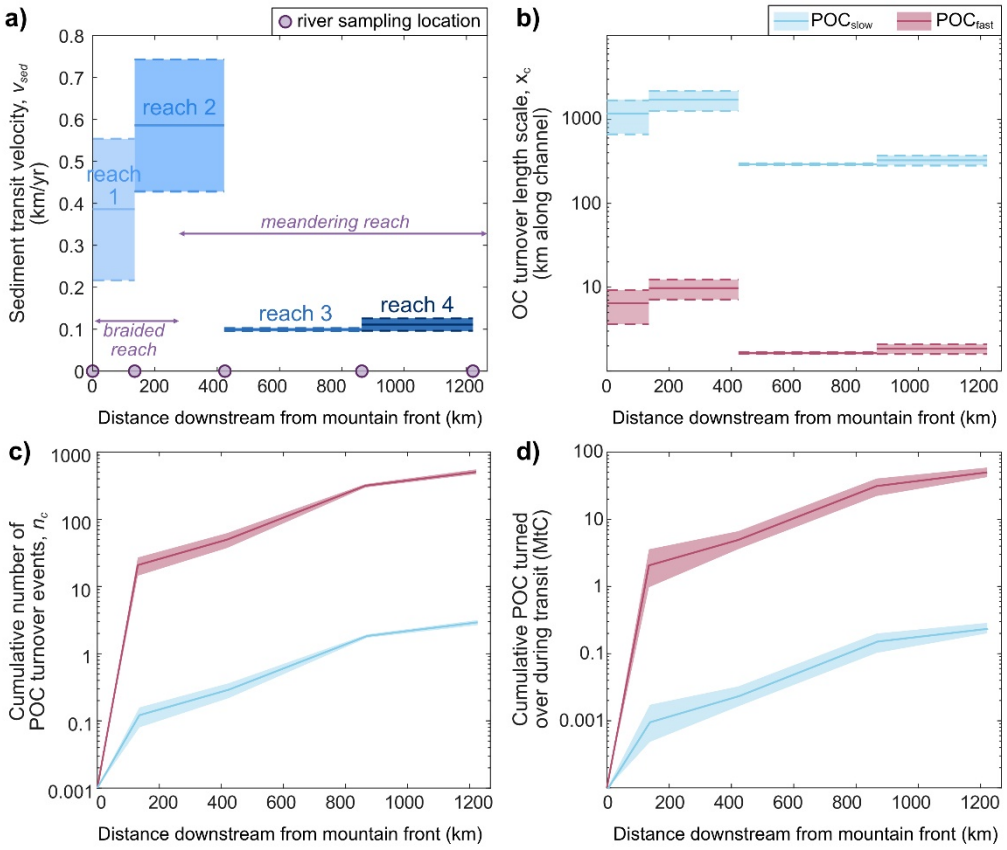

Figure 5.4. **a)** Mean sediment transit velocity (v_{sed}) for the four study reaches bound by the sediment sampling locations, **b)** POC turnover length scale (x_c) for the four study reaches, **c)** cumulative number of POC turnover cycles (n_c) that occur during transit along the Rio Bermejo, **d)** cumulative amount of POC oxidized during transit along the river, all plotted against distance downstream along the channel from the last tributary confluence at the Andean mountain front. Bold lines represent mean values and shaded areas represent the range of uncertainty.

is braided, (**Fig. 5.4**). These differences highlight the control of channel morphodynamics on the fate of fluvial POC in lowland river basins.

5.6 Controls on the fluvial OC budget

Our data show that sediment transit time and mineral protection are primary controls on the fate of fluvial POC during source-to-sink transit. Furthermore, our parameterization of the carbon turnover length scale and number of turnover cycles allows quantification of the respective roles of these governing mechanisms. Here we define a transit time-dependent fluvial POC budget:

$$Q_{out} - Q_{hw} = Q_{lat} - \frac{(n_c * f_{slow} * POC_{in})_{slow} + (n_c * f_{fast} * POC_{in})_{fast}}{t} \quad (5.4)$$

The last term on the right side of equation (4) represents the total Q_{ox} from POC_{slow} and POC_{fast} oxidation during transit, where f is the fraction of POC_{slow} or POC_{fast} contributing to POC_{in}. Whether $Q_{out} - Q_{hw}$ is positive or negative determines whether a river is a net OC sink or source, respectively, over ~10^4 yr timescales.

Our estimates for the Rio Bermejo, Q_{out} (~2.24x10^5 tC/yr) > Q_{hw} (~1.85x10^5 tC/yr), make this lowland segment of the river a net OC sink. Given the POC oxidation flux of ~6080 tC/yr, equation (4) yields Q_{lat} ~4.58x10^4 tC/yr, resulting from lateral erosion into floodplain forests. This agrees with estimates from measured channel migration rates and net primary productivity (**Methods**). Q_{lat} is nearly an order of magnitude greater than Q_{ox}, offsetting the CO_2 release. Using equation (4), we test the sensitivity of the fluvial OC budget by varying environmental boundary conditions. Q_{ox} is linearly proportional to v_{sed} and k (equations (2-4)). Holding all else constant, decreasing v_{sed} by an order of magnitude would render the Rio Bermejo OC neutral. Removing mineral protection (all POC_{fast}), or reducing Q_{lat} by an order of magnitude would shift the system near OC neutral. Doubling k for POC_{fast} would make the system a weak OC source. These tests suggest that the modern Rio Bermejo is a strong OC sink, and drastic changes in boundary conditions are required to tip the system to a net OC source. However, the key variables are linked in complex ways by external forces, including climate, hydrology, vegetation, tectonics, and even anthropogenic disturbance (Wohl et al., 2017), and associated feedbacks may be important.

At a global scale, v_{sed} and k can vary greatly across different climatic and tectonic settings. Using equations (1-4), we loosely estimated the carbon budgets of the Amazon (tropics) and Mackenzie (arctic) Rivers where Q_{out}, k, and v_{sed} have been constrained. In the Amazon, where POC_{fast} turnover is fast, <7 yr (Carvalhais et al., 2014; Mayorga et al., 2005), and v_{sed} ~0.21

km/yr (Dosseto et al., 2006), Q_{ox} is one order of magnitude less than Q_{out}, and a Q_{lat} of several MtC/yr balances the POC budget. In the Mackenzie River, where POC_{fast} turnover is slow, >70 yr (Carvalhais et al., 2014), and v_{sed} ~0.09 km/yr, Q_{ox} is two orders of magnitude less than Q_{out}. Although high latitude floodplains have lower NPP, significant Q_{lat} from eroding permafrost makes the Mackenzie a net OC sink (Hilton et al., 2015). Applying this model to rivers globally may yield more robust estimates of river-atmosphere OC fluxes, advancing our grasp on the global carbon cycle. Finally, our results suggest that lateral erosion into OC-rich floodplains is key for balancing the fluvial carbon budget. River engineering can significantly reduce Q_{lat} (Wohl et al., 2017), potentially tipping river systems toward stronger CO_2 sources.

5.7 Acknowledgements

We thank Manfred Strecker for support through the StRATEGy international research training group (Deutsche Forschungsgemeinschaft (DFG) grant STR 373/34-1 and the Brandenburg Ministry of Sciences, Research and Cultural Affairs (Germany)). We are grateful for assistance from Daniel Montluçon for compound-specific radiocarbon and mineral specific surface area measurements, the ETH Laboratory of Ion Beam Physics for AMS support. Nina Golombek for sample preparation, and Ricardo Szupiany and Roberto Lopez during field work.

5.8 Author Contributions

M.R., J.S.S., N.H., and D.S. designed the study and contributed to data interpretation and model development. M.R. and J.S. collected and processed samples, with help from D.S., N.H., and H.W.. H.W. provided analytical assistance reactive metal extraction and measurement. M.L., N.H., and T.E. provided the radiocarbon measurements. M.R. analyzed the data, produced the figures, and authored the manuscript (with significant input from J.S.S., N.H., D.S., and M.L.). All co-authors reviewed, commented on, and approved the manuscript.

5.9 Data availability

The data that support the findings of this study are available in the Extended Data Tables and the Pangaea data repository.

5.10 Methods

5.10.1 River sediment sampling

We collected 24 river suspended sediment samples between 13 and 25 March 2017, during the South American Monsoon season, with 75^{th} - 85^{th} percentile water discharge conditions (over a 50-yr gauging record) (673 to 1079 m^3 s^{-1}). We sampled river water from depth profiles (two to five sampling depths, depending on total water depth) at four locations along the mainstem Rio Bermejo, one location on the Rio Bermejo 10 km upstream of the Rio

San Francisco confluence, and one location on the Rio San Francisco 15 km upstream from the confluence (Fig. 5.1). River water was sampled by boat using a weighted 8-liter horizontal sampling bottle. Sediment was recovered by filtering river water under pressure through 0.22 µm polyethersulfone filter paper in a custom filtration device. Sediment was dried in an oven at 40°C and subsequently disaggregated and homogenized with a mortar and pestle. Suspended sediment concentrations were calculated as dry sediment mass normalized by the volume of water sampled.

5.10.2 POC concentrations and isotope measurements

For bulk organic carbon analyses, sediment samples were powdered in a disc mill and inorganic carbon was removed following Galy et al. (Galy et al., 2007). Sediment was decarbonated by leaching in 4% HCl solution, discarding the supernatant, rinsing with deionized water, and drying prior to measurement. Total organic carbon (TOC_{POC}) and $\delta^{13}C_{POC}$ were measured in duplicate at Durham University using a Costech elemental analyzer (EA) coupled to a CONFLO III and Thermo Scientific Delta V Advantage isotope ratio mass spectrometer (IRMS). Radiocarbon content was measured using an EA coupled to an accelerator mass spectrometer (EA-AMS) at ETH Zurich (Ruff et al., 2010). We report ^{14}C content as fraction modern ($F^{14}C_{POC}$), by normalizing measurements to 95% of the 1950 NBS Oxalic Acid II standard ($\delta^{13}C$ = -17.8‰) and correcting for mass-dependent fractionation using a common $\delta^{13}C$ value of -25‰.

5.10.3 Grain size and SSA measurements

Grain size and mineral specific surface area measurements were reported in Repasch et al. (2020).

5.10.4 Acid-extractable metals

To extract the Al, Fe, Mg, and Mn ions from the reactive grain coatings of the suspended sediment samples, we used a two-step leaching procedure adapted from Wittmann et al. (2012). We first dried 0.5-1.0 g sediment aliquots at 110°C overnight. After drying, samples were immediately sealed and weighed upon cooling. Reactive amorphous oxyhydroxide phases were leached with 10 ml 0.5M HCl solution, with mild shaking at room temperature for 24 hr. Crystalline oxide phases were leached in 10 ml 1M Hydroxylamine-hydrochloride solution (NH_2OH x HCl in 1M HCl) in an ultrasonic bath at 80°C for 4 hr, with shaking every 10 min. The leachates were dried completely, treated with aqua regia to destroy matrices, and then diluted in 3M HNO_3 for measurement. Al, Fe, Mg, and Mn concentrations were measured via inductively coupled plasma-optical emission spectroscopy (ICP-OES). Concentrations are

normalized by initial dry sample mass. Measurements of amorphous and crystalline phases were combined to obtain total reactive metal concentrations.

5.10.5 Depth-integration and POC fluxes

For each river depth profile, we calculated depth-integrated $\delta^{13}C_{POC}$ and $F^{14}C_{POC}$ values as the weighted means of the measured values for individual samples. Depth-integrated values were weighted by suspended sediment concentration (SSC) and TOC_{POC} measured for each sampling depth (**Table C1**). We estimated uncertainty as the standard error of the weighted mean.

We quantified the annual fluxes of POC delivered to and exported from the mainstem Rio Bermejo as the product of mean annual suspended sediment flux and POC concentration of the suspended sediment. We used the long-term suspended sediment fluxes measured at gauging stations at river km 0 and km 1086 reported by Repasch et al. (2020), and depth-integrated POC concentrations measured at downstream km 0 and downstream km 1220 (this study).

5.10.6 n-alkane radiocarbon measurements

We measured compound specific ^{14}C content of leaf wax *n*-alkanes to trace the radiocarbon signature of vascular plant-derived POC. Lipid compounds were extracted from bulk sediment using a Dionex Accelerated Solvent Extraction System (ASE 350), and the *n*-alkanes were further isolated by solid phase extraction over silica gel columns following the manual procedure of Rach et al. (Rach et al., 2020). C_{27}, C_{29}, C_{31}, and C_{33} *n*-alkanes were then purified from the saturated lipid fraction using preparative capillary gas chromatography (PCGC), following Eglinton et al. (1996). The purified long-chain *n*-alkanes were transferred to tin capsules using DCM and placed in combusted glass vials. Radiocarbon measurements were made by EA-AMS at ETH Zurich following Haghipour et al. (2019). Sample sizes ranged from 21-63 μg. ^{14}C measurements were corrected using the measured ^{14}C content of process blanks and empty tin capsules.

5.10.7 Bayesian isotope mixing model – MixSIAR

To determine the relative contributions of different OC sources to riverine POC, we used a three end-member Bayesian isotope mixing model constrained by bulk POC $\delta^{13}C$ and $F^{14}C$ data for the end-members. Input to the model included the mean and standard deviation of measured isotopic values for sample sets of leaf litter (n = 6), floodplain sediment (n = 51), and topsoil (n = 17) (Table S2). We calculated the fractional contribution of each end-member to all suspended sediment sample "mixtures" using the R package MixSIAR (Stock et al., 2018). We ran the MixSIAR model with an uninformative prior, making no initial assumptions about

the source contributions to the samples. The Markov Chain Monte Carlo method was performed with $1x10^6$ iterations, burn-in of $5x10^5$ iterations, thinning factor of 500, and three chains. For each river sediment sample this analysis yielded three posterior distributions, which contained the full range of possible fractional contributions of the three OC sources, respectively. We calculated the mean and standard deviation of the posterior distribution for each source to obtain the most probable values (Table S3). We combined the leaf litter and topsoil values to represent the proportion of POC_{fast} in each sample, and the floodplain sediment values to represent POC_{slow}. We estimated the proportions of these two pools for all suspended sediment samples, and then calculated the depth-integrated mean contributions of POC_{fast} and POC_{slow} at the headwaters, resulting in 0.53±0.17 and 0.47±0.10, respectively. We calculated the mean annual headwater fluxes (Q_{hw}) of POC_{fast} and POC_{slow} as the product of these values and the mean annual headwater POC flux.

5.10.8 Calculating decomposition rate constants

We calculated a characteristic decomposition rate, k, for POC_{fast} and POC_{slow}. We estimated k for POC_{fast} and POC_{slow} following the method of Torn et al. (2009):

$$k = \frac{\lambda * F^{14}C}{1 - F^{14}C} \qquad (5.5)$$

where, λ is the ^{14}C decay constant ($1.21x10^4$ yr^{-1}) and $F^{14}C$ is a representative fraction modern value for the POC pool of interest. The turnover time corresponding to the POC pool is simply $1/k$ (Torn et al., 2009), resulting in short turnover times for fast decomposition rates, and long turnover times for slow decomposition rates. By selecting just one characteristic $F^{14}C$ value to input into equation (5.5), we assume that the entire POC pool being modeled decomposes at the same rate through time.

5.10.9 Validating the modeled lateral POC influx

Balancing the Rio Bermejo carbon budget (equation (5.4)) revealed that the lateral influx of floodplain POC significantly influences the strength of the carbon sink. We estimated the possible lateral influx of POC into the Rio Bermejo from the floodplain due to lateral channel migration as:

$$Q_{lat} = m_{lat} * L * NPP \qquad (5.6)$$

where m_{lat} is the mean lateral channel migration rate (m/yr), L is the total channel length (m), and NPP is the net primary productivity of floodplain biomass (kgC). Lateral channel migration rates for the Rio Bermejo range from 0 to 30 m/yr, averaging 14.9±6.2 m/yr. The length of the lowland segment of the Rio Bermejo is 1267 km. We calculated the mean NPP for the lowland portion of the Rio Bermejo catchment (east of the mountain front) using the

MODIS MOD17A3H V6 annual NPP product for the year 2014 (500m pixel resolution). The mean NPP for the ~70,000 km^2 area was 3623±4373 kgC/m^2. Applying equation (5.6) gives Q_{lat} = 6.84±2.85x10^4 tC/yr, which agrees well with our model estimate of 4.58x10^4 tC/yr derived from equation (5.4).

6 SYNTHESIS AND CONCLUSIONS

In this dissertation, I addressed three key knowledge gaps in our understanding of how rivers regulate source-to-sink organic carbon transfer:

1) The duration of source-to-sink transit

In Chapter 3, I tested the application of cosmogenic meteoric ^{10}Be as a chronometer to record the source-to-sink river sediment transit time. After estimating a timescale for fluvial sediment transit, I tested the hypothesis that sediment transit time is set by channel morphodynamics, including lateral migration, channel depth and width, and avulsion frequency. While meteoric ^{10}Be extraction and measurement is a labor-intensive process, my results showed that this isotope does accumulate in river sediment during fluvial transit and therefore records the mean duration of source-to-sink sediment routing. In the Rio Bermejo, the mean sediment transit time is ~8.5 kyr, which is largely a function of lateral channel migration and remobilization of sediment that has been stored for up to ~20 kyr.

2) The role of hydrodynamic sorting in modifying sediment and organic carbon fluxes during long-distance fluvial transit

In Chapter 4, I tested the hypothesis that longitudinal hydrodynamic sorting results in increased export of fine sediment and mineral-associated organic carbon relative to coarse sediment and labile organic carbon. In addition, I tested the hypothesis that mineral-associated organic carbon has a different isotopic signature from labile organic carbon, resulting in biased export of ^{13}C-enriched organic carbon to downstream sedimentary basins. My results support that the fraction of fine, mineral-bound POC increases with distance downstream, due to overbank deposition and comminution during floodplain storage. However, my results show that the suspended POC load is dominated by relatively labile organic particles, which may be transported efficiently to depositional basins, driving long-term CO_2 drawdown.

3) The oxidation and chemical transformation of organic carbon during fluvial transit.

In Chapter 5, I tested the hypothesis that organo-mineral complexation protects a fraction of fluvial organic carbon during transit, allowing it to survive deposition on the floodplain and age. Additionally, I tested the hypothesis that labile organic carbon is oxidized during transit, acting as a CO_2 source to the atmosphere. My results show that reactive oxyhydroxide mineral phases can significantly reduce the decomposition rate of fluvial POC and stabilize it over

millennial timescales. During episodes of deposition and remobilization along the mainstem Rio Bermejo, I estimated that mineral-bound POC largely escapes oxidation, while labile POC is turned over >500 times during transit. Despite this large flux, every year the river exports more POC to downstream systems than is oxidized during transit, resulting in a net organic carbon sink.

In the following sections I highlight the key findings from these three chapters in more detail and expand on their contributions to the fields of Earth surface processes and biogeochemical cycling. Furthermore, I present a conceptual model for particulate organic carbon cycling at a global scale and discuss potential research avenues that would bridge the gap between this dissertation and global-scale modeling efforts.

6.1 The timescale of fluvial sediment routing

Estimating fluvial sediment transit time is non-trivial, as sediment may reside in river floodplains for 10^1 to 10^5 years before being transported downstream out of a river system, and in some cases sediment is never exported due to subsidence in inland basins (Bradley & Tucker, 2013; Granet et al., 2010; Pizzuto et al., 2017). Because sediment transit time drives the rate at which particulate matter can be transported downstream in rivers, it modulates weathering reactions, biogeochemical cycling, and overall sediment fluxes. As such, quantifying sediment transit time is a grand challenge in the field of Earth surface processes.

In Chapter 3, I demonstrated that meteoric ^{10}Be ($^{10}Be_m$) can be used as a geochemical chronometer for mean fluvial sediment transit time. Due to its lack of tributaries, the Rio Bermejo was an ideal pilot site for evaluating the accumulation of ^{10}Be in river sediment with increasing transit distance. It was clear that $^{10}Be_m$ concentrations increased with distance downstream, and elevated $^{10}Be_m$ concentrations in floodplain sediment profiles supported that this increase was driven by lateral erosion of sediment stored in the floodplain. Variability in channel morphodynamics across the Rio Bermejo lowland basin also revealed that subsidence and sediment aggradation in the Andean foredeep basin limited the remobilization of floodplain sediment, leading to long-term storage in the foredeep basin, and shorter apparent transit times through the upstream reaches. In this braided upstream reach, I also observed the highest rates of lateral channel movement and measured the smallest increase in $^{10}Be_m$ concentrations, leading to the conclusion that braided systems have shorter sediment transit times than meandering systems, due to rapid reworking of sediment deposits.

Through this study, I confirmed that sediment transit time scales with channel length, such that longer transport pathways, like continental-scale rivers, will store sediment for longer

durations than short transport pathways, such as ocean-island rivers. However, transit timescales will differ from river to river depending on the sediment transit velocity (i.e., the rate at which the sediment load is exchanged with stored floodplain sediment) and the grain size distribution of the sediment load. In a river system with a wide, low-sloping floodplain, transit time is modulated by the rate of lateral channel migration and avulsion frequency. In rivers confined to narrow valleys, the sediment transit time will be determined by the available accommodation space for sediment storage, and the frequency and intensity of floods that can efficiently evacuate sediment. Sediment transit time may also differ for different particle sizes, due to selective deposition and differential probabilities of re-mobilization. For example, despite its larger particle size, bedload may have a shorter transit time than fine suspended load. Fine sediment transported near the top of the water column has a higher probability of overbank deposition, and thus may experience more intermediate storage than coarse particles that never leave the active channel and are slowly, but continuously transported downstream. This theory requires further exploration.

For long-term geochemical processes, such as weathering reactions and chemical oxidation, $^{10}Be_m$ may be a sufficient chronometer for mean sediment residence time, because most geochemical measurements represent the mean of a heterogeneous mixture. However, for geomorphic processes spanning a range of timescales, it may be more useful to know the full distribution of sediment transit times. Particles with different grain size, shape and density will travel through river systems at different rates, due to selective deposition and hydrodynamic sorting processes, and thus chronometers that are more sensitive over shorter timescales may be needed.

Additional fallout radionuclides, in conjunction with $^{10}Be_m$, may be key to resolving full sediment transit time distributions. Fallout radionuclides bind to pedogenic grain coatings (e.g., secondary oxyhydroxide minerals composed of Al, Ca, Fe, and Mn), and thus concentrate in fine sediment at Earth's surface (Singleton et al., 2017). Short transit times are expected for relatively steep river systems with short transit pathways, and thus cosmogenic nuclides with a short half-life may be useful chronometers for fluvial transit. ^{7}Be is formed through the same process as $^{10}Be_m$ (cosmic ray spallation of O and N atoms), but it has a half-life of just 53.2 days, such than <1% of the initial ^{7}Be will remain after one year. The presence of ^{7}Be in sediment deposits indicates recent deposition (i.e. within ~150 days of measurement). ^{137}Cs is an anthropogenic radionuclide formed primarily as a result of above-ground nuclear weapons testing, which peaked in the 1960s. ^{137}Cs has a half-life of 30.2 yr, and thus can be useful for

constraining decadal-scale sediment transit. Unsupported/exchangeable ^{210}Pb ($^{210}Pb_{ex}$) is formed in the atmosphere through U-series decay of ^{222}Rn that is slowly released from igneous rocks. $^{210}Pb_{ex}$ has a half-life of 22.3 yr, and thus may be useful for constraining annual to decadal sediment residence time. By applying these fallout radionuclides to trace sediment through river systems, it may be possible to coarsely resolve sediment transit time distributions. I view this as an avenue of future research aiming to comprehensively resolve the numerous sediment routing pathways in a river system and determine their characteristic time scales.

6.2 The effect of sediment routing on fluvial organic carbon

Many studies have focused on the composition and fluxes of exported fluvial particulate organic carbon (POC) (e.g., Bouchez et al., 2014; Clark et al., 2017; Galy et al., 2011; McClelland et al., 2016; Waterson, 2005), but few studies have investigated the imbalances between POC fluxes entering and leaving river systems. In Chapters 4 and 5, I aimed to fill this knowledge gap by taking advantage of the flume-like properties of the Rio Bermejo. In Chapter 4, I showed that selective deposition of coarse material and remobilization of weathered floodplain sediment results in increased export of fine-grained, mineral-bound POC. My data also revealed that hydraulic sorting can drive different vertical distributions of mineral-bound POC and discrete organic particles in the water column, due to differences in particle size, shape, and density. In Chapter 5, I linked sediment transit time to POC decomposition to estimate the compositional transformation and oxidation of POC during source-to-sink transit. Through these two studies, I showed that sediment routing can significantly alter the composition and amount of POC exported from rivers, and that channel-floodplain connectivity is a significant factor in the degree of source-to-sink POC modification.

Chapter 4 focused on the effects of hydrodynamic sorting processes on fluvial POC. By integrating suspended sediment concentration data, particle size analysis, *n*-alkane stable isotope measurements, SEM imaging, and NanoSIMS analysis, I showed that particle size and shape primarily influences how hydraulic forces partition POC in active river transport. This study included the first application of NanoSIMS to organic matter in river sediment, revealing that mineral-bound POC is concentrated in <4 μm platy particles that are more heavily concentrated near the water surface. Sediment transported deeper in the water column is more concentrated in labile plant debris. Because sediment traveling at the water surface is more likely to be deposited on the floodplain during overbank flooding, mineral-bound POC may experience multiple cycles of deposition and remobilization during source-to-sink transit. During these storage episodes, POC can be oxidized or undergo carbon isotope fractionation,

becoming more enriched in ^{13}C relative to ^{12}C due to degradation processes related to soil development (e.g., Hirave et al., 2020). Because of its low density and platy shape, once exported to the oceans, this mineral-bound POC is more likely to be transported farther offshore, where sedimentation rates are lower. Alternatively, if the outlet is an estuary like the Rio de la Plata, this mineral-bound POC may have high preservation potential. At the freshwater-saltwater interface, salinity-induced flocculation can increase the effective settling velocity of mineral-bound POC, enhancing sedimentation (Bauer et al., 2013). In rivers that transport POC to the coast with large sediment fluxes, high transport capacity and high deltaic sedimentation rates may facilitate efficient transport and burial of labile plant debris in the sedimentary record (Bianchi et al., 2007; Hage et al., 2020; Lee et al., 2019; Sparkes et al., 2015).

The fates of these two POC pools likely differs across rivers with different suspended sediment fluxes, topographic gradients, deltaic subsidence rates, and near-shore sediment retention rates, but more quantitative work is needed to understand the fates of these large POC fluxes across different source-to-sink pathways. Often, studies focus only on POC in river sediment, or POC extracted from delta and shelf sediments, but to create a complete understanding of the effects of source-to-sink processes at the river-ocean interface, studies need to investigate POC amount and composition through the fluvial transport pathway and into the depositional setting. Using a space-for-time approach, these changes could be examined in exhumed fossil sedimentary sequences, by tracing organic carbon from outcrops of fluvial sedimentary rocks to lithified shelf-slope deposits (e.g., Sparkes, 2012).

In Chapter 5, I used radiocarbon data to show that POC can be preserved in the Rio Bermejo for 10^3 yr, but organic carbon aging is also accompanied by significant oxidation and replacement of original POC (i.e., turnover). POC may be deposited on floodplains via overbank flow, point-bar deposition, or channel cut-off. POC can remain in floodplain deposits for thousands of years, during which pedogenic processes can modify its original composition. Photooxidation and heterotrophic metabolism result in oxidation of labile POC, but pedogenic processes can also act to stabilize organic matter through organo-mineral complexation, or formation of mineral aggregates with organic matrices (Berhe et al., 2012; Kramer et al., 2012; Mikutta et al., 2006; Rasmussen et al., 2018). Deposition and storage of fluvial organic carbon and mineral sediment in lowland river floodplains can enhance development of organo-mineral associations, leading to significant amounts of POC stored in floodplains (D'Elia et al., 2017; Lininger et al., 2018, 2019; Sutfin et al., 2016). Subsequent erosion of OC-rich floodplain soils

via lateral channel migration or large-scale channel avulsion can re-mobilize and transport POC downstream to depositional basins. Despite POC stabilizations mechanisms, I found that while clastic sediment resided in the river system for ~8500 yr, on average, the mean radiocarbon age of *n*-alkanes was only ~2000 yr, suggesting that even refractory POC is turned over several times during fluvial transit. The number of turnover cycles is likely related to the strength of organo-mineral bonds. Weak organo-mineral bonds will lead to degradation and remineralization to CO_2 or more oxidized carbon phases. Strong organo-mineral bonds may facilitate long-term preservation and burial in terrestrial and marine sediments, resulting in long-term CO_2 drawdown.

6.3 Developing a global-scale model for fluvial organic carbon cycling

Results from this dissertation help paint a clear picture of the role that river systems play in the organic carbon cycle. Placed within the context of existing work, these new findings can be developed into a model for the physical mechanisms driving fluvial POC cycling at a global scale (Aufdenkampe et al., 2011; Butman et al., 2015; Galy et al., 2015; Hage et al., 2020; Hemingway et al., 2019; Hilton et al., 2011; Hilton & West, 2020; Mayorga et al., 2005; McClelland et al., 2016; Menges et al., 2020; Raymond et al., 2013; Richey, 2004; Scheingross et al., 2019a; Torres et al., 2017; Tranvik et al., 2009). While long-term POC transport by rivers and delivery to the oceans is related to suspended sediment discharge, chapters 4 and 5 show that fluvial POC is composed of at least two major pools that differ in chemical stability at Earth's surface and thus have residence times that differ from clastic sediment. This suggests

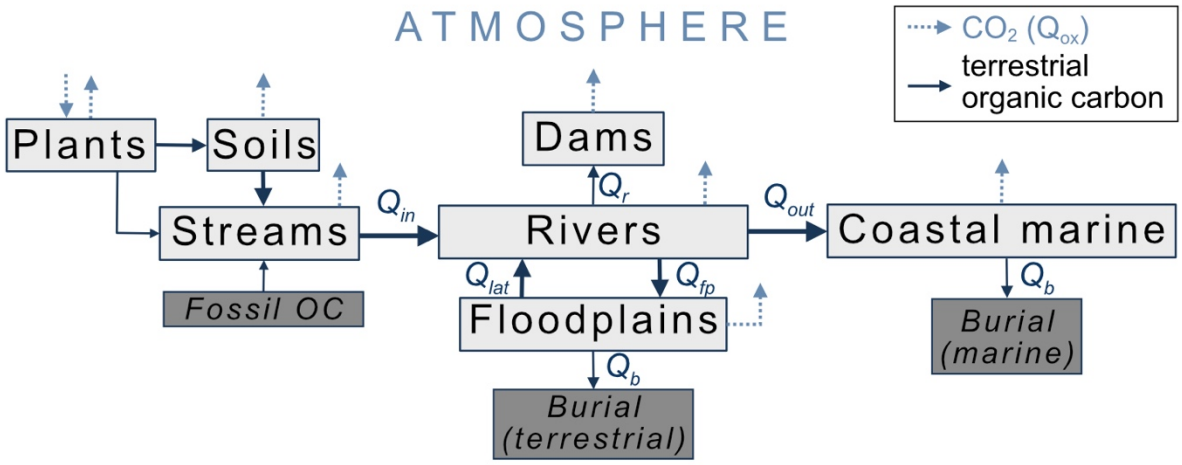

Figure 6.1. Fluvial carbon budget model. Conceptual model for organic carbon reservoirs (boxes) and fluxes (arrows) in a fluvial system, adapted from Richey (2004). Solid arrows represent fluxes of particulate organic carbon in its reduced form, while grey dashed arrows represent fluxes of oxidized organic carbon to the atmosphere in the form of CO_2. Q_{in} is the flux of organic carbon to a river system via tributaries, soil erosion, or runoff. Q_{lat} is the lateral input of organic carbon from lateral channel erosion. Q_{out} is the flux of organic carbon out of a river to a marine depositional setting. Q_r is the flux of organic carbon retained in reservoirs behind dams. Q_b is the flux of organic carbon buried and preserved in marine and terrestrial sediments.

that fluvial POC is decoupled from suspended sediment, and this decoupling needs to be factored into global fluvial carbon cycle models.

Here I present a simple, but novel framework for calculating the fluvial POC budget and therefore determining whether a river is a net atmospheric CO_2 source or sink (**Fig. 6.1**). Building on the work presented in Chapter 5, the POC budget (Q_{net}) of a river can be expressed simply as:

$$Q_{net} = Q_{in} + Q_{lat} - Q_{ox} - Q_{fp} - Q_r - (1 - Q_b) \qquad (6.1)$$

where Q_{in} is the annual POC flux into the river from headwater streams, Q_{lat} is the lateral POC influx from floodplain soil and vegetation eroded during lateral channel migration, Q_{ox} is the annual flux of CO_2 from the river due to POC oxidation during transit, Q_{fp} is the POC flux lost to floodplain storage via overbank flow, Q_r is the POC flux retained in reservoirs behind dams, and Q_b is the deltaic POC burial flux, all in units of kgC/yr. The term Q_b denotes the POC flux buried in near-shore depositional zones, and thus the term $(1 - Q_b)$ represents POC lost to across-shelf transport or to the open ocean where its fate is uncertain. The magnitude of Q_{net} determines the potential for rivers to contribute to long-term POC burial, where rivers with a larger Q_{net} have greater potential for transferring biospheric POC to geologic storage sites.

The fluvial carbon budget model presented in equation (6.1) may be used to estimate the net organic carbon budget of hundreds of rivers at a global scale. To implement such a model would require spatially-explicit global scale datasets providing key variables needed to parameterize equations (5.1), (5.2), (5.3) and (6.1). Recent work on fluvial POC composition and sediment routing has spawned global-scale data compilations (Galy et al., 2015; Hemingway et al., 2019; Marwick et al., 2015), carbon turnover times (Carvalhais et al., 2014), sediment fluxes over modern and geologic timescales (Covault et al., 2013; Peucker-Ehrenbrink, 2018), lateral channel migration rates (Rowland & Schwenk, 2019), and sediment burial efficiency in deltas (Nienhuis & Cohen, 2019). If successfully modeled, I would expect the results to reveal patterns in Q_{net} that are systematic with respect to latitude, climate, tectonic setting, or the degree of anthropogenic influence. Identifying and describing systematic responses of the fluvial POC budget to these controlling factors would advance our ability to model the global carbon cycle.

However, a global scale model with multiple loosely bound variables will undoubtedly yield large uncertainties in estimating Q_{net}. For example, calculating Q_{in} relies on estimates of POC fluxes into large river systems from their headwaters, which are rarely reported. To

minimize uncertainty, POC fluxes could be predicted using the WBMsed model, which is a spatially and temporally explicit model for river suspended sediment fluxes (Cohen et al., 2013, 2014). A major advantage of WBMsed is its capability to simulate river sediment fluxes at daily temporal resolution and pixel-scale spatial resolution, allowing prediction of daily, monthly, and long-term (30+ yr) average sediment flux or yield at any point along a river channel at a global scale. Based on correlations derived by Galy et al. (2015), the fluxes of POC_{bio} (Q_{bio}) and POC_{petro} (Q_{petro}) can be estimated at any point along a large lowland river as:

$$Q_{bio} = 0.081 * {Y_{sed}}^{0.56} * A_{up} \quad (6.2)$$

$$Q_{petro} = 0.0007 * {Y_{sed}}^{1.11} * A_{up} \quad (6.3)$$

where Y_{sed} is the suspended sediment yield and A_{up} is the upstream drainage basin area. A confidence interval on this relationship would be needed to constrain uncertainty on Q_{in} values. WBMsed can also include overbank flow and sediment trapping behind dams, such that we can constrain Q_{fp} and Q_r with decadal-scale average values.

Constraining Q_{ox} requires information about the sediment transit time. At a global scale, sediment transit time may range from days in small mountain streams to 10^5 yr in large lowland rivers with vast floodplains. Work presented in Chapter 3 showed that sediment transit time can be roughly constrained using a steady-state, mass-balanced sediment budgeting approach, although many rivers are not in steady state with respect to sediment transport. Additionally, in Chapter 5, I showed that Q_{ox} is also dependent on the POC decomposition rate constant, k (**Fig. 6.2a**). In soils, k is regulated by the interplay of temperature, soil moisture, nitrogen availability, carbon supply, and microbial activity (Sierra et al., 2015), and thus will vary across spatial and

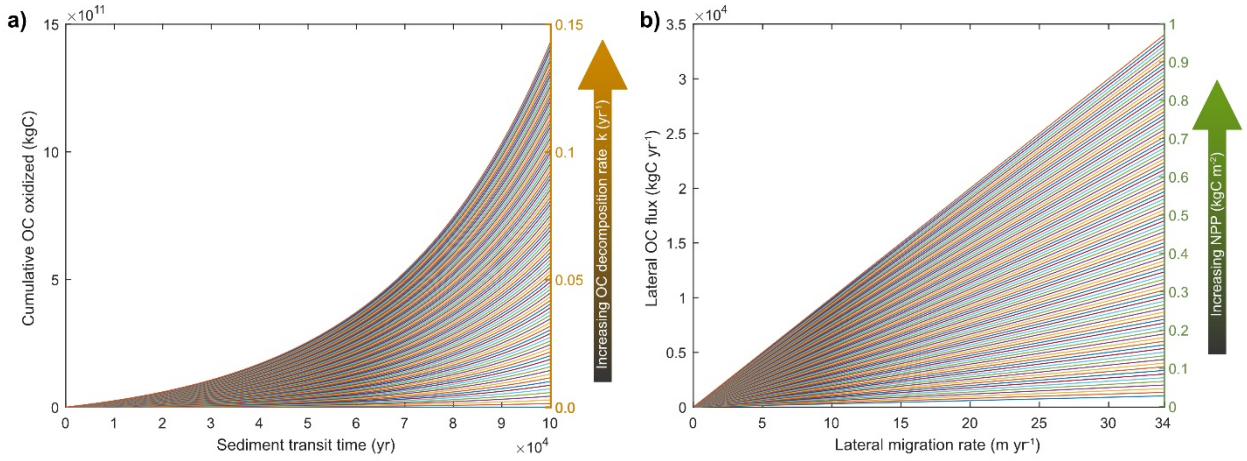

Figure 6.2. Effects of transit time, decomposition rate, and NPP on Q_{ox}. **a)** Cumulative organic carbon oxidation as a function of sediment transit time (ranging from 0 to 100,000 yr), where each line represents a different decomposition rate (k, right y-axis, ranging from 0 to 0.14 yr^{-1}). **b)** Relationship between lateral channel migration rate and lateral influx of organic carbon (OC), where each line represents a different value for net primary productivity (NPP), ranging from 0.03 to 1 kgC m^{-2} (right y-axis). Lateral migration rates represent the range of global measurements reported by Rowland and Schwenk (2019).

temporal scales. Globally averaged, ecosystem carbon turnover times have been estimated, such that a catchment-averaged k could be estimated for every large river on the planet (Carvalhais et al., 2014). Given the recent spawning of global datasets containing channel geometries and erosion rates (Rowland & Schwenk, 2019), as well as carbon turnover times (Carvalhais et al., 2014), it may be possible to estimate Q_{ox} for rivers at a global scale.

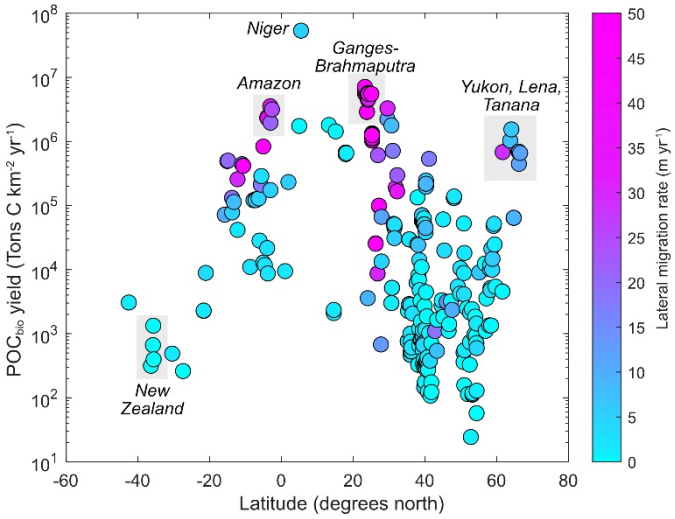

Figure 6.3. Global variability in river biospheric POC yield. Global relationship between latitude and biospheric POC (POC_{bio}) yield for rivers compiled in the global channel migration rate database (Rowland and Schwenk, 2019). Points are colored by lateral channel migration rate (blue = low, pink = high). The POC_{bio} yield was calculated using the relationship between sediment yield and POC_{bio} yield reported by Galy et al. (2015).

Q_{lat} may be key to balancing fluvial POC budgets, as shown in Chapter 5, but lateral POC input to a river also varies across climatic and geomorphic settings. Q_{lat} is a function of the spatially-averaged lateral channel migration rate, which can vary from 0 to >30 m/yr (Rowland & Schwenk, 2019), and floodplain net primary productivity (NPP), which ranges globally from 0.03 to 1 kgC/m^2 (Running et al., 2000) (**Fig. 6.2b**). Lateral channel migration rates scale with suspended sediment supply (Constantine et al., 2014), suggesting that rivers draining actively uplifting mountain ranges or glaciated catchments experience more channel-floodplain exchange. Globally, rivers with the highest channel migration rates and highest POC yields are located in the tropics and in the arctic (**Fig. 6.3**). In these locations, there are significant carbon stocks in the lowland flood basins that are susceptible to mobilization by river erosion. Using global datasets of lateral channel migration rates, channel length, and mean floodplain NPP, it is possible to calculate Q_{lat} at a global scale to evaluate how lateral migration influences fluvial POC cycling. However, significant variability in lateral migration rates and POC yield at every latitude suggests there will be large uncertainties on modeled POC budgets.

An important component of the fluvial source-to-sink system not addressed in Chapters 3-5 is long-term POC burial, Q_b. Terrestrial organic carbon burial in sediments is a mechanism for long-term CO_2 drawdown, but estimating this flux is challenging (Berner, 1982; Burdige, 2005; Schlünz & Schneider, 2000). POC can be buried in both terrestrial and marine depositional environments (**Fig. 6.1**). Subsidence in lowland basins can drive deep burial of floodplain POC, such that it can no longer be remobilized by active river systems. Unless the

river incises deeply during periods of base-level fall, buried sediment and POC will be sequestered and remain in the lithosphere over geologic timescales. POC that escapes inland burial is delivered to the coasts. Delta-shelf systems are known hotspots for burial of terrestrial organic carbon, but have also been described as organic carbon "incinerators" due to resuspension and the "priming effect" (Bianchi, 2011). To quantify marine POC burial, many studies focus on the global POC flux exported by rivers, but POC burial in delta-shelf systems is a complex function of sediment retention in the delta and shelf, the sedimentation rate, and the organic carbon preservation potential. Additionally, passive margins have wider continental shelves than active margins (~88 km vs. 31 km on average, respectively) (Harris & Macmillan-Lawler, 2016), which influences the degree of sediment preservation after export to marine settings (Bao et al., 2018). These mechanisms are becoming increasingly understood, such that the field is poised to re-evaluate the long-term terrestrial OC burial flux.

A final factor for consideration in the global fluvial POC budget is anthropogenic activity. Because the Rio Bermejo is a largely natural, undammed river with little land-use change, work in Chapters 3-5 do not address human impacts on fluvial sediment routing and organic carbon cycling. Anthropogenic activity has modified sediment fluxes in 73% of our planet's large rivers (by number) (Grill et al., 2019). Studies have proposed that river engineering impacts fluvial carbon cycling, but the net effects on the global carbon cycle remain unknown. Sediment trapping behind dams increases POC storage time in catchments and may enhance fluvial POC oxidation (e.g., Maavara et al., 2017). Estimated CO_2 emissions from active river channels and corridors (~1.8 GtC/yr) are currently estimated to be two times the total OC export to the oceans (~0.9 Gt/yr) (Aufdenkampe et al., 2011; Battin et al., 2008; Raymond et al., 2013), and OC oxidation may be enhanced by OC degradation in man-made reservoirs. Reduced lateral channel mobility via channel engineering may curtail POC inputs to river systems and limit POC spillover onto floodplains, reducing terrestrial organic carbon burial. Bank stabilization would also significantly reduce the large flux of modern biomass traveling near the river bed, as described in Chapter 4, which is derived largely from direct lateral input of leaf litter and floodplain vegetation. Human-induced soil erosion drives increased POC delivery to rivers, typically through deforestation and agricultural activity that destabilizes soil organic carbon stocks. Often, this POC is aged, suggesting that human activity is depleting the soil carbon reservoir and introducing aged carbon into the modern carbon cycle (Butman et al., 2015). To truly model the fluvial POC cycle at a global scale, human factors cannot be ignored.

The ultimate goal of modeling the fluvial organic carbon budget is to determine whether fluvial sediment routing across the landscape results in more long-term POC oxidation or more long-term burial. By estimating this at a global scale, we can test hypotheses about the factors that regulate the fluvial organic carbon cycle. Climate conditions (e.g., temperature, precipitation, net primary productivity, flood frequency) may regulate the amount and the decomposition rate of POC eroded into river channels or deposited onto floodplains. The tectonic setting (e.g., uplift-driven erosion, inland subsidence, channel slope reduction) may regulate the sediment transit time, the potential for long-term burial in inland basins, and amount of channel floodplain exchange. Anthropogenic impacts, including sediment trapping behind dams and reduced lateral channel mobility via river bank stabilization may enhance fluvial POC oxidation, and soil erosion may drive increased fluxes of aged, and degraded POC to marine basins. Only by analyzing fluvial carbon budgets at a global scale can we understand the cumulative influence of these major factors on the fluvial organic carbon budget.

In conclusion, the results of this dissertation contributed 1) a novel method for estimating river sediment transit time, 2) new observations on the chemical transformation, aging, and hydrodynamic sorting of organic carbon during source-to-sink transit, and 3) conceptual models for quantifying the fluvial organic carbon budget. By integrating geomorphic and biogeochemical processes, this dissertation filled major knowledge gaps in our understanding of the mechanisms driving sediment and organic carbon transfer across the landscape. The novel combination of geochemical tools with geomorphic and hydrologic measurements allowed for the development of mechanistic theories and conceptual models that were not previously constrained. Through these studies of the Rio Bermejo as a model lowland alluvial river, I developed a detailed understanding of how geomorphology and hydrodynamic processes influence the composition, age, and fluxes of POC during source-to-sink fluvial transit. These findings leave us poised to scale-up these conceptual models and test their practicability at a global scale.

BIBLIOGRAPHY

Abril, G., Martinez, J. M., Artigas, L. F., Moreira-Turcq, P., Benedetti, M. F., Vidal, L., et al. (2014). Amazon River carbon dioxide outgassing fuelled by wetlands. *Nature*, *505*(7483), 395–398. https://doi.org/10.1038/nature12797

Allen, P. A. (2008). From landscapes into geological history. *Nature*, *451*(17), 274–276. https://doi.org/10.1038/nature06586

Amsler, M. L., & Drago, E. C. (2009). A review of the suspended sediment budget at the confluence of the Paraná and Paraguay Rivers. *Hydrological Processes*, *23*(22), 3230–3235. https://doi.org/10.1002/hyp.7390

Armitage, J. J., Duller, R. A., Whittaker, A. C., & Allen, P. A. (2011). Transformation of tectonic and climatic signals from source to sedimentary archive. *Nature Geoscience*, *4*(4), 231–235. https://doi.org/10.1038/ngeo1087

Aufdenkampe, A. K., Mayorga, E., Raymond, P. A., Melack, J. M., Doney, S. C., Alin, S. R., et al. (2011). Riverine coupling of biogeochemical cycles between land, oceans, and atmosphere. *Frontiers in Ecology and the Environment*, *9*(1), 53–60. https://doi.org/10.1890/100014

Bao, R., van der Voort, T. S., Zhao, M., Guo, X., Montluçon, D. B., McIntyre, C., & Eglinton, T. I. (2018). Influence of Hydrodynamic Processes on the Fate of Sedimentary Organic Matter on Continental Margins. *Global Biogeochemical Cycles*, *32*(9), 1420–1432. https://doi.org/10.1029/2018GB005921

Bao, R., Uchida, M., Zhao, M., Haghipour, N., Montlucon, D., McNichol, A., et al. (2018). Organic Carbon Aging During Across-Shelf Transport. *Geophysical Research Letters*, *45*(16), 8425–8434. https://doi.org/10.1029/2018GL078904

Barber, A., Brandes, J., Leri, A., Lalonde, K., Balind, K., Wirick, S., et al. (2017). Preservation of organic matter in marine sediments by inner-sphere interactions with reactive iron. *Scientific Reports*, *7*(1). https://doi.org/10.1038/s41598-017-00494-0

Baronas, J. J., Stevenson, E. I., Hackney, C. R., Darby, S. E., Bickle, M. J., Hilton, R. G., et al. (2020). Integrating suspended sediment flux in large alluvial river channels: Application of a synoptic Rouse-based model to the Irrawaddy and Salween rivers. *Journal of Geophysical Research: Earth Surface*, 1–21. https://doi.org/10.1029/2020jf005554

Battin, T. J., Kaplan, L. A., Findlay, S., Hopkinson, C. S., Marti, E., Packman, A. I., et al. (2008). Biophysical controls on organic carbon fluxes in fluvial networks. *Nature Geoscience*, *1*, 95–101. https://doi.org/10.1038/ngeo602

Bauer, J. E., Cai, W. J., Raymond, P. A., Bianchi, T. S., Hopkinson, C. S., & Regnier, P. A. G. (2013). The changing carbon cycle of the coastal ocean. *Nature*, *504*(7478), 61–70. https://doi.org/10.1038/nature12857

Beer, J., Andree, M., Oeschger, H., Siegenthaler, U., Bonani, G., Hofmann, H., et al. (1984). The camp century 10Be record: Implications for long-term variations of the geomagnetic dipole moment. *Nuclear Inst. and Methods in Physics Research, B*, *5*(2), 380–384. https://doi.org/10.1016/0168-583X(84)90545-7

Belmont, P., Willenbring, J. K., Schottler, S. P., Marquard, J., Kumarasamy, K., & Hemmis, J. M. (2014). Toward generalizable sediment fingerprinting with tracers that are conservative and nonconservative over sediment routing timescales. *Journal of Soils and Sediments*,

14(8), 1479–1492. https://doi.org/10.1007/s11368-014-0913-5

Berhe, A. A., Harden, J. W., Torn, M. S., Kleber, M., Burton, S. D., & Harte, J. (2012). Persistence of soil organic matter in eroding versus depositional landform positions. *Journal of Geophysical Research: Biogeosciences*, *117*(2), n/a-n/a. https://doi.org/10.1029/2011JG001790

Berner, R. A. (1982). Burial of organic carbon and pyrite sulfur in the modern ocean: its geochemical and environmental significance. *American Journal of Science*, *282*, 451–473.

Berner, R. A. (1997). The rise of plants and their effect on weathering and atmospheric CO2. *Science*, *276*, 544–546.

Berner, R. A., & Caldeira, K. (1997). The need for mass balance and feedback in the geochemical carbon cycle. *GEOLOGY*, 955–956. Retrieved from https://pubs.geoscienceworld.org/gsa/geology/article-pdf/25/10/955/3517099/i0091-7613-25-10-955.pdf

Bianchi, T. S. (2011). The role of terrestrially derived organic carbon in the coastal ocean: A changing paradigm and the priming effect. *Proceedings of the National Academy of Sciences of the United States of America*. https://doi.org/10.1073/pnas.1017982108

Bianchi, T. S., Galler, J. J., & Allison, M. A. (2007). Hydrodynamic sorting and transport of terrestrially derived organic carbon in sediments of the Mississippi and Atchafalaya Rivers. *Estuarine, Coastal and Shelf Science*, *73*, 211–222.

Bianchi, T. S., Garcia-Tigreros, F., Yvon-Lewis, S. A., Shields, M., Mills, H. J., Butman, D., et al. (2013). Enhanced transfer of terrestrially derived carbon to the atmosphere in a flooding event. *Geophysical Research Letters*, *40*(1), 116–122. https://doi.org/10.1029/2012GL054145

Bianchi, T. S., Cui, X., Blair, N. E., Burdige, D. J., Eglinton, T. I., & Galy, V. (2018). Centers of organic carbon burial and oxidation at the land-ocean interface. *Organic Geochemistry*, *115*, 138–155. https://doi.org/10.1016/J.ORGGEOCHEM.2017.09.008

Blair, N., & Aller, R. (2012). The fate of terrestrial organic carbon in the marine environment. *Annual Review of Marine Science*, *4*(1), 401–423. https://doi.org/10.1146/annurev-marine-120709-142717

von Blanckenburg, F., Bouchez, J., & Wittmann, H. (2012). Earth surface erosion and weathering from the 10Be (meteoric)/ 9Be ratio. *Earth and Planetary Science Letters*, *351–352*, 295–305. https://doi.org/10.1016/j.epsl.2012.07.022

Blattmann, T. M., Liu, Z., Zhang, Y., Zhao, Y., Haghipour, N., Montluçon, D. B., et al. (2019). Mineralogical control on the fate of continentally derived organic matter in the ocean. *Science*, *366*(6466), 742–745. https://doi.org/10.1126/science.aax5345

Blom, A., & Parker, G. (2004). Vertical sorting and the morphodynamics of bed form-dominated rivers: A modeling framework. *Journal of Geophysical Research: Earth Surface*, *109*(F2), n/a-n/a. https://doi.org/10.1029/2003JF000069

Bolin, B., & Rodhe, H. (1973). A note on the concepts of age distribution and transit time in natural reservoirs. *Tellus*, *25*(1), 58–62. https://doi.org/10.3402/tellusa.v25i1.9644

Bookhagen, B., & Strecker, M. R. (2012). Spatiotemporal trends in erosion rates across a pronounced rainfall gradient: Examples from the southern Central Andes. *Earth and Planetary Science Letters*, *327–328*, 97–110. https://doi.org/10.1016/j.epsl.2012.02.005

Bouchez, J., Beyssac, O., Galy, V., Gaillardet, J., & France-Lanord, C. (2010). Oxidation of

petrogenic organic carbon in the Amazon floodplain as a source of atmospheric CO2. *Geology*, *38*(3), 255–258. https://doi.org/10.1130/G30608>

Bouchez, J., Gaillardet, J., France-Lanord, C., Maurice, L., & Dutra-Maia, P. (2011). Grain size control of river suspended sediment geochemistry: Clues from Amazon River depth profiles. *Geochemistry, Geophysics, Geosystems*, *12*(3), 1–24. https://doi.org/10.1029/2010GC003380

Bouchez, J., Lupker, M., Gaillardet, J., France-Lanord, C., & Maurice, L. (2011). How important is it to integrate riverine suspended sediment chemical composition with depth? Clues from Amazon River depth-profiles. *Geochimica et Cosmochimica Acta*, *75*(22), 6955–6970. https://doi.org/10.1016/j.gca.2011.08.038

Bouchez, J., Galy, V., Hilton, R. G., Gaillardet, J., Moreira-Turcq, P., Pérez, M. A., et al. (2014). Source, transport and fluxes of Amazon River particulate organic carbon: Insights from river sediment depth-profiles. *Geochimica et Cosmochimica Acta*, *133*, 280–298. https://doi.org/10.1016/j.gca.2014.02.032

Bowling, D. R., Pataki, D. E., & Randerson, J. T. (2008, April 1). Carbon isotopes in terrestrial ecosystem pools and CO2 fluxes. *New Phytologist*. John Wiley & Sons, Ltd. https://doi.org/10.1111/j.1469-8137.2007.02342.x

Bradley, D. N., & Tucker, G. E. (2013). The storage time, age, and erosion hazard of laterally accreted sediment on the floodplain of a simulated meandering river. *Journal of Geophysical Research: Earth Surface*, *118*(3), 1308–1319. https://doi.org/10.1002/jgrf.20083

Bröder, L., Tesi, T., Salvadó, J. A., Semiletov, I. P., Dudarev, O. V, & Gustafsson, O. (2016). Fate of terrigenous organic matter across the Laptev Sea from the mouth of the Lena River to the deep sea of the Arctic interior. *Biogeosciences*, *13*(17), 5003–5019. https://doi.org/10.5194/bg-13-5003-2016

Brook, E. (2008). Windows on the greenhouse. *Nature*, *453*(7193), 291–292. https://doi.org/10.1038/453291a

Burdige, D. J. (2005). Burial of terrestrial organic matter in marine sediments: A re-assessment. *Global Biogeochemical Cycles*, *19*(4), 1–7. https://doi.org/10.1029/2004GB002368

Burdige, D. J. (2007). Preservation of organic matter in marine sediments: Controls, mechanisms, and an imbalance in sediment organic carbon budgets? *Chemical Reviews*, *107*(2), 467–485. https://doi.org/10.1021/cr050347q

Bush, R. T., & McInerney, F. A. (2013). Leaf wax n-alkane distributions in and across modern plants: Implications for paleoecology and chemotaxonomy. *Geochimica et Cosmochimica Acta*, *117*, 161–179. https://doi.org/10.1016/j.gca.2013.04.016

Butman, D. E., Wilson, H. F., Barnes, R. T., Xenopoulos, M. a., & Raymond, P. a. (2015). Increased mobilization of aged carbon to rivers by human disturbance. *Nature Geoscience*, *8*(February), 112–116. https://doi.org/10.1038/NGEO2322

Calmels, D., Gaillardet, J., Brenot, A., & France-Lanord, C. (2007). Sustained sulfide oxidation by physical erosion processes in the Mackenzie River basin: Climatic perspectives. *Geology*, *35*(11), 1003–1006. https://doi.org/10.1130/G24132A.1

Carvalhais, N., Forkel, M., Khomik, M., Bellarby, J., Jung, M., Migliavacca, M., et al. (2014). Global covariation of carbon turnover times with climate in terrestrial ecosystems. *Nature*, *514*(7521), 213–217. https://doi.org/10.1038/nature13731

Chanton, J., Zhao, T., Rosenheim, B. E., Joye, S., Bosman, S., Brunner, C., et al. (2015). Using natural abundance radiocarbon to trace the flux of petrocarbon to the seafloor following the deepwater horizon oil spill. *Environmental Science and Technology*, *49*(2), 847–854. https://doi.org/10.1021/es5046524

Chmeleff, J., von Blanckenburg, F., Kossert, K., & Jakob, D. (2010). Determination of the10Be half-life by multicollector ICP-MS and liquid scintillation counting. *Nuclear Instruments and Methods in Physics Research, Section B: Beam Interactions with Materials and Atoms*, *268*(2), 192–199. https://doi.org/10.1016/j.nimb.2009.09.012

Clark, K. E., Hilton, R. G., West, A. J., Robles Caceres, A., Gröcke, D. R., Marthews, T. R., et al. (2017). Erosion of organic carbon from the Andes and its effects on ecosystem carbon dioxide balance. *Journal of Geophysical Research: Biogeosciences*, *122*(3), 449–469. https://doi.org/10.1002/2016JG003615

Cohen, A., McGlue, M. M., Ellis, G. S., Zani, H., Swarzenski, P. W., Assine, M. L., & Silva, A. (2015). Lake formation, characteristics, and evolution in retroarc deposystems: A synthesis of the modern Andean orogen and its associated basins, *1212*(16), 309–335. https://doi.org/10.1130/2015.1212(16)

Cohen, S., Kettner, A. J., Syvitski, J. P. M., & Fekete, B. M. (2013). WBMsed, a distributed global-scale riverine sediment flux model: Model description and validation. *Computers and Geosciences*, *53*, 80–93. https://doi.org/10.1016/j.cageo.2011.08.011

Cohen, S., Kettner, A. J., & Syvitski, J. P. M. (2014). Global suspended sediment and water discharge dynamics between 1960 and 2010: Continental trends and intra-basin sensitivity. *Global and Planetary Change*, *115*, 44–58. https://doi.org/10.1016/j.gloplacha.2014.01.011

Cole, J. J., & Caraco, N. F. (2001). Carbon in catchments: Connecting terrestrial carbon losses with aquatic metabolism. In *Marine and Freshwater Research* (Vol. 52, pp. 101–110). https://doi.org/10.1071/MF00084

Constantine, J. A., Dunne, T., Ahmed, J., Legleiter, C., & Lazarus, E. D. (2014). Sediment supply as a driver of river evolution in the Amazon Basin. *Nature Geoscience*, *7*, 899–903. https://doi.org/10.1038/NGEO2282

Coplen, T. B. (1996). New guidelines for reporting stable hydrogen, carbon, and oxygen isotope-ratio data. *Geochimica et Cosmochimica Acta*, *60*(17), 3359–3360. https://doi.org/10.1016/0016-7037(96)00263-3

Covault, J. A., Craddock, W. H., Romans, B. W., Fildani, A., & Gosai, M. (2013). Spatial and temporal variations in landscape evolution: Historic and longer-term sediment flux through global catchments. *Journal of Geology*, *121*(1), 35–56. https://doi.org/10.1086/668680

Craig, H. (1953). The geochemistry of the stable carbon isotopes. *Geochimica et Cosmochimica Acta*, *3*(2–3), 53–92. https://doi.org/10.1016/0016-7037(53)90001-5

Czuba, J. A., Foufoula-Georgiou, E., Clark, M. P., Nijssen, B., Lundquist, J. D., Kavetski, D., et al. (2015). Dynamic connectivity in a fluvial network for identifying hotspots of geomorphic change. *Water Resources Research*, *51*(3), 2498–2514. https://doi.org/10.1002/2015WR017200.A

D'Elia, A. H., Liles, G. C., Viers, J. H., & Smart, D. R. (2017). Deep carbon storage potential of buried floodplain soils. *Scientific Reports*, *7*(1). https://doi.org/10.1038/s41598-017-06494-4

Dade, W. B., & Friend, P. F. (1998). Grain-size, sediment-transport regime, and channel slope in alluvial rivers. *Journal of Geology*, *106*(6), 661–675. https://doi.org/10.1086/516052

Degens, E. T. (1969). Biogeochemistry of Stable Carbon Isotopes. In *Organic Geochemistry* (pp. 304–329). https://doi.org/10.1007/978-3-642-87734-6_14

Deines, P. (1980). THE ISOTOPIC COMPOSITION OF REDUCED ORGANIC CARBON. In P. Fritz & J. C. Fontes (Eds.), *andbook of Environmental Isotope Geochemistry* (pp. 329–406). New York: Elsevier. https://doi.org/10.1016/b978-0-444-41780-0.50015-8

Depaolo, D. J., Maher, K., & Christensen, J. N. (2006). Sediment transport time measured with U-Series isotopes: Results from ODP North Atlantic Drill Site 984 Publication Date. Retrieved from https://escholarship.org/uc/item/0cg176qg

Depetris, P. J., & Cascante, E. (1985). Carbon transport in the Parana River. In *SCOPE/UNEP Sonderband* (pp. 299–304).

Dewald, A., Heinze, S., Jolie, J., Zilges, A., Dunai, T., Rethemeyer, J., et al. (2013). CologneAMS, a dedicated center for accelerator mass spectrometry in Germany. In *Nuclear Instruments and Methods in Physics Research, Section B: Beam Interactions with Materials and Atoms* (Vol. 294, pp. 18–23). https://doi.org/10.1016/j.nimb.2012.04.030

Dietrich, W. E. (1982). Settling velocity of natural particles. *Water Resources Research*, *18*(6), 1615–1626.

Dietrich, W. E., & et al. (2003). Geomorphic transport laws for predicting the form and evolution of landscapes. *Prediction in Geomorphology, Geophysical Monographs*, *135*, 103–132.

Dietrich, W. E., Dunne, T., Humphrey, N. F., & Reid, L. M. (1982). Construction of sediment budgets for drainage basins. *Workshop on Sediment Budgets and Routing in Forested Drainage Basins: Proc.*, 5–23. Retrieved from https://www.fs.fed.us/psw/publications/reid/Reid82a.pdf

Dixon, J. L., Chadwick, O. A., & Pavich, M. J. (2018). Climatically controlled delivery and retention of meteoric 10Be in soils. *Geology*, *46*(10), 899–902. https://doi.org/10.1130/G45176.1

Dogliotti, A. I., Ruddick, K., & Guerrero, R. (2016). Seasonal and inter-annual turbidity variability in the Río de la Plata from 15 years of MODIS: El Niño dilution effect. *Estuarine, Coastal and Shelf Science*, *182*, 27–39. https://doi.org/10.1016/j.ecss.2016.09.013

Dosseto, A, Bourdon, B., Gaillardet, J., Allègre, C. J., & Filizola, N. (2006). Time scale and conditions of weathering under tropical climate: Study of the Amazon basin with U-series. *Geochimica et Cosmochimica Acta*, *70*(1), 71–89. https://doi.org/10.1016/j.gca.2005.06.033

Dosseto, Anthony, Bourdon, B., & Turner, S. P. (2008). Uranium-series isotopes in river materials: Insights into the timescales of erosion and sediment transport. *Earth and Planetary Science Letters*, *265*(1–2), 1–17. https://doi.org/10.1016/j.epsl.2007.10.023

Douglas, P. M. J., Pagani, M., Eglinton, T. I., Brenner, M., Hodell, D. A., Curtis, J. H., et al. (2014). Pre-aged plant waxes in tropical lake sediments and their influence on the chronology of molecular paleoclimate proxy records. *Geochimica et Cosmochimica Acta*, *141*, 346–364. https://doi.org/10.1016/j.gca.2014.06.030

Drenzek, N. J., Montluçon, D. B., Yunker, M. B., Macdonald, R. W., & Eglinton, T. I. (2007).

Constraints on the origin of sedimentary organic carbon in the Beaufort Sea from coupled molecular 13C and 14C measurements. *Marine Chemistry*, *103*(1–2), 146–162. https://doi.org/10.1016/j.marchem.2006.06.017

Drenzek, N. J., Hughen, K. A., Montlucecon, D. B., Southon, J. R., dos Santos, G. M., Druffel, E. R. M., et al. (2009). A new look at old carbon in active margin sediments. *Geology*, *37*(3), 239–242. https://doi.org/10.1130/G25351A.1

Dunne, T, & Aalto, R. E. (2013). Large River Floodplains. In J. Shroder (Ed.), *Treatise on Geomorphology* (Volume 9, Vol. 9, pp. 645–678). San Diego, CA: Academic Press. https://doi.org/10.1016/B978-0-12-374739-6.00258-X

Dunne, Thomas, Mertes, L. A. K., Meade, R. H., Richey, J. E., & Forsberg, B. R. (1998). Exchanges of sediment between the flood plain and channel of the Amazon River in Brazil. *Bulletin of the Geological Society of America*, *110*(4), 450–467. https://doi.org/10.1130/0016-7606(1998)110<0450:EOSBTF>2.3.CO;2

Eglinton, T. I., Aluwihare, L., Bauer, J. E., Druffel, E. R. M., & McNichol, A. P. (1996). Gas chromatographic isolation of individual compounds from complex matrices for radiocarbon dating. *Analytical Chemistry*, *68*(5), 904–912. https://doi.org/10.1016/j.cognition.2008.05.007

Eglinton, T. I., Benitez-nelson, B. C., Pearson, A., Mcnichol, A. P., Bauer, J. E., & Druffel, E. R. M. (1997). Variability in Radiocarbon Ages of Individual Organic Compounds from Marine Sediments Published by : American Association for the Advancement of Science Stable URL : http://www.jstor.org/stable/2893122. *Science*, *277*, 796–799.

Engelund, F., & Hansen, E. (1967). *A monograph on sediment transport in alluvial streams*. *Technical University of Denmark 0stervoldgade 10, Copenhagen K.* TEKNISKFORLAG Skelbrekgade 4 Copenhagen V, Denmark. Retrieved from https://repository.tudelft.nl/islandora/object/uuid%3A81101b08-04b5-4082-9121-861949c336c9

Everitt, B. L. (1968). Use of the Cottonwood in an investigation of the recent history of a flood plain. *American Journal of Science*, *266*, 417–439.

Falkowski, P. G., & Godfrey, L. V. (2008). Electrons, life and the evolution of Earth's oxygen cycle. In *Philosophical Transactions of the Royal Society B: Biological Sciences* (Vol. 363, pp. 2705–2716). https://doi.org/10.1098/rstb.2008.0054

Feakins, S. J., Wu, M. S., Ponton, C., Galy, V., & West, A. J. (2018). Dual isotope evidence for sedimentary integration of plant wax biomarkers across an Andes-Amazon elevation transect. *Geochimica et Cosmochimica Acta*, *242*, 64–81. https://doi.org/10.1016/j.gca.2018.09.007

Feng, X., Benitez-Nelson, B. C., Montluçon, D. B., Prahl, F. G., McNichol, A. P., Xu, L., et al. (2013). 14C and 13C characteristics of higher plant biomarkers in Washington margin surface sediments. *Geochimica et Cosmochimica Acta*, *105*, 14–30. https://doi.org/10.1016/j.gca.2012.11.034

Feng, X., Vonk, J. E., van Dongen, B. E., Gustafsson, O., Semiletov, I. P., Dudarev, O. V, et al. (2013). Differential mobilization of terrestrial carbon pools in Eurasian Arctic river basins. *Proceedings of the National Academy of Sciences*, *110*(35), 14168–14173. https://doi.org/10.1073/pnas.1307031110

Feng, X., Feakins, S. J., Liu, Z., Ponton, C., Wang, R. Z., Karkabi, E., et al. (2016). Source to sink: Evolution of lignin composition in the Madre de Dios River system with connection

to the Amazon basin and offshore. *Journal of Geophysical Research G: Biogeosciences*, *121*(5), 1316–1338. https://doi.org/10.1002/2016JG003323

Fisher, G. B., Bookhagen, B., & Amos, C. B. (2013). Channel planform geometry and slopes from freely available high-spatial resolution imagery and DEM fusion: Implications for channel width scalings, erosion proxies, and fluvial signatures in tectonically active landscapes. *Geomorphology*, *194*, 46–56. https://doi.org/10.1016/j.geomorph.2013.04.011

Foster, G. L., Royer, D. L., & Lunt, D. J. (2017). Future climate forcing potentially without precedent in the last 420 million years. *Nature Communications*, *8*. https://doi.org/10.1038/ncomms14845

French, K. L., Hein, C. J., Haghipour, N., Wacker, L., Kudrass, H. R., Eglinton, T. I., & Galy, V. (2018). Millennial soil retention of terrestrial organic matter deposited in the Bengal Fan. *Scientific Reports*, *8*(1), 11997. https://doi.org/10.1038/s41598-018-30091-8

Friedlingstein, P., Jones, M. W., O'Sullivan, M., Andrew, R. M., Hauck, J., Peters, G. P., et al. (2019). Global carbon budget 2019. *Earth System Science Data*, *11*(4), 1783–1838. https://doi.org/10.5194/essd-11-1783-2019

Frings, R. M. (2008). Downstream fining in large sand-bed rivers. *Earth-Science Reviews*, *87*(1–2), 39–60. https://doi.org/10.1016/j.earscirev.2007.10.001

Galvez, M. E., Fischer, W. W., Jaccard, S. L., & Eglinton, T. I. (2020). Materials and pathways of the organic carbon cycle through time. *Nature Geoscience*. https://doi.org/10.1038/s41561-020-0563-8

Galy, V., & Eglinton, T. (2011). Protracted storage of biospheric carbon in the Ganges–Brahmaputra basin. *Nature Geoscience*, *4*(12), 843–847. https://doi.org/10.1038/ngeo1293

Galy, V., Bouchez, J., & France-Lanord, C. (2007). Determination of Total Organic Carbon Content and δ 13 C in Carbonate-Rich Detrital Sediments. *Geostandards and Geoanalytical Research*, *31*(3), 199–207.

Galy, V., France-Lanord, C., & Lartiges, B. (2008). Loading and fate of particulate organic carbon from the Himalaya to the Ganga-Brahmaputra delta. *Geochimica et Cosmochimica Acta*, *72*(7), 1767–1787. https://doi.org/10.1016/j.gca.2008.01.027

Galy, V., Eglinton, T., France-Lanord, C., & Sylva, S. (2011). The provenance of vegetation and environmental signatures encoded in vascular plant biomarkers carried by the Ganges-Brahmaputra rivers. *Earth and Planetary Science Letters*, *304*(1–2), 1–12. https://doi.org/10.1016/j.epsl.2011.02.003

Galy, V., Peucker-Ehrenbrink, B., & Eglinton, T. (2015). Global carbon export from the terrestrial biosphere controlled by erosion. *Nature*, *521*(7551), 204–207. https://doi.org/10.1038/nature14400

Ganti, V., Straub, K. M., Foufoula-Georgiou, E., & Paola, C. (2011). Space-time dynamics of depositional systems: Experimental evidence and theoretical modeling of heavy-tailed statistics. *Journal of Geophysical Research: Earth Surface*, *116*(2), 1–17. https://doi.org/10.1029/2010JF001893

Ganti, V., Chu, Z., Lamb, M. P., Nittrouer, J. A., & Parker, G. (2014). Testing morphodynamic controls on the location and frequency of river avulsions on fans versus deltas: Huanghe (Yellow River), China. *Geophysical Research Letters*, *41*(22), 7882–7890. https://doi.org/10.1002/2014GL061918

Gasparini, N. M., Tucker, G. E., & Bras, R. L. (1999). Downstream fining through selective particle sorting in an equilibrium drainage network. *Geology*, *27*(12), 1079–1082. https://doi.org/10.1130/0091-7613(1999)027<1079:DFTSPS>2.3.CO;2

Godwin, H. (1962). Half-life of radiocarbon. *Nature*, *195*(4845), 984. https://doi.org/10.1038/195984a0

Goni, M. A., Ruttenberg, K. C., & Eglinton, T. I. (1997). Sources and contribution of terrigenous organic carbon to surface sediments in the Gulf of Mexico. *Nature*, *389*, 275–278.

Gordon, E. S., & Goñi, M. A. (2004). Controls on the distribution and accumulation of terrigenous organic matter in sediments from the Mississippi and Atchafalaya river margin. In *Marine Chemistry* (Vol. 92, pp. 331–352). https://doi.org/10.1016/j.marchem.2004.06.035

Gottesfeld, A. S., & Gottesfeld, L. M. (1990). Floodplain dynamics of a wandering river, dendrochronology of the Morice River, British Columbia, Canada. *Geomorphology*, *3*(2), 159–179. https://doi.org/10.1016/0169-555X(90)90043-P

Graly, J. A., Bierman, P. R., Reusser, L. J., & Pavich, M. J. (2010). Meteoric 10Be in soil profiles - A global meta-analysis. *Geochimica et Cosmochimica Acta*, *74*(23), 6814–6829. https://doi.org/10.1016/j.gca.2010.08.036

Graly, J. A., Reusser, L. J., & Bierman, P. R. (2011). Short and long-term delivery rates of meteoric 10 Be to terrestrial soils. *Earth and Planetary Science Letters*, *302*, 329–336. https://doi.org/10.1016/j.epsl.2010.12.020

Granet, M., Chabaux, F., Stille, P., France-Lanord, C., & Pelt, E. (2007). Time-scales of sedimentary transfer and weathering processes from U-series nuclides: Clues from the Himalayan rivers. *Earth and Planetary Science Letters*, *261*(3–4), 389–406. https://doi.org/10.1016/j.epsl.2007.07.012

Granet, M., Chabaux, F., Stille, P., Dosseto, A., France-Lanord, C., & Blaes, E. (2010). U-series disequilibria in suspended river sediments and implication for sediment transfer time in alluvial plains: The case of the Himalayan rivers. *Geochimica et Cosmochimica Acta*, *74*(10), 2851–2865. https://doi.org/10.1016/j.gca.2010.02.016

Gray, H. J., Tucker, G. E., Mahan, S. A., McGuire, C., & Rhodes, E. J. (2017). On extracting sediment transport information from measurements of luminescence in river sediment. *Journal of Geophysical Research: Earth Surface*, *122*(3), 654–677. https://doi.org/10.1002/2016JF003858

Gray, H. J., Tucker, G. E., & Mahan, S. A. (2018). Application of a Luminescence-Based Sediment Transport Model. *Geophysical Research Letters*, *45*, 6071–6080. https://doi.org/10.1029/2018GL078210

Grill, G., Lehner, B., Thieme, M., Geenen, B., Tickner, D., Antonelli, F., et al. (2019). Mapping the world's free-flowing rivers. *Nature*, *569*(7755), 215–221. https://doi.org/10.1038/s41586-019-1111-9

Hage, S., Galy, V., Cartigny, M. J. B., Acikalin, S., Clare, M. A., Grocke, D. R., et al. (2020). Efficient preservation of young terrestrial organic carbon in sandy turbidity-current deposits. *GEOLOGY*, *48*, 1–13. https://doi.org/10.1130/G47320.1

Haghipour, N., Ausin, B., Usman, M. O., Ishikawa, N., Wacker, L., Welte, C., et al. (2019). Compound-Specific Radiocarbon Analysis by Elemental Analyzer-Accelerator Mass Spectrometry: Precision and Limitations. *Analytical Chemistry*, *91*(3), 2042–2049.

https://doi.org/10.1021/acs.analchem.8b04491

Handley, H. K., Turner, S., Afonso, J. C., Dosseto, A., & Cohen, T. (2013). Sediment residence times constrained by uranium-series isotopes: A critical appraisal of the comminution approach. *Geochimica et Cosmochimica Acta*, *103*, 245–262. https://doi.org/10.1016/j.gca.2012.10.047

Harris, P. T., & Macmillan-Lawler, M. (2016). Global Overview of Continental Shelf Geomorphology Based on the SRTM30_ PLUS 30-Arc Second Database. In C. W. Finkl & C. Makowski (Eds.), *Seafloor Mapping along Continental Shelves: Research and Techniques for Visualizing Benthic Environments* (pp. 169–190). Springer International Publishing Switzerland. https://doi.org/10.1007/978-3-319-25121-9_7

Hartley, A. J., Weissmann, G. S., Bhattacharyya, P., Nichols, G. J., Scuderi, L. A., Davidson, S. K., et al. (2013). Soil Development on Modern Distributive Fluvial Systems: Preliminary Observations with Implications for Interpretation of Paleosols in the Rock Record. In *New Frontiers in Paleopedology and Terrestrial Paleoclimatology: Paleosols and Soil Surface Analog Systems* (pp. 149–158). https://doi.org/10.2110/sepmsp.104.10

Hayes, J M, Freeman, K. H., Popp, B. N., & Hoham, C. H. (1989). Compound - specific isotopic analyses : A novel tool for reconstruction of ancient biogeochemical processes. *Org . Geochem*, *16*(6), 111–1128. https://doi.org/10.1016/0146-6380(90)90147-R

Hayes, John M. (1983). Practice and principles of isotopic measurements in organic geochemistry. *Organic Geochemistry of Contemporaneous and Ancient Sediments*, *5*(August), e5. https://doi.org/10.2307/1938584

Hayes, John M. (2004). Isotopic order, biogeochemical processes, and earth history: Goldschmidt lecture, Davos, Switzerland, August 2002. *Geochimica et Cosmochimica Acta*, *68*(8), 1691–1700. https://doi.org/10.1016/j.gca.2003.10.023

Heckman, K., Lawrence, C. R., & Harden, J. W. (2018). A sequential selective dissolution method to quantify storage and stability of organic carbon associated with Al and Fe hydroxide phases. *Geoderma*, *312*, 24–35. https://doi.org/10.1016/j.geoderma.2017.09.043

Hedges, J. I., Ertel, J. R., Quay, P. D., Grootes, P. M., Richey, J. E., Devol, A. H., et al. (1986). Organic carbon-14 in the Amazon River system. *Science*, *231*(4742), 1129–1131. https://doi.org/10.1126/science.231.4742.1129

Heikkilä, U., & von Blanckenburg, F. (2015). *The global distribution of Holocene meteoric 10 Be fluxes from atmospheric models. Distribution maps for terrestrial Earth surface applications*. Potsdam, Germany. https://doi.org/10.5880/GFZ.3.4.2015.001.

Hein, C. J., Usman, M., Eglinton, T. I., Haghipour, N., & Galy, V. V. (2020). Millennial-scale hydroclimate control of tropical soil carbon storage. *Nature*, *581*(7806), 63–66. https://doi.org/10.1038/s41586-020-2233-9

Hemingway, J. D., Schefuß, E., Spencer, R. G. M., Dinga, B. J., Eglinton, T. I., McIntyre, C., & Galy, V. V. (2017). Hydrologic controls on seasonal and inter-annual variability of Congo River particulate organic matter source and reservoir age. *Chemical Geology*, *466*, 454–465. https://doi.org/10.1016/j.chemgeo.2017.06.034

Hemingway, J. D., Rothman, D. H., Grant, K. E., Rosengard, S. Z., Eglinton, T. I., Derry, L. A., & Galy, V. V. (2019). Mineral protection regulates long-term global preservation of natural organic carbon. *Nature*, *570*(7760), 228–231. https://doi.org/10.1038/s41586-019-1280-6

Herrmann, A. M., Ritz, K., Nunan, N., Clode, P. L., Pett-Ridge, J., Kilburn, M. R., et al. (2007). Nano-scale secondary ion mass spectrometry - A new analytical tool in biogeochemistry and soil ecology: A review article. *Soil Biology and Biochemistry*, *39*(8), 1835–1850. https://doi.org/10.1016/j.soilbio.2007.03.011

Hilton, R. G. (2017). Climate regulates the erosional carbon export from the terrestrial biosphere. *Geomorphology*, *277*, 118–132. https://doi.org/10.1016/j.geomorph.2016.03.028

Hilton, R. G., & West, A. J. (2020). Mountains, erosion and the carbon cycle. *Nature Reviews Earth & Environment*, *1*(6), 284–299. https://doi.org/10.1038/s43017-020-0058-6

Hilton, R. G., Galy, A., Hovius, N., Horng, M. J., & Chen, H. (2011). Efficient transport of fossil organic carbon to the ocean by steep mountain rivers: An orogenic carbon sequestration mechanism. *Geology*, *39*(1), 71–74. https://doi.org/10.1130/G31352.1

Hilton, R. G., Galy, A., Hovius, N., Kao, S. J., Horng, M. J., & Chen, H. (2012). Climatic and geomorphic controls on the erosion of terrestrial biomass from subtropical mountain forest. *Global Biogeochemical Cycles*, *26*(3), 1–12. https://doi.org/10.1029/2012GB004314

Hilton, R. G., Galy, V., Gaillardet, J., Dellinger, M., Bryant, C., O'Regan, M., et al. (2015). Erosion of organic carbon in the Arctic as a geological carbon dioxide sink. *Nature*, *524*(7563), 84–87. https://doi.org/10.1038/nature14653

Hirave, P., Wiesenberg, G. L. B., Birkholz, A., & Alewell, C. (2020). Understanding the effects of early degradation on isotopic tracers: Implications for sediment source attribution using compound-specific isotope analysis (CSIA). *Biogeosciences*, *17*(8), 2169–2180. https://doi.org/10.5194/bg-17-2169-2020

Horton, B., & DeCelles, P. (1997). The modern foreland basin system adjacent to the Central Andes. *Geology*, *25*(10).

Horton, B. K., & Decelles, P. G. (2001). Modern and ancient fluvial megafans in the foreland basin system of the Central Andes, Southern Bolivia: Implications for drainage network evolution if foldthrust belts. *Basin Research*, *13*(1), 43–63. https://doi.org/10.1046/j.1365-2117.2001.00137.x

IPCC. (2013). *Climate Change 2013: The Physical Science Basis. Contribution of Working Group I to the Fifth Assessment Report of the Intergovern- mental Panel on Climate Change*. (T. F. Stocker, D. Qin, G.-K. Plattner, M. Tignor, S. K. Allen, J. Boschung, et al., Eds.). Cambridge, United Kingdom and New York, NY, USA: Cambridge University Press. https://doi.org/10.1017/CBO9781107415324.Summary

Iriondo, Martin H. (2007). The Middle Paraná River. In M.H. Iriondo, J. C. Paggi, & M. J. Parma (Eds.), *The Middle Paraná River* (pp. 33–51). Springer Berlin Heidelberg. https://doi.org/10.1007/978-3-540-70624-3

Jelinski, N. A., Campforts, B., Willenbring, J. K., Schumacher, T. E., Li, S., Lobb, D. A., et al. (2019). Meteoric Beryllium-10 as a Tracer of Erosion Due to Postsettlement Land Use in West-Central Minnesota, USA. *Journal of Geophysical Research: Earth Surface*, *124*(4), 874–901. https://doi.org/10.1029/2018JF004720

Jerolmack, D. J., & Mohrig, D. (2007). Conditions for branching in depositional rives. *Geology*, *35*(5), 463–466. https://doi.org/10.1130/G23308A.1

Jerolmack, D. J., & Paola, C. (2010). Shredding of environmental signals by sediment transport. *Geophysical Research Letters*, *37*(19). https://doi.org/10.1029/2010GL044638

Johnson, K., Purvis, G., Lopez-Capel, E., Peacock, C., Gray, N., Wagner, T., et al. (2015). Towards a mechanistic understanding of carbon stabilization in manganese oxides. *Nature Communications*, *6*. https://doi.org/10.1038/ncomms8628

Joseph, G. G., Zenit, R., Hunt, M. L., & Rosenwinkel, A. M. (2001). Particle-wall collisions in a viscous fluid. *Journal of Fluid Mechanics*, *433*, 329–346. https://doi.org/10.1017/S0022112001003470

Jouzel, J., Masson-Delmotte, V., Cattani, O., Dreyfus, G., Falourd, S., Hoffmann, G., et al. (2007). Orbital and millennial antarctic climate variability over the past 800,000 years. *Science*, *317*(5839), 793–796. https://doi.org/10.1126/science.1141038

Keeling, C. D. (1979). The Suess effect: 13Carbon-14Carbon interrelations. *Environment International*, *2*(4–6), 229–300. https://doi.org/10.1016/0160-4120(79)90005-9

Keil, R. G., Montluçon, D. B., Prahl, F. G., & Hedges, J. I. (1994). Sorptive preservation of labile organic matter in marine sediments. *Nature*, *370*(6490), 549–552. https://doi.org/10.1038/370549a0

Keil, R. G., Mayer, L. M., Quay, P. D., Richey, J. E., & Hedges, J. I. (1997). Loss of organic matter from riverine particles in deltas. *Geochimica et Cosmochimica Acta*, *61*(7), 1507–1511. https://doi.org/10.1016/S0016-7037(97)00044-6

Kleber, M., Sollins, P., & Sutton, R. (2007). A conceptual model of organo-mineral interactions in soils: Self-assembly of organic molecular fragments into zonal structures on mineral surfaces. *Biogeochemistry*, *85*(1), 9–24. https://doi.org/10.1007/s10533-007-9103-5

Korschinek, G., Bergmaier, A., Faestermann, T., Gerstmann, U. C., Knie, K., Rugel, G., et al. (2010). A new value for the half-life of 10Be by Heavy-Ion Elastic Recoil Detection and liquid scintillation counting. *Nuclear Instruments and Methods in Physics Research, Section B: Beam Interactions with Materials and Atoms*, *268*(2), 187–191. https://doi.org/10.1016/j.nimb.2009.09.020

Kramer, M. G., Sanderman, J., Chadwick, O. A., Chorover, J., & Vitousek, P. M. (2012). Long-term carbon storage through retention of dissolved aromatic acids by reactive particles in soil. *Global Change Biology*, *18*(8), 2594–2605. https://doi.org/10.1111/j.1365-2486.2012.02681.x

Kusch, S., Rethemeyer, J., Schefuß, E., & Mollenhauer, G. (2010). Controls on the age of vascular plant biomarkers in Black Sea sediments. *Geochimica et Cosmochimica Acta*, *74*(24), 7031–7047. https://doi.org/10.1016/j.gca.2010.09.005

Lalonde, K., Mucci, A., Ouellet, A., & Gélinas, Y. (2012). Preservation of organic matter in sediments promoted by iron. *Nature*, *483*(7388), 198–200. https://doi.org/10.1038/nature10855

Lamb, M. P., Leeuw, J. De, Fischer, W., Moodie, A. J., Venditti, J., Nittrouer, J., et al. (2020). Mud in rivers is transported as flocculated and bed material. *Nature Geoscience*, 1–19. https://doi.org/10.1038/s41561-020-0602-5

Lancaster, S. T., Underwood, E. F., & Frueh, W. T. (2010). Sediment reservoirs at mountain stream confluences: Dynamics and effects of tributaries dominated by debris-flow and fluvial processes. *Bulletin of the Geological Society of America*, *122*(11–12), 1775–1786. https://doi.org/10.1130/B30175.1

Lane, S. N., Parsons, D. R., Best, J. L., Orfeo, O., Kostaschuk, R. A., & Hardy, R. J. (2008). Causes of rapid mixing at a junction of two large rivers: Rio Parana and Rio Paraguay, Argentina. *Journal of Geophysical Research: Earth Surface*, *113*(2).

https://doi.org/10.1029/2006JF000745

Lane, Stuart N, & Richards, K. S. (1997). Linking river channel form and process: time, space and causality revisited. *Earth Surface Processes and Landforms*, *22*, 249–260.

Lauer, J. W., & Parker, G. (2008a). Modeling framework for sediment deposition, storage, and evacuation in the floodplain of a meandering river: Application to the Clark Fork River, Montana. *Water Resources Research*, *44*(8), 1–16. https://doi.org/10.1029/2006WR005529

Lauer, J. W., & Parker, G. (2008b). Net local removal of floodplain sediment by river meander migration. *Geomorphology*, *96*(1–2), 123–149. https://doi.org/10.1016/j.geomorph.2007.08.003

Lawrence, C. R., Harden, J. W., Xu, X., Schulz, M. S., & Trumbore, S. E. (2015). Long-term controls on soil organic carbon with depth and time: A case study from the Cowlitz River Chronosequence, WA USA. *Geoderma*, *247–248*, 73–87. https://doi.org/10.1016/j.geoderma.2015.02.005

Lee, H., Galy, V., Feng, X., Ponton, C., Galy, A., France-Lanord, C., & Feakins, S. J. (2019). Sustained wood burial in the Bengal Fan over the last 19 My. *Proceedings of the National Academy of Sciences*, 201913714. https://doi.org/10.1073/pnas.1913714116

Leithold, E. L., Blair, N. E., & Wegmann, K. W. (2016, February 1). Source-to-sink sedimentary systems and global carbon burial: A river runs through it. *Earth-Science Reviews*. Elsevier. https://doi.org/10.1016/j.earscirev.2015.10.011

Lininger, K. B., Wohl, E., & Rose, J. R. (2018). Geomorphic Controls on Floodplain Soil Organic Carbon in the Yukon Flats, Interior Alaska, From Reach to River Basin Scales. *Water Resources Research*, *54*(3), 1934–1951. https://doi.org/10.1002/2017WR022042

Lininger, K. B., Wohl, E., Rose, J. R., & Leisz, S. J. (2019). Significant Floodplain Soil Organic Carbon Storage Along a Large High-Latitude River and its Tributaries. *Geophysical Research Letters*, *46*(4), 2121–2129. https://doi.org/10.1029/2018GL080996

Lupker, M., France-Lanord, C., Lavé, J., Bouchez, J., Galy, V., Métivier, F., et al. (2011). A Rouse-based method to integrate the chemical composition of river sediments: Application to the Ganga basin. *Journal of Geophysical Research: Earth Surface*, *116*(4), F04012. https://doi.org/10.1029/2010JF001947

Lüthi, D., Le Floch, M., Bereiter, B., Blunier, T., Barnola, J. M., Siegenthaler, U., et al. (2008). High-resolution carbon dioxide concentration record 650,000-800,000 years before present. *Nature*, *453*(7193), 379–382. https://doi.org/10.1038/nature06949

Lyons, W. B., Nezat, C. A., Carey, A. E., & Hicks, D. M. (2002). Organic carbon fluxes to the ocean from high-standing islands. *Geology*, *30*(5), 443–446. https://doi.org/10.1130/0091-7613(2002)030<0443:OCFTTO>2.0.CO;2

Maavara, T., Lauerwald, R., Regnier, P., & Van Cappellen, P. (2017). Global perturbation of organic carbon cycling by river damming. *Nature Communications*, *8*(May), 1–10. https://doi.org/10.1038/ncomms15347

Martin, A. N., Dosseto, A., May, J. H., Jansen, J. D., Kinsley, L. P. J., & Chivas, A. R. (2019). Sediment residence times in catchments draining to the Gulf of Carpentaria, northern Australia, inferred by uranium comminution dating. *Geochimica et Cosmochimica Acta*, *244*, 264–291. https://doi.org/10.1016/j.gca.2018.09.031

Martin, Y., & Church, M. (2004). Numerical modelling of landscape evolution:

Geomorphological perspectives. *Progress in Physical Geography*, *28*(3), 317–339. https://doi.org/10.1191/0309133304pp412ra

Marwick, T. R., Tamooh, F., Teodoru, C. R., Borges, A. V., Darchambeau, F., & Bouillon, S. (2015). The age of river-transported carbon: A global perspective. *Global Biogeochemical Cycles*, *29*(2), 122–137. https://doi.org/10.1002/2014GB004911

Mayorga, E., Aufdenkampe, A. K., Masiello, C. A., Krusche, A. V, Hedges, J. I., Quay, P. D., et al. (2005). Young organic matter as a source of carbon dioxide outgassing from Amazonian rivers. *Nature*, *436*(7050), 538–541. https://doi.org/10.1038/nature03880

McClelland, J. W., Holmes, R. M., Peterson, B. J., Raymond, P. A., Striegl, R. G., Zhulidov, A. V, et al. (2016). Particulate organic carbon and nitrogen export from major Arctic rivers. *Global Biogeochemical Cycles*, *30*(5), 629–643. https://doi.org/10.1002/2015GB005351

McGlue, M. M., Smith, P. H., Zani, H., Silva, A., Carrapa, B., Cohen, A. S., & Pepper, M. B. (2016). An Integrated Sedimentary Systems Analysis of the RíO Bermejo (Argentina): Megafan Character in the Overfilled Southern Chaco Foreland Basin. *Journal of Sedimentary Research*, *86*(12), 1359–1377. https://doi.org/10.2110/jsr.2016.82

McKinney, C. R., McCrea, J. M., Epstein, S., Allen, H. A., & Urey, H. C. (1950). Improvements in mass spectrometers for the measurement of small differences in isotope abundance ratios. *Review of Scientific Instruments*, *21*(8), 724–730. https://doi.org/10.1063/1.1745698

McNown, J. S., & Malaika, J. (1950). Effects of particle shape on settling velocity at low Reynolds numbers. *Eos, Transactions American Geophysical Union*, *31*(1), 74–82. https://doi.org/10.1029/TR031i001p00074

Mead, R. N., & Goñi, M. A. (2008). Matrix protected organic matter in a river dominated margin: A possible mechanism to sequester terrestrial organic matter? *Geochimica et Cosmochimica Acta*, *72*(11), 2673–2686. https://doi.org/10.1016/j.gca.2008.03.007

Menges, J., Hovius, N., Andermann, C., Lupker, M., Haghipour, N., Märki, L., & Sachse, D. (2020). Variations in organic carbon sourcing along a trans-Himalayan river determined by a Bayesian mixing approach. *Geochimica et Cosmochimica Acta*, *286*, 159–176. https://doi.org/10.1016/j.gca.2020.07.003

Mikutta, R., Kleber, M., Torn, M. S., & Jahn, R. (2006). Stabilization of soil organic matter: Association with minerals or chemical recalcitrance? *Biogeochemistry*, *77*(1), 25–56. https://doi.org/10.1007/s10533-005-0712-6

Mikutta, R., Schaumann, G. E., Gildemeister, D., Bonneville, S., Kramer, M. G., Chorover, J., et al. (2009). Biogeochemistry of mineral-organic associations across a long-term mineralogical soil gradient (0.3-4100 kyr), Hawaiian Islands. *Geochimica et Cosmochimica Acta*, *73*(7), 2034–2060. https://doi.org/10.1016/j.gca.2008.12.028

Mollenhauer, G., & Eglinton, T. I. (2007). Diagenetic and sedimentological controls on the composition of organic matter preserved in California Borderland Basin sediments. *Limnology and Oceanography*, *52*(2), 558–576. https://doi.org/10.4319/lo.2007.52.2.0558

Monaghan, M. C., Krishnaswami, S., & Thomas, J. H. (1983). 10Be concentrations and the long-term fate of particle-reactive nuclides in five soil profiles from California. *Earth and Planetary Science Letters*, *65*(1), 51–60. https://doi.org/10.1016/0012-821X(83)90189-9

Moore, J. W., & Semmens, B. X. (2008). Incorporating uncertainty and prior information into stable isotope mixing models. *Ecology Letters*, *11*(5), 470–480.

https://doi.org/10.1111/j.1461-0248.2008.01163.x

Mueller, C. W., Kölbl, A., Hoeschen, C., Hillion, F., Heister, K., Herrmann, A. M., & Kögel-Knabner, I. (2012). Submicron scale imaging of soil organic matter dynamics using NanoSIMS - From single particles to intact aggregates. *Organic Geochemistry*, *42*(12), 1476–1488. https://doi.org/10.1016/j.orggeochem.2011.06.003

Mulch, A., Uba, C. E., Strecker, M. R., Schoenberg, R., & Chamberlain, C. P. (2010). Late Miocene climate variability and surface elevation in the central Andes. *Earth and Planetary Science Letters*, *290*(1–2), 173–182. https://doi.org/10.1016/j.epsl.2009.12.019

Murphy, B. P., Czuba, J. A., & Belmont, P. (2019). Post-wildfire sediment cascades: A modeling framework linking debris flow generation and network-scale sediment routing. *Earth Surface Processes and Landforms*, *44*(11), 2126–2140. https://doi.org/10.1002/esp.4635

Nadelhoffer, K. J., & Fry, B. (1988). Controls on natural nitrogen-15 and carbon-13 abundances in forest soil organic matter. *Soil Science of America Journal*, *52*(6), 1633–1640. https://doi.org/10.2136/sssaj1988.03615995005200060024x

Nakamura, F., & Kikuchi, S. I. (1996). Some methodological developments in the analysis of sediment transport processes using age distribution of floodplain deposits. *Geomorphology*, *16*(2), 139–145. https://doi.org/10.1016/0169-555X(95)00139-V

Nienhuis, J., & Cohen, S. (2019). The efficiency of land formation for 10,000 deltas. In *AGU Fall Meeting Abstracts*. San Francisco: AGU Fall Meeting Abstracts. Retrieved from https://agu.confex.com/agu/fm19/meetingapp.cgi/Paper/493651

Nishiizumi, K., Imamura, M., Caffee, M. W., Southon, J. R., Finkel, R. C., & McAninch, J. (2007). Absolute calibration of 10 Be AMS standards. *Nuclear Instruments and Methods in Physics Research, Section B: Beam Interactions with Materials and Atoms*, *258*(2), 403–413. https://doi.org/10.1016/j.nimb.2007.01.297

Page, J. (1889). The Gran Chaco and its rivers. *Proceedings of the Royal Geographical Society and Monthly Record of Geography*, *11*(3), 129–152. Retrieved from https://about.jstor.org/terms

Paola, C., & Martin, J. M. (2012). Mass-Balance Effects In Depositional Systems. *Journal of Sedimentary Research*, *82*(6), 435–450. https://doi.org/10.2110/jsr.2012.38

Paola, C., & Seal, R. (1995). Grain size patchiness as a cause of selective deposition and downstream fining. *Water Resources Research*, *31*(5), 1395–1407. https://doi.org/10.1029/94WR02975

Pavich, M. J., Brown, L., Klein, J., & Middleton, R. (1984). 10Be accumulation in a soil chronosequence. *Earth and Planetary Science Letters*, *68*(2), 198–204. https://doi.org/10.1016/0012-821X(84)90151-1

Pedrozo, F., & Bonetto, C. (1987). Nitrogen and phosphorus transport in the Bermejo River (South America). *Reviews of Hydrobiology in the Tropics*, *20*(2), 91–99. Retrieved from https://www.researchgate.net/profile/Carlos_Bonetto/publication/32984120_Nitrogen_and_phosphorus_transport_in_the_Bermejo_River_South_America/links/00b7d51755eee4b910000000.pdf

Peterse, F., & Eglinton, T. I. (2017). Grain Size Associations of Branched Tetraether Lipids in Soils and Riverbank Sediments: Influence of Hydrodynamic Sorting Processes. *Frontiers in Earth Science*, *5*(June), 1–8. https://doi.org/10.3389/feart.2017.00049

Peucker-Ehrenbrink, B. (2018). *Land2Sea database, version 2.0*. PANGAEA. https://doi.org/10.1594/PANGAEA.892680

Phillips, J. D., Marden, M., & Gomez, B. (2007). Residence time of alluvium in an aggrading fluvial system. *Earth Surface Processes and Landforms*, *32*, 307–316. https://doi.org/10.1002/esp

Piquer-Rodríguez, M., Torella, S., Gavier-Pizarro, G., Volante, J., Somma, D., Ginzburg, R., & Kuemmerle, T. (2015). Effects of past and future land conversions on forest connectivity in the Argentine Chaco. *Landscape Ecology*, *30*(5), 817–833. https://doi.org/10.1007/s10980-014-0147-3

Pizzuto, J., Schenk, E. R., Hupp, C. R., Gellis, A., Noe, G., Williamson, E., et al. (2014). Characteristic length scales and time-averaged transport velocities of suspended sediment in the mid-Atlantic Region, USA. *Water Resources Research*, *50*(2), 790–805. https://doi.org/10.1002/2013WR014485

Pizzuto, J., Keeler, J., Skalak, K., & Karwan, D. (2017). Storage filters upland suspended sediment signals delivered from watersheds. *Geology*, *45*(2), 151–154. https://doi.org/10.1130/G38170.1

Quay, P. D., Wilbur, D. 0., Richey, J. E., Hedges, J. I., Devol, A. H., & Victoria, R. (1992, June 1). Carbon cycling in the Amazon River: Implications from the 13C compositions of particles and solutes. *Limnology and Oceanography*. John Wiley & Sons, Ltd. https://doi.org/10.4319/lo.1992.37.4.0857

Rach, O., Hadeen, X., & Sachse, D. (2020). An automated solid phase extraction procedure for lipid biomarker purification and stable isotope analysis. *Organic Geochemistry*, *142*. https://doi.org/10.1016/j.orggeochem.2020.103995

Rahaman, W., Wittmann, H., & von Blanckenburg, F. (2017). Denudation rates and the degree of chemical weathering in the Ganga River basin from ratios of meteoric cosmogenic 10 Be to stable 9 Be. *Earth and Planetary Science Letters*, *469*, 156–169. https://doi.org/10.1016/j.epsl.2017.04.001

Rasmussen, C., Heckman, K., Wieder, W. R., Keiluweit, M., Lawrence, C. R., Berhe, A. A., et al. (2018). Beyond clay: towards an improved set of variables for predicting soil organic matter content. *Biogeochemistry*, *137*(3), 297–306. https://doi.org/10.1007/s10533-018-0424-3

Raymond, P. A., Hartmann, J., Lauerwald, R., Sobek, S., McDonald, C., Hoover, M., et al. (2013). Global carbon dioxide emissions from inland waters. *Nature*, *503*(7476), 355–359. https://doi.org/10.1038/nature12760

Reid, L. M., & Dunne, T. (2016). *Sediment budgets as an organizing framework in fluvial geomorphology*. https://doi.org/10.1002/9781118648551.ch16

Repasch, M., Wittmann, H., Scheingross, J. S., Sachse, D., Szupiany, R., Orfeo, O., et al. (2020). Sediment Transit Time and Floodplain Storage Dynamics in Alluvial Rivers Revealed by Meteoric 10Be. *Journal of Geophysical Research: Earth Surface*, *125*(7), 1–19. https://doi.org/10.1029/2019jf005419

Reusser, L., & Bierman, P. (2010). Using meteoric 10Be to track fl uvial sand through the Waipaoa River basin, New Zealand. *Geology*, *38*(1), 47–50. https://doi.org/10.1130/G30395.1

Reusser, L., Graly, J., Bierman, P., & Rood, D. (2010). Calibrating a long-term meteoric 10Be accumulation rate in soil. *Geophysical Research Letters*, *37*(19).

https://doi.org/10.1029/2010GL044751

Richey, J. E. (2004). Pathways of Atmospheric CO2 through Fluvial Systems. *The Global Carbon Cycle: Integrating Humans, Climate, and the Natural World*, 329–340.

Richey, J. E., Brock, J. T., Naiman, R. J., Wissmar, R. C., & Stallard, R. F. (1980). Organic carbon: Oxidation and transport in the Amazon River. *Science*, *207*(4437), 1348–1351. https://doi.org/10.1126/science.207.4437.1348

Rohrmann, A., Sachse, D., Mulch, A., Pingel, H., Tofelde, S., Alonso, R. N., & Strecker, M. R. (2016). Miocene orographic uplift forces rapid hydrological change in the southern central Andes. *Nature Publishing Group*. https://doi.org/10.1038/srep35678

Romans, B. W., Castelltort, S., Covault, J. A., Fildani, A., & Walsh, J. P. (2016). Environmental signal propagation in sedimentary systems across timescales. *Earth-Science Reviews*. https://doi.org/10.1016/j.earscirev.2015.07.012

Rosenheim, B. E., & Galy, V. (2012). Direct measurement of riverine particulate organic carbon age structure. *Geophysical Research Letters*, *39*(19), 1–6. https://doi.org/10.1029/2012GL052883

Rosenheim, B. E., Roe, K. M., Roberts, B. J., Kolker, A. S., Allison, M. A., & Johannesson, K. H. (2013). River discharge influences on particulate organic carbon age structure in the Mississippi/Atchafalaya River System. *Global Biogeochemical Cycles*, *27*(1), 154–166. https://doi.org/10.1002/gbc.20018

Rouse, H. (1937). Modern conceptions of the mechanics of turbulence. *Transactions of the American Society of Civil Engineers*, *102*, 463–543.

Rowland, J. C., & Schwenk, J. (2019). *Global meta-analysis of published river bank erosion and migration rates*. https://doi.org/10.5063/F11Z42JX

Rowland, J. C., Lepper, K., Dietrich, W. E., Wilson, C. J., & Sheldon, R. (2005). Tie channel sedimentation rates, oxbow formation age and channel migration rate from optically stimulated luminescence (OSL) analysis of floodplain deposits. *Earth Surface Processes and Landforms*, *30*(9), 1161–1179. https://doi.org/10.1002/esp.1268

Roy, M., McManus, J., Goñi, M. A., Chase, Z., Borgeld, J. C., Wheatcroft, R. A., et al. (2013). Reactive iron and manganese distributions in seabed sediments near small mountainous rivers off Oregon and California (USA). *Continental Shelf Research*, *54*, 67–79. https://doi.org/10.1016/j.csr.2012.12.012

Ruff, M., Fahrni, S., Gäggeler, H. W., Hajdas, I., Suter, M., Synal, H. A., et al. (2010). On-line radiocarbon measurements of small samples using elemental analyzer and MICADAS gas ion source. *Radiocarbon*, *52*(4), 1645–1656. https://doi.org/10.1017/S003382220005637X

Running, S. W., Thornton, P. E., Nemani, R., & Glassy, J. M. (2000). Global Terrestrial Gross and Net Primary Productivity from the Earth Observing System. In *Methods in Ecosystem Science* (pp. 44–57). Springer New York. https://doi.org/10.1007/978-1-4612-1224-9_4

Sachse, D., Billault, I., Bowen, G. J., Chikaraishi, Y., Dawson, T. E., Feakins, S. J., et al. (2012). Molecular paleohydrology: interpreting the hydrogen-isotopic composition of lipid biomarkers from photosynthesizing organisms. *Annual Review of Earth and Planetary Sciences*, *40*, 221–249. https://doi.org/10.1146/annurev-earth-042711-105535

Sauer, P. E., Eglinton, T. I., Hayes, J. M., Schimmelmann, A., & Sessions, A. L. (2001). Compound-specific DH ratios of lipid biomarkers from sediments as a proxy for

environmental and climatic condition.pdf. *Geochimica et Cosmochimica Acta*, *65*(2), 213–222. Retrieved from http://s3.amazonaws.com/academia.edu.documents/12310137/sauer2001.pdf?AWSAccessKeyId=AKIAIWOWYYGZ2Y53UL3A&Expires=1493891771&Signature=SLgIKTjsdwMMwCXNS4pn2rZtGEk%3D&response-content-disposition=inline%3Bfilename%3DCompound-specific_D_H_ratios_of_lipid

Schefuß, E., Eglinton, T. I., Spencer-Jones, C. L., Rullkötter, J., De Pol-Holz, R., Talbot, H. M., et al. (2016). Hydrologic control of carbon cycling and aged carbon discharge in the Congo River basin. *Nature Geoscience*, *9*(9), 687–690. https://doi.org/10.1038/ngeo2778

Scheingross, J. S., Hovius, N., Dellinger, M., Hilton, R. G., Repasch, M., Sachse, D., et al. (2019a). Preservation of organic carbon during active fluvial transport and particle abrasion. *Geology*, *47*(10), 958–962. https://doi.org/10.1130/G46442.1

Scheingross, J. S., Hovius, N., Dellinger, M., Hilton, R. G., Repasch, M., Sachse, D., et al. (2019b). Preservation of organic carbon during active fluvial transport and particle abrasion. *Geology*, *47*(10), 958–962. https://doi.org/10.1130/G46442.1

Schlünz, B., & Schneider, R. R. (2000). Transport of terrestrial organic carbon to the oceans by rivers: Re-estimating flux- and burial rates. *International Journal of Earth Sciences*, *88*(4), 599–606. https://doi.org/10.1007/s005310050290

Sheets, B. A., Hickson, T. A., & Paola, C. (2002). Assembling the stratigraphic record: Depositional patterns and time-scales in an experimental alluvial basin. *Basin Research*, *14*(3), 287–301. https://doi.org/10.1046/j.1365-2117.2002.00185.x

Shen, C., Beer, J., Kubik, P. W., Suter, M., Borkovec, M., & Liu, T. S. (2004). Grain size distribution, 10Be content and magnetic susceptibility of micrometer-nanometer loess materials. In *Nuclear Instruments and Methods in Physics Research, Section B: Beam Interactions with Materials and Atoms* (Vol. 223–224, pp. 613–617). North-Holland. https://doi.org/10.1016/j.nimb.2004.04.113

Sierra, C. A., Trumbore, S. E., Davidson, E. A., Vicca, S., & Janssens, I. A. (2015). Sensitivity of decomposition rates of soil organic matter with respect to simultaneous changes in temperature and moisture. *Journal of Advances in Modeling Earth Systems*, *7*, 335–356. https://doi.org/10.1002/2014MS000358.Received

Sierra, C. A., Müller, M., Metzler, H., Manzoni, S., & Trumbore, S. E. (2017). The muddle of ages, turnover, transit, and residence times in the carbon cycle. *Global Change Biology*, *23*(5), 1763–1773. https://doi.org/10.1111/gcb.13556

Singleton, A. A., Schmidt, A. H., Bierman, P. R., Rood, D. H., Neilson, T. B., Greene, E. S., et al. (2017). Effects of grain size, mineralogy, and acid-extractable grain coatings on the distribution of the fallout radionuclides 7Be, 10Be, 137Cs, and 210Pb in river sediment. *Geochimica et Cosmochimica Acta*, *197*, 71–86. https://doi.org/10.1016/j.gca.2016.10.007

Snyder, N. P., Rubin, D. M., Alpers, C. N., Childs, J. R., Curtis, J. A., Flint, L. E., & Wright, S. A. (2004). Estimating accumulation rates and physical properties of sediment behind a dam: Englebright Lake, Yuba River, northern California. *Water Resources Research*, *40*(11), 11301. https://doi.org/10.1029/2004WR003279

Sparkes, R. B. (2012). *Marine Sequestration of Particulate Organic Carbon from Mountain Belts*. Retrieved from http://eprints.esc.cam.ac.uk/2618/

Sparkes, R. B., Lin, I. T., Hovius, N., Galy, A., Liu, J. T., Xu, X., & Yang, R. (2015).

Redistribution of multi-phase particulate organic carbon in a marine shelf and canyon system during an exceptional river flood: Effects of Typhoon Morakot on the Gaoping River-Canyon system. *Marine Geology*, *363*, 191–201. https://doi.org/10.1016/j.margeo.2015.02.013

Sparkes, R. B., Hovius, N., Galy, A., & Liu, J. T. (2020). Survival of graphitized petrogenic organic carbon through multiple erosional cycles. *Earth and Planetary Science Letters*, *531*, 115992. https://doi.org/10.1016/j.epsl.2019.115992

Sternberg, H. (1875). Untersuchungen uber Langen- und Querprofil geschiebefuhrender Flusse. *Zeitschrift Fur Bauwesen*, *25*, 483–506.

Stock, B. C., Jackson, A. L., Ward, E. J., Parnell, A. C., Phillips, D. L., & Semmens, B. X. (2018). Analyzing mixing systems using a new generation of Bayesian tracer mixing models. *PeerJ*, *2018*(6), 1–27. https://doi.org/10.7717/peerj.5096

Stout, J. C., Belmont, P., Schottler, S. P., & Willenbring, J. K. (2014). Identifying Sediment Sources and Sinks in the Root River, Southeastern Minnesota. *Annals of the Association of American Geographers*, *104*(1), 20–39. https://doi.org/10.1080/00045608.2013.843434

Strong, N., Sheets, B., Hickson, T., & Paola, C. (2005). A Mass-Balance Framework for Quantifying Downstream Changes in Fluvial Architecture. *Spec. Publs Int. Ass. Sediment.*, *35*, 243–253. https://doi.org/10.1002/9781444304350.ch14

Stuiver, M., & Polach, H. A. (1977). Reporting of 14C Data. *Radiocarbon*, *19*(3), 355–363.

Sutfin, N. A., Wohl, E. E., & Dwire, K. A. (2016). Banking carbon: A review of organic carbon storage and physical factors influencing retention in floodplains and riparian ecosystems. *Earth Surface Processes and Landforms*, *41*(1), 38–60. https://doi.org/10.1002/esp.3857

Tao, S., Eglinton, T. I., Montluçon, D. B., Mcintyre, C., & Zhao, M. (2015). Pre-aged soil organic carbon as a major component of the Yellow River suspended load: Regional significance and global relevance. *Earth and Planetary Science Letters*, *414*, 77–86. https://doi.org/10.1016/j.epsl.2015.01.004

Tipple, B. J., & Pagani, M. (2007). The Early Origins of Terrestrial C 4 Photosynthesis. *Annu . Rev . Earth Planet . Sci*, *35*, 435–61. https://doi.org/10.1146/annurev.earth.35.031306.140150

Torn, M. S., Trumbore, S. E., Chadwick, O. A., Vitousek, P. M., & Hendricks, D. M. (1997). Mineral control of soil organic carbon storage and turnover. *Nature*, *389*(6647), 170–173. https://doi.org/10.1038/38260

Torn, M. S., Swanston, C. W., Castanha, C., & Trumbore, S. E. (2009). Storage and Turnover of Organic Matter in Soil. In *Biophysico-Chemical Processes Involving Natural Nonliving Organic Matter in Environmental Systems* (pp. 219–272). https://doi.org/10.1002/9780470494950.ch6

Torres, M. A., West, A. J., & Li, G. (2014). Sulphide oxidation and carbonate dissolution as a source of CO2 over geological timescales. *Nature*, *507*(7492), 346–349. https://doi.org/10.1038/nature13030

Torres, M. A., Limaye, A. B., Ganti, V., Lamb, M. P., West, A. J., & Fischer, W. W. (2017). Model predictions of long-lived storage of organic carbon in river deposits. *Earth Surf. Dynam*, *5*, 711–730. https://doi.org/10.5194/esurf-5-711-2017

Torres, M. A., Kemeny, P. C., Lamb, M. P., Cole, T. L., & Fischer, W. W. (2020). Long-Term Storage and Age-Biased Export of Fluvial Organic Carbon: Field Evidence From West

Iceland. *Geochemistry, Geophysics, Geosystems*, *21*(4), 1–23. https://doi.org/10.1029/2019gc008632

Tranvik, L. J., Downing, J. A., Cotner, J. B., Loiselle, S. A., Striegl, R. G., Ballatore, T. J., et al. (2009). Lakes and reservoirs as regulators of carbon cycling and climate. *Limnology and Oceanography*, *54*(6 PART 2), 2298–2314. https://doi.org/10.4319/lo.2009.54.6_part_2.2298

Turowski, J. M., Hilton, R. G., & Sparkes, R. (2016). Decadal carbon discharge by a mountain stream is dominated by coarse organic matter. *Geology*, *44*(1), 27–30. https://doi.org/10.1130/G37192.1

Urey, H. C. (1952). *ON THE EARLY CHEMICAL HISTORY OF THE EARTH AND THE ORIGIN OF LIFE*. *Proceedings of the National Academy of Sciences of the United States of America* (Vol. 38). https://doi.org/10.1515/9781400882199

Vogel, C., Mueller, C. W., Höschen, C., Buegger, F., Heister, K., Schulz, S., et al. (2014). Submicron structures provide preferential spots for carbon and nitrogen sequestration in soils. *Nature Communications*, *5*, 2947. https://doi.org/10.1038/ncomms3947

Vonk, J. E., Dickens, A. F., Giosan, L., Hussain, Z. A., Kim, B., Zipper, S. C., et al. (2016). Arctic Deltaic Lake Sediments As Recorders of Fluvial Organic Matter Deposition. *Frontiers in Earth Science*, *4*(August), 1–24. https://doi.org/10.3389/feart.2016.00077

Vonmoos, M., Beer, J., & Muscheler, R. (2006). Large variations in Holocene solar activity: Constraints from 10Be in the Greenland Ice Core Project ice core. *Journal of Geophysical Research: Space Physics*, *111*(10). https://doi.org/10.1029/2005JA011500

van der Voort, T. S., Zell, C. I., Hagedorn, F., Feng, X., McIntyre, C. P., Haghipour, N., et al. (2017). Diverse Soil Carbon Dynamics Expressed at the Molecular Level. *Geophysical Research Letters*, *44*(23), 11,840-11,850. https://doi.org/10.1002/2017GL076188

Wagai, R., & Mayer, L. M. (2007). Sorptive stabilization of organic matter in soils by hydrous iron oxides. *Geochimica et Cosmochimica Acta*, *71*(1), 25–35. https://doi.org/10.1016/j.gca.2006.08.047

Wagai, R., Mayer, L. M., Kitayama, K., & Shirato, Y. (2011). Association of organic matter with iron and aluminum across a range of soils determined via selective dissolution techniques coupled with dissolved nitrogen analysis. *Biogeochemistry*, *112*(1–3), 95–109. https://doi.org/10.1007/s10533-011-9652-5

Wagai, R., Kajiura, M., Asano, M., & Hiradate, S. (2015). Nature of soil organo-mineral assemblage examined by sequential density fractionation with and without sonication: Is allophanic soil different? *Geoderma*, *241–242*, 295–305. https://doi.org/10.1016/j.geoderma.2014.11.028

Wakeham, S. G., Canuel, E. A., Lerberg, E. J., Mason, P., Sampere, T. P., & Bianchi, T. S. (2009). Partitioning of organic matter in continental margin sediments among density fractions. *Marine Chemistry*, *115*(3–4), 211–225. https://doi.org/10.1016/j.marchem.2009.08.005

Walling, D. E., & He, Q. (1993). Use of cesium-137 as a tracer in the study of rates and patterns of floodplain sedimentation. *Tracers in Hydrology. Proc. International Symposium, Yokohama, 1993*, (215), 319–328. Retrieved from https://www.researchgate.net/publication/237404964

Wang, X., Ma, H., Li, R., Song, Z., & Wu, J. (2012). Seasonal fluxes and source variation of organic carbon transported by two major Chinese Rivers: The Yellow River and

Changjiang (Yangtze) River. *Global Biogeochemical Cycles*, *26*(2), 1–10. https://doi.org/10.1029/2011GB004130

Waterson, E. (2005). Sources of sedimentary organic matter in the Mississippi river and adjacent Gulf of Mexico. Retrieved from http://www.elsevier.com/copyright

Wedin, D. A., Tieszen, L. L., Dewey, B., & Pastor, J. (1995). Carbon isotope dynamics during grass decomposition and soil organic matter formation. *Ecology*, *76*(5), 1383–1392. https://doi.org/10.2307/1938142

Wild, B., Andersson, A., Bröder, L., Vonk, J., Hugelius, G., McClelland, J. W., et al. (2019). Rivers across the Siberian Arctic unearth the patterns of carbon release from thawing permafrost. *Proceedings of the National Academy of Sciences of the United States of America*, *116*(21), 10280–10285. https://doi.org/10.1073/pnas.1811797116

Willenbring, J. K., & von Blanckenburg, F. (2010). Meteoric cosmogenic Beryllium-10 adsorbed to river sediment and soil: Applications for Earth-surface dynamics. *Earth-Science Reviews*, *98*(1–2), 105–122. https://doi.org/10.1016/j.earscirev.2009.10.008

Wittmann, H., & Blanckenburg, F. Von. (2016). The geological significance of cosmogenic nuclides in sediment of large lowland basins. *Earth Science Reviews*, *14*(2009), 12721. https://doi.org/10.1016/j.earscirev.2016.06.001

Wittmann, H., Von Blanckenburg, F., Bouchez, J., Dannhaus, N., Naumann, R., Christl, M., & Gaillardet, J. (2012). The dependence of meteoric 10 Be concentrations on particle size in Amazon River bed sediment and the extraction of reactive 10 Be/ 9 Be ratios. *Chemical Geology*, *318–319*, 126–138. https://doi.org/10.1016/j.chemgeo.2012.04.031

Wittmann, H., Von Blanckenburg, F., Dannhaus, N., Bouchez, J., Gaillardet, J., Guyot, J. L., et al. (2015). A test of the cosmogenic 10Be(meteoric)/9Be proxy for simultaneously determining basin-wide erosion rates, denudation rates, and the degree of weathering in the Amazon basin. *Journal of Geophysical Research F: Earth Surface*, *120*(12), 2498–2526. https://doi.org/10.1002/2015JF003581

Wittmann, H., Oelze, M., Roig, H., & von Blanckenburg, F. (2018). Are seasonal variations in river-floodplain sediment exchange in the lower Amazon River basin resolvable through meteoric cosmogenic10Be to stable9Be ratios? *Geomorphology*, *322*(September), 148–158. https://doi.org/10.1016/j.geomorph.2018.08.045

Wohl, E., Hall, R. O., Lininger, K. B., Sutfin, N. A., & Walters, D. M. (2017). Carbon dynamics of river corridors and the effects of human alterations. *Ecological Monographs*, *87*(3), 379–409. https://doi.org/10.1002/ecm.1261

Wright, S., & Parker, G. (2005). Modeling downstream fining in sand-bed rivers. I: Formulation. *Journal of Hydraulic Research*, *43*(6), 613–620. https://doi.org/10.1080/00221680509500381

Wyshnytzky, C. E., Ouimet, W. B., McCarthy, J., Dethier, D. P., Shroba, R. R., Bierman, P. R., & Rood, D. H. (2015). Meteoric 10Be, clay, and extractable iron depth profiles in the Colorado Front Range: Implications for understanding soil mixing and erosion. *Catena*, *127*, 32–45. https://doi.org/10.1016/j.catena.2014.12.008

Yu, M., Eglinton, T. I., Haghipour, N., Montluçon, D. B., Wacker, L., Wang, Z., et al. (2019). Molecular isotopic insights into hydrodynamic controls on fluvial suspended particulate organic matter transport. *Geochimica et Cosmochimica Acta*, *262*, 78–91.

APPENDIX A

Supporting Information for

Chapter 3: Meteoric ^{10}Be as a fluvial sediment transit time proxy

Introduction

The following supporting information describes additional methods, calculations, and extended data analysis that aid this study. We describe additional information needed to reproduce the geomorphic and hydrologic analyses and document the sediment budget based transit time estimates. We also present additional grain size, surface area, and floodplain soil inventory data that address uncertainties mentioned in the text and help substantiate the $^{10}Be_m$ transit time method.

Text A1. Constraining geomorphic parameters and sediment fluxes

We estimate important geomorphic characteristics of the Rio Bermejo using GIS tools. To measure the remobilization depth (*h* in Equation (3.5), equal to the channel incision depth), we analyzed a 12 m DEM of the channel floodplain system (TanDEM-X). We traced out the active channel thalweg using the DEM as reference, extracted the elevation profile from these points, and then fit a ramped plane to the elevation data. We then subtracted the ramped plane topography from the DEM to calculate the elevation difference between the channel and floodplain surrounding the active channel belt. We calculated the minimum, median, and maximum of the difference values and use the median values for the incision depths. We calculated the mean and standard deviation incision depth along the channel for the entire main stem Rio Bermejo, as well as the four reaches discussed in Section 7.3 of the main text. Because the TanDEM-X satellite cannot resolve the river channel bathymetry, we added the flow depths measured by ADCP in the four reaches to yield a final remobilization depth, *h*, in these reaches.

We estimated channel migration rates by tracing the channel from four different Landsat images captured between 1986 and 2015, calculating the centerline using the *ChanGeom* tool in Matlab (Fisher et al., 2013), and computing the lateral offset between the different years at all points along the channel. From this dataset, mean migration rates were calculated for the mainstem and the four reaches discussed in section 5.4 of the main text. Channel width and channel belt width were also calculated using *ChanGeom* applied to traces of the channel and belt features.

We calculated sediment fluxes for the three gauging stations on the mainstem Rio Bermejo, using data from the National System of Hydrologic Information of Argentina (https://snih.hidricosargentina.gob.ar/). Two of these gauging stations are located upstream of the RSF confluence, one on the Rio Bermejo at Pozo Sarmiento (PS), gauging the northern half of the headwater drainage area (24,128 km^2) and one on the RSF, gauging the southern half of the headwater area (26,508 km^2). The third station is on the mainstem Rio Bermejo at El Colorado (EC), at river km ~942 (550 km linear distance downstream from the mountain front), with a catchment area of 104,000 km^2. Water discharge data was recorded from 1970 to present, while suspended sediment data was recorded from 1995 to present at EC, and 2010 to present at PS and RSF. Discharge-sediment concentration rating curves were computed for each sediment gauging record. We combined the two upstream gauging station records because they are both upstream of the Rio San Francisco confluence. The rating curve was applied to the full discharge record, and long-term mean annual sediment fluxes were estimated using standard hydrological analyses. We also calculated the relative contributions of suspended load from PS and RSF, which are 91% and 9%, respectively, which were used to calculate the sediment load-weighted concentrations reported in Section 5.2.

Table A1. Sample descriptions.

Sample ID	Distance along channel[a]	Latitude	Longitude	Water Sampling Depth[b]	Total Channel Depth[c]	SSC[d]	SSC_{DI}	D_{50}[e]	SSA[f]	SSA_{DI}	Fraction silt + clay[g]	River water pH
	km	Decimal degrees	Decimal degrees	m	m	mg L^{-1}	mg L^{-1}	µm	m^2 g^{-1}	m^2 g^{-1}		
AR17MR-30	RSF*	-23.35554	-64.18391	1.0	1.0	-		193.35	2.59	7.594	0.06	7.484
AR17MR-31		-23.35554	-64.18391	0.0		-		7.30	12.60		0.80	
AR17DS-001	-20*	-23.14422	-64.19886	0.0	-	-		7.30	12.27		0.92	7.86
AR17MR-24	-10*	-23.25094	-64.13403	0.0	3.4	3979	7049	7.70	10.83	6.92	0.91	7.837
AR17MR-25		-23.25094	-64.13403	1.0		6942		150.15	7.76		0.38	
AR17MR-26		-23.25094	-64.13403	2.0		6625		109.36	7.28		0.42	
AR17MR-27		-23.25094	-64.13403	3.4				325.23	1.16		0.00	
AR17MR-32	135	-23.75598	-63.07393	3.0	4.0	4590	5320	9.81	11.48	11.32	0.85	7.365
AR17MR-33		-23.75598	-63.07393	2.0		7120		11.48	8.96		0.73	
AR17MR-34		-23.75598	-63.07393	1.0		6282		22.43	10.67		0.62	
AR17MR-35		-23.75598	-63.07393	0.0		3714		8.41	14.00		0.91	
AR17MR-36		-23.75598	-63.07393	4.0		-		133.08	3.18		0.05	
AR17MR-11	422	-24.31326	-61.83789	0.0	3.0	6826	18672	6.25	23.15	11.95	0.96	7.651
AR17MR-12		-24.31326	-61.83789	1.0		12348		15.00	12.25		0.77	
AR17MR-13		-24.31326	-61.83789	1.5		23913		37.49	11.37		0.61	
AR17MR-14		-24.31326	-61.83789	2.5		17000		16.14	12.77		0.75	
AR17MR-42	865	-25.6638	-60.11595	4.5	5.7	15435	11005	39.75	12.25	16.49	0.62	7.67
AR17MR-43		-25.6638	-60.11595	3.5		9238		12.22	16.08		0.84	
AR17MR-44		-25.6638	-60.11595	2.0		7858		10.30	19.66		0.92	
AR17MR-45		-25.6638	-60.11595	0.0		5908		7.79	22.49		0.96	
AR17MR-46		-25.6638	-60.11595	5.7		-		160.19	2.16		0.03	
AR17MR-05	1221	-26.66087	-58.63467	2.7	4.0	17070	13020	11.04	18.32	20.94	0.90	7.73
AR17MR-06		-26.66087	-58.63467	0.0		10670		6.18	22.43		0.98	
AR17MR-07		-26.66087	-58.63467	2.0		10520		7.79	22.00		0.94	
AR17MR-08		-26.66087	-58.63467	1.2		9830		8.90	25.41		0.77	

Note: subscript DI denotes depth-integrated values

* Indicates tributary reach upstream of the mainstem Rio Bermejo

[a] Measured downstream from the Rio Bermejo-Rio San Francisco confluence

[b] Measured with a pressure transducer attached to the water sampling bottle

[c] Measured by ADCP in bottom track mode

[d] Suspended sediment concentration; calculated as dry sediment weight divided by total water volume filtered

[e] Median grain size

[f] Specific surface area

[g] percentage of grains below 63 µm diameter, calculated from sample grain size distributions

Table A2. Individual sample and depth-integrated Beryllium concentrations.

Sample ID	Distance downstream	$[^{10}Be]_m$*	$[^{10}Be]_{m\text{-}DI}$	$[^{9}Be]_{reac}$	$[^{9}Be]_{reac\text{-}DI}$	$(^{10}Be/^{9}Be)_{reac}$	$(^{10}Be/^{9}Be)_{r\ eac\text{-}DI}$	$[^{10}Be]_{norm}$	$[^{10}Be]_{norm\text{-}DI}$
	km	x10^7 at g^{-1}	x10^7 at g^{-1}	x10^{16} at g^{-1}	x10^{16} at g^{-1}	x10^{-10}	x10^{-10}	x10^7 at g^{-1}	x10^7 at g^{-1}
AR17MR-30	RSF	0.21 ± 0.01	0.54 ± 0.0	0.55 ± 0.03	1.46 ± 0.91	3.87 ± 0.35	3.76 ± 0.11	0.21 ± 0.05	0.97 ± 0.1
AR17MR-31		0.86 ± 0.04		2.37 ± 0.14		3.64 ± 0.29		0.86 ± 0.2	
AR17DS-001	-20	1.45 ± 0.06		2.89 ± 0.17		5.01 ± 0.37		1.45 ± 0.33	
AR17MR-24	-10	1.37 ± 0.08	0.89 ± 0.1	3.46 ± 0.21	2.26 ± 0.1	3.95 ± 0.33	3.82 ± 0.32	1.37 ± 0.31	0.89 ± 0.08
AR17MR-25		0.94 ± 0.06		2.5 ± 0.15		3.75 ± 0.32		0.94 ± 0.22	
AR17MR-26		1.06 ± 0.06		2.5 ± 0.15		4.24 ± 0.34		1.06 ± 0.24	
AR17MR-27		0.13 ± 0.02		0.39 ± 0.02		3.3 ± 0.47		0.13 ± 0.03	
Confluence			0.86 ± 0.1		2.19 ± 0.92		3.81 ± 0.34		0.90 ± 0.08
AR17MR-32	135	1.4 ± 0.06	1.25 ± 0.08	2.5 ± 0.15	2.34 ± 0.09	5.59 ± 0.41	5.33 ± 0.17	1.4 ± 0.32	1.25 ± 0.04
AR17MR-33		0.95 ± 0.05		1.84 ± 0.11		5.14 ± 0.39		0.95 ± 0.22	
AR17MR-34		1.12 ± 0.06		2.12 ± 0.13		5.28 ± 0.42		1.12 ± 0.26	
AR17MR-35		1.52 ± 0.07		2.87 ± 0.17		5.31 ± 0.39		1.52 ± 0.34	
AR17MR-36		0.31 ± 0.02		0.62 ± 0.04		5 ± 0.39		0.31 ± 0.07	
AR17MR-11	422	2.3 ± 0.08	1.61 ± 0.11	4.7 ± 0.28	2.91 ± 0.11	4.89 ± 0.34	4.78 ± 0.2	2.3 ± 0.52	1.39 ± 0.05
AR17MR-12		1.54 ± 0.06		3.07 ± 0.18		5 ± 0.36		1.54 ± 0.35	
AR17MR-13		1.28 ± 0.05		2.72 ± 0.16		4.7 ± 0.34		1.28 ± 0.29	
AR17MR-14		1.4 ± 0.06		3.03 ± 0.18		4.63 ± 0.34		1.4 ± 0.32	
AR17MR-42	865	1.16 ± 0.07	2.29 ± 0.34	1.72 ± 0.1	3.14 ± 0.39	6.75 ± 0.56	7.15 ± 0.27	1.16 ± 0.27	2.29 ± 0.07
AR17MR-43		2.44 ± 0.11		3.29 ± 0.2		7.42 ± 0.56		2.44 ± 0.55	
AR17MR-44		2.91 ± 0.12		3.9 ± 0.23		7.47 ± 0.55		2.91 ± 0.66	
AR17MR-45		3.18 ± 0.14		4.38 ± 0.26		7.25 ± 0.54		3.18 ± 0.72	
AR17MR-46		0.31 ± 0.02		0.5 ± 0.03		6.12 ± 0.59		0.31 ± 0.07	
AR17MR-05	1221	2.49 ± 0.09	2.99 ± 0.4	2.59 ± 0.16	3.03 ± 0.39	9.62 ± 0.68	9.37 ± 0.1	2.49 ± 0.56	2.99 ± 0.02
AR17MR-06		3.47 ± 0.12		3.6 ± 0.22		9.63 ± 0.67		3.47 ± 0.78	
AR17MR-07		2.99 ± 0.11		3.16 ± 0.19		9.45 ± 0.66		2.99 ± 0.67	
AR17MR-08		2.99 ± 0.11		3.17 ± 0.19		9.42 ± 0.66		2.99 ± 0.67	

*Mean AMS $^{10}Be/^{9}Be$ for process blanks = 1.7 ± 2.0 x10^{15}

Text A2. Grain size-specific surface area relationships

Previous studies using $^{10}Be_m$ in river sediment (Wittmann et al., 2012, 2015, 2018) calculate depth-integrated nuclide concentrations using the relationship between $[^{10}Be]_m$ and grain size. Our data show that $[^{10}Be]_m$ has a non-linear relationship with grain size, but a strong linear relationship with specific surface area in individual river depth profiles (Figure 3.3). Our data demonstrate that specific surface area (SSA) follows a power-law relationship with median grain size (D_{50}), with an exponent of 0.55 (R^2 = 0.77) (Figure A1), supporting the use of SSA for depth-integration of nuclide concentrations.

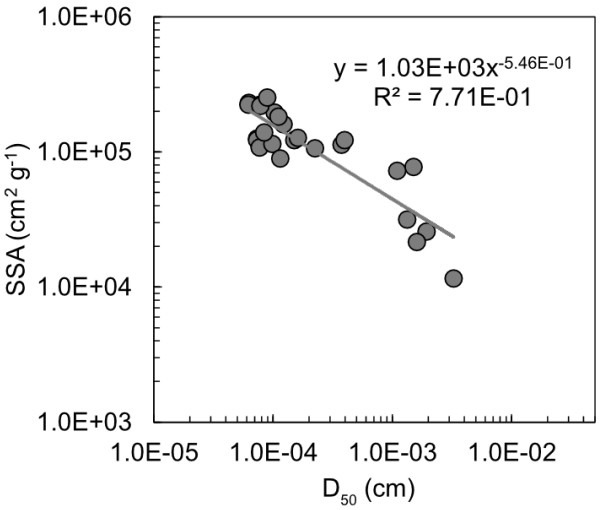

Figure A1. Median particle diameter (D50) vs. mineral specific surface area (SSA).

SSA increases from upstream to downstream (Figure A2), suggesting either grain-size fining, or increased particle irregularity through long-range transit. The former suggests selective transport of finer grain size fractions, while the latter reflects floodplain sediment weathering and development of high surface area secondary clay minerals and oxyhydroxide coatings. We evaluate sediment particle size and shape evolution using D_{50} and SSA data. Surface suspended sediment samples have the highest SSA/D_{50} ratio, suggesting that these

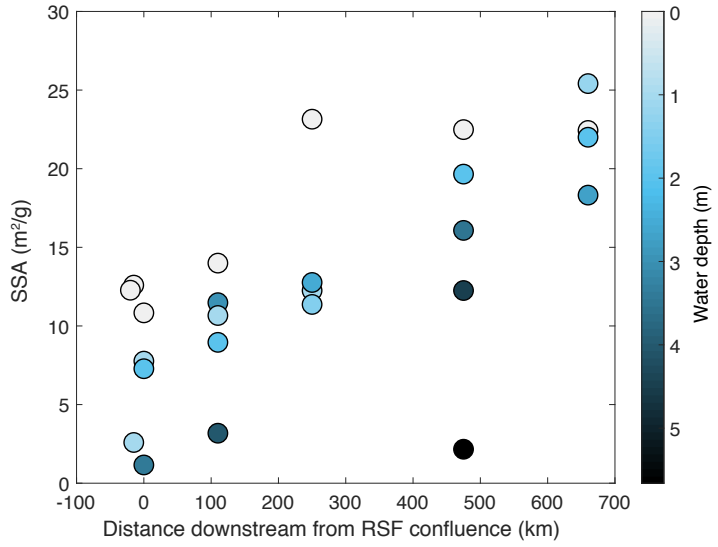

Figure A2. Specific surface area (SSA) versus distance downstream from the mountain front/RSF confluence.

particles have higher irregularity in shape and surface texture than samples at depth (Figure A3). SSA/D_{50} is generally higher downstream, suggesting that the sediment becomes more weathered during transit across the lowland floodplain. The concomitant increase in $[^{10}Be]_m$ effectively records the duration needed to produce this downstream trend in SSA/D_{50}.

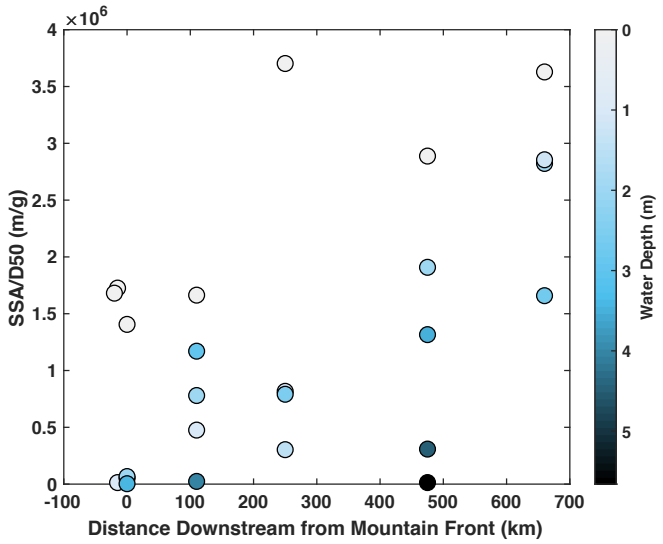

Figure A3. Specific surface area (SSA) to median grain size (D_{50}) ratio versus distance downstream from the mountain front/RSF confluence.

Text A3. Floodplain sediment: OSL ages and $^{10}Be_m$ profiles

To determine the depositional ages of the analyzed floodplain sediment cores, we applied the optically stimulated luminescence (OSL) method. We collected light-sealed samples for OSL analyses by driving an opaque tube into our floodplain cores at select depths. We processed nine samples for quartz coarse grain OSL analysis in order to retrieve sedimentation ages (Aitken, 1998) of four different floodplain deposits (Table A3). Under subdued red light, the outer 2 cm of each sample core was taken for gamma spectrometry analysis (dose rate estimation based on specific activity of U, Th, and K using a HPGe detector) and water content analysis (dose rate correction). Quartz extraction from the inner core material involved: sieving to 63-90µm, carbonate (10% HCl) and organic removal (30% H2O2), feldspar flotation (0.2% HF, pH 2.4-2.7, dodecylamine), density separation (sodium polytungstate 2.62 g/cm3 and 2.67g/cm3) and etching (40% HF). Extracted quartz was fixed on aluminum cups in grain monolayers with 2 mm diameter aliquots. Negligible infrared stimulated luminescence documented successful extraction of pure quartz without feldspar contaminations. OSL measurements were performed using a Risø DA 15 OSL/TL reader equipped with a 90Sr beta irradiator (4.9 Gy/min). OSL signals were stimulated with blue LEDs (470 nm, 50 s, 125 ºC) and detected through an optical filter (U 340 Hoya). For each sample, 40 aliquots were

measured using the single-aliquot regenerative dose (SAR) protocol (Murray and Wintle, 2000) for equivalent dose determination. Reliable OSL properties were checked based on signal recuperation, recycling ratio, sensitivity changes and dose-recovery tests (Murray and Wintle, 2003). Measured data was processed in R (https://www.R-project.org/) using the package 'Luminescence' (Kreutzer et al., 2012). Based on statistical descriptors, we used the central age model (CAM (Galbraith et al., 1999)) for luminescence age calculation. Results are reported in Table A3.

In floodplain profiles SP 2 and SP 3, we observe high $^{10}Be_m$ concentrations at depths down to 5 m (Table A4, Figure 3.5). This could suggest low $^{10}Be_m$ retention in floodplain sediments, or low sorption capacity due to grain size or aluminum concentration, which competes with Be for binding sites. With near neutral pH conditions in the Rio Bermejo river water and groundwater, $^{10}Be_m$ should be readily absorbed to sedimentary particles. Authigenic clay minerals can form during weathering in the floodplain, and mobile Be may be incorporated into their mineral lattices, which are often multi-layered and have high specific surface area.$^{10}Be_m$ can move into deeper parts of the soil column via through-flow, translocation of fine particles, or bioturbation. $^{10}Be_m$-laden waters may rapidly infiltrate soils with high through-flow rates, depending on grain size and porosity. Below we evaluate the possibility for ^{10}Be loss from fluvial sediment in the Rio Bermejo system.

Clay content of sediment appears to have some control on the retention of $^{10}Be_m$ in floodplain sediment (Figure A4), as shown in other studies (e.g. Graly et al., 2010; Wyshnytzky et al., 2015). SP 2, the oldest profile located near downstream km 422 (OSL depositional age of 13.3-20.2 kyr), has near uniform clay content with depth, and a near uniform $^{10}Be_m$ concentration. SP 3 (OSL depositional age of 2.1-3.7 kyr) also has near uniform clay content throughout, but has a broader range of $^{10}Be_m$ concentrations. In a closed system, we can estimate the expected $^{10}Be_m$ inventories in the soil profile, assuming a constant $F^{10}Be_m$ since deposition (3.00×10^6 at cm^{-2} yr^{-1}). For SP 2, we would expect an inventory of 4.0×10^{10} – 6.6×10^{10} at cm^{-2}, and our calculated inventory based on profile concentrations is 2.2×10^{10} at cm^{-2}. This discrepancy represents a possible 45-65% loss of $^{10}Be_m$ from the upper 5 m of the floodplain at site SP 2, likely due to downward percolation of meteoric waters through relatively coarse floodplain sediments. For SP 3, with deposition dated to 2.1-3.7 ka, we would expect an inventory of 6.3×10^9 to 1.1×10^{10} at cm^{-2}, and our calculated inventory based on profile concentrations is 6.44×10^9 at cm^{-2}. This discrepancy represents a potential 0-46% loss of $^{10}Be_m$ from the upper 5 m of the floodplain at site SP 2. Because our sediment profiles do not go

deeper than 5 m, we do not know whether high $^{10}Be_m$ concentrations persist to greater depths. If high concentrations do persist down to 8 m, or about the full depth of the floodplain above the channel bottom, it would be possible to have full $^{10}Be_m$ retention in floodplain sediment.

Table A3. Optically stimulated luminesce results for floodplain sediment cores.

Soil Profile ID	Sample Name	Depth	Aliquot mass	N	PD	error	skewness	DRtest	age	error
		[cm]	[mg]		[Gy]	[Gy]		vDR [%]	[yr]	±
SP1	AR16JS19-A	190-215	1900	36	1.36	0.036	0.84	9.2	900	100
	AR16JS19-B	210-235	1900	36	2.7	0.12	0.64	5.85	1700	200
SP2	AR16JS10-A	490-515	2000	35	27.23	1.39	0.27	3.9	17700	2500
	AR16JS10-B	510-530	2000	35	23.45	0.88	0.41	3.15	15300	2000
SP3	AR16JS08-B	480-505	1000	35	10.31	0.28	0.04	6.05	3300	400
	AR16JS08-C	50-75	2000	39	7.32	0.24	0.08	3.5	2400	300
	AR16JS08-D	75-100	1700	34	8.81	0.3	0.44	4.4	2900	400
SP4	AR16JS15-A	150-175	2000	36	1.29	0.031	0.6	10.95	500	100
	AR16JS15-B	175-200	1100	34	2.02	0.063	0.61	6	800	100

OSL analysis used quartz of 63-90 µm, 2 mm aliquots and the central age model (CAM, Galbraith et al., 1999). N = number of accepted aliquots (recuperation < 5%, recycling ration < 10%, equivalent dose error < 10%), PD = paleodose calculated using the CAM, DR-test = dose recovery test, vDR = coefficient of variation calculated based on dose-recovery tests.

Table A4. Data collected for samples in floodplain sediment profiles SP1 to SP4.

Sample ID	Soil Profile ID	Latitude	Longitude	Deposit Age Range[a]	Sample Mid-Depth[b]	D_{50}	Clay content	$[^{10}Be]_m$	$[^{9}Be]_{reac}$	$(^{10}Be/^{9}Be)_{reac}$
		Decimal degrees	Decimal degrees	kyr	cm	µm	%	x10^{7} at g^{-1}	x10^{16} at g^{-1}	x10^{-10}
19 - 0	SP1	-23.3574	-63.51871	0.8-1.9	10	3.01	33.75	4.89 ± 0.18	7.11 ± 0.36	6.87 ± 0.43
19 - 20					35	3.15	32.93	4.71 ± 0.16	8.17 ± 0.41	5.76 ± 0.35
19 - 50					70	4.51	29.98	2.31 ± 0.12	4.85 ± 0.24	4.77 ± 0.34
19 - 130					150	79.64	3.37	0.8 ± 0.05	2 ± 0.1	4.01 ± 0.32
19 - 225					230	170.97	0.72	0.28 ± 0.07	0.81 ± 0.04	3.45 ± 0.88
10-0	SP2	-24.0963	-61.94221	13.3-20.2	10	175.69	3.31	2.78 ± 0.14	0.88 ± 0.04	3.18 ± 0.23
10-20					35	184.97	2.95	2.59 ± 0.25	0.8 ± 0.04	3.22 ± 0.35
10-50					70	198.28	3.46	2.85 ± 0.15	1.05 ± 0.05	2.71 ± 0.2
10-130					150	177.64	6.71	2.96 ± 0.21	1.3 ± 0.06	2.28 ± 0.2
10-210					230	201.56	4.01	2.71 ± 0.2	1.19 ± 0.06	2.27 ± 0.2
10-290					310	187.48	4.01	2.27 ± 0.12	1.18 ± 0.06	1.92 ± 0.14
10-370					390	200.39	3.14	2.31 ± 0.17	0.96 ± 0.05	2.4 ± 0.21
10-450					470	196.87	3.89	2.52 ± 0.24	1.11 ± 0.06	2.27 ± 0.25
8-0	SP3	-24.2417	-61.9421	2.1-3.7	10	36.80	4.93	3.36 ± 0.2	1.56 ± 0.08	2.15 ± 0.17
8-20					35	41.89	5.29	3.04 ± 0.27	1.84 ± 0.09	1.65 ± 0.17
8-140					160	54.93	4.23	1.56 ± 0.14	1.94 ± 0.1	0.8 ± 0.08
8-220					240	66.98	3.43	0.9 ± 0.16	1.12 ± 0.06	0.8 ± 0.15
8-300					320	37.97	5.10	1.81 ± 0.16	2.58 ± 0.13	0.7 ± 0.07
8-340					360	19.01	7.49	1.97 ± 0.16	2.69 ± 0.13	0.73 ± 0.07
8-380					400	29.93	5.94	2.42 ± 0.16	3.34 ± 0.17	0.72 ± 0.06
8-420					440	15.16	8.84	2.31 ± 0.16	3.2 ± 0.16	0.72 ± 0.06
15 - 0	SP4	-25.7924	-60.14648	0.4-0.9	10	19.79	5.68	2.13 ± 0.12	3.1 ± 0.16	6.85 ± 0.52
15 - 20					35	15.32	7.49	1.92 ± 0.08	3.06 ± 0.15	6.29 ± 0.42
15 - 50					70	15.08	8.14	2.01 ± 0.12	3.56 ± 0.18	5.65 ± 0.43
15 - 130					150	66.21	3.12	0.74 ± 0.06	1.58 ± 0.08	4.7 ± 0.46
15 - 210					230	71.20	2.69	0.81 ± 0.08	1.86 ± 0.09	4.34 ± 0.5
15 - 330					350	84.16	1.57	0.47 ± 0.06	1.29 ± 0.06	3.69 ± 0.49
15 - 370					390	114.74	0.42	0.43 ± 0.07	1.03 ± 0.05	4.2 ± 0.73

[a]OSL ages reported in Supporting Information Table A3

[b]Mid-point of a sample that integrates over a larger depth interval

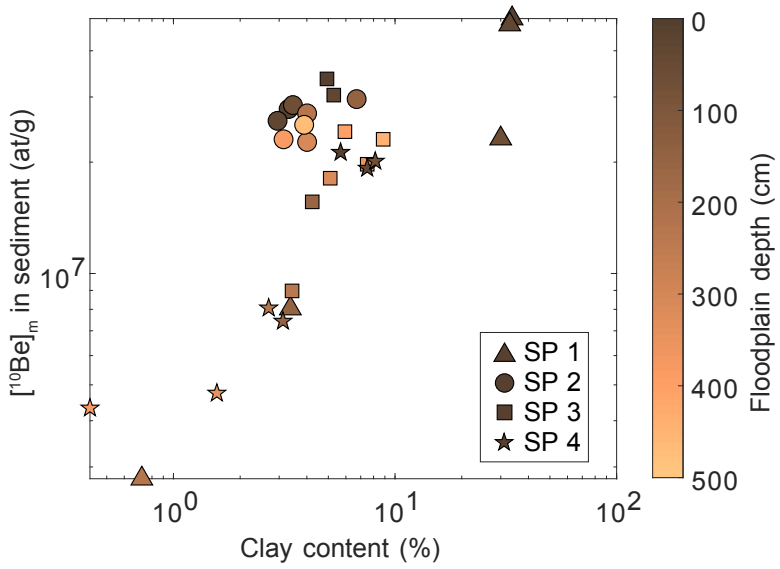

Figure A4. Floodplain sediment clay content versus $[^{10}Be]_m$, with samples colored by depth in the sediment profile (dark brown at the surface, and yellow at depth).

Text A4. Estimating sediment transit time with volumetric sediment budgeting

A4.1 Theory

Here we estimate sediment transit time using a volumetrically-balanced sediment budget approach, assuming the river system is in a volumetric steady-state over 10^4 yr timescales. While sediment flux and channel geometry likely vary over this timescale, such variability is difficult to measure, and, lacking better data, we use modern channel morphometrics in our analysis below. The estimates calculated here require numerous assumptions to be made, including a river system that is in a volumetric steady-state over 10^4 yr. Our goal is to exploit basic principles of mass balance to derive a simple set of equations to predict mean sediment transit times over large spatial (~10^3 km) and temporal scales (~10^4 km) (*sensu* Dietrich et al., 2003). Accordingly, we adopt a conceptual model, similar to the Rio Bermejo system, where a lowland river has built a large fluvial fan where sediment is stored. We assume the channel continually migrates back and forth across an active channel belt that occupies a small portion of the total fan surface area. The channel periodically avulses to occupy new areas of the fan, repeating this process until the entire fan surface has been reworked. This conceptual model allows for two separate transit time estimates, a relatively short transit time that represents the time for sediment to transit the active channel belt, and a relatively long transit time that accounts for the timescale of sediment storage outside of the active channel belt.

We estimate the transit time of sediment through the active channel belt, t_{belt}, as:

$$t_{belt} = n_{trans} * t_c \,, \quad \text{(A1)}$$

where n_{trans} is the number of individual transport events needed to transit a channel of length, l, and t_c is a characteristic sediment storage timescale. Following Torres et al (2017), we solve the number of transport events as:

$$n_{trans} = \frac{l}{x_{trans}} . \quad \text{(A2)}$$

Here, x_{trans} is a bulk sediment transport length scale, which represents the average distance needed to exchange the fluvial sediment load with the floodplain and can be solved as:

$$x_{trans} = \frac{Q_s}{m_{lat} * h}, \quad \text{(A3)}$$

where Q_s is the volumetric sediment flux, m_{lat} is the lateral channel migration rate, and h is the mean channel incision depth, which are assumed to be spatially and temporally constant over the time and length scales of interest. If Q_s is high (with all else held constant), x_{trans} must increase to exchange all in-channel sediment with floodplain sediment, leading to a shorter t_{belt}. Conversely, if channel migration rates are high (with all else held constant), sediment can be fully exchanged over a short x_{trans}, creating more storage events and a longer t_{belt}. We estimate t_c as the time needed to rework sediment across the active channel belt, under four simplifying assumptions: (1) the active channel belt maintains a constant width through time, (2) lateral channel migration rate is constant in time, (3) the river migrates continually and steadily in one direction across the channel belt and only reverses course upon reaching the active channel belt boundary, and (4) sediment is eroded exclusively from within the active channel belt. Under these assumptions, we calculate t_c as:

$$t_c = \frac{w_{belt}}{m_{lat}}, \quad \text{(A4)}$$

where w_{belt} is the mean width of the active channel belt and m_{lat} is the mean lateral channel migration rate. Combining Equations (A1) to (A4) yields a composite equation for t_{belt}:

$$t_{belt} = n_{trans} * t_c = \frac{l\, m_{lat}\, h}{Q_s} * \frac{w_{belt}}{m_{lat}} . \quad \text{(A5)}$$

Importantly, assumptions (3) and (4) above ensure that t_{belt} approximates a relatively short timescale by excluding the influence of eroding sediment from outside of the channel belt that may be stored for timescales significantly longer than t_c.

To account for reworking of material outside of the active channel belt we consider the timescale of channel avulsion, following Jerolmack & Mohrig (2007). We estimate a sediment

storage timescale based on the time needed for a periodically avulsing river to rework the entire Bermejo fluvial fan, using the following set of equations. The time needed to rework the entire fan, t_{fan}, can be expressed as:

$$t_{fan} = t_a * \mathrm{N}_a * R_t, \quad \text{(A6)}$$

where t_a is a characteristic avulsion timescale, which approximates the average amount of time between two channel avulsions, N_a is the number of avulsions needed to rework sediment across the megafan, and R_t is a scaling ratio between the avulsion timescale and the time needed to transit the channel belt. Following Jerolmack and Mohrig (2007) we estimate t_a as:

$$t_a = \frac{h_{apex}}{v_{agg}}, \quad \text{(A7)}$$

where h_{apex} is the channel incision depth near the fan apex where the avulsion node is located, and v_{agg} is a representative aggradation rate for the Bermejo channel belt. When t_a is reached, the channel will have aggraded its full depth and overtopped its levees, to allow avulsion to a new location in an adjacent topographic low. We estimate a characteristic v_{agg} as:

$$v_{agg} = \frac{Q_{s,up} - Q_{s,down}}{A_{belt}}, \quad \text{(A8)}$$

where $Q_{s,up}$ and $Q_{s,down}$ are the volumetric sediment discharges into and out of the fluvial fan and A is the area of the active channel belt where the modern river frequently floods and deposits sediment.

We approximate the number of avulsions theoretically needed to rework sediment across the fan, N_a, as:

$$N_a = \frac{w_{fan}}{w_{belt}}, \quad \text{(A9)}$$

where w_{fan} is the average cross-sectional width of the fluvial fan, and w_{belt} is the width of the active channel belt, which we assume is constant on average over the duration of fluvial fan development.

If t_a is shorter than t_{belt}, an avulsion will occur before all sediment in the channel belt has been transported out of the system. To account for the additional time needed to evacuate all sediment within each channel belt after the fan has been reworked by N_a avulsions, the total sediment transit time needs to be scaled by R_t, the scaling ratio of t_{belt} to t_a:

$$R_t = \frac{t_{belt}}{t_a}. \quad \text{(A10)}$$

Combining Equations (A6) to (A10) yields a composite equation for t_{fan} as follows:

$$t_{fan} = \frac{h_{apex}\ w_{fan}}{v_{agg}\ w_{belt}} * \frac{t_{belt}}{t_a}, \quad \text{(A11)}$$

which approximates the average bulk transit time for sediment delivered from the eroding mountains to the fluvial fan over the last 10^4 years.

A4.2 Transit time estimates

Parameters needed to apply the sediment budget transit time framework to the Rio Bermejo were constrained using methods described in Text A1, and values are reported in Table A1. We estimate x_{trans} ~278 km, using the sediment flux recorded at the downstream-most gauging station, and n_{trans} ~4.4, suggesting that sediment particles are exchanged between the channel and floodplain ~4.4 times on average over a transit distance of 1221 km between the upstream and downstream-most sampling sites (Table A2). The active channel migrates laterally at a rate of 18 m yr^{-1} across its $2.51x10^3$ m-wide belt, suggesting that the time needed to rework sediment across the active channel belt, T_c, ~0.14 kyr. Applying Equation (A5) yields a total mean channel belt transit time $t_{belt} \approx$ 0.61 kyr.

To calculate v_{agg} for the Rio Bermejo, we employ Equation (A8) setting $Q_{s\text{-}up}$ and $Q_{s\text{-}down}$ equal to the volumetric sediment fluxes at the Rio Bermejo-Rio San Francisco confluence and El Colorado (river km 942), respectively. A_{belt} is the area of the active channel belt between the two gauging stations. Using the values reported in Table A1, we determine that the Rio Bermejo deposits ~23 Mt of sediment per year onto the area A_{belt}, resulting in a minimum v_{agg} of 3.6 mm yr^{-1} (Table A2). We evaluate the avulsion timescale, t_a, for the ~1.5 m deep braided reach, which contains the avulsion node (Page, 1889), yielding ~0.41 kyr as the average time between two avulsion events, t_a. In order to rework the $8.5x10^4$ m-wide megafan, the river would theoretically need $N_a = 34$. Because t_a is shorter than t_{belt}, each avulsion will likely occur before all sediment within the active channel belt has been transported out of the system, so although avulsions have swept across the entire fan, a fraction of sediment from each pre-existing channel belt may still be stored in the fan. To account for the additional time needed to transport this relict sediment out of the fan, we calculate the scaling ratio, $R_t = 1.51$, implying that ~51 avulsions are needed to export all initial sediment from the fluvial fan system. Finally we use Equation (A11) to estimate a $t_{fan} \approx$ 20.7 kyr, the theoretical time needed for all sediment entering the fan to be transported out of the system.

Table A5. Channel metrics and sediment budget data for the Rio Bermejo.

Parameter (units)	Notation	Value
Mean channel migration rate (m yr^{-1})	m_{lat}	18
Mean incision depth (m)	h	6.03 ± 2.12
Mean channel width (m)	w	414
Mean channel belt width (m)	w_{belt}	2.52 $x10^3$
Channel length (km)	l	1.27 $x10^6$
Area of active channel belt (m^2)	A_{belt}	2.41 $x10^9$
Fan width (m)	w_{fan}	8.50 $x10^4$
Upstream sediment flux ($m^3\ yr^{-1}$)	$Q_{s\text{-}up}$	3.89 $x10^7$
Downstream sediment flux ($m^3\ yr^{-1}$)	$Q_{s\text{-}down}$	3.02 $x10^7$
Channel incision depth near fan apex (m)	h_{apex}	1.46

Table A6. Sediment budget-based transit time estimates for the Rio Bermejo.

x_{trans}	n_{trans}	t_c	t_{belt}	v_{agg}	t_a	N_a	R_t	t_{fan}
km		kyr	kyr	m yr^{-1}	kyr			kyr
278	4.4	0.14	0.61	$3.60x10^{-3}$	0.41	34	1.51	20.7

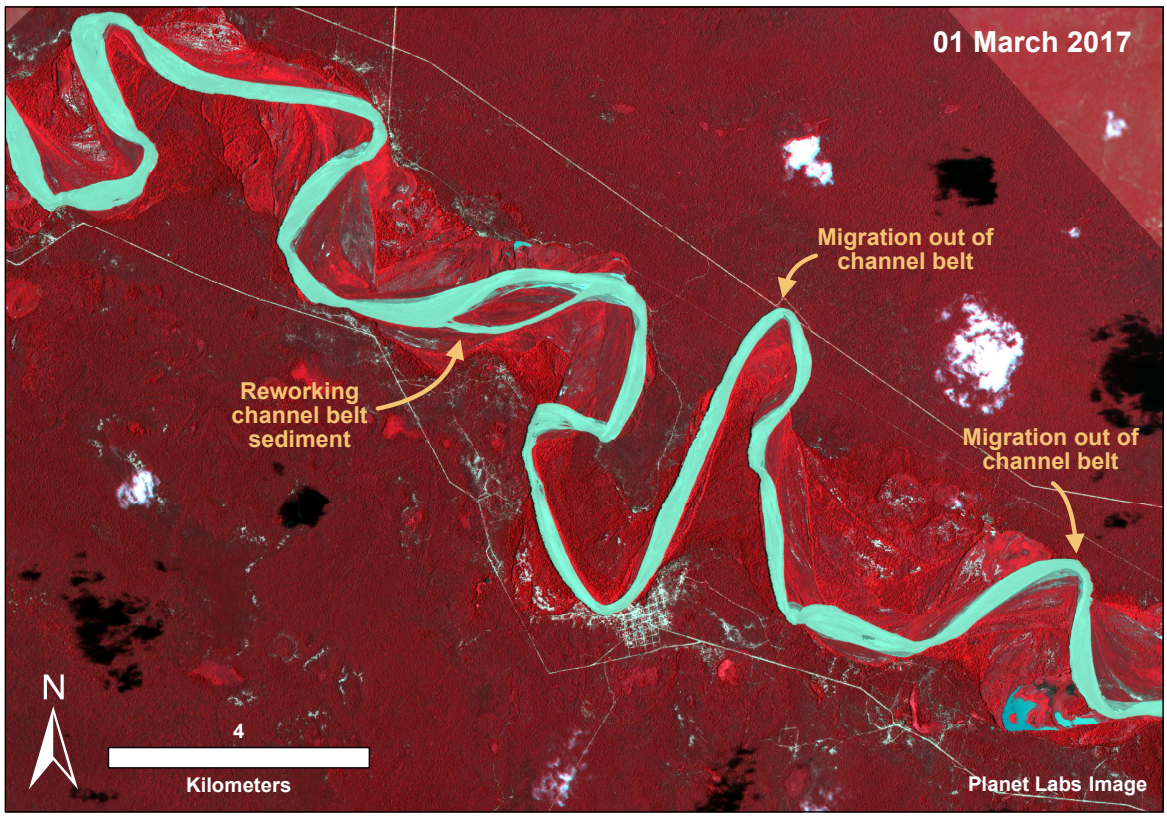

Figure A5. False color Planet satellite image (3 m resolution) of the Rio Bermejo highlighting examples of locations where the channel is breaching the modern channel belt and eroding into old fluvial fan deposits vs. reworking active channel belt sediment. Image is centered at -24.2808° latitude, -61.9103° longitude.

APPENDIX B

Supplementary Material for

Chapter 4: Hydrodynamic sorting effects on fluvial organic carbon export

Introduction

In this supplementary material, we show additional results for biomarker, NanoSIMS, and particle size measurements, which complement the data shown in the main text. Additionally, we describe the methodology used to calculate particle settling velocity and estimate the fluxes of POC associated with different grain size fractions. We also provide supplementary figures and tables referenced in the main text.

Text B1. Additional NanoSIMS data

Figures B1 and B2 show additional NanoSIMS images of discrete organic particles and mineral-associated organic carbon, respectively, within aliquots of river suspended sediment from the Rio Bermejo. In general, the NanoSIMS data show that discrete organic particles have low ^{14}N content, suggesting that these organic particles are plant derived and not microbially-processed. This is not the case for particles identified as fungal hypha (Fig. B1), which are known to be enriched in nitrogen. Discrete organic particles also have very low ^{16}O secondary ion signals, supporting the hypothesis that these particles are composed of reduced organic compounds, and are likely derived from fresh plant material (Fig. B3). Mineral-associated organic matter (Fig. B2) often has a high ^{14}N secondary ion intensity, co-located with ^{12}C. In addition to NanoSIMS analyses of river suspended sediment, we investigated several aliquots of floodplain sediment sampled from different depths (Fig. B4). NanoSIMS images for floodplain sediment show that ^{12}C and ^{27}Al are generally co-located in <4 μm particles, supporting the hypothesis that the fine, mineral-associated organic carbon in surface water samples is derived from weathered floodplain soil and sediment. Interestingly, we observed very labile organic matter in shallow floodplain soil (20-50 cm), such that it was dissolved during sample preparation in milliQ water, and/or destabilized by the electron beam during SEM analysis (Fig. B4). This suggests the presence of labile organic carbon that can be transferred to the dissolved phase with rainfall and runoff, or in river water when floodplain sediment is entrained via lateral channel migration.

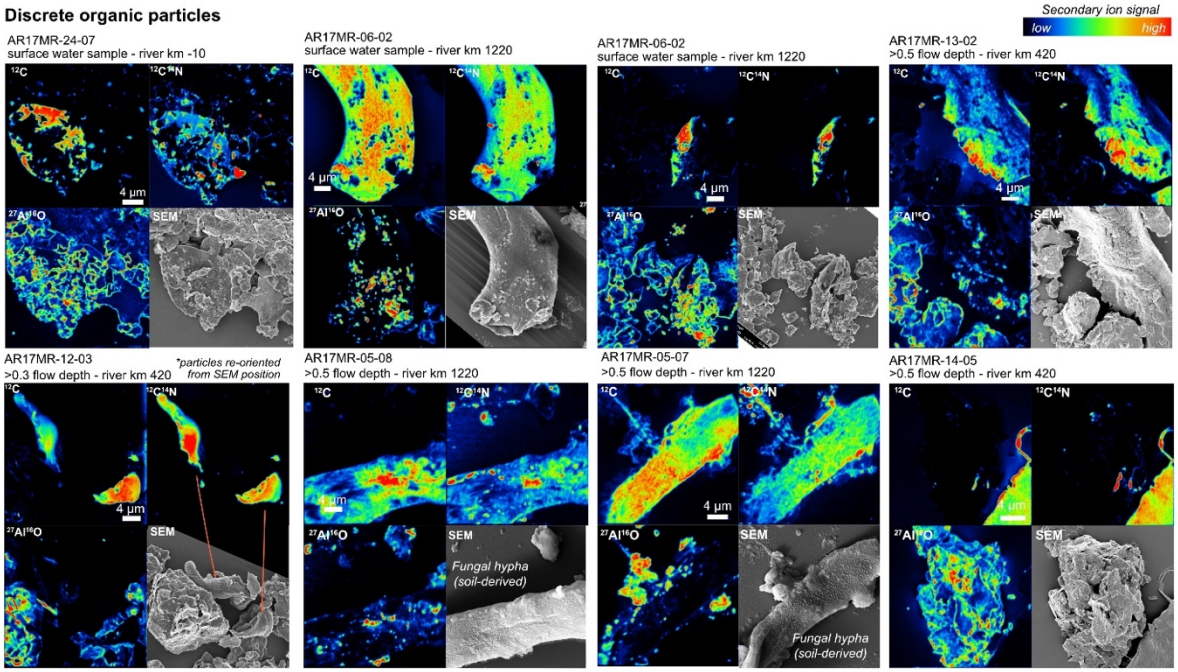

Figure B2. Eight additional examples of discrete organic particles identified by NanoSIMS. For each area of interest (AOI), we show ^{12}C, $^{12}C^{14}N$, and $^{27}Al^{16}O$ ion images, and an SEM image.

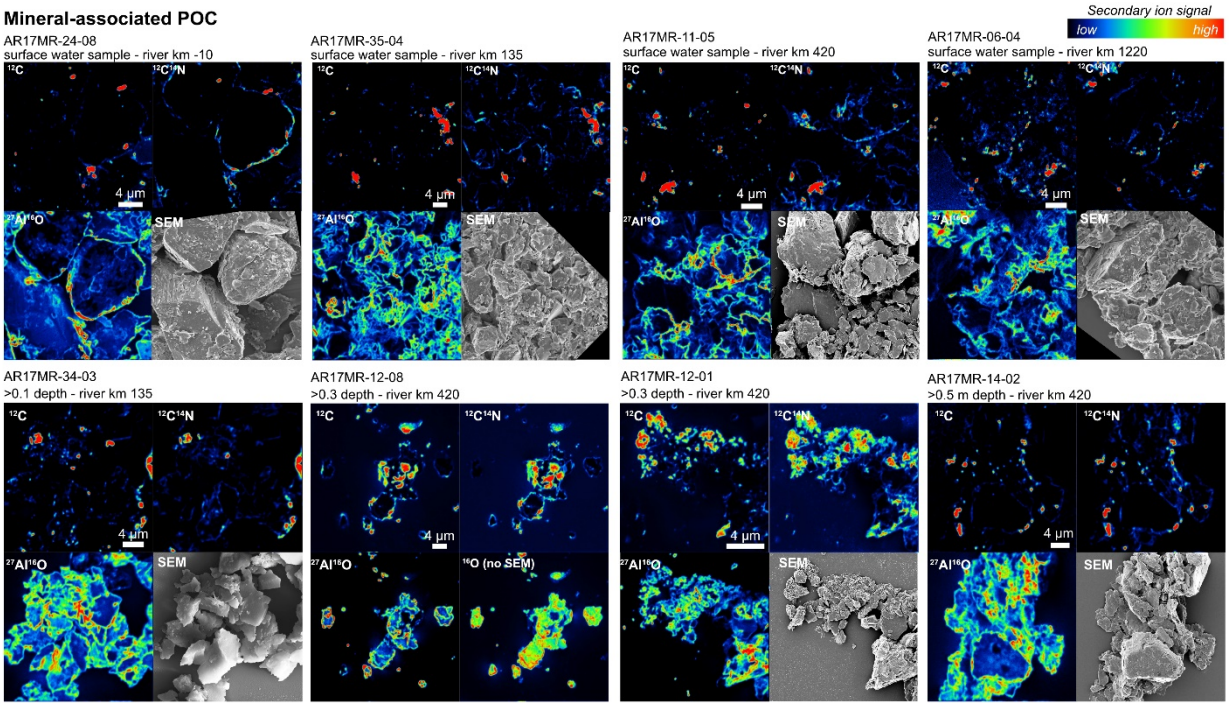

Figure B3. Eight additional examples of mineral-associated organic carbon identified by NanoSIMS. For each AOI, we show ^{12}C, $^{12}C^{14}N$, and $^{27}Al^{16}O$ secondary ion images, and an SEM image.

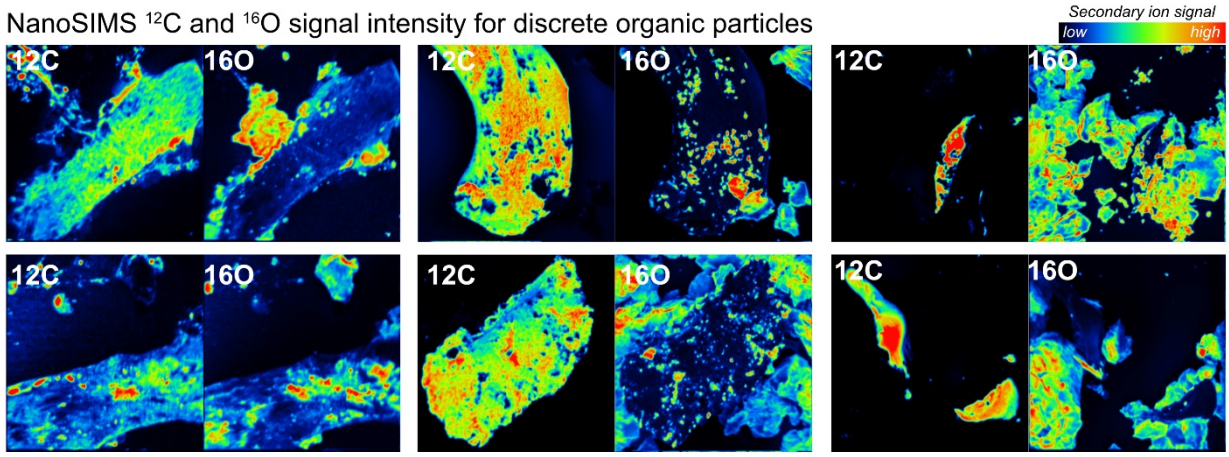

Figure B3. NanoSIMS images showing ^{12}C and ^{16}O signals for six examples of discrete organic particles. Low oxygen content is indicative of reduced organic matter, whereas higher oxygen content is characteristic of mineral particles (e.g., quartz, silicates, oxyhydroxides).

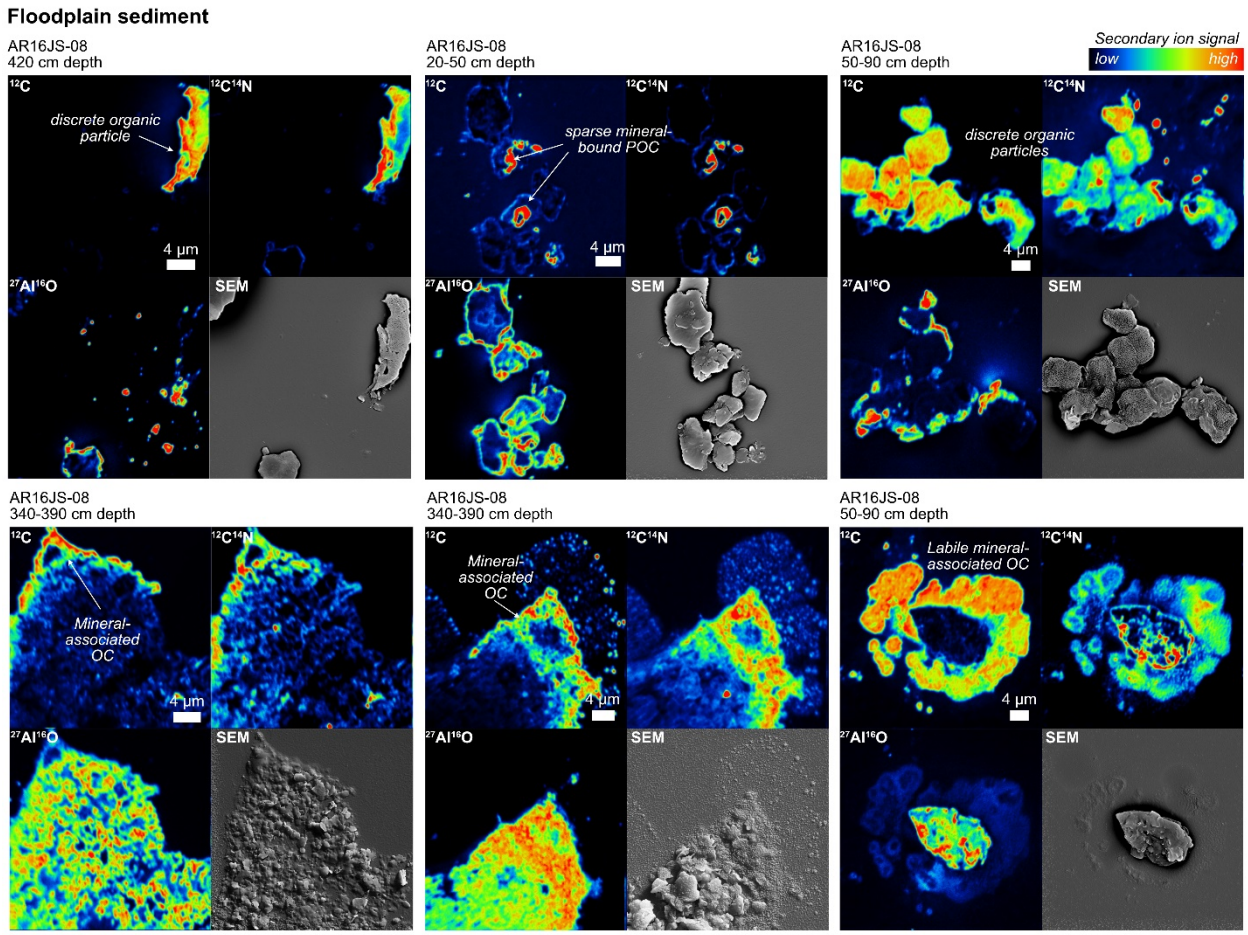

Figure B4. NanoSIMS signal intensity maps and SEM images of six AOIs selected from aliquots of floodplain sediment. Images highlight both mineral-associated organic matter and discrete organic particles.

Text B2. *n*-alkane isotope composition and seasonality

n-alkanes in river suspended sediment

We compared the mean *n*-alkane distribution of surface water suspended sediment samples and samples from >0.1 flow depth (**Fig. B5**). Overall, surface water samples have higher *n*-alkane concentrations per gram sediment than samples from depth, likely because deeper samples have coarser grains with higher mineral mass. While still dominated by nC_{27} to nC_{33} alkanes, surface water samples had higher concentrations of nC_{17} to nC_{25} alkanes, which may be derived from aquatic algae/phytoplankton (Bush & McInerney, 2013) or possibly microbial degradation (Hirave et al., 2020).

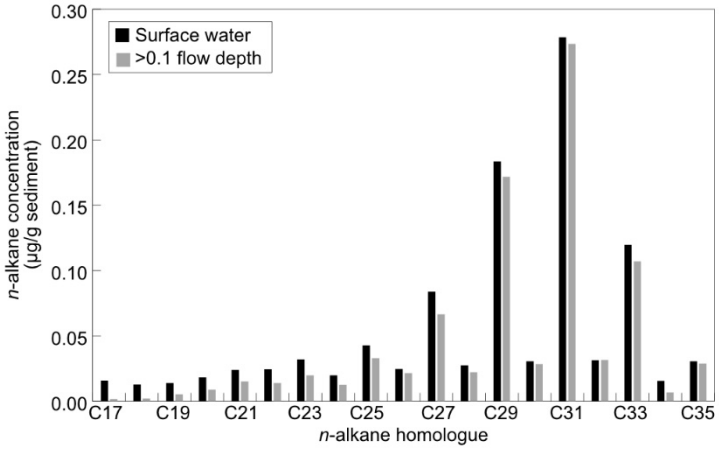

Figure B5. Mean *n*-alkane distributions for surface water suspended sediment (black) and suspended sediment sampled >0.5 m below the surface (gray).

$\delta^{13}C_{alk}$ of the nC_{27}, nC_{31}, and nC_{33} also revealed a strong difference between surface water and samples collected from >0.1 flow depth, supporting the vertical sorting of POC in the water column (**Fig. B6**). *n*-alkane $\delta^{13}C$ and $\delta^{2}H$ values for the fine and coarse fractions remained relatively constant during long distance river transport, through multiple episodes of

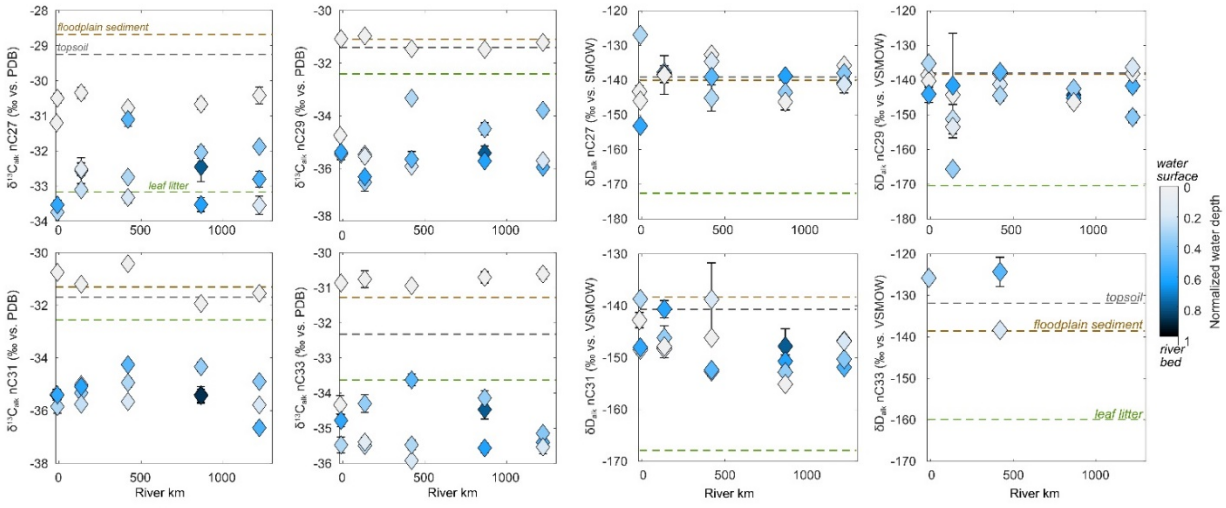

Figure B6. $\delta^{13}C_{alk}$ and $\delta^{2}H_{alk}$ values for C27-C33 odd *n*-alkane homologues plotted against distance downstream along the channel. River km 0 represents the Bermejo-San Francisco confluence at the mountain front. Samples are colored by their relative depth within the water column. Error bars represent analytical uncertainty determined by triplicate or duplicate measurements. Horizontal dashed lines represent the mean values of POC sources in the Bermejo lowland basin (leaf litter = green, topsoil = gray, floodplain sediment = brown).

deposition and erosion along the channel. However, the δ^2H_{alk} values for nC_{31} alkanes gradually became more depleted with increasing distance downstream, possibly suggesting increased input of grasses from the floodplain, which tend to have more negative δ^2H_{alk} values than shrubs (Sachse et al., 2012). Overall, δ^2H_{alk} values for Rio Bermejo suspended sediment are more variable than $\delta^{13}C_{alk}$ values (**Fig. B6**). While we observed a strong vertical sorting effect on $\delta^{13}C_{alk}$ values in the suspended load, there was no apparent systematic vertical sorting effect on δ^2H_{alk} values, suggesting that hydrogen isotopes are relatively insensitive to alteration during episodes of deposition, storage and re-entrainment.

By comparing $\delta^{13}C_{OC}$ and $\delta^{13}C_{alk}$ values of river suspended POC (**Fig. B7**), we found that $\delta^{13}C_{OC}$ values were overall more positive than $\delta^{13}C_{alk}$ values. We found no statistically significant relationships between $\delta^{13}C_{OC}$ and $\delta^{13}C_{alk}$ values, together suggesting that the *n*-alkane data reveal compositional differences between surface water samples and samples from depth that cannot be detected with bulk carbon isotope analysis.

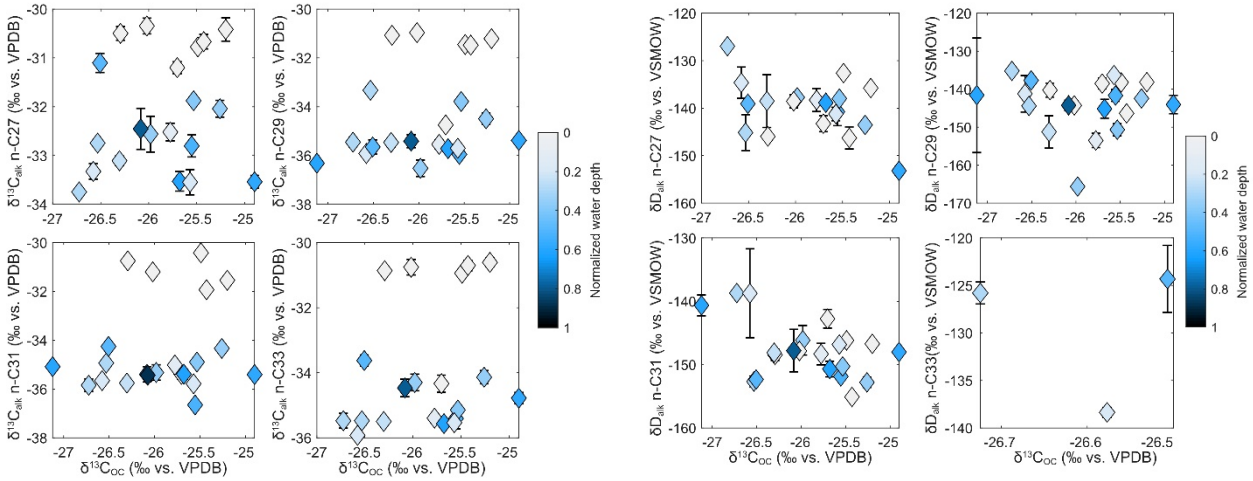

Figure B7. $\delta^{13}C_{alk}$ and δ^2H_{alk} values plotted against $\delta^{13}C_{OC}$. Samples are colored by their relative depth within the water column. Error bars represent analytical uncertainty determined by triplicate or duplicate measurements.

Text B3. Contributions of floodplain POC to river POC

Bayesian mixing model

To estimate the relative contributions of endmember OC sources to fluvial POC in the Rio Bermejo suspended sediment samples, we implemented a three-endmember Bayesian isotope mixing model using the MixSIAR package in R (Moore & Semmens, 2008; Stock et al., 2018). We estimated the relative contributions of floodplain sediment (>20 cm), topsoil (<20 cm), and leaf litter to each river sample using the $\delta^{13}C$ and $\delta^{2}H$ values of n-C_{27}, n-C_{29}, n-C_{31}, and n-C_{33} alkane compounds as tracers, totaling eight unique descriptors. We defined the endmember compositions using the descriptor means and standard deviations for sample sets of floodplain sediment (n = 15), topsoil (n = 15), and leaf litter (n = 6). Using the MixSIAR package for R, we modeled the contributions of the three sources to the river samples with a Markov Chain Monte Carlo method. We ran the model for $1x10^{6}$ iterations with an uninformative prior, a burn-in of $5x10^{5}$ iterations, a thinning factor of 500, and three chains. We tested for model convergence using the Gelman-Rubin and Geweke diagnostics. For each river sediment sample, this analysis yielded three posterior distributions containing the full range of possible fractional contributions of the three OC sources, respectively. To obtain the most probable values for each source, we calculated the mean and standard deviation of each posterior distribution.

Mixing model results

We estimated the relative contributions of floodplain sediment, leaf litter, and topsoil to actively-transported Rio Bermejo POC using a Bayesian isotope mixing model, parameterized

with $\delta^{13}C_{alk}$ and $\delta^{2}H_{alk}$ measurements from samples collected throughout the Bermejo lowland basin. While there are large uncertainties associated with the mixing model results, some general patterns can be observed by comparing the mean values of each endmember posterior distribution (**Fig. B8**, **Table B4**). We estimate that floodplain-derived POC (>20 cm soil depth) contributes 0.36-0.67, topsoil (<20 cm soil depth) contributes 0.15-0.24, and leaf litter contributes 0.11-0.45 of the isotopic composition of river suspended POC. Averaged across all samples, floodplain POC had the highest contribution to river POC (0.51±0.08). Surface water suspended sediment samples had the highest proportions of floodplain-derived POC (0.56-0.67), and the lowest proportions of leaf litter-derived POC (0.11-0.19). We observed no statistically significant downstream trends in the proportions of these three endmember POC sources.

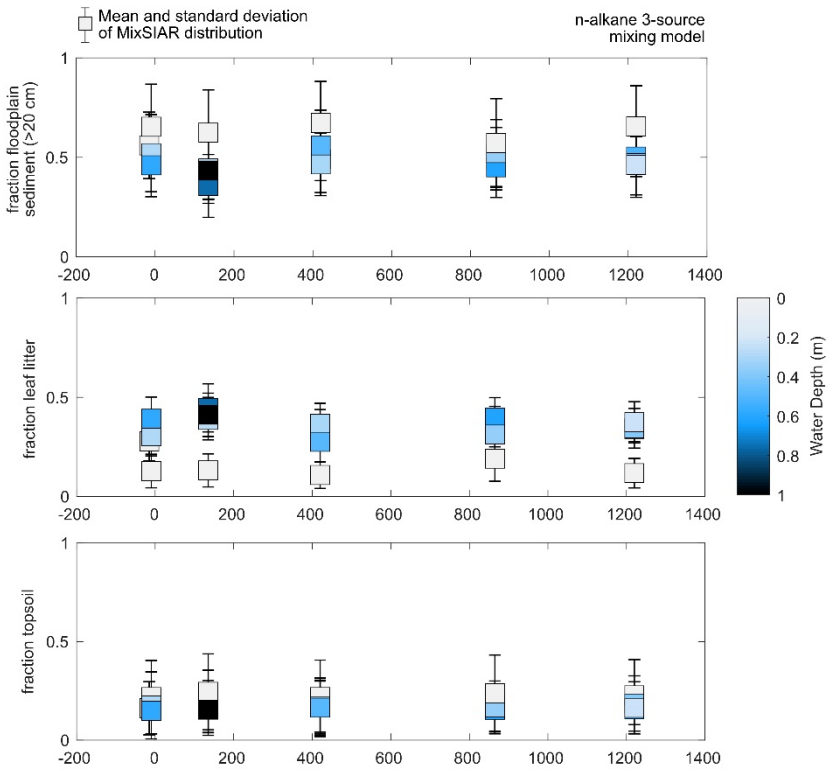

Figure B8. Relative proportions of each POC end-member to the Bermejo (floodplain sediment, leaf litter, and topsoil). Data points represent the mean values of the MixSIAR posterior distributions, and error bars represent one standard deviation from the mean. Data points are colored by their relative depth within the water column.

Text B4. Grain size distributions

Grain size distributions were generally unimodal for river bed sediment and bimodal for suspended sediment, indicating the presence of a population of fine-grained particles in the suspended load (**Fig. B9, Table B6**). In the suspended sediment distributions, the trough between the two modes has a minimum ~30 μm. Surface water suspended sediment had the

highest fraction of fine (<4 µm) sediment (f_f), ranging from 0.83-0.92 of the sample, while f_f for samples at depth (>0.5 m below the surface) was lower, ranging from 0.33-0.85. Bed sediment f_f ranged from 0.00 to 0.04, however, our bed sediment grain size distributions are likely skewed toward coarse sediment because sampling with a mesh net excluded fine grain sizes. Overall, we observed grain size coarsening from the water surface to the river bed. The largest grain sizes were observed at river km -10, where the bedload D_{50} was 325 µm. At river km 135, grain size populations were significantly finer, where the bedload D_{50} was just 133 µm.

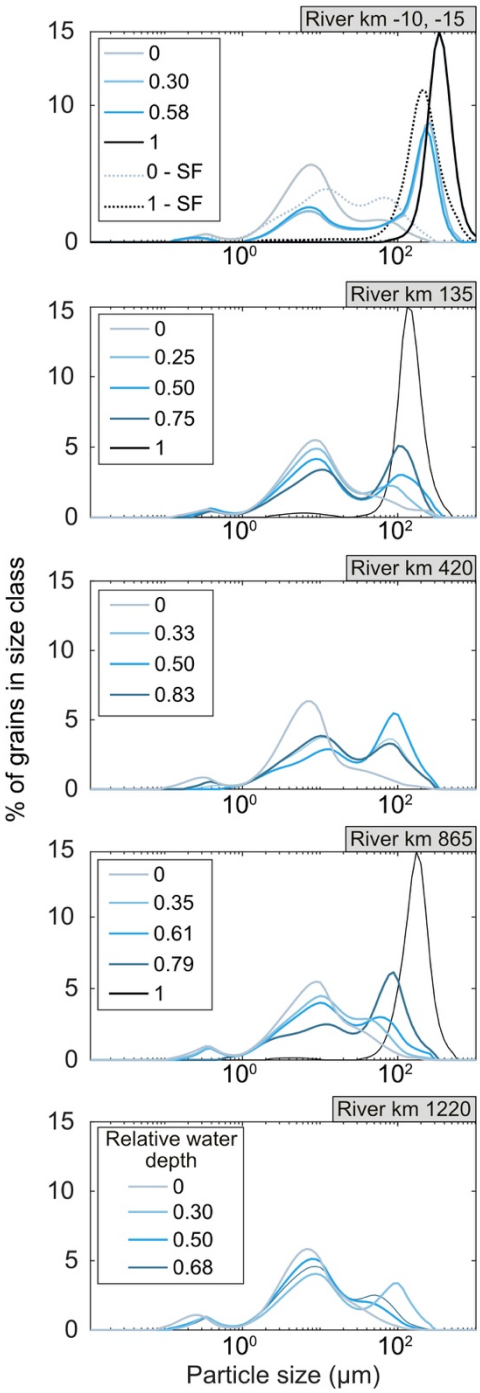

Figure B9. Particle size distributions for suspended sediment depth profile samples. The top panel shows data for the Rio San Francisco (-15 km, SF), and the Rio Bermejo upstream of the SF confluence (-10 km). Lines are colored by relative depth within the water column (light blue = surface water, black = river bed).

Text B5. Drivers of vertical POC sorting

Our data from the Rio Bermejo show that aged, ^{13}C-enriched organic matter is concentrated in <4 µm sediment at the water surface, while modern discrete organic particles dominate POC at depth (**Fig. 4.4**). This vertical distribution in the water column is driven by differences in size, shape, and density of mineral-associated POC vs. discrete organic particles. While we do not have density data, here we use particle size and shape data to determine relative particle settling velocities of these two pools.

Particle size distributions of surface water samples are characterized by one peak at ~10 µm, while samples from depth have two peaks at ~10 µm and ~100 µm (**Fig. S9**), indicating that surface water samples are characterized by the absence of coarse particles. We found no statistically significant difference between the <4 µm populations at the surface versus depth, suggesting that <4 µm mineral-bound POC is present at all depths, but the presence/absence of discrete organic particles is more important for the overall POC composition.

In SEM images, we observed that fine (<4 μm) particles often have platy shapes, which may reduce their settling velocity relative to more spherical particles (McNown & Malaika, 1950). To evaluate particle shape, we calculated the Corey Shape Factor (CSF) and particle settling velocity for 46 representative sediment particles (Dietrich, 1982).

Particle shape analysis

The Corey Shape Factor (CSF) has been used to describe the relative sphericity of sediment particles (Dietrich, 1982). We calculated the Corey Shape Factor for representative particles in aliquots taken from seven river suspended sediment samples as:

$$CSF = \frac{c}{(ab)^{1/2}} \quad \text{(B1)}$$

where *a*, *b*, and *c* are the lengths of the long, intermediate, and short axes for an individual particle, which are mutually perpendicular. Values of CSF fall between 0 and 1, with lower values representing more platy particles, and higher values representing more spherical particles. Particles with small CSF values (less spherical) have lower settling velocities than particles of the same diameter with large CSF values (more spherical).

Following equation (B1), we calculated CSF values for 46 suspended sediment particles selected from the SEM images of NanoSIMS AOIs. These aliquots represent a finer fraction of the suspended sediment, with all particles falling within the <30 μm size fraction. Analyzed particles included both discrete organic particles and mineral particles with associated organic carbon. Using Fiji/ImageJ software, we identified particles in the SEM images of the NanoSIMS AOIs. We measured major axes *a*, *b*, and *c* for 46 total particles where all three axes could be measured with confidence. This was challenging for platy particles that tend to lay flat and the short axis is not always visible, so we limited the analysis to 46 particles.

Particle settling velocity

We calculated the particle settling velocity of each particle for which CSF was measured, following Dietrich (1982). We first converted the CSF to an empirical geometric shape factor, *E*, (equation 12 in Dietrich (1982)):

$$E = CSF\left(\frac{3}{\frac{a}{b}+\frac{b}{a}+CSF^2}\right)^{1/2} \quad \text{(B2)}$$

We then calculated the particle settling velocity, W_s, for each particle using an empirical equation (equation 13 in Dietrich (1982)):

$$W_s = \frac{1}{18}\frac{1}{\mu}(\rho_s - \rho_w)gD^2E^{0.28} \quad \text{(B3)}$$

where μ is the kinematic viscosity of the water (0.8926 mm^2/s), ρ_s is the particle density, ρ_w is the water density, g is the acceleration due to gravity, and D is the median particle size of the sample.

Results

Overall, coarse particles, including discrete organic particles, have larger CSF values and higher settling velocities than fine platy particles (**Fig. 4.4, Table B5**). This drives higher concentrations of plant debris particles deeper in the water column, which is consistent with our geochemical data. While particle size is a first order control on vertical sorting, particle shape can be an important modulating factor driving differences in POC fluxes.

Text B6. POC flux calculations and Rouse profile modeling

Methods

Our goal was to calculate the instantaneous organic carbon flux, Q_s (kg/s), for two particle size fractions (<4 μm and >4 μm) at each sampling station along the Rio Bermejo. First, we calculated the suspended sediment fluxes for each particle size fraction following the generalized equation:

$$Q_s = w * \int_0^H SSC * v \, dz \quad \text{(B4)}$$

where w is a characteristic channel width at the sampling location, SSC is the suspended sediment concentration of a given particle size fraction, v is the flow velocity at depth z in the water column, and H is the total flow depth. To determine SSC as a function of depth for each size fraction in the water column, we fit a Rouse-type profile (Rouse, 1937) to our data:

$$SSC_z = SSC_b \left[\frac{(H-z)/z}{(H-b)/b}\right]^R \quad \text{(B5)}$$

In equation (B5), SSC_z is the modeled suspended sediment concentration of a given size fraction at height z above the river bed, SSC_b is the concentration at near-bed reference height $z = b$ for a given grain size fraction, H is the flow depth, and R is the Rouse number for the given size fraction (Table S8). To determine the best-fit R for each grain size fraction at each sampling location, we used nonlinear least squares regression to fit the Rouse profile to our measured SSC data. The measured SSC of fine (<4 μm, SSC_f) and coarse (>4 μm, SSC_c) suspended sediment were calculated using the equations:

$$SSC_f = f_f * SSC, SSC_c = f_c * SSC \quad \text{(B6)}$$

where f_f and f_c are the fractions of particles within the fine and coarse particle size fractions, respectively, measured from grain size distributions.

We calculated the flow velocity as a function of depth v_z, using the logarithmic law of the wall equation:

$$v_z = \frac{u_*}{\mathrm{K}} \ln\left(\frac{z}{z_0}\right) \quad \text{(B7)}$$

where u_* is the shear velocity of the water column, K is the von Kármán constant (0.41), z is the height above the bed, and z_0 is the near-bed reference height. u_* was estimated by fitting the modeled flow velocity at the top of the water column to the measured flow velocity at the top of the water column at each location.

To determine a characteristic particulate organic carbon concentration for the <4 μm size fraction (TOC_f), we calculated the best-fit relationship between the fraction of <4 μm particles (f_f) and total organic carbon concentration (TOC):

$$TOC_f = a * {f_f}^b \quad \text{(B8)}$$

where a = 0.5036 (95% CI = 0.3692 - 0.638) and b = 0.4009 (95% CI = 0.2412 - 0.5606) (**Fig. B10**).

To determine a characteristic TOC content of the >4 μm fraction (TOC_c), we solved the following mass balance equation:

$$TOC = f_f * TOC_f + f_c * TOC_c \quad \text{(B9)}$$

Finally, we estimated the instantaneous fine and coarse POC fluxes (Q_{POC}) following the equations:

$$Q_{POC,f} = TOC_f * Q_{s,f}, \quad Q_{POC,c} = TOC_c * Q_{s,c} \qquad \text{(B10)}$$

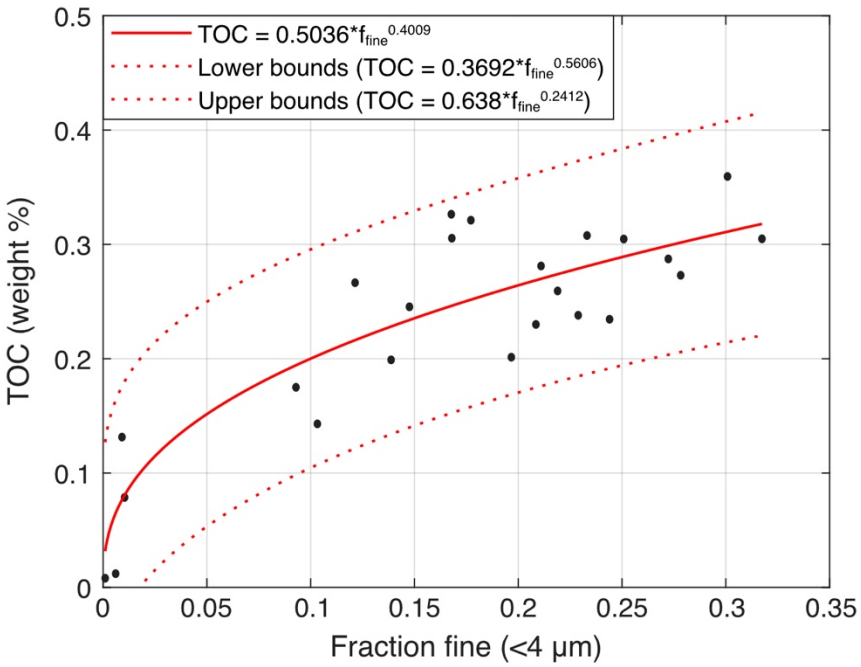

Figure B10. Best-fit relationship between f_f and total organic carbon concentration (TOC), used to estimate the TOC content of the fine and coarse particle size fractions studied here.

6.3.1 Calculated fluxes

In the Rio Bermejo, we observed that mineral-associated POC is hosted primarily by the <4 µm particle size fraction and discrete organic particles are predominantly in the >4 µm fraction. To determine the relative importance of these two POC pools for the overall POC flux of the river, we estimated the instantaneous fluxes of mineral-associated (<4 µm) POC and discrete (>4 µm) POC, as described above.

At each location along the Rio Bermejo, the coarse fraction (>4 µm) dominated the total suspended sediment concentrations (**Figs. B11, B12**). <4 µm suspended sediment comprised ~10% of the total suspended sediment load at river km -10 and increased to ~28% at river km 1220. Depth-integrated POC concentrations were similar for both particle size fractions, ranging from 0.10 to 0.33 weight % organic carbon (within 95% confidence bounds). Resulting instantaneous POC fluxes reveal that <4 µm POC accounted for 11-30% of the total flux, while the >4 µm fraction was the dominant component of fluvial POC at every location along the river. Based on our NanoSIMS analyses, these estimates suggest that relatively labile discrete organic particles are the dominant component of fluvial POC in the Rio Bermejo, while mineral-associated organic carbon comprises a smaller component.

However, downstream particle size fining via selective deposition causes the relative proportion of mineral-associated POC to increase with distance downstream. At the time of sampling, we observed greater Q_{POC} in the downstream reaches than at the mountain front, increasing from 1033 kgC/s at river km 135 to 2239 kgC/s at river km 1220, suggesting that a large flux of POC comes from the lowland floodplain. To account for different water discharge conditions, we normalized Q_{POC} values to the water discharge at the time of sampling (**Fig. B12**). The discharge-normalized $Q_{POC\text{-}fine}$ increases consistently with distance downstream, while the discharge-normalized $Q_{POC\text{-}coarse}$ increases from river km -10 to river km 420, then decreases downstream to the river mouth (**Fig. B12**). While there is some variability along the channel, overall, the ratio of fine to coarse POC increased from 0.25 at river km 135 to 0.41 at river km 1220.

Table B8. Data used to estimate Rouse profiles and depth-integrated concentrations of fine and coarse suspended sediment.

River km	Rouse Number <4 µm	Rouse Number >4 µm	SSC_{DI} <4 µm mg/L	SSC_{DI} >4 µm mg/L	Shear velocity (u*) m/s	Nominal channel width (w) m	Best-fit equation for SSC_f vs. f_f	R-squared value
-10	0.11	0.24	666	6542	0.08	200	f_f = -5.19E-05*SSC + 0.450	0.999
135	0.06	0.12	1089	4557	0.13	200	f_f = -1.61E-05*SSC + 0.284	0.475
420	0.07	0.27	2619	13378	0.1	200	f_f = -9.71E-06*SSC + 0.338	0.842
865	0.04	0.18	1944	9153	0.11	215	f_f = -1.38E-05*SSC + 0.346	0.96
1220	0.01	0.08	3250	9849	0.08	110	f_f = -6.68E-06*SSC + 0.365	0.539

SSC_{DI} = depth-integrated suspended sediment concentration for river depth profile

f_f = fraction of fine (<4 um) sediment in river sediment samples

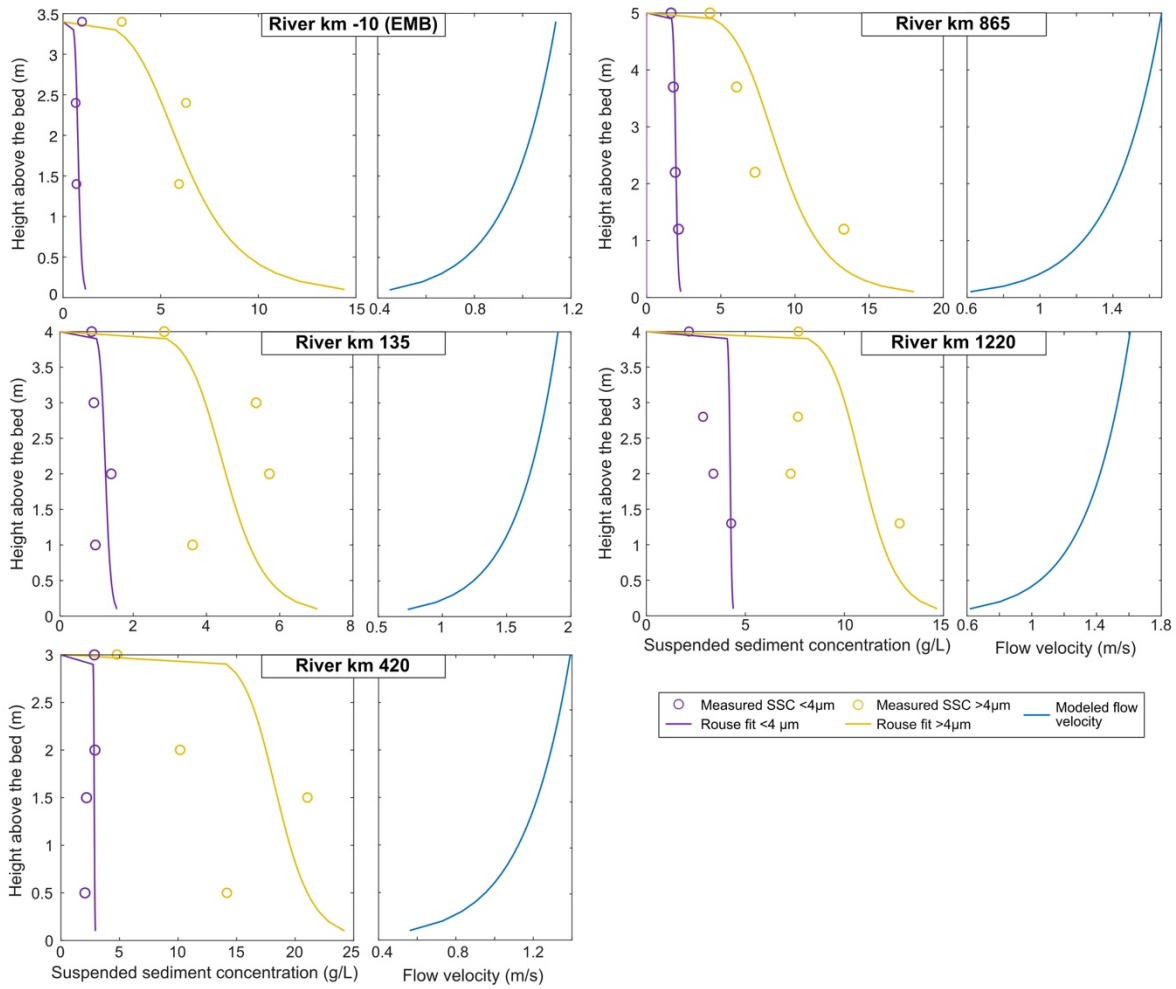

Figure B11. Modeled Rouse suspended sediment concentration profiles and modeled flow velocity profiles derived for the five sampling stations along the Rio Bermejo. Data points show measured values for suspended sediment concentrations.

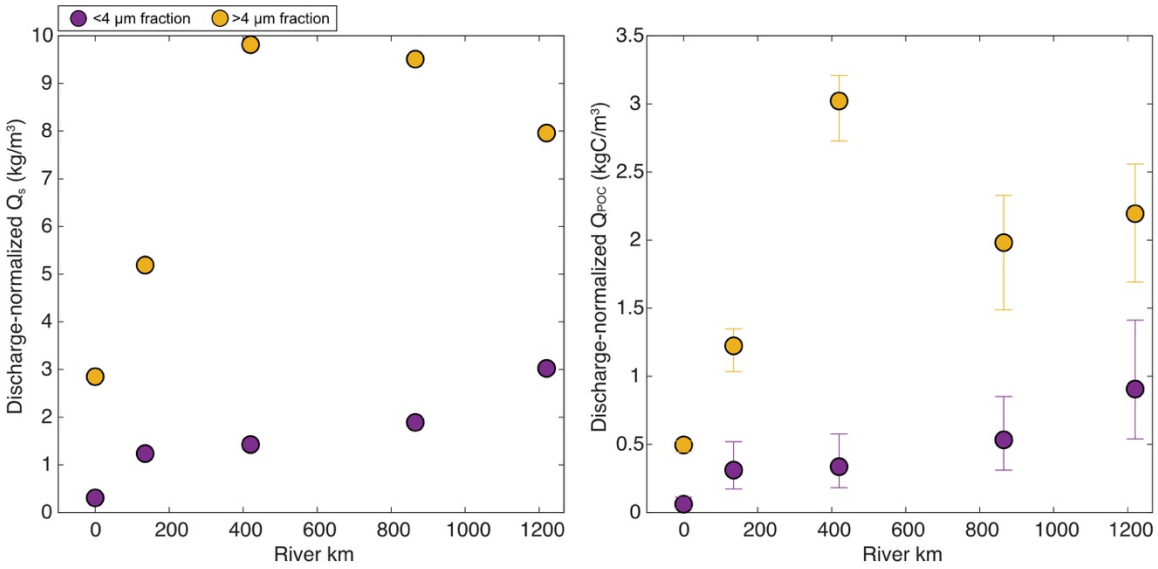

Figure B12. Discharge-normalized suspended sediment flux (Q_s) and particulate organic carbon flux (Q_{poc}) calculated at each sampling station along the Rio Bermejo. Error bars on Q_{poc} represent the 95% confidence interval for the best fit power function between f_f and TOC (Fig. S10).

Supplementary Data Tables

Table B1. Sample locations, bulk organic carbon (OC) composition, and n-alkane composition data for river sediment depth profile samples collected in March 2017.

Sample ID	Sample Type	Latitude	Longitude	Location Name	Sediment sample mass	River km
		decimal degrees			g	km
AR17MR-30	SS	-23.35554	-64.18391	Rio San Francisco		-15
AR17MR-31	SS	-23.35554	-64.18391	Rio San Francisco	60.2495	-15
AR17MR-24	SS	-23.25094	-64.13403	Embarcacion	74.752	-10
AR17MR-25	SS	-23.25094	-64.13403	Embarcacion	128.072	-10
AR17MR-26	SS	-23.25094	-64.13403	Embarcacion	116.0544	-10
AR17MR-27	SS	-23.25094	-64.13403	Embarcacion	339.85	-10
AR17MR-32	SS	-23.75598	-63.07393	El Colgado	46.2366	135
AR17MR-33	SS	-23.75598	-63.07393	El Colgado	110.5507	135
AR17MR-34	SS	-23.75598	-63.07393	El Colgado	114.0431	135
AR17MR-35	SS	-23.75598	-63.07393	El Colgado	61.804	135
AR17MR-36	SS	-23.75598	-63.07393	El Colgado	325.94	135
AR17MR-11	SS	-24.31326	-61.83789	Reserva Natural Formosa	82.1434	420
AR17MR-12	SS	-24.31326	-61.83789	Reserva Natural Formosa	140.7443	420
AR17MR-13	SS	-24.31326	-61.83789	Reserva Natural Formosa	120.5566	420
AR17MR-14	SS	-24.31326	-61.83789	Reserva Natural Formosa	48.4156	420
AR17MR-42	SS	-25.6638	-60.11595	Puerto Lavalle	50.0722	865
AR17MR-43	SS	-25.6638	-60.11595	Puerto Lavalle	120.3978	865
AR17MR-44	SS	-25.6638	-60.11595	Puerto Lavalle	138.1526	865
AR17MR-45	SS	-25.6638	-60.11595	Puerto Lavalle	112.421	865
AR17MR-46	SS	-25.6638	-60.11595	Puerto Lavalle	331.22	865
AR17MR-05	SS	-26.66087	-58.63467	General Mansilla	61.6231	1220
AR17MR-06	SS	-26.66087	-58.63467	General Mansilla	110.7326	1220
AR17MR-07	SS	-26.66087	-58.63467	General Mansilla	119.5043	1220
AR17MR-08	SS	-26.66087	-58.63467	General Mansilla	138.1621	1220
BEDLOAD ORGANIC MATTER (BOM)						
AR17MR-30-BOM	BOM	-23.35554	-64.18391	Rio San Francisco	16.1	-15
AR17MR-17	BOM	-24.31598	-61.83567	Reserva Natural Formosa	10.0	420
AR17MR-57	BOM	-25.61071	-60.36328	El Colorado	5.0	1085
AR17MR-05-BOM	BOM	-26.66087	-58.63467	Grl Mansilla	10.3	1220

Table B1. (continued) Sample locations, bulk organic carbon (OC) composition, and n-alkane composition data for river sediment depth profile samples collected in March 2017.

							n-alkane concentrations		
Sample ID	Year	Depth below surface	Normalized water depth	TOC	OC:N	$\delta^{13}C_{OC}$	C17	C18	C19
		m		weight %		‰	µg/g sed	µg/g sed	µg/g sed
AR17MR-30	2017	1.00	1.00	0.08	14.60	-27.27			
AR17MR-31	2017	0.00	0.00	0.33	4.57	-25.70	0.02	0.01	0.01
AR17MR-24	2017	0.00	0.00	0.23	2.95	-26.29	0.01	0.01	0.01
AR17MR-25	2017	1.00	0.30	0.18	3.60	-26.72			
AR17MR-26	2017	2.00	0.59	0.14	4.20	-24.90	0.01	0.01	0.01
AR17MR-27	2017	3.37	0.89	0.01	5.39	-26.29			
AR17MR-32	2017	3.00	0.36	0.28	3.86	-25.98	0.01	0.02	0.02
AR17MR-33	2017	2.00	0.24	0.20	2.84	-26.30			0.01
AR17MR-34	2017	1.00	0.12	0.25	4.36	-25.78			
AR17MR-35	2017	0.00	0.00	0.31	3.74	-26.02		0.01	0.01
AR17MR-36	2017	4.00	0.60	0.13	9.88	-27.12			
AR17MR-11	2017	0.00	0.00	0.36	3.47	-25.49	0.02	0.01	0.01
AR17MR-12	2017	1.00	0.20	0.32	4.29	-26.58			
AR17MR-13	2017	1.50	0.30	0.27	4.22	-26.53	0.01	0.01	0.01
AR17MR-14	2017	2.50	0.49	0.31	4.09	-26.51			0.01
AR17MR-42	2017	4.50	0.80	0.20	5.44	-26.08			0.02
AR17MR-43	2017	3.50	0.62	0.23	5.09	-25.68		0.01	
AR17MR-44	2017	2.00	0.35	0.24	4.82	-25.26			
AR17MR-45	2017	0.00	0.00	0.27	4.75	-25.43	0.01	0.01	0.01
AR17MR-46	2017	5.66	0.88	0.01	4.81	-26.07			
AR17MR-05	2017	2.70	0.52	0.30	5.17	-25.55			
AR17MR-06	2017	0.00	0.00	0.30	3.34	-25.20	0.03	0.02	0.01
AR17MR-07	2017	2.00	0.38	0.29	3.59	-25.53	0.01	0.00	0.01
AR17MR-08	2017	1.20	0.19	0.26	3.58	-25.57			
Bedload organic matter (BOM)									
AR17MR-30-BOM	2017	1.00	1.00		nm	-28.1			
AR17MR-17	2017	3	1.00	27.40	nm	-28.80			0.16
AR17MR-57	2017	nm	1.00	4.50	nm	-24.70			0.13
AR17MR-05-BOM	2017	4	1.00	28.31	nm	-27.93		0.10	0.48

TOC = total organic carbon concentration

OC:N = ratio of organic carbon to nitrogen concentrations

$\delta^{13}C_{OC}$ = stable carbon isotope composition of bulk particulate organic carbon (OC)

Table B1. (continued) Sample locations, bulk organic carbon (OC) composition, and *n*-alkane composition data for river sediment depth profile samples collected in March 2017.

	n-alkane concentrations													
Sample ID	C20	C21	C22	C23	C24	C25	C26	C27	C28	C29	C30	C31	C32	C33
	µg/g sed	µg/g sed	µg/g sed	µg/g sed	µg/g sed	µg/g sed	µg/g sed	µg/g sed	µg/g sed	µg/g sed	µg/g sed	µg/g sed	µg/g sed	µg/g sed
AR17MR-30														
AR17MR-31	0.03	0.03	0.01	0.03	0.02	0.06	0.03	0.13	0.03	0.25	0.04	0.39	0.04	0.17
AR17MR-24	0.02	0.02	0.02	0.02	0.02	0.03	0.02	0.06	0.02	0.14	0.03	0.21	0.03	0.10
AR17MR-25		0.01	0.01	0.01	0.01	0.02	0.01	0.04	0.01	0.12	0.02	0.19	0.04	0.08
AR17MR-26	0.01	0.01	0.01	0.01	0.01	0.03	0.01	0.05	0.01	0.10	0.02	0.14	0.02	0.06
AR17MR-27	0.00	0.00	0.00	0.00	0.00	0.00	0.00	0.00	0.00	0.00	0.00	0.00	0.00	0.00
AR17MR-32	0.03	0.03	0.04	0.05	0.03	0.07	0.04	0.12	0.04	0.28	0.04	0.38	0.05	0.14
AR17MR-33	0.01	0.01	0.01	0.02	0.01	0.03	0.02	0.06	0.02	0.15	0.03	0.24	0.03	0.11
AR17MR-34		0.01	0.01	0.01	0.01	0.02	0.02	0.06	0.03	0.16	0.02	0.29	0.04	0.11
AR17MR-35	0.02	0.03	0.02	0.04	0.02	0.04	0.03	0.10	0.03	0.19	0.03	0.29	0.04	0.12
AR17MR-36		0.00		0.00		0.00	0.00	0.00	0.00	0.00	0.00	0.00	0.00	0.00
AR17MR-11	0.02	0.03	0.03	0.04	0.03	0.04	0.03	0.09	0.03	0.20	0.03	0.31	0.04	0.13
AR17MR-12		0.01	0.02	0.02	0.02	0.03	0.02	0.08	0.02	0.23	0.03	0.39	0.04	0.14
AR17MR-13	0.01	0.02	0.02	0.03	0.01	0.04	0.02	0.08	0.03	0.23	0.04	0.36	0.04	0.13
AR17MR-14	0.02	0.04	0.04	0.05	0.03	0.10	0.05	0.16	0.05	0.45	0.08	0.62	0.06	0.24
AR17MR-42	0.02	0.02	0.03	0.03	0.02	0.05	0.06	0.10	0.03	0.23	0.04	0.37	0.04	0.13
AR17MR-43	0.01	0.01	0.01	0.01	0.01	0.03	0.03	0.06	0.02	0.14	0.02	0.23	0.03	0.10
AR17MR-44		0.01	0.01	0.01	0.01	0.03	0.02	0.05	0.02	0.16	0.02	0.28	0.03	0.11
AR17MR-45	0.01	0.03	0.01	0.03	0.01	0.03	0.02	0.08	0.02	0.15	0.03	0.26	0.03	0.14
AR17MR-46								0.00		0.01		0.01		0.00
AR17MR-05	0.02	0.03	0.02	0.04	0.02	0.05	0.03	0.10	0.03	0.24	0.03	0.37	0.04	0.13
AR17MR-06	0.02	0.02	0.02	0.02	0.01	0.04	0.02	0.07	0.02	0.14	0.03	0.23	0.02	0.09
AR17MR-07	0.01	0.01	0.01	0.02	0.01	0.04	0.02	0.07	0.03	0.18	0.03	0.30	0.03	0.12
AR17MR-08				0.01		0.02	0.02	0.06	0.02	0.15	0.04	0.28	0.04	0.11
BEDLOAD ORGANIC MATTER (BOM)														
AR17MR-30-BOM														
AR17MR-17	0.21	0.42	0.18	0.87	0.28	2.24	1.71	2.91	0.75	7.51	0.73	9.94	0.65	2.54
AR17MR-57	0.10	0.19	0.15	0.29	0.11	1.17	0.37	0.81	0.30	2.24	0.35	2.39	0.43	0.88
AR17MR-05-BOM	0.51	2.81	0.90	0.11	4.59	1.44	1.94	13.03	3.75	35.75	3.89	41.94	3.32	12.24

Table B1. (continued) Sample locations, bulk organic carbon (OC) composition, and n-alkane composition data for river sediment depth profile samples collected in March 2017.

Sample ID	C34	C35	Total *n*-alkane concentration	Total *n*-alkane mass	*n*-alkane concentration OC	CPI (C21-C35)	ACL (C21-C35)	C31+C33/ C27+C29
	µg/g sed	µg/g sed	µg/g sed	µg	µg/gOC			
AR17MR-30	0.02	0.04	0.00	0.0	0			
AR17MR-31		0.02	1.36	82.0	428	3.92	29.63	1.45
AR17MR-24		0.05	0.79	59.4	339	2.80	29.33	1.51
AR17MR-25		0.02	0.62	79.8	356	2.88	29.98	1.61
AR17MR-26			0.54	62.3	376	2.85	29.27	1.36
AR17MR-27	0.04	0.05	0.00	0.0	0.31	0.52	27.45	1.11
AR17MR-32		0.02	1.48	68.7	528	3.11	29.25	1.29
AR17MR-33	0.01	0.02	0.79	87.4	393	3.41	29.67	1.65
AR17MR-34		0.03	0.83	94.7	338	3.29	29.95	1.81
AR17MR-35			1.03	63.5	334	3.39	29.24	1.44
AR17MR-36	0.01	0.03	0.00	0.0	0.02	0.73	28.13	1.11
AR17MR-11		0.03	1.14	93.4	316	2.99	29.25	1.54
AR17MR-12	0.01	0.03	1.07	150.8	334	4.27	29.78	1.71
AR17MR-13	0.05	0.09	1.13	136.3	424	3.53	29.66	1.58
AR17MR-14	0.03	0.04	2.13	103.0	697	4.06	29.66	1.41
AR17MR-42		0.02	1.28	64.1	643	2.81	29.44	1.53
AR17MR-43		0.03	0.74	88.9	321	3.15	29.63	1.70
AR17MR-44	0.01	0.02	0.79	108.8	331	3.55	29.96	1.87
AR17MR-45			0.91	101.8	332	3.46	29.54	1.70
AR17MR-46		0.03	0.02	7.5	188		30.13	1.37
AR17MR-05	0.02	0.02	1.18	72.9	388	3.77	29.30	1.49
AR17MR-06	0.01	0.03	0.83	91.9	272	2.79	29.40	1.56
AR17MR-07		0.03	0.95	113.2	330	3.42	29.78	1.69
AR17MR-08			0.78	107.9	301	3.52	30.33	1.90
BEDLOAD ORGANIC MATTER (BOM)								
AR17MR-30-BOM	0.17	0.50						
AR17MR-17		0.42	32.72	327.95	11.97	29.41	29.15	1.20
AR17MR-57	1.02	3.63	10.34	51.70	11.49	10.39	28.99	1.07
AR17MR-05-BOM			144.44	1492.48	50.60	110.11	29.61	1.11

CPI = carbon preference index

ACL = average chain length

Table B1. (continued) Sample locations, bulk organic carbon (OC) composition, and n-alkane composition data for river sediment depth profile samples collected in March 2017.

					$\delta^{13}C_{alk}$			
Sample ID	nC27	nC27 SD	nC29	nC29 SD	nC31	nC31 SD	nC33	nC33 SD
	‰ vs. PDB	‰ vs. PDB	‰ vs. PDB	‰ vs. PDB	‰ vs. PDB	‰ vs. PDB	‰ vs. PDB	‰ vs. PDB
AR17MR-30								
AR17MR-31	-31.20	0.12	-34.75	0.16	-35.40	0.20	-34.33	0.26
AR17MR-24	-30.50	0.14	-31.07	0.16	-30.75	0.07	-30.86	0.11
AR17MR-25	-33.75	0.03	-35.45	0.21	-35.85	0.26	-35.48	0.23
AR17MR-26	-33.54	0.13	-35.38	0.14	-35.41	0.17	-34.78	0.17
AR17MR-27								
AR17MR-32	-32.56	0.37	-36.52	0.34	-35.33	0.32	-34.30	0.25
AR17MR-33	-33.11	0.10	-35.46	0.18	-35.76	0.02	-35.50	0.09
AR17MR-34	-32.52	0.18	-35.54	0.18	-35.02	0.13	-35.40	0.13
AR17MR-35	-30.35	0.16	-30.97	0.05	-31.20	0.11	-30.76	0.24
AR17MR-36			-36.32	0.13	-35.09	0.13		
AR17MR-11	-30.78	0.07	-31.45	0.10	-30.42	0.13	-30.94	0.07
AR17MR-12	-33.33	0.16	-35.92	0.09	-35.66	0.16	-35.92	0.04
AR17MR-13	-32.75	0.09	-33.33	0.14	-34.94	0.17	-35.48	0.14
AR17MR-14	-31.10	0.20	-35.65	0.29	-34.26	0.15	-33.62	0.17
AR17MR-42	-32.45	0.42	-35.41	0.26	-35.40	0.32	-34.47	0.27
AR17MR-43	-33.53	0.20	-35.72	0.15	-35.39	0.21	-35.56	0.13
AR17MR-44	-32.04	0.17	-34.49	0.23	-34.34	0.17	-34.14	0.20
AR17MR-45	-30.67	0.15	-31.48	0.08	-31.93	0.07	-30.70	0.16
AR17MR-46					-35.44	0.25		
AR17MR-05	-32.80	0.23	-35.95	0.15	-36.65	0.18	-35.41	0.32
AR17MR-06	-30.42	0.24	-31.21	0.13	-31.55	0.07	-30.61	0.14
AR17MR-07	-31.88	0.05	-33.79	0.17	-34.90	0.12	-35.15	0.12
AR17MR-08	-33.55	0.26	-35.70	0.08	-35.79	0.03	-35.54	0.10
BEDLOAD ORGANIC MATTER (BOM)								
AR17MR-30-BOM								
AR17MR-17	-33.88	0.28	-34.13	0.22	-34.95	0.17	-36.36	0.28
AR17MR-57	-34.42	0.19	-35.21	0.19	-33.28	0.20	-33.88	0.19
AR17MR-05-BOM	-35.71	0.16	-36.83	0.12	-37.34	0.08	-36.42	0.29

$\delta^{13}C_{alk}$ = n-alkane stable carbon isotope composition

SD = standard deviation

Table B1. (continued) Sample locations, bulk organic carbon (OC) composition, and n-alkane composition data for river sediment depth profile samples collected in March 2017.

	δ^2H_{alk}							
Sample ID	nC27	nC27 SD	nC29	nC29 SD	nC31	nC31 SD	nC33	nC33 SD
	‰ vs. VSMOW	‰ vs. √SMOW	‰ vs. VSMOW	‰ vs. VSMOW	‰ vs. VSMOW	‰ vs. VSMOW	‰ vs. VSMOW	‰ vs. VSMOW
AR17MR-30								
AR17MR-31	-143.26	1.70	-138.52	1.42	-142.76	1.47		
AR17MR-24	-145.95	0.15	-140.24	1.84	-148.47	0.90		
AR17MR-25	-126.95	0.51	-135.19	0.46	-138.69	0.15	-125.79	1.16
AR17MR-26	-153.18	0.97	-144.03	2.41	-148.01	0.52		
AR17MR-27								
AR17MR-32	-137.71	0.00	-165.62	0.00	-146.16	2.33		
AR17MR-33	-138.50	5.57	-151.23	4.24	-148.12	0.44		
AR17MR-34	-138.28	2.44	-153.50	1.88	-148.32	1.70		
AR17MR-35	-138.54	1.38	-144.28	1.20	-147.84	0.19		
AR17MR-36			-141.56	15.07	-140.64	1.65		
AR17MR-11	-132.61	0.20	-138.22	0.12	-146.17	0.26		
AR17MR-12	-134.63	3.30	-141.21	4.82	-138.74	7.02	-138.36	0.52
AR17MR-13	-145.14	3.78	-144.41	0.19	-152.67	0.88		
AR17MR-14	-139.06	0.57	-137.68	0.69	-152.35	0.36	-124.32	3.53
AR17MR-42			-144.24	1.32	-147.79	3.37		
AR17MR-43	-138.84	0.06	-145.16	2.48	-150.69	1.23		
AR17MR-44	-143.52	0.45	-142.44	0.42	-152.80	0.79		
AR17MR-45	-146.27	2.32	-146.36	0.36	-155.11	0.41		
AR17MR-46								
AR17MR-05	-140.75	2.95	-141.66	1.56	-151.86	0.42		
AR17MR-06	-135.76	0.11	-138.14	1.01	-146.71	0.13		
AR17MR-07	-137.98	0.05	-150.66	1.60	-150.28	0.37		
AR17MR-08	-141.23	1.42	-136.27	0.91	-146.83	0.12		
BEDLOAD ORGANIC MATTER (BOM)								
AR17MR-30-BOM								
AR17MR-17	-173.32	0.72	-164.67	0.02	-163.33	0.66		
AR17MR-57			-160.51	1.44	-143.37	1.07		
AR17MR-05-BOM	-162.61	0.69	-159.16	0.41	-158.92	2.84		

δ^2H_{alk} = *n*-alkane hydrogen isotope composition

SD = standard deviation

Table B2. Statistics comparing the n-alkane composition of surface water suspended sediment (SS) vs. samples collected >0.5 m below the water surface.

n-alkane	Mean $\delta^{13}C_{alk}$ surface water SS	Mean $\delta^{13}C_{alk}$ SS >0.5 m	difference	p-value (k-s test)	Mean n-alkane Concentration - surface	SD n-alkane Concentration - surface	Mean n-alkane Concentration - depth	SD n-alkane Concentration - depth
	‰ vs. PDB	‰ vs. PDB	‰ vs. PDB		µg/gOC	µg/gOC	µg/gOC	µg/gOC
C27	-30.65	-32.78	2.13	0.0004	nc	nc	nc	nc
C29	-31.82	-35.38	3.55	0.0018	nc	nc	nc	nc
C31	-31.87	-35.32	3.45	0.0016	nc	nc	nc	nc
C33	-31.37	-35.05	3.68	0.0021	nc	nc	nc	nc
Average	-31.43	-34.63	3.20		420	142	355	128

$\delta^{13}C_{alk}$ = n-alkane stable carbon isotope composition

SD = standard deviation

nc = not calculated

Table B3. Sample locations, bulk organic carbon (OC) composition, and n-alkane composition data for endmember OC samples.

Sample ID	River km	Latitude	Longitude	Location Name	Year sampled	Soil depth	TOC	$\delta^{13}C_{OC}$
	km	decimal degrees	decimal degrees			cm	weight %	‰ vs. PDB
LEAF LITTER								
AR15DS-027	-10	-23.35611	-64.18429	Embarcacion	2017		47.30	-27.20
AR17MR-29	135	-23.35554	-64.18391	El Colgado	2017		40.15	-29.24
AR17MR-49	865	-25.651642	-60.137531	Puerto lavalle	2017		43.84	-27.88
AR17MR-55	1085	-26.33225	-59.36058	El Colorado	2017		36.73	-19.14
MR18-PLV-LL	865	-25.651642	-60.137531	Puente Lavalle	2018		26.50	-21.30
MR18-SZ-LL	420	-24.3048	-61.83518	Sauzalito	2018		39.40	-29.30
TOPSOIL								
AR15DS-024-S	-10	-23.33255	-63.99657	Embarcacion	2015	5	0.48	-26.92
AR15DS-046-S-5	420	-24.24166	-61.9421	Reserva Natural Formosa	2015	5		
AR15DS-052-S	500	-25.6312	-60.25533	Villa Rio Bermejito	2015	5	1.45	-27.84
AR15DS-063-S	1260	-26.82827	-58.39757	Bermejo at Rio Paraguay	2015	5	0.24	-26.28
AR15DS-38-S-5	420	-23.75183	-63.05281	Reserva Natural Formosa	2015	5		-32.12
AR16JS-01	-20	-23.14422	-64.19886	Pozo Sarmiento	2016	5		
AR17MR-18	420	-24.3048	-61.83518	Reserva Natural Formosa	2017	5	4.52	-27.07
AR17MR-38	135	-23.75192	-63.05231	El Colgado	2017	5	1.68	-28.84
AR17MR-48	865	-25.651642	-60.137531	Puerto Lavalle	2017	5	0.49	-27.24
AR17MR-54	1085	-26.33225	-59.36058	El Colorado	2017	5	0.70	-22.67
MR18-SZ-Soil	420	-24.4142	-61.69201	Reserva Natural Formosa	2018	5		
ST15-52	8	-23.24817	-64.13563	RSF-RB confluence	2015	5	0.62	-26.57
AR15DS-038-S-10	110	-23.75183	-63.05281	El Colgado	2015	10		
AR15DS-045-S-10	420	-24.24166	-61.9421	Reserva Natural Formosa	2015	10	1.57	-25.01
AR15DS-052-S-15	500	-25.6312	-60.25533	Villa Rio Bermejito	2015	15	1.20	-28.60
AR15DS-057	1085	-26.33367	-59.36293	El Colorado	2015	15	0.19	-24.71
AR15DS-060-S-15	1220	-26.66009	-58.63266	Grl Mansilla	2015	15		
AR15DS-063-S-15	1260	-26.82827	-58.39757	Bermejo at Rio Paraguay	2015	15	0.20	-26.90
FLOODPLAIN SEDIMENT								
AR16JS-10-A	420	-24.09626	-61.942213	Reserva Natural Formosa	2016	20	0.19	-17.90
AR15DS-048-S-30	420	-25.65142	-60.12772	Reserva Natural Formosa	2015	30		-25.63
AR15DS-045-S-40	420	-24.24166	-61.9421	Reserva Natural Formosa	2015	40	1.40	-25.60
AR15DS-057-S	583	-26.33367	-59.36293	El Colorado	2015	40	0.27	-24.05
AR15DS-060-S-40	660	-26.66009	-58.63266	Grl Mansilla	2015	40		
AR15DS-048-S-60	475	-25.65142	-60.12772	Puente Lavalle	2015	60		

Table B3. Sample locations, bulk organic carbon (OC) composition, and n-alkane composition data for endmember OC samples.

Sample ID	River km	Latitude	Longitude	Location Name	Year sampled	Soil depth	TOC	$\delta^{13}C_{OC}$
	km	decimal degrees	decimal degrees			cm	weight %	‰ vs. PDB
AR16JS-10-B	420	-24.09626	-61.942213	Reserva Natural Formosa	2016	90	0.12	-14.58
AR15DS-057-S-100	580	-26.33367	-59.36293	El Colorado	2015	100	0.20	-24.70
AR17JS10-D	420	-24.30496	-61.83445	Reserva Natural Formosa	2017	110	0.31	-23.35
AR16JS-10-C	420	-24.09626	-61.942213	Reserva Natural Formosa	2016	210	0.04	-17.93
AR17JS10-G	420	-24.30496	-61.83445	Reserva Natural Formosa	2017	230	0.20	-21.86
AR16JS-08-A	420	-24.265117	-61.882488	Reserva Natural Formosa	2016	240	0.05	-22.25
AR17JS10-I	420	-24.30496	-61.83445	Reserva Natural Formosa	2017	300	0.03	-23.76
AR16JS-08-B	420	-24.265117	-61.882488	Reserva Natural Formosa	2016	400	0.09	-22.87
AR16JS-08-C	420	-24.265117	-61.882488	Reserva Natural Formosa	2016	440	0.10	-22.00
AR16JS-10-D	420	-24.09626	-61.942213	Reserva Natural Formosa	2016	450	0.04	-18.03

$\delta^{13}C_{OC}$ = stable carbon isotope composition of bulk particulate organic carbon

Table B3. (continued) Sample locations, bulk organic carbon (OC) composition, and n-alkane composition data for endmember OC samples.

		n-alkane concentrations									
Sample ID	Aliquot mass	C17	C18	C19	C20	C21	C22	C23	C24	C25	C26
	g	µg/g sed	µg/g sed	µg/g sed	µg/g sed	µg/g sed	µg/g sed	µg/g sed	µg/g sed	µg/g sed	µg/g sed
LEAF LITTER											
AR15DS-027	4.3									1.70	
AR17MR-29	10.0	0.10	0.10	0.10	0.10	0.20	0.19	0.35	0.28	0.67	0.21
AR17MR-49	5.0	0.10	0.11	0.29	0.46	1.23	1.30	2.82	1.96	5.10	2.98
AR17MR-55	5.5				0.21	0.45	0.41	0.80	0.29	1.02	4.08
MR18-PLV-LL	7.1						0.12	0.53	0.19	1.25	0.52
MR18-SZ-LL	10.3						0.16	0.43	0.35	0.91	
TOPSOIL											
AR15DS-024-S	59.7	0.05	0.01	0.01	0.01	0.01	0.01	0.02	0.02	0.05	0.02
AR15DS-046-S-5	31.9							0.31	0.08	0.60	0.12
AR15DS-052-S	63.4					0.02		0.03		0.10	0.04
AR15DS-063-S	73.2	0.01	0.02		0.01	0.01	0.01	0.01	0.01	0.03	0.01
AR15DS-38-S-5	53.4	0.09	0.06	0.09	0.06	0.06	0.06	0.19	0.09	0.33	0.09
AR16JS-01	50.4	0.06	0.02	0.03	0.02	0.01	0.01	0.02	0.02	0.05	0.02
AR17MR-18	56.5	0.02	0.03	0.02	0.03	0.04	0.03	0.16	0.05	0.33	0.10
AR17MR-38	52.5				0.03	0.04	0.02	0.08	0.04	0.19	0.07
AR17MR-48	60.1	0.01		0.01	0.01	0.02	0.01	0.03	0.01	0.04	0.02
AR17MR-54	61.1		0.02	0.02	0.04	0.02	0.01	0.03	0.02	0.07	0.03
MR18-SZ-Soil	49.5										
ST15-52	47.7	0.12	0.11	0.05	0.05	0.06	0.07	0.11	0.13	0.19	0.16
AR15DS-038-S-10	37.4		0.02							0.01	
AR15DS-045-S-10	63.6	0.03	0.02	0.04		0.01	0.01	0.05	0.02	0.10	0.03
AR15DS-052-S-15	36.6							0.01		0.04	0.02
AR15DS-057	55.1	1.59	1.88	1.96	2.13	2.24	2.35	2.46	2.56	2.65	2.75
AR15DS-060-S-15	38.8		0.01		0.01	0.01		0.03	0.03	0.36	0.12
AR15DS-063-S-15	36.9									0.03	0.02
FLOODPLAIN SEDIMENT											
AR16JS-10-A	35.9										
AR15DS-048-S-30	57.9		0.04	0.05			0.06	0.08	0.05	0.21	0.11
AR15DS-045-S-40	36.2	0.02	0.04					0.08	0.03	0.16	0.06
AR15DS-057-S	61.8		0.02		0.01	0.01	0.01	0.01	0.01	0.03	0.01
AR15DS-060-S-40	40.5							0.01	0.01	0.13	0.04
AR15DS-048-S-60	39.8									0.01	
AR16JS-10-B	39.9			0.02	0.03						
AR15DS-057-S-100	32.7		0.01		0.02			0.01	0.01	0.03	0.02
AR17JS10-D	49.8					0.20	0.01	0.01	0.01	0.03	0.01
AR16JS-10-C	43.4	0.03			0.03						
AR17JS10-G	45.7										
AR16JS-08-A											
AR17JS10-I	50.1										
AR16JS-08-B											
AR16JS-08-C											
AR16JS-10-D	39.4										

Table B3. (continued) Sample locations, bulk organic carbon (OC) composition, and n-alkane composition data for endmember OC samples.

	n-alkane concentrations										
Sample ID	C27 µg/g sed	C28 µg/g sed	C29 µg/g sed	C30 µg/g sed	C31 µg/g sed	C32 µg/g sed	C33 µg/g sed	C34 µg/g sed	C35 µg/g sed	C36 µg/g sed	C37 µg/g sed
LEAF LITTER											
AR15DS-027	11.8	6.28	68.1	2.94	12.2		2.83				
AR17MR-29	2.50	1.01	32.3	6.87	1620	4.41	8.12	0.13	0.44		
AR17MR-49	18.4	7.41	111	10.1	138	4.86	9.69	0.62	2.22		
AR17MR-55	1.78	16.5	3.06	37.3	2.27	17.2	1.66	6.44			
MR18-PLV-LL	4.84	1.68	12.3	2.80	25.7	1.68	17.1	0.94	6.59		
MR18-SZ-LL	1.72	0.68	17.3	3.22	80.28	3.90	14.6	0.93	1.62		
TOPSOIL											
AR15DS-024-S	0.10	0.04	0.28	0.05	0.39	0.05	0.16	0.02	0.03		
AR15DS-046-S-5	0.90	0.19	1.03	0.14	0.82	0.15	0.91	0.12	0.26	0.19	0.37
AR15DS-052-S	0.34	0.13	2.39	0.19	2.25	0.23	1.36	0.07	0.24		0.03
AR15DS-063-S	0.05	0.02	0.14	0.02	0.17	0.01	0.07		0.02		
AR15DS-38-S-5	0.33	0.06	0.82	0.09	0.31	0.09	0.22	0.09	0.22		
AR16JS-01	0.05	0.02	0.15	0.02	0.21	0.02	0.21	0.01	0.08		
AR17MR-18	0.96	0.28	1.49	0.18	1.44	0.24	1.50	0.11	0.24	0.02	0.04
AR17MR-38	0.70	0.14	0.95	0.11	0.78	0.12	0.89	0.07	0.19		
AR17MR-48	0.10	0.03	0.39	0.04	0.61	0.04	0.15	0.01	0.04		
AR17MR-54	0.17	0.05	0.46	0.06	0.72	0.11	0.78	0.07	0.32	0.01	0.06
MR18-SZ-Soil											
ST15-52	0.25	0.13	0.45	0.10	0.67	0.09	0.38	0.04	0.10		
AR15DS-038-S-10	0.02		0.01		0.03		0.02				
AR15DS-045-S-10	0.20	0.05	0.28	0.04	0.31	0.06	0.43	0.04	0.12	0.02	0.06
AR15DS-052-S-15	0.16	0.05	0.68	0.06	0.70	0.09	0.58	0.08	0.25	0.02	0.02
AR15DS-057	2.84	2.93	3.02	3.10	3.18	3.26	3.32	3.41	3.46		
AR15DS-060-S-15	0.44	0.03	0.13	0.02	0.24	0.03	0.30	0.03	0.13		
AR15DS-063-S-15	0.06	0.02	0.18	0.02	0.24	0.01	0.08		0.02		
FLOODPLAIN SEDIMENT											
AR16JS-10-A	0.05		0.04		0.07		0.17		0.12		
AR15DS-048-S-30	0.31	0.09	0.44	0.08	0.67	0.10	0.73	0.06	0.23		
AR15DS-045-S-40	0.41	0.11	0.64	0.10	0.72	0.14	1.01	0.09	0.27	0.05	0.12

	n-alkane concentrations										
Sample ID	C27 µg/g sed	C28 µg/g sed	C29 µg/g sed	C30 µg/g sed	C31 µg/g sed	C32 µg/g sed	C33 µg/g sed	C34 µg/g sed	C35 µg/g sed	C36 µg/g sed	C37 µg/g sed
AR15DS-057-S	0.04	0.01	0.09	0.02	0.16	0.01	0.07		0.02		
AR15DS-060-S-40	0.16	0.01	0.05	0.01	0.11	0.01	0.13	0.01	0.06		
AR15DS-048-S-60	0.02		0.03		0.04		0.04				
AR16JS-10-B											
AR15DS-057-S-100	0.04	0.02	0.09	0.02	0.16	0.01	0.06		0.02		
AR17JS10-D	0.06	0.02	0.14	0.02	0.22	0.02	0.10	0.02	0.68		
AR16JS-10-C							0.03				
AR17JS10-G											
AR16JS-08-A											
AR17JS10-I											
AR16JS-08-B											
AR16JS-08-C											
AR16JS-10-D											

Table B3. (continued) Sample locations, bulk organic carbon (OC) composition, and n-alkane composition data for endmember OC samples.

					$\delta^{13}C_{alk}$							
Sample ID	Total n-alkane concentration	OC-norm. alkane con	CPI (C21-C35)	ACL (C21-C35)	nC27	nC27 SD	nC29	nC29 SD	nC31	nC31 SD	nC33	nC33 SD
	µg/g sed	µg/gOC			‰ vs. PDB	‰ vs. PDB	‰ vs. PDB	‰ vs. PDB	‰ vs. PDB	‰ vs. PDB	‰ vs. PDB	‰ vs. PDB
LEAF LITTER												
AR15DS-027	93.4	37.1	101.8	29.0	-33.37	0.21	-35.01	0.07	-40.34	0.20		
AR17MR-29	105.8	9.9	214.1	30.7	-36.12	0.04	-37.24	0.12	-35.82	0.14	-37.09	0.21
AR17MR-49	220.2	24.2	292.3	29.7	-37.59	0.19	-35.57	0.37	-35.47	0.40	-36.16	0.03
AR17MR-55	319.7	30.0	11.1	29.9			-22.42	0.39	-25.80	0.45	-25.28	0.42
MR18-PLV-LL	76.3	20.4	66.1	31.0	-23.63	0.21	-23.26	0.08	-25.53	0.18	-26.30	0.26
MR18-SZ-LL	126.1	33.1	121.6	30.9	-35.13	0.13	-34.88	0.13	-32.38	0.18	-43.31	0.11
TOPSOIL												
AR15DS-024-S	1.4	175.8	3.6	29.8	-29.24	0.23	-32.59	0.21	-32.72	0.18		
AR15DS-046-S-5	4.9		7.6	29.2	-31.29	0.24	-32.56	0.35	-33.41	0.20	-34.22	0.03
AR15DS-052-S	7.4	4.8	11.5	30.5	-26.16	0.10	-32.58	0.10	-32.14	0.05	-31.64	0.07
AR15DS-063-S	0.6	747.7	3.8	29.6	-28.13	0.11	-31.10	0.18	-31.19	0.16	-27.79	0.11
AR15DS-38-S-5	0.0		4.3	28.7	-30.49	0.06	-28.60	0.35	-30.28	0.17	-31.18	0.12
AR16JS-01	1.1		4.3	30.3	-31.12	0.19	-30.61	0.20	-27.50	0.01	-25.48	0.33
AR17MR-18	7.4	91.8	9.0	29.9	-26.08	0.14	-28.62	0.12	-31.24	0.14	-31.37	0.24
AR17MR-38	4.4	138.1	7.0	29.8	-25.71	0.04	-27.63	0.15	-28.64	0.13	-28.85	0.15
AR17MR-48	1.6	192.5	5.2	29.9			-29.16	0.21	-30.72	0.21		
AR17MR-54	3.1	266.8	5.9	31.1	-22.43	0.16	-24.91	0.04	-26.87	0.16	-28.60	0.20
MR18-SZ-Soil	0.0				-34.51	0.17	-36.40	0.26	-35.33	0.30	-38.67	0.05
ST15-52	3.4	262.0	3.6	29.0	-32.32	0.18	-35.50	0.21	-35.87	0.16	-37.39	0.26
AR15DS-038-S-10	2.9			29.4	-30.71	0.22	-31.22	0.15	-28.50	0.19		
AR15DS-045-S-10	2.0	79.0	4.4	30.2	-27.76	0.05	-28.44	0.04	-29.76	0.14	-29.66	0.14
AR15DS-052-S-15	6.9	96.3	6.1	30.9	-34.30	0.11	-33.56	0.37	-33.13	0.24	-35.21	0.04
AR15DS-057	0.0		20.2	28.6	-31.41	0.06	-32.62	0.05	-32.87	0.09	-34.24	0.10
AR15DS-060-S-15	8.9		4.5	28.8	-23.66	0.18	-28.29	0.23	-32.61	0.16	-34.88	0.22
AR15DS-063-S-15	10.9	1211.0	5.2	30.1	-31.98	0.18	-35.28	0.21	-37.64	0.10	-35.68	0.21
FLOODPLAIN SEDIMENT												
AR16JS-10-A	0.4	86.1		32.2	-27.73	0.06	-32.37	0.07	-28.60	0.14	-27.06	0.11
AR15DS-048-S-30	0.0		4.9	30.0	-27.69	0.25	-32.93	0.08	-31.48	0.32	-31.60	0.11
AR15DS-045-S-40	3.9	1837.5	6.2	30.5	-30.42	0.12	-31.22	0.16	-32.49	0.05	-33.26	0.12
AR15DS-057-S	0.5	878.4	3.1	29.4	-27.12	0.18	-30.46	0.12	-29.72	0.27		
AR15DS-060-S-40	9.9		3.5	29.1	-23.47	0.19	-27.22	0.17	-28.22	0.17	-28.47	0.15
AR15DS-048-S-60	5.9			29.8		0.15		0.18		0.21		0.23
AR16JS-10-B	0.0	15.1										

					$\delta^{13}C_{alk}$							
Sample ID	Total n-alkane concentration	OC-norm. alkane con	CPI (C21-C35)	ACL (C21-C35)	nC27	nC27 SD	nC29	nC29 SD	nC31	nC31 SD	nC33	nC33 SD
	µg/g sed	µg/gOC			‰ vs. PDB	‰ vs. PDB	‰ vs. PDB	‰ vs. PDB	‰ vs. PDB	‰ vs. PDB	‰ vs. PDB	‰ vs. PDB
AR15DS-057-S-100	7.9	230.7	3.3	29.7	-31.29	0.16	-34.82	0.27	-34.27	0.14	-33.10	0.17
AR17JS10-D	1.6	183.4	6.3	30.9	-30.91	0.27	-33.10	0.10	-32.85	0.15	-31.80	0.14
AR16JS-10-C	0.1	94.4		33.0								
AR17JS10-G	0.0	0.0			-29.38	0.19	-34.28	0.03	-33.35	0.08	-32.44	0.21
AR16JS-08-A	0.0	0.0					-32.65	0.04	-29.52	0.16	-31.36	0.13
AR17JS10-I	0.0	0.0										
AR16JS-08-B	0.0	0.0					-33.75	0.10	-31.57	0.11	-31.57	0.14
AR16JS-08-C	0.0	0.0			-30.09	0.04	-33.71	0.09	-32.48	0.15	-32.18	0.08
AR16JS-10-D	0.0	0.0										

OC = organic carbon

CPI = carbon preference index

ACL = average n-alkane chain length

$\delta^{13}C_{alk}$ = *n*-alkane stable carbon isotope composition

SD = standard deviation of triplicate measurements

Table B3. (continued) Sample locations, bulk organic carbon (OC) composition, and n-alkane composition data for endmember OC samples.

Sample ID	δ^2H_{alk}							
	nC27 ‰ vs. VSMOW	nC27 SD ‰ vs. VSMOW	nC29 ‰ vs. VSMOW	nC29 SD ‰ vs. VSMOW	nC31 ‰ vs. VSMOW	nC31 SD ‰ vs. VSMOW	nC33 ‰ vs. VSMOW	nC33 SD ‰ vs. VSMOW
LEAF LITTER								
AR15DS-027	-187.08	0.53	-155.43	1.99	-162.54	0.38	-155.47	2.41
AR17MR-29	-166.29	2.38	-169.06	1.16	-152.20	1.70	-136.31	1.63
AR17MR-49	-144.83	10.60	-145.13	6.01	-158.14	0.76		
AR17MR-55	-181.87	1.76	-196.05	0.05	-195.43	0.18	-183.18	1.06
MR18-PLV-LL	-175.07	0.49	-174.50	0.35	-173.96	0.35	-173.06	0.36
MR18-SZ-LL	-181.85	2.33	-182.15	0.27	-165.38	0.51	-151.39	0.26
TOPSOIL								
AR15DS-024-S	-130.17	3.41	-133.82	1.28	-135.93	0.30	-119.13	3.37
AR15DS-046-S-5	-150.03	1.65	-152.38	0.63	-155.75	1.21	-141.27	0.42
AR15DS-052-S	-140.51	0.66	-131.38	0.02	-139.20	1.03	-137.67	1.78
AR15DS-063-S	-113.17	4.40	-119.04	3.25	-116.52	1.72	-103.04	1.24
AR15DS-38-S-5	-122.89	1.08	-94.52	0.91	-117.16	1.23		
AR16JS-01			-154.95	2.24	-154.14	0.11		
AR17MR-18	-87.26	0.88	-114.61	0.54	-132.35	0.28	-124.01	0.45
AR17MR-38	-125.84	0.42	-128.99	0.50	-132.71	0.31	-122.38	0.03
AR17MR-48	-139.96	2.20	-140.87	0.99	-147.91	0.20	-125.02	1.76
AR17MR-54	-157.53	3.03	-165.52	1.67	-158.70	1.37	-151.21	2.28
MR18-SZ-Soil	-166.60	0.33	-173.88	0.11				
ST15-52	-133.20	0.73	-139.17	0.83	-148.76	1.02		
AR15DS-038-S-10	-137.22	1.54						
AR15DS-045-S-10	-130.39	1.04	-124.26	0.58	-131.36	1.16	-123.00	0.42
AR15DS-052-S-15	-156.33	7.31	-149.69	0.83	-146.23	7.83	-142.46	7.83
AR15DS-057	-129.18	1.46	-126.22	0.09	-137.14	0.73		
AR15DS-060-S-15	-196.27	0.17	-147.31	2.08	-151.11	0.50	-159.68	1.02
AR15DS-063-S-15	-147.59	0.00	-148.13	0.22	-145.69	0.26	-134.73	0.89
FLOODPLAIN SEDIMENT								
AR16JS-10-A	-133.76	4.97	-184.23	0.97	-139.35	3.93	-156.15	0.01
AR15DS-048-S-30	-147.42	0.52	-134.18	0.37	-145.63	0.48		
AR15DS-045-S-40	-142.73	1.24	-141.34	0.15	-147.01	2.16	-138.42	5.84
AR15DS-057-S	-123.35	1.32	-126.61	3.22	-135.17	1.41	-121.31	1.92
AR15DS-060-S-40	-191.77	1.02	-146.75	1.61	-157.08	0.38	-165.67	0.87

Sample ID	δ^2H_{alk}							
	nC27 ‰ vs. VSMOW	nC27 SD ‰ vs. VSMOW	nC29 ‰ vs. VSMOW	nC29 SD ‰ vs. VSMOW	nC31 ‰ vs. VSMOW	nC31 SD ‰ vs. VSMOW	nC33 ‰ vs. VSMOW	nC33 SD ‰ vs. VSMOW
AR15DS-048-S-60	-130.09		-125.23	0.76	-129.91	1.67	-134.29	0.20
AR16JS-10-B			-131.74	1.52	-143.28	2.60		
AR15DS-057-S-100	-136.29	1.67	-137.78	1.10	-135.99	5.69	-131.20	0.34
AR17JS10-D	-146.66	1.87	-146.26	0.77	-148.18	0.78		
AR16JS-10-C								
AR17JS10-G	-134.84	6.04	-137.45	0.72	-140.89	1.03		
AR16JS-08-A			-139.50	3.03	-123.40	0.42		
AR17JS10-I			-144.31	3.06	-125.73	0.42		
AR16JS-08-B	-115.15	0.42	-118.81	0.97	-133.15	0.24	-136.11	1.48
AR16JS-08-C			-119.24	1.69	-131.38	3.06	-125.73	0.25
AR16JS-10-D								

δ^2H_{alk} = *n*-alkane hydrogen isotope composition

SD = standard deviation of triplicate measurements

Table B4. Relative contributions of endmember OC sources (floodplain sediment, leaf litter, and topsoil) to individual suspended sediment samples.

Sample ID	River km km	Normalized water depth	Floodplain sediment*	SD floodplain	Leaf litter*	SD leaf litter	Topsoil*	SD topsoil
AR17MR-31	-15	0.00	0.56	0.17	0.28	0.10	0.16	0.13
AR17MR-24	-10	0.00	0.65	0.21	0.13	0.08	0.22	0.19
AR17MR-25	-10	0.30	0.52	0.19	0.30	0.10	0.18	0.17
AR17MR-26	-10	0.59	0.46	0.16	0.39	0.11	0.15	0.12
AR17MR-32	135	0.75	0.36	0.16	0.45	0.12	0.20	0.16
AR17MR-33	135	0.50	0.44	0.15	0.40	0.10	0.16	0.12
AR17MR-34	135	0.25	0.44	0.16	0.39	0.10	0.17	0.13
AR17MR-35	135	0.00	0.62	0.22	0.13	0.08	0.24	0.19
AR17MR-36	135	1.00	0.43	0.16	0.41	0.11	0.15	0.13
AR17MR-11	420	0.00	0.67	0.21	0.11	0.07	0.22	0.19
AR17MR-12	420	0.20	0.49	0.17	0.34	0.10	0.17	0.15
AR17MR-13	420	0.30	0.46	0.16	0.37	0.10	0.17	0.13
AR17MR-14	420	0.49	0.56	0.18	0.28	0.10	0.16	0.14
AR17MR-42	865	0.80	0.49	0.16	0.35	0.10	0.15	0.12
AR17MR-43	865	0.62	0.45	0.15	0.40	0.10	0.15	0.12
AR17MR-44	865	0.35	0.52	0.17	0.31	0.10	0.17	0.13
AR17MR-45	865	0.00	0.57	0.22	0.19	0.11	0.24	0.19
AR17MR-46	865	1.00	nd	nd	nd	nd	nd	nd
AR17MR-05	1220	0.52	0.50	0.10	0.34	0.06	0.16	0.08
AR17MR-06	1220	0.00	0.66	0.20	0.12	0.07	0.23	0.18
AR17MR-07	1220	0.38	0.47	0.16	0.34	0.10	0.19	0.14
AR17MR-08	1220	0.23	0.46	0.16	0.37	0.10	0.16	0.13

* mean value of MixSIAR modeled posterior distributions for each sample

SD = standard deviation

nd = no data

Table B5. Corey shape factor (CSF) measurements for 46 particles representative of the areas of interest for NanoSIMS analyses.

SEM image	surface or depth	Particle #	Particle type	long axis (a)*	intermediate axis (b)*	short axis (c)*	CSF	D_{50} (mm)	E (Dietrich, 1982)	Ws (Dietrich, 1982)
sample 06_02	surface	1	organic	546	243	106	0.29	0.006	0.30	0.01
sample 06_02	surface	2	organic	259	157	52	0.26	0.006	0.29	0.01
sample 06_02	surface	3	mineral	205	156	38	0.21	0.006	0.25	0.01
sample 06_02	surface	4	mineral	195	115	28	0.19	0.006	0.21	0.01
sample 06_06	surface	5	mineral	55	38	12	0.26	0.006	0.31	0.01
sample 06_06	surface	2	mineral	170	131	29	0.19	0.006	0.23	0.01
sample 06_06	surface	3	mineral	155	55	14	0.15	0.006	0.15	0.01
sample 06_06	surface	4	mineral	133	91	10	0.09	0.006	0.11	0.01
sample 06_06	surface	5	organic	311	69	55	0.38	0.006	0.29	0.01
sample 11_03	surface	1	mineral	385	264	84	0.26	0.006	0.31	0.01
sample 11_03	surface	2	mineral	370	195	84	0.31	0.006	0.34	0.01
sample 11_03	surface	3	mineral	82	70	18	0.24	0.006	0.29	0.01
sample 24_02	surface	1	mineral	181	50	21	0.22	0.008	0.19	0.01
sample 24_02	surface	2	mineral	335	279	78	0.26	0.008	0.31	0.02
sample 24_02	surface	3	mineral	49	20	11	0.35	0.008	0.35	0.02
sample 24_02	surface	4	mineral	87	55	33	0.48	0.008	0.53	0.02
sample 35_04	surface	1	mineral	181	110	30	0.21	0.008	0.24	0.02
sample 35_04	surface	2	mineral	227	143	44	0.24	0.008	0.28	0.02
sample 35_04	surface	3	mineral	168	108	36	0.27	0.008	0.31	0.02
sample 35_04	surface	4	mineral	142	96	17	0.15	0.008	0.17	0.02
sample 35_04	surface	5	mineral	66	36	14	0.29	0.008	0.32	0.02
sample 35_04	surface	6	mineral	52	29	7	0.18	0.008	0.20	0.02
sample12_01	depth	1	mineral	429	387	195	0.48	0.015	0.55	0.07
sample12_01	depth	2	mineral	382	311	56	0.16	0.015	0.20	0.05
sample12_01	depth	3	mineral	236	110	53	0.33	0.015	0.35	0.06
sample12_01	depth	4	mineral	137	101	65	0.55	0.015	0.62	0.07
sample12_04	depth	1	mineral	119	57	23	0.28	0.015	0.30	0.06
sample12_04	depth	2	mineral	154	86	27	0.23	0.015	0.26	0.06
sample12_04	depth	3	mineral	444	290	124	0.35	0.015	0.39	0.06
sample12_04	depth	4	mineral	128	87	12	0.11	0.015	0.13	0.05
sample12_04	depth	5	organic	353	96	60	0.33	0.015	0.28	0.06
sample12_04	depth	6	organic	214	96	45	0.31	0.015	0.33	0.06
sample05_01	depth	1	mineral	272	233	47	0.19	0.011	0.23	0.03
sample05_01	depth	2	mineral	145	72	10	0.10	0.011	0.11	0.02
sample05_01	depth	3	mineral	30	26	4	0.14	0.011	0.17	0.03
sample05_01	depth	4	mineral	33	23	3	0.11	0.011	0.13	0.02
sample05_01	depth	5	mineral	70	44	5	0.09	0.011	0.10	0.02
sample05_05	depth	1	mineral	256	210	65	0.28	0.011	0.33	0.03
sample05_05	depth	2	mineral	168	87	49	0.41	0.011	0.43	0.04
sample05_05	depth	3	mineral	33	24	5	0.18	0.011	0.21	0.03
sample05_05	depth	4	mineral	37	21	3	0.11	0.011	0.12	0.02
sample05_05	depth	5	mineral	78	34	7	0.14	0.011	0.14	0.03
sample34_01	depth	1	mineral	166	129	14	0.10	0.022	0.12	0.10
sample34_01	depth	2	mineral	97	81	30	0.34	0.022	0.40	0.14
sample34_01	depth	3	mineral	104	55	39	0.52	0.022	0.55	0.15
sample34_01	depth	4	mineral	180	102	18	0.13	0.022	0.15	0.10
	Number of particles	46				Average CSF	0.25			

*Axis measurements (a, b, and c) were measured from SEM images in ImageJ, in the unit of pixels

CSF = corey shape factor

D_{50} = median particle diameter

E = empirical geometric shape factor (Dietrich, 1982)

Ws = particle settling velocity

Table B6. Grain Size distributions for Rio Bermejo suspended sediment samples collected in March 2017.

Sample ID	D_{10}	D_{16}	D_{50}	D_{84}	D_{90}	fraction <4 µm	fraction 4-63 µm	fraction 63-125 µm	fraction 125-250 µm	fraction 250-500 µm	fraction 500-1000 µm	fraction >1000 µm
	µm	µm	µm	µm	µm							
AR17MR-30	85.1	128.1	193.4	339.4	388.7	0.01	0.05	0.12	0.46	0.33	0.06	0.00
AR17MR-31	2.1	3.7	7.3	70.9	32.7	0.17	0.63	0.14	0.06	0.00	0.00	0.00
AR17MR-24	2.0	2.8	7.7	32.6	55.3	0.24	0.67	0.07	0.02	0.00	0.00	0.00
AR17MR-25	4.3	6.1	150.2	274.2	312.6	0.09	0.29	0.08	0.27	0.27	0.01	0.00
AR17MR-26	3.8	5.5	109.4	251.1	280.0	0.10	0.32	0.08	0.28	0.21	0.01	0.00
AR17MR-27	202.3	226.1	325.2	465.3	522.9	0.00	0.00	0.01	0.16	0.73	0.18	0.00
AR17MR-32	2.2	3.1	9.8	56.2	81.9	0.21	0.64	0.11	0.04	0.00	0.00	0.00
AR17MR-33	2.1	3.5	11.5	121.8	142.5	0.20	0.53	0.13	0.12	0.02	0.00	0.00
AR17MR-34	2.9	4.2	22.4	115.8	146.7	0.15	0.48	0.21	0.15	0.01	0.00	0.00
AR17MR-35	2.1	2.9	8.4	31.1	58.4	0.23	0.68	0.05	0.03	0.01	0.00	0.00
AR17MR-36	79.2	90.7	133.1	194.2	220.7	0.01	0.04	0.30	0.56	0.08	0.00	0.00
AR17MR-11	1.4	2.3	6.3	17.9	30.2	0.30	0.66	0.03	0.01	0.00	0.00	0.00
AR17MR-12	2.5	3.6	15.0	79.1	108.3	0.18	0.59	0.15	0.07	0.01	0.00	0.00
AR17MR-13	3.4	5.2	37.5	109.1	133.4	0.12	0.49	0.25	0.12	0.01	0.00	0.00
AR17MR-14	2.7	3.7	16.1	83.4	106.5	0.17	0.58	0.17	0.07	0.01	0.00	0.00
AR17MR-42	3.0	4.6	39.7	99.9	123.6	0.14	0.48	0.27	0.10	0.01	0.00	0.00
AR17MR-43	2.0	3.0	12.2	59.3	80.9	0.21	0.63	0.12	0.04	0.00	0.00	0.00
AR17MR-44	1.8	2.7	10.3	39.4	55.3	0.23	0.69	0.07	0.01	0.00	0.00	0.00
AR17MR-45	1.5	2.3	7.8	23.4	39.2	0.28	0.68	0.03	0.01	0.00	0.00	0.00
AR17MR-46	89.9	103.6	160.2	230.6	260.3	0.01	0.02	0.19	0.61	0.16	0.00	0.00
AR17MR-05	1.8	2.6	11.0	41.1	103.4	0.25	0.66	0.08	0.01	0.00	0.00	0.00
AR17MR-06	1.0	2.1	6.2	17.6	25.3	0.32	0.66	0.02	0.00	0.00	0.00	0.00
AR17MR-07	1.6	2.4	7.8	28.8	46.2	0.27	0.67	0.05	0.01	0.00	0.00	0.00
AR17MR-08	1.7	2.9	8.9	81.8	57.2	0.22	0.55	0.15	0.07	0.00	0.00	0.00

D*n* = *n*th percentile particle diameter (e.g., D_{10} = 10^{th} percentile particle size)

Table B7. Sediment and organic carbon flux results.

Sample name	River km	Flow depth	Q_w	Sample height above bed	Normalized water depth	D_{10}	D_{50}	D_{90}	fraction <4 μm (f_f)	$f_{f\text{-}DI}$
	km	m	m3/s	m		μm	μm	μm		
AR17MR-30	-15	1.0	129	0.0	1.0	85	193	389	0.01	
AR17MR-31	-15	1.0	129	1.0	0.0	2	7	33	0.17	
AR17MR-24	0	3.4	866	3.4	0.0	2	8	55	0.24	0.10
AR17MR-25	0	3.4	866	2.4	0.3	4	150	313	0.09	
AR17MR-26	0	3.4	866	1.4	0.6	4	109	280	0.10	
AR17MR-27	0	3.4	866	0.0	1.0	202	325	523	0.00	
AR17MR-32	135	4.0	673	1.0	0.8	2	10	82	0.21	0.18
AR17MR-33	135	4.0	673	2.0	0.5	2	11	142	0.20	
AR17MR-34	135	4.0	673	3.0	0.3	3	22	147	0.15	
AR17MR-35	135	4.0	673	4.0	0.0	2	8	58	0.23	
AR17MR-36	135	4.0	673	0.0	1.0	79	133	221	0.01	
AR17MR-11	420	3.0	744	3.0	0.0	1	6	30	0.30	0.15
AR17MR-12	420	3.0	744	2.0	0.3	2	15	108	0.18	
AR17MR-13	420	3.0	744	1.5	0.5	3	37	133	0.12	
AR17MR-14	420	3.0	744	0.5	0.8	3	16	106	0.17	
AR17MR-42	865	5.7	1079	1.2	0.8	3	40	124	0.14	0.24
AR17MR-43	865	5.7	1079	2.2	0.6	2	12	81	0.21	
AR17MR-44	865	5.7	1079	3.7	0.4	2	10	55	0.23	
AR17MR-45	865	5.7	1079	5.7	0.0	1	8	39	0.28	
AR17MR-46	865	5.7	1079	0.0	1.0	90	160	260	0.01	
AR17MR-05	1220	4.0	722	1.3	0.7	2	11	103	0.25	0.27
AR17MR-06	1220	4.0	722	4.0	0.0	1	6	25	0.32	
AR17MR-07	1220	4.0	722	2.0	0.5	2	8	46	0.27	
AR17MR-08	1220	4.0	722	2.8	0.3	2	9	57	0.15	

Q_w = water discharge

Normalized water depth = sample depth divided by total water depth (surface water = 0, river bed = 1)

D*n* = *n*th percentile particle diameter (e.g., D_{10} = 10th percentile particle size)

f_f = fraction of fine (<4 μm) suspended sediment in a river sediment sample

Table B7. (continued) Sediment and organic carbon flux results.

Sample name	SSC	SSC_{DI}	<4 µm SSC	<4 µm SSC_{DI}	>4 µm SSC	>4 µm SSC_{DI}	% <4 µm	Qs <4 µm	Qs >4 µm	TOC	TOC_{DI}
	mg/L	mg/L	mg/L	mg/L	mg/L	mg/L	%	kg/s	kg/s	weight %	weight %
AR17MR-30	nm									0.08	0.19
AR17MR-31	nm									0.33	
AR17MR-24	3979	7049	971	666	3008	6542	10	577	5665	0.23	0.18
AR17MR-25	6942		645		6297					0.18	
AR17MR-26	6625		684		5941					0.14	
AR17MR-27										0.01	
AR17MR-32	4590	5320	968	1089	3622	4557	24	733	3067	0.28	0.24
AR17MR-33	7120		1400		5720					0.20	
AR17MR-34	6282		927		5355					0.25	
AR17MR-35	3714		866		2848					0.31	
AR17MR-36	nm									0.13	
AR17MR-11	6826	18672	2053	2619	4773	13378	20	1949	9953	0.36	0.30
AR17MR-12	12348		2188		10160					0.32	
AR17MR-13	23913		2903		21010					0.27	
AR17MR-14	17000		2856		14144					0.31	
AR17MR-42	15435	11005	2142	1944	13293	9153	21	2098	9876	0.20	0.23
AR17MR-43	9238		1926		7311					0.23	
AR17MR-44	7858		1799		6060					0.24	
AR17MR-45	5908		1644		4264					0.27	
AR17MR-46	nm									0.01	
AR17MR-05	17070	13020	4282	3250	12788	9849	33	2347	7111	0.30	0.28
AR17MR-06	10670		3387		7283					0.30	
AR17MR-07	10520		2865		7655					0.29	
AR17MR-08	9830		2153		7677					0.26	

SSC = suspended sediment concentration
Qs = suspended sediment flux
DI = depth-integrated value for a river depth profile
TOC = total organic carbon concentration

Table B7. (continued) Sediment and organic carbon flux data.

Sample name	<4 µm TOC_{DI}	>4 µm TOC_{DI}	<4 µm Q_{POC}	>4 µm Q_{POC}	% Q_{POC} <4 um	Q_{POC} total	Q_{POC}/Q_w	<4 µm Q_{POC}/Q_w	>4 µm Q_{POC}/Q_w
	weight %	weight %	kgC/s	kgC/s	%	kgC/s	kgC/m3	kgC/m3	kgC/m3
AR17MR-30									
AR17MR-31									
AR17MR-24	0.20	0.17	53	430	11	482	0.56	0.06	0.50
AR17MR-25									
AR17MR-26									
AR17MR-27									
AR17MR-32	0.25	0.24	210	824	20	1033	1.54	0.31	1.22
AR17MR-33									
AR17MR-34									
AR17MR-35									
AR17MR-36									
AR17MR-11	0.24	0.31	250	2248	10	2498	3.36	0.34	3.02
AR17MR-12									
AR17MR-13									
AR17MR-14									
AR17MR-42	0.28	0.21	576	2138	21	2714	2.51	0.53	1.98
AR17MR-43									
AR17MR-44									
AR17MR-45									
AR17MR-46									
AR17MR-05	0.30	0.28	654	1584	29	2239	3.10	0.91	2.19
AR17MR-06									
AR17MR-07									
AR17MR-08									

DI = depth-integrated value for a river depth profile
TOC = total organic carbon concentration
POC = volumetric particulate organic carbon concentration
Q_{POC} = fluvial particulate organic carbon flux
Q_w = water discharge

Table B8. Data used to estimate Rouse profiles and depth-integrated concentrations of fine and coarse suspended sediment

River km	Rouse Number <4 μm	Rouse Number >4 μm	SSC_{DI} <4 μm	SSC_{DI} >4 μm	Best-fit equation for SSC_f vs. f_f	R-squared value	Best-fit equation for f_f vs. POC_f	R-squared value
			mg/L	mg/L				
-10	-0.11	0.2	666	6542	f_f = -5.19E-05*SSC + 0.450	0.999	POC_f = 0.874* f_f + 0.044	0.842
135	0.06	0.12	1089	4557	f_f = -1.61E-05*SSC + 0.284	0.475	POC_f = 0.701* f_f + 0.121	0.304
420	0.07	0.27	2619	13378	f_f = -9.71E-06*SSC + 0.338	0.842	POC_f = 0.476* f_f + 0.222	0.901
865	0.04	0.18	1944	9153	f_f = -1.38E-05*SSC + 0.346	0.96	POC_f = 0.949* f_f + 0.027	0.942
1220	0.01	0.08	3250	9849	f_f = -6.68E-06*SSC + 0.365	0.539	POC_f = 0.275* f_f + 0.221	0.769

SSC_{DI} = depth-integrated suspended sediment concentration for a river depth profile

SSC_f = fine (<4 μm) suspended sediment concentration for a river depth profile

f_f = fraction of fine (<4 μm) suspended sediment in a river sediment sample

Table B9. Time-series samples collected at river km 865 (PLV).

Sample ID	Info	Q_w m^3/s	Date	Month	Day	Year
PLV_01062017	June 1 + June 9	314	6/6/17	June	6	2017
PLV_12062017	June 12, 22, 28	252	6/12/17	June	12	2017
PLV_09072017	July 9, 12, 21, 26	150	7/9/17	July	9	2017
PLV_07092017	September 7, 14, 22, 29, Oct 09, 19, 29	66	9/7/17	September	7	2017
PLV_11122017	single sample	112	12/11/17	December	11	2017
PLV_12012018	single sample	386	1/12/18	January	12	2018
PLV_21022018	single sample	1162	2/21/18	February	21	2018
PLV_16032018	single sample	1290	3/16/18	March	16	2018

Q_w = water discharge

APPENDIX C

Supporting Information for

Chapter 5: The role of sediment transit time and mineral protection in fluvial organic carbon cycling

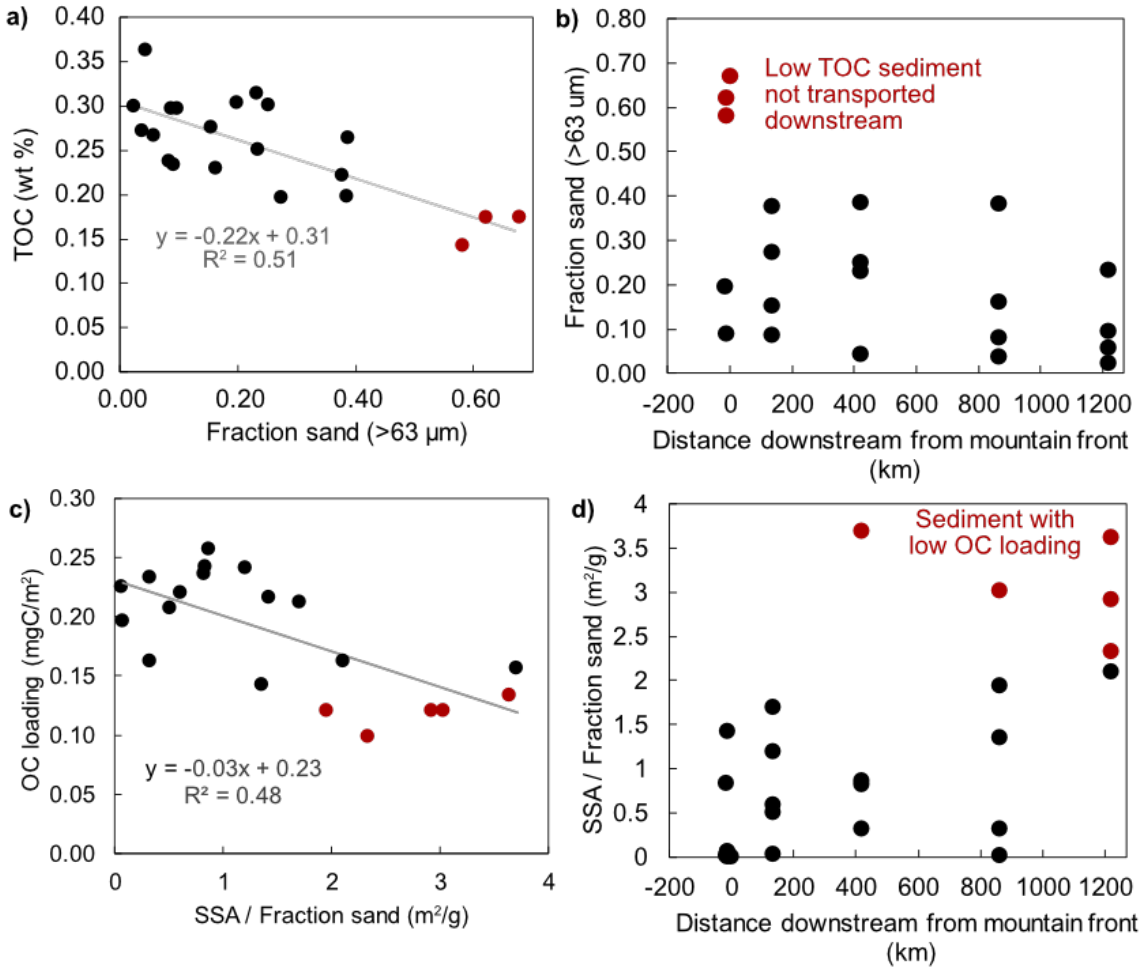

Figure C1. Effects of sediment grain size and specific surface area (SSA) on along-channel changes in POC content and loading. A) fraction of sand-sized particles vs. TOC (weight %), b) distance downstream along the channel vs. fraction of sand-sized particles, c) Specific surface area (SSA) normalized by fraction of sand-sized particles vs. OC loading, and d) distance downstream along the channel vs. SSA normalized by fraction of sand-sized particles.

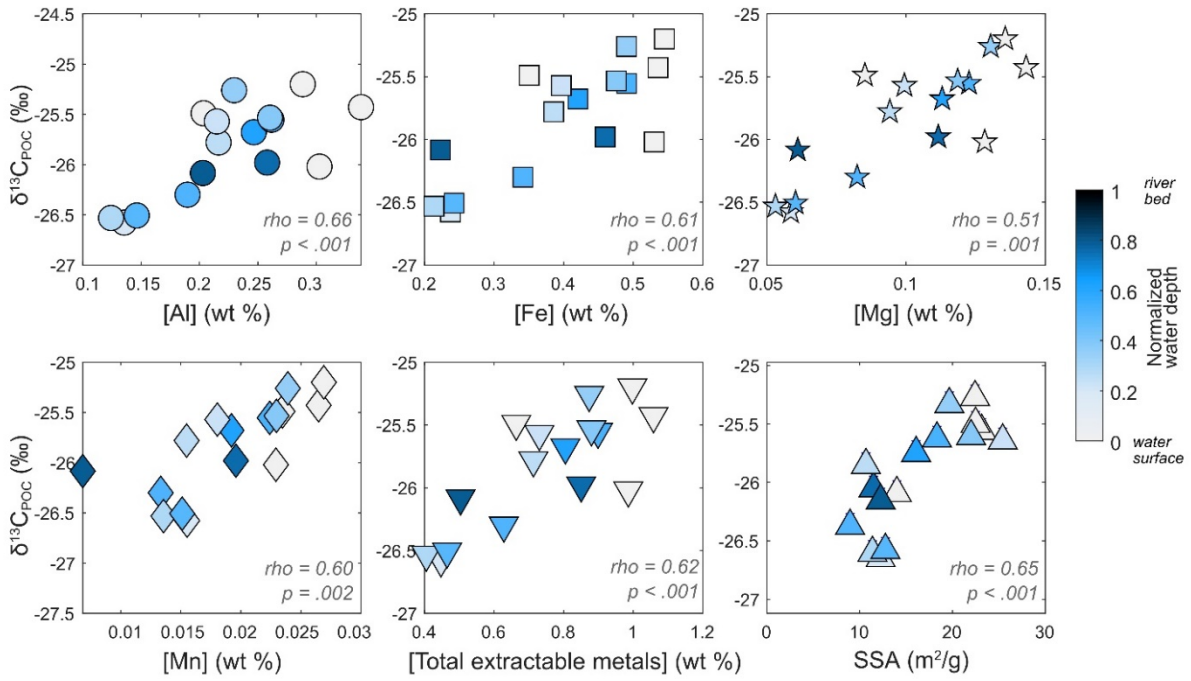

Figure C2. Relationships between acid extractable metal concentrations, specific surface area (SSA), and $\delta^{13}C$ values of organic carbon in suspended sediment samples ($\delta^{13}C_{POC}$). Rho is the Pearson correlation coefficient, and the p-value indicates the statistical significance of those relationships.

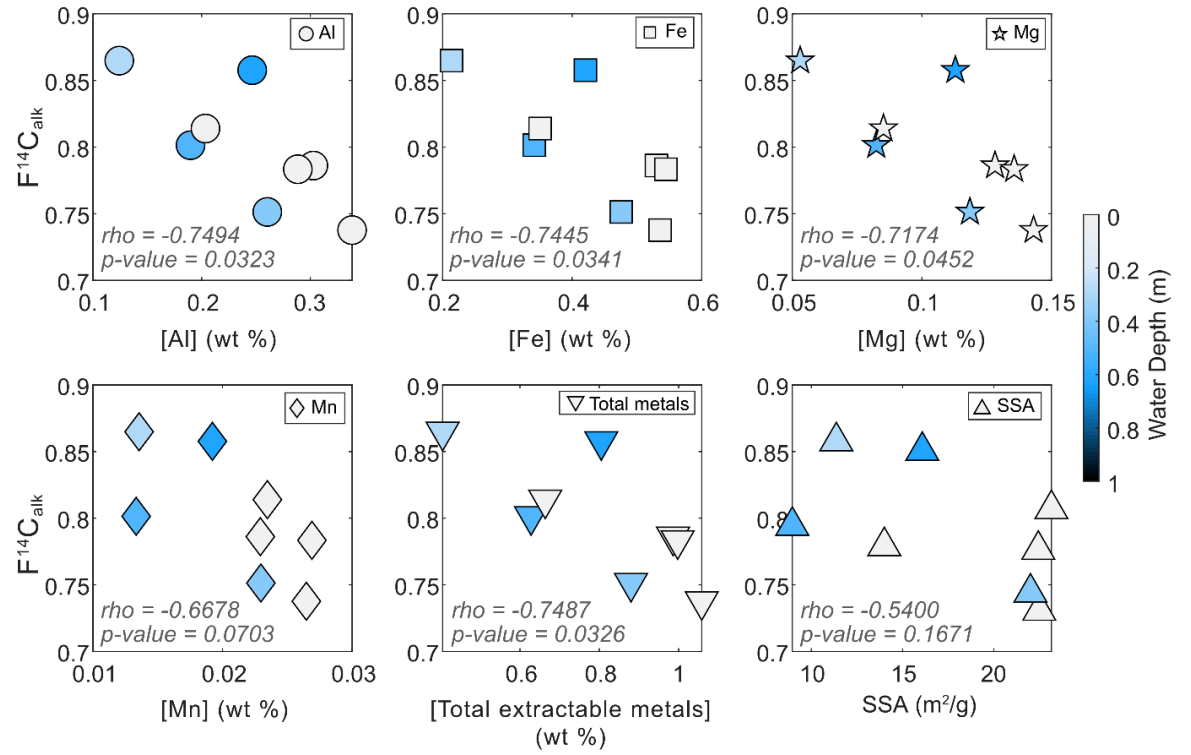

Figure C3. Relationships between acid extractable metal concentrations, specific surface area (SSA), and $F^{14}C$ values of C_{27}, C_{29}, C_{31}, and C_{33} *n*-alkanes in suspended sediment samples ($F^{14}C_{alk}$). Rho is the Pearson correlation coefficient, and the p-value indicates the statistical significance of those relationships.

Table C1. Data collected for suspended sediment samples from granulometric, carbon isotope, and extractable metal ion measurements.

Sample ID	Distance downstream[a]	Sediment transit time	Relative water depth[b]	D_{50}[c]	Fraction sand	SSC[d]	SSC_{DI}	TOC	TOC_{DI}	SSA[e]	SSA_{DI}
	km	yr		μm		mg/L	mg/L	%	wt %	m^2/g	m^2/g
AR17MR-31	-15		0.00	15.2	0.20	4000		0.31	0.19 ± 0.12	12.60	7.59
AR17MR-30			1.00	209.7	0.94			0.07		2.59	
AR17MR-24	-10		0.00	7.6	0.09	3979	7049	0.23	0.18 ± 0.04	10.83	6.92
AR17MR-25			0.30	140.7	0.62	6942		0.18		7.76	
AR17MR-26			0.59	112.9	0.58	6625				7.28	
AR17MR-27			1.00	324.2	1.00			0.01		1.16	
CONFLUENCE	0	0			0.67		7000		0.18 ± 0.06		5.88
AR17MR-35	135	350 ± 270	0.00	8.2	0.09	3714	5320	0.30	0.24 ± 0.04	14.00	11.32
AR17MR-34			0.25	21.0	0.38	6282		0.22		10.67	
AR17MR-33			0.50	15.0	0.27	7120		0.20		8.96	
AR17MR-32			0.75	9.6	0.15	4590		0.28		11.48	
AR17MR-36			1.00	132.4	0.95			0.06		3.18	
AR17MR-11	420	840 ± 324	0.00	6.3	0.04	6826	18672	0.36	0.30 ± 0.04	23.15	11.95
AR17MR-12			0.20	14.2	0.23	12348		0.32		12.25	
AR17MR-13			0.30	35.5	0.39	23913		0.27		11.37	
AR17MR-14			0.49	15.7	0.25	17000		0.30		12.77	
AR17MR-45	865	5330 ± 340	0.00	7.4	0.04	5908	11005	0.27	0.23 ± 0.03	22.49	16.49
AR17MR-44			0.35	10.1	0.08	7858		0.24		19.66	
AR17MR-43			0.62	11.9	0.16	9238		0.23		16.08	
AR17MR-42			0.80	38.4	0.38	15435		0.20		12.25	
AR17MR-46			1.00	160.3	0.97			0.01		2.16	
AR17MR-06	1220	8520 ± 596	0.00	6.2	0.02	10670	13020	0.30	0.28 ± 0.02	22.43	20.94
AR17MR-08			0.23	10.9	0.23	9830		0.25		25.41	
AR17MR-07			0.38	7.6	0.06	10520		0.27		22.00	
AR17MR-05			0.52	8.7	0.10	17070		0.30		18.32	

[a] Distance downstream = along-channel distance from the Rio San Francisco-Rio Bermejo confluence

[b] Relative water depth is normalized to the total channel depth in the thalweg

[c] D_{50} = 50th percentile particle size diameter

[d] SSC = suspended sediment concentration

[e] SSA = mineral specific surface area

Subscript DI = depth-integrated value

Table C1. (continued) Data collected for suspended sediment samples from granulometric, carbon isotope, and extractable metal ion measurements.

OC loading	OC loading	$\delta^{13}C$	$\delta^{13}C_{DI}$	$F^{14}C$	$F^{14}C_{DI}$	$F^{14}C_{alk}$	Al_{reac}	Fe_{reac}	Mg_{reac}	Mn_{reac}	Total reactive metals
mgC/m^2	mgC/m^2	‰	‰				wt %	wt %	wt %	wt %	wt %
0.24	0.26 ± 0.0	-25.70 ± 0.2	-26.49	0.91 ± 0.0	0.92 ±		0.25	0.39	0.12	0.02	0.78
0.28		-27.27 ± 0.2	0.43	0.92 ± 0.0	0.01		0.07	0.10	0.03	0.00	0.21
0.22	0.21 ± 0.0	-26.29 ± 0.2	-26.04	0.80 ± 0.0	0.82 ±		0.30	0.64	0.22	0.03	1.19
0.23		-26.72 ± 0.2		0.86 ± 0.0			0.21	0.41	0.09	0.02	0.74
0.20		-24.90 ± 0.2	0.30	0.78 ± 0.0	0.01		0.22	0.38	0.09	0.02	0.72
0.07		-26.29 ± 0.2		0.49 ± 0.0			0.12	0.19	0.04	0.00	0.36
	0.22 ± 0.0	-26.10 ± 0.2			0.83 ± 0.02						
0.21		-26.02 ± 0.20		0.88 ± 0.01		0.79 ± 0.01	0.30	0.53	0.13	0.02	0.99
0.21		-25.78 ± 0.20		0.88 ± 0.01			0.22	0.39	0.09	0.02	0.71
0.22	0.22 ± 0.01	-26.30 ± 0.20	-25.96 ± 0.26	0.88 ± 0.01	0.88 ± 0.01	0.80 ± 0.01	0.19	0.34	0.08	0.01	0.63
0.24		-25.98 ± 0.20		0.89 ± 0.01			0.26	0.46	0.11	0.02	0.85
0.18		-27.12 ± 0.20		0.78 ± 0.01			0.07	0.13	0.03	0.00	0.24
0.16		-25.49 ± 0.20		0.87 ± 0.01		0.81 ± 0.01	0.20	0.35	0.09	0.02	0.66
0.26	0.23 ± 0.04	-26.58 ± 0.20	-26.39 ± 0.28	0.94 ± 0.01	0.92 ± 0.01		0.14	0.24	0.06	0.02	0.45
0.23		-26.53 ± 0.20		0.91 ± 0.01		0.86 ± 0.01	0.12	0.21	0.05	0.01	0.41
0.24		-26.51 ± 0.20		0.92 ± 0.01			0.15	0.24	0.06	0.02	0.46
0.12		-25.43 ± 0.20		0.85 ± 0.01		0.74 ± 0.01	0.34	0.54	0.14	0.03	1.06
0.12		-25.26 ± 0.20		0.85 ± 0.01			0.23	0.49	0.13	0.02	0.87
0.14	0.14 ± 0.02	-25.68 ± 0.20	-25.68 ± 0.27	0.87 ± 0.01	0.88 ± 0.01	0.86 ± 0.01	0.25	0.42	0.11	0.02	0.80
0.16		-26.08 ± 0.20		0.92 ± 0.01			0.20	0.22	0.06	0.01	0.50
0.06		-26.07 ± 0.20		0.59 ± 0.01			0.07	0.08	0.02	0.00	0.17
0.13		-25.20 ± 0.20		0.83 ± 0.01		0.78 ± 0.01	0.29	0.54	0.14	0.03	1.00
0.10	0.13 ± 0.02	-25.57 ± 0.20	-25.47 ± 0.27	0.88 ± 0.01	0.86 ± 0.01		0.21	0.40	0.10	0.02	0.73
0.12		-25.53 ± 0.20		0.84 ± 0.01		0.75 ± 0.02	0.26	0.48	0.12	0.02	0.88
0.16		-25.55 ± 0.20		0.88 ± 0.01			0.26	0.49	0.12	0.02	0.90

$\delta^{13}C$ = stable carbon isotope composition of POC

$F^{14}C$ = radiocarbon content of POC expressed as fraction modern

reac = extracted from the reactive secondary mineral coating

DI = depth-integrated value for river depth-profile

Table C2. Mean isotopic values of floodplain sediment, topsoil, and leaf litter samples within the catchment.

Source file[a]					
Source	Mean δ13C	SD δ13C	Mean F14C	SD F14C	n
Topsoil	-24.41	3.63	0.98	0.06	17
Floodplain sediment	-22.17	2.94	0.77	0.15	51
Leaf litter	-25.68	4.37	1.00	0.01	6

SD = standard deviation of the mean

[a] Means and standard deviations are derived from sets of topsoil, floodplain sediment, and leaf litter samples collected throughout the catchment

Table C3. Mixing model results representing the fraction of floodplain OC, leaf litter OC, and topsoil OC in each suspended sediment sample.

Sample Name	Fraction floodplain[a]	Fraction leaf litter[a]	Fraction topsoil[a]	POCfast[b]	POCslow
AR17MR-31	0.44 ± 0.09	0.38 ± 0.14	0.19 ± 0.14	0.56 ± 0.20	0.44 ± 0.09
AR17MR-24	0.54 ± 0.17	0.29 ± 0.17	0.17 ± 0.16	0.46 ± 0.23	0.54 ± 0.17
AR17MR-25	0.50 ± 0.17	0.32 ± 0.17	0.18 ± 0.17	0.50 ± 0.25	0.50 ± 0.17
AR17MR-26	0.42 ± 0.17	0.37 ± 0.20	0.21 ± 0.20	0.58 ± 0.28	0.42 ± 0.17
AR17MR-32	0.44 ± 0.17	0.35 ± 0.19	0.21 ± 0.19	0.56 ± 0.27	0.44 ± 0.17
AR17MR-33	0.27 ± 0.16	0.51 ± 0.24	0.23 ± 0.22	0.73 ± 0.33	0.27 ± 0.16
AR17MR-34	0.32 ± 0.17	0.45 ± 0.22	0.23 ± 0.22	0.68 ± 0.31	0.32 ± 0.17
AR17MR-35	0.30 ± 0.16	0.47 ± 0.23	0.23 ± 0.22	0.70 ± 0.31	0.30 ± 0.16
AR17MR-11	0.56 ± 0.16	0.28 ± 0.16	0.16 ± 0.15	0.44 ± 0.22	0.56 ± 0.16
AR17MR-12	0.44 ± 0.17	0.36 ± 0.19	0.20 ± 0.19	0.56 ± 0.27	0.44 ± 0.17
AR17MR-13	0.62 ± 0.15	0.24 ± 0.14	0.15 ± 0.14	0.38 ± 0.20	0.62 ± 0.15
AR17MR-14	0.35 ± 0.17	0.42 ± 0.22	0.23 ± 0.21	0.65 ± 0.30	0.35 ± 0.17
AR17MR-42	0.40 ± 0.17	0.38 ± 0.20	0.21 ± 0.20	0.60 ± 0.29	0.40 ± 0.17
AR17MR-43	0.41 ± 0.17	0.38 ± 0.20	0.22 ± 0.20	0.59 ± 0.28	0.41 ± 0.17
AR17MR-44	0.41 ± 0.17	0.39 ± 0.20	0.21 ± 0.20	0.59 ± 0.29	0.41 ± 0.17
AR17MR-45	0.42 ± 0.17	0.36 ± 0.20	0.21 ± 0.20	0.58 ± 0.28	0.42 ± 0.17
AR17MR-05	0.31 ± 0.17	0.46 ± 0.23	0.23 ± 0.21	0.69 ± 0.31	0.31 ± 0.17
AR17MR-06	0.44 ± 0.17	0.35 ± 0.19	0.20 ± 0.19	0.56 ± 0.27	0.44 ± 0.17
AR17MR-07	0.50 ± 0.17	0.31 ± 0.18	0.19 ± 0.18	0.50 ± 0.25	0.50 ± 0.17
AR17MR-08	0.48 ± 0.16	0.33 ± 0.18	0.19 ± 0.18	0.52 ± 0.26	0.48 ± 0.16
Mean at river km 0[c]				0.53 ± 0.17	0.47 ± 0.10

[a] uncertainty reported as standard deviation of MixSIAR posterior distributions

[b] POCfast = fraction leaf litter + fraction topsoil

[c] weighted mean of AR17MR-31, 24, 25, and 26, weighted by suspended sediment concentration; uncertainty reported as standard error of the weighted mean

Table C4. Radiocarbon data used to estimate decomposition rates for POCslow and POCfast.

C pool	$F^{14}C$	λ	τ	k	source
		1/yr	yr	1/yr	
POC_{slow}	0.740	1.21E-04	2905	4.00E-04	this study
POC_{fast}	0.998	1.21E-04	17	6.00E-02	Carvalhais et al. 2014

λ = ^{14}C decay constant (1.21×10^{-4})

τ = organic carbon turnover time

k = organic carbon decomposition rate

Table C5. Organic carbon turnover estimates for the Rio Bermejo.

	Distance along channel	Reach length	Mean transit time through reach	Mean sediment velocity	Sediment deposition-erosion cycles	Turnover length scale POC_{slow}[a]	Turnover length scale POC_{fast}[a]	Number of POC_{slow} turnover cycles[a]	Number of POC_{fast} turnover cycles[a]	POC_{slow} total turnover[b]	POC_{fast} total turnover[b]	POC_{slow} oxidation flux[b]	POC_{fast} oxidation flux[b]
	km	km	yr	km/yr		km	km			MtC	MtC	tC/yr	tC/yr
Reach 1	0 - 135	135	350 ± 270	0.39 ± 0.17	0.50	953 ± 415	6.43 ± 2.80	0.12 ± 0.04	21.0 ± 6.36	0.01 (+0.01/-0.01)	2.33 (+1.48/-1.08)	29.5 (+22.9/-16.4)	5880 (+4240/-3100)
Reach 2	135 - 422	287	490 ± 180	0.59 ± 0.16	1.70	1450 ± 388	9.77 ± 2.62	0.17 ± 0.04	29.39 ± 6.21	0.01 (+0.01/-0.01)	3.26 (+1.73/-1.34)	29.6 (+19.2/-14.7)	5880 (+3530/-2730)
Reach 3	422 - 866	444	4490 ± 100	0.10 ± 0.00	3.37	244 ± 5.56	1.65 ± 0.04	1.52 ± 0.03	269 ± 5.98	0.13 (+0.05/-0.05)	29.9 (+9.24/-8.86)	29.5 (+11.6/-11.1)	5880 (+2060/-1970)
Reach 4	866-1221	355	3190 ± 490	0.11 ± 0.02	3.88	274 ± 37.0	1.85 ± 0.25	1.09 ± 0.13	192 ± 22.8	0.10 (+0.05/-0.04)	21.30 (+8.99/-7.56)	29.6 (+15.5/-13.0)	5900 (+2820/-2370)
Averaged over full river length	0 - 1267	1267	8520 ± 596	0.15 ± 0.07	4.50	358 ± 161	2.42 ± 1.08	2.97 ± 0.92	524 ± 162	0.26 (+0.20/-0.14)	58.2 (+37.5/-27.3)	30.4 (+23.8/-17.0)	6050 (+4410/-3210)

[a] Uncertainty propagated from sediment transit velocity

[b] Uncertainty represents maximum and minimum range propagated from sediment transit time and mixing model uncertainties